Title
Development of bioluminescent sensors for interrogating cyclic di-nucleotide signaling

Author
Dippel, Andrew B

Publication Date
2019

Peer reviewed|Thesis/dissertation

Development of bioluminescent sensors for interrogating cyclic di-nucleotide signaling

By

Andrew B Dippel

A dissertation submitted in partial satisfaction of the
requirements for the degree of
Doctor of Philosophy
in
Chemistry
in the
Graduate Division
of the
University of California, Berkeley

Committee in charge:

Professor Ming C. Hammond, Co-Chair
Professor Matthew B. Francis, Co-Chair
Professor Michelle C. Y. Chang
Professor Donald C. Rio

Summer 2019

Abstract

Development of bioluminescent sensors for interrogating

cyclic di-nucleotide signaling

By

Andrew B Dippel

Doctor of Philosophy in Chemistry

University of California, Berkeley

Professor Ming C. Hammond, Co-Chair

Bioluminescence is the spectacular natural phenomenon in which living organisms produce and emit light. Natural bioluminescent protein systems have been discovered and characterized in over 30 species, ranging from fireflies to fungi and bacteria. Significant effort has been put towards engineering and improving these natural systems so that they may be used as tools for interrogating biological processes. As opposed to fluorescence, because bioluminescence requires no excitation light to produce a signal, it has proven extremely useful for imaging in highly autofluorescent samples, such as within deep tissues of whole organisms. To date, however, most bioluminescent imaging systems have been developed solely for the study of eukaryotic systems, and few have focused on the study of bacteria. Bacteria naturally colonize highly diverse and complex environments, from gastrointestinal tracts to soil and plant surfaces, that have proven difficult to study with currently available fluorescent tools. To allow for the study of bacterial signaling within these complex environments, new bioluminescent sensors developed specifically for bacterial signaling are needed.

Here, we describe the development and application of bioluminescent sensors for the bacterial cyclic di-nucleotide (CDN) signaling molecule cyclic di-GMP. Cyclic di-GMP is nearly ubiquitous in bacteria and plays a key role in the controlling motility and biofilm formation. As a first-generation bioluminescent sensor system, we developed intensity-based bioluminescent sensors for cyclic di-GMP. These sensors proved useful as in vitro tools for studying cyclic di-GMP, however were not amenable to live cell imaging. To move beyond purely in vitro systems, we developed next-generation ratiometric bioluminescent sensors for cyclic di-GMP. This next-generation system led to significantly improved sensor properties and allowed for the imaging of small numbers of live bacterial cells in an animal tissue-like model system. Finally, to expand these sensor systems to CDNs other than cyclic di-GMP, we applied a novel directed evolution approach to find sensors that respond to cyclic GMP-AMP. The first round of directed evolution was not successful, but work is ongoing on this front. Collectively, the work presented here lays the groundwork for using bioluminescent sensor systems to interrogate signaling in bacteria in their natural environments, which was previously not possible.

For Sophia

TABLE OF CONTENTS

ACKNOWLEDGEMENTS

Given the fact that both of my grandfathers were PhD chemists, it was almost inevitable that I ended up following a similar path. While growing up I always knew I had an affinity for math, chemistry, and physics, I certainly had no idea that I would end up heading to grad school and pursuing a PhD. Along the way, there have been many people that were instrumental in helping to get where I am today.

My first thanks goes to my undergraduate research advisor, Professor Christine Phillips-Piro. If you hadn't taken me aside during our intro biochem lab to ask me if I was interested in doing research in your lab that summer, I am not sure that I would be where I am today! Before joining your lab I had no idea what grad school really was, and beyond that, that you even get paid (although not a lot…) to attend! That next year in your lab showed me what being a scientist is really about, and that you can live a normal, fun life outside of the lab. I found that I really enjoyed the research process, and my love of all things fluorescent and luminescent began. Your support and guidance in helping me apply to grad school was instrumental in me ultimately ending up at Berkeley.

At Berkeley, obviously, none of this work would have been possible without the guidance and support of Professor Ming Hammond. When I first came to Berkeley, I frankly had no idea about the Hammond lab. It was not until my rotation that I saw how supportive and fun the lab culture was, and I knew that it would be the best place for me to complete my PhD. Ming, I am incredibly grateful that you gave me the freedom to develop a project in a completely new research area in the lab, and your passion and excitement for science continue to be an incredible example for me to aspire to. Despite the ups and downs and uncertainty associated with the tenure decision, I would not have had it any other way.

Also, of course, I would not have had such a positive experience in grad school without the rest of the members of the Hammond lab. Huge thanks to the senior-most students, Zach and Cindy, for your incredible insight and advice in those early years of grad school. To Yichi, I am so happy to be able to call you both a colleague and a friend. The way that you planned, executed, and communicated your science was a huge inspiration to me, and I am happy to say that I was finally able to develop my own "excellent" assay. To the graduate students from my cohort – Todd, Johnny, and Rebekah – I know for a fact that I would not have had such a positive experience in grad school had you all not been there with me. We got to experience all of the ups and downs together, and I am happy to call you all friends for life. To Wyatt, it has been incredible seeing how far you have progressed since initially joining the lab, and I couldn't have asked for a better undergrad to mentor – I'm sure you will be incredibly successful at whichever med school you end up attending! To Zhesen, it has been great having you around – I will fondly remember the winter of 2018-2019 for the rest of my life! To the new students, Scotty and Kylie, it has been great seeing you grow and take on responsibility within the lab at such an early stage, and I'm sure the lab will be in good hands with you both. Outside of the Hammond lab, I am thankful for the friends I made throughout the department. To Greg, especially, I'm happy that we crossed paths so early on in grad school, and I know that I can always count on you for a for a good time.

Outside of Berkeley, I also would not be where I am today without the support of friends and family. To the “group chat” crew, I’m happy to say that even though we’ve all been in different states for the past five years, it feels like I always know what’s going on in your lives. To Sam and Andrew, I am so incredibly grateful for our friendship. Honestly, the biggest bummer about leaving Berkeley was no longer being able to hang out with you guys all the time. Thankfully, this just means I always have a reason to visit San Francisco! To my parents, thank you for the support throughout my entire education. You instilled in the importance of my education from an early age, and that mindset has stuck with me throughout all my years of school. Without your love and support I likely wouldn’t have ended up at F&M, which likely means I would not have ended up at Berkeley! It will be exciting living closer to home again.

And finally, the biggest thanks to Sophia. Throughout everything, you have always been a constant in my life. You stuck with me unconditionally throughout all of the weirdness of grad school, and I am happy to call you my soon-to-be wife. We’ve lived many different lives together throughout these past five years, but I’m most excited to see what comes next.

Chapter One

Bioluminescence as a tool for studying biological systems

Portions of this chapter have been published in:

Wright, T. A., Dippel, A. B., Hammond, M. C. “Cyclic di-GMP signaling gone astray: cGAMP signaling via Hypr GGDEF and HD-GYP enzymes” In Chou, S.-H., Guilliani, N., Lee, V., Romling U. (ed), Microbial cyclic di-nucleotide signaling.

Luminescence is the spectacular natural phenomenon of the light emission by a substance. We see luminescence all over the world, from glow sticks, to “black light” paints, to fireflies. Broadly, the luminescence process occurs by the excited state of a molecule releasing energy – in the form of light – upon relaxation to the ground state. There are many sub-types of luminescence that are differentiated by the way in which the excited state intermediate is generated. The most common of these are photoluminescence and chemiluminescence. In photoluminescence, the excited state is generated by the absorption of light. The form of photoluminescence we are all familiar with, specifically, is fluorescence, and it is what causes “black light” paints to produce their characteristic glow when we shine light on them. In fluorescence, the compound that absorbs/emits light is called the fluorophore. Chemiluminescence, on the other hand, describes situations in which the excited state is generated by a chemical reaction, typically a redox reaction. One of the most common ways we see chemiluminescence is in glow sticks. When you “crack” a glow stick, you are mixing two compounds that react to form an excited state intermediate, which relaxes to give off the characteristic glow. Bioluminescence, such as what we see in fireflies, is a specialized type of chemiluminescence that is differentiated by the fact that the reaction is catalyzed by an enzyme. These enzymes, called luciferases, catalyze the oxidation of a small molecule, called a luciferin, to generate the excited state intermediate. While in North America we are probably most familiar with this phenomenon in fireflies, it has been evolved in many different organisms, including deep sea shrimp, sea pansies, jellyfish, click beetles, glow worms, and bacteria, to name a few. Luminescent systems, both fluorescent and chemiluminescent, beyond their wondrous visual qualities, have proven to be extremely versatile tools for studying biology.

Advantages of bioluminescence imaging

The discovery and development of the green fluorescent protein (GFP), for which the 2008 Nobel Prize was awarded, fundamentally changed the way we are able to visualize biomolecular process (Tsien, 1998). By producing a luminescent signal that is observable by a microscope, FPs can be used to watch processes that were previously invisible inside cells. Since the initial discovery and characterization of GFP, extensive efforts have been put towards the development and engineering of new FPs with ever-improving properties (Rodriguez et al., 2017). These improved properties, from new protein classes, altered colored palettes, and improved brightness, have together led to an astonishing number of different FP-based research applications, and there is no end in sight to the improvements that can be engineered and discovered naturally in these systems (Brakemann et al., 2019). However, while FP and fluorescence-based systems have proven invaluable for interrogating biological processes in the “culture dish”, there are some inherent drawbacks to fluorescence-based systems that preclude them from being applicable to imaging in more complex biological systems, such as within tissues and whole organisms (Contag et al., 1998; Rathbun and Prescher, 2017; Weissleder and Ntziachristos, 2003).

The limitations of fluorescence imaging generally arise due to the requirement of excitation light to produce a signal, and there are two main drawbacks to this: phototoxicity and autofluorescence. Firstly, the strong excitation light used in conventional fluorescence imaging to excite the fluorescent probes (small molecules or FPs) can lead

to phototoxicity and photobleaching in the biological samples being analyzed (Icha et al., 2017). Phototoxicity generally arises due to reactive oxygen species (ROS) being generated from the probes themselves, or from natural biological compounds, such as flavins and porphyrins. These ROS, including superoxide radicals and hydrogen peroxide, can directly oxidize DNA, causing mutations, or oxidize proteins, making them non-functional. This phototoxicity can produce unexpected side-effects that may ultimately reduce the reliability and reproducibility of the data obtained. Photobleaching, a related effect, occurs from the repeated excitation of fluorophore compounds. Once a fluorophore is photobleached, it is permanently degraded, and will no longer produce any fluorescent signal.

Both phototoxicity and photobleaching are especially problematic in long-term imaging experiments due to the amount of excitation light used. One solution to phototoxicity issues is the use of advanced microscopes have that provide “gentler” illumination that conventional epifluorescence microscopes. These illumination schemes, such as those used in total internal reflection fluorescence (TIRF) microscopy and light sheet fluorescence microscopy (LSFM), illuminate only the focal plane being analyzed, rather than the entire sample, which reduces overall phototoxicity (Icha et al., 2017). LSFM is currently the gentlest fluorescence microscopy technique available, and a recently developed LSFM technique allowed for imaging cell nuclei for >7 hours at high temporal resolution with no noticeable photodamaging effects (Fadero et al., 2018). One downside to the cutting-edge nature of these techniques, however, is that the most powerful LSFM microscopes are typically “homemade” and available to only a few labs worldwide (Power and Huisken, 2017).

Secondly, the excitation light required for fluorescence imaging is incompatible with samples that are highly autofluorescent, or samples that are engineered to respond to specific wavelengths of light (i.e. optogenetic systems). In autofluorescent samples, the sample itself absorbs excitation light and produces a highly fluorescent background signal, which can obscure the desired signal produced by the fluorescent probe, complicating analysis. Examples of highly autofluorescent samples include blood and animal tissue (due to porphyrins, flavins), and plant tissue (due to chlorophyll, pigments) (Monici, 2005; Zipfel et al., 2003). Beyond being highly autofluorescent, animal tissues significantly absorb any excitation light <600 nm, which is in the range used for many conventional fluorophores. In deep tissues (>mm depth) this effect is even more pronounced: excitation light is significantly absorbed and scattered, which prevents the use of conventional fluorescent probes for imaging in deep-tissues of whole organisms. In optogenetic systems, on the other hand, samples are engineered to produce a biological response after light absorption. One commonly used example of this is the activation of channelrhodopsin-expressing neurons via excitation with blue light (Wietek and Prigge, 2016). Channelrhodopsins are typically incompatible with the use of fluorescent probes, as cross-excitation between fluorophores and the channelrhodopsin leads to undesired perturbation of the process under study. Currently available solutions to these problems include the use of near infrared (NIR) fluorescent probes and multi-photon microscopy (MPM).

NIR probes absorb and emit photons >650 nm, which are outside the range of autofluorescence of most biological samples, and outside the activation range for many

optogenetic probes. Accordingly, NIR probes allow for a greatly improved signal to noise ratio compared to fluorescent probes in the visible range, and they have been used extensively in neuroimaging applications (Li et al., 2019). Similarly, red-shifted fluorescent probes have been used in combination with blue-light activated optogenetic systems (Shen et al., 2018). In MPM, fluorophore molecules are excited by absorption of multiple long-wavelength photons (~1300 nm or 1700 nm) which are not significantly absorbed or scattered by tissue. Accordingly, MPM is routinely used for imaging at depths beyond 1 mm (Miller et al., 2017), and recent work has even used MPM with the genetically encodable Ca^{2+} biosensor, GCaMP6, to image activity of neurons deep within intact mouse brain (Ouzounov et al., 2017). While these advancements in probe and microscope development have significantly alleviated the problems of light absorption and autofluorescence in biological samples, these techniques still require high power excitation light to produce a signal, which can lead to phototoxicity and tissue damage in the samples under study.

In contrast to fluorescence, chemiluminescence/bioluminescence can be used to generate a visible light signal without the need for external illumination, which neatly overcomes all of the above issues. Accordingly, several chemiluminescent and bioluminescent technologies have been developed in recent years that allow for analysis of samples that are not amenable to fluorescence imaging. In general, the advancement of these chemiluminescent systems mirrors that of FPs, with new colors, increased brightness, and improved properties continually being discovered and developed (Prescher and Contag, 2010; Yao et al., 2018). Here, I will describe the major innovations in these bioluminescent systems and how they have been applied to the development of sensors for analyzing biomolecular processes.

Natural bioluminescent systems

As mentioned previously, naturally occurring bioluminescent protein systems have evolved separately in many different organisms (Kaskova et al., 2016). In these systems, the luciferases (enzymes that catalyze bioluminescence reactions) have specific substrate molecules (luciferins), with the structures of both the luciferase enzymes and luciferin substrates often being highly divergent between each system. Of these many luciferase-luciferin systems, two have been extensively studied and utilized for bioimaging applications. These are the D-luciferin utilizing systems from beetles, and coelenterazine utilizing systems from marine organisms (Figure 1.1).

Bioluminescent systems using D-luciferin, which was the first luciferin molecule discovered, have historically been the most extensively used for *in vivo* imaging (Zhao et al., 2005). The luciferase from the North American firefly, *Photinus pyralis*, is the founding member of D-luciferin utilizing systems. Firefly luciferase (FLuc) is a 61 kDa protein that oxidizes D-luciferin to produce a broad emission spectrum with a yellow-orange peak (λ_{max} = 612 nm at 37 °C). This red-shifted emission has proven extremely useful for *in vivo* imaging as living tissue does not absorb significantly at wavelengths >600 nm. Luciferases from the luminous click beetle, *Pyrophorus plagiophtalamus*, that utilize D-luciferin have also been widely used (Miloud et al., 2007). There are multiple variants of click beetle luciferases which are distinguished by the color of their emission. Two of the most commonly used variants, red click beetle luciferase (CBR) and green click beetle

luciferase (CBG), are 61 kDa proteins that produce emission maxima at 611 nm and 544 nm, respectively. To catalyze the oxidation of D-luciferin, all beetle luciferases requires both ATP, Mg^{2+}, and O_2 as cofactors. This ATP dependence has made these luciferases valuable tools for the qualitative analysis of ATP levels in clinical samples, however it precludes the use of these luciferases in systems where ATP may be limiting, such as in extracellular spaces.

Coelenterazine-utilizing luciferase systems, on the other hand, require only O_2 to catalyze their bioluminescent reactions, and do not require ATP or Mg^{2+}. The luciferase from the sea pansy *Renilla reniformis* is the founding member of coelenterazine-utilizing systems. *Renilla* luciferase (RLuc) is a 36 kDa protein that oxidizes coelenterazine to produce an emission maximum at 480 nm (Matthews et al., 1977). Although the emission of RLuc is more blue-shifted than FLuc, making it slightly less attractive for use *in vivo*, because it uses a completely different substrate, it can be used in combination with FLuc to perform dual-reporter imaging studies (Bhaumik et al., 2004). The luciferase from the marine copepod *Gaussia princeps* is another commonly used coelenterazine-utilizing luciferase (Tannous et al., 2005). *Gaussia* luciferase (GLuc) is a 20 kDa enzyme that similarly produces an emission maximum at 480 nm. GLuc is naturally secreted to the extracellular space, which can be a benefit for *in vitro* reporter assays, however membrane-bound variants have also been engineered for use in live animal imaging (Santos et al., 2009).

Natural bioluminescent protein systems utilizing both D-luciferin and coelenterazine have proven extremely useful for many *in vivo* imaging applications. However, to expand the bioluminescent protein toolkit and permit the analysis of exceedingly hard-to-interrogate biological systems, a number of advancements have been made in engineering and optimizing these systems. In general, these advancements have come about as the result of a combination of enzyme evolution, luciferin analog development, and bioluminescence resonance energy transfer (BRET).

Engineered bioluminescent systems

As mentioned previously, FLuc has been the most widely utilized bioluminescent reporter for *in vivo* imaging, largely due to its red-shifted emission spectra. Some drawbacks to FLuc, however, are its low catalytic activity and low thermal stability, which ultimately cause the enzyme to produce a lower than desired signal within biological samples. Accordingly, many efforts have focused on improving these properties via directed enzyme evolution, and there are multiple FLuc mutants available that exhibit improvements in these properties (Kaskova et al., 2016; Pozzo et al., 2018). Similar efforts have focused on engineering improved properties in RLuc, and have resulted in mutants with increased light output (RLuc8) (Loening et al., 2006) and red-shifted emission (RLuc8.6-535) (Loening et al., 2007). Directed evolution of natural luciferases is inherently limited by the emissive properties of the luciferin substrate, however, so considerable effort has also focused on developing new and improved luciferin substrates in parallel with directed evolution of the luciferase enzymes (Figure 1.2).

Improvements in D-luciferin substrate systems have focused on red shifting emission, improving signal intensity, and creating orthogonal luciferase-luciferin pairs for multi-component imaging (Jones et al., 2017; Kaskova et al., 2016; Rathbun and

Prescher, 2017; Rathbun et al., 2017). In recent years, D-luciferin analog development has focused on rigidifying the aromatic core (Evans et al., 2014; Mofford et al., 2014), extending the conjugated π system (Hall et al., 2018; Kuchimaru et al., 2016), or incorporating heteroatoms into the structure (Conley et al., 2012). The two most sensitive "D-luciferin" type systems engineered to date appear to be a mutant CBR luciferase (CBR2) paired with naphthyl luciferin analogs (Hall et al., 2018), and a mutant FLuc luciferase (Akaluc) paired with the AkaLumine luciferin substrate (Iwano et al., 2018). Akaluc has 28 amino acid substitutions relative to FLuc that result in an improved catalytic activity with its preferred substrate, AkaLumine, and improved thermostability and expression compared to FLuc. This luciferase-luciferin pair produces a bright signal with an emission maximum at 650 nm which was capable of imaging single cells within mice, and neurons in the deep brain of live monkeys.

Improvements in coelenterazine substrate systems have similarly focused on improving substrate stability and solubility, red shifting emission, and improving signal intensity (Kaskova et al., 2016; Zhao et al., 2004). To specifically address substrate stability *in vivo*, Promega created EnduRen and ViviRen (Kaskova et al., 2016). These compounds contain protective esters that lead to reduced auto-oxidation *in vivo* compared to native coelenterazine. Additionally, in the cellular environment, these esters are cleaved by endogenous esterase enzymes, leading to a slow release of coelenterazine substrate and extended production of luminescent signal. More recent developments in coelenterazine analogs have focused on rigidifying and extending the conjugated π system (Hosoya et al., 2015; Nishihara et al., 2015), and incorporating heteroatoms into the structure (Yeh et al., 2017) to produce red-shifted emissions and increased signal intensity. One other problem unique to coelenterazine systems is solubility in aqueous solution, which both limits the amount of substrate that can be injected into animals for *in vivo* imaging, and affects the tissue distribution of substrate (Yeh et al., 2019a). Accordingly, efforts have been made to increase the solubility of coelenterazine analogues that allow for increased loading into animals (Yeh et al., 2019b). Apart from these advances, one of the most significant improvements in coelenterazine substrate systems has been the development and engineering of the NanoLuc (NLuc) system from the deep sea shrimp *Oplophorus gracilirostris* (England et al., 2016; Hall et al., 2012). NLuc was evolved to utilize the coelenterazine analog furimazine, and has remarkable thermal stability and high pH and salt tolerance. NLuc produces signal intensity ~150-fold greater than either FLuc or RLuc under similar conditions, with an emission maximum at 460 nm. At only 19 kDa, NLuc is among the smallest of all commonly used luciferases, making it very useful for bioimaging in situations where larger luciferases are not amenable, such as in fusion proteins or viruses. Since its initial development, NLuc has served as the basis for much of the advancements in coelenterazine-utilizing bioluminescent systems.

Beyond enzyme and substrate engineering, the emission wavelength and intensity of bioluminescent protein systems can be altered via bioluminescence resonance energy transfer (BRET) processes (Figure 1.2). By fusing an acceptor fluorophore to a luciferase, energy from the luciferase catalyzed reaction is transferred via a Förster resonance energy transfer (FRET) process to excite the attached fluorophore, producing an emission corresponding to the fluorophore, rather than the luciferase-luciferin pair. This efficiency

of this process is highly dependent upon both the spectral overlap of the luciferase donor and the fluorophore acceptor, as well as the proximity of the acceptor and donor in space. This technique has been applied extensively to coelenterazine utilizing systems specifically, as it allows for a red shifting of the luciferase emission without additional directed evolution/substrate engineering efforts. One of the early examples of this was BRET6, which fused red-shifted RLuc variants (RLuc8.6) to different red FPs to produce emission maxima up to 640 nm (Dragulescu-Andrasi et al., 2011). Besides leading to a red shifting of the luciferase emission, the BRET process can also lead to increased signal intensity overall. This effect was first observed in the development of Nano-lanterns, which fused RLuc8 to the yellow FP, Venus (Saito et al., 2012). The resulting protein, YNL, produced over 5x higher signal than RLuc8 alone, with an emission peak at 530 nm. Different colored Nano-lantern proteins were subsequently developed by using different FP acceptors, showcasing the versatility of this technique (Takai et al., 2015).

Since the development of NLuc, similar approaches have been applied to developing BRET systems with NLuc as the donor moiety to alter the emission for improved *in vivo* imaging properties. One of the first examples of this was in the development of enhanced Nano-lanterns (eNL), which fused NLuc to a variety of different colored FP acceptors to produce five bright color variants of NLuc with emission maxima up to 585 nm (Suzuki et al., 2016). The most red-shifted variants of NLuc developed to date are based on the fusion of a cyan excitable, orange emitting FP (CyOFP1) with NLuc (Chu et al., 2016). The resulting protein, Antares, has an emission peak at 584 nm and emits ~30% of its signal >600 nm. Antares2 was subsequently developed by replacing NLuc in Antares with teLuc, a teal-emitting NLuc mutant, resulting in ~4x more photon output >600 nm (Yeh et al., 2017).

The discovery, development, and engineering of bioluminescent protein systems has led to huge improvements in the capabilities of bioluminescent imaging (BLI). Given the many options available in the bioluminescent protein “toolbox”, researchers now can more easily perform BLI experiments in a variety of different situations (Prescher and Contag, 2010; Rathbun and Prescher, 2017). While historically BLI has proven very useful for tracking cells and gene expression in animals (Contag et al., 1998), luciferase-based probes have also been developed that allow for imaging specific biological processes, such as the production of metabolites and second-messenger signaling molecules.

Interrogating biology with bioluminescent imaging (BLI) systems

Luciferase-based bioluminescent sensors typically fall into one of three categories: complementation of split luciferase (CSL), BRET, or combination CSL-BRET sensors (Figure 1.3). In CSL systems, a sensor domain is used to split the luciferase protein into two nonfunctional halves, such that analyte binding results in a conformational change that reconstitutes the luciferase to produce a change in signal intensity. In BRET systems, the sensor domain is inserted between a fluorescent protein acceptor on one side and an intact luciferase donor on the other side. Analyte binding leads to a change in energy transfer efficiency between donor and acceptor, which is measured by a change in BRET ratio. CSL-BRET systems marry these two approaches and fuse a CSL-type sensor to an intact FP acceptor on the N- or C-terminus. These are functionally equivalent to CSL sensors in that analyte binding reconstitutes the luciferase to produce a change in signal

intensity (not a change in BRET), but the emission signal intensity is typically improved over standard CSL sensors due to efficient BRET. CSL biosensors generally produce large signal changes; however, their signal intensity can be low due to poor reconstitution of luciferase activity. BRET biosensors generally have high signal intensity and are ratiometric; however, their signal change upon analyte binding is typically small. A variety of bioluminescent sensors have been developed using both D-luciferin and coelenterazine-utilizing systems for a variety of signaling molecules.

Some of the first work on developing CSL-type sensors for signaling molecules was carried out by Promega using split FLuc (Fan et al., 2008). To develop a sensor for the second messenger cyclic AMP (cAMP), a cAMP-binding domain was inserted at different positions within FLuc with linkers of varying lengths flanking the binding domain. The structurally conserved domain undergoes a conformation change upon cAMP binding that ultimately results in reconstitution of luciferase activity. The optimized sensor construct displayed a ~100-fold increase in luminescence when bound to cAMP and was used to image cAMP dynamics in tissue culture. The sensor was further optimized via directed evolution after global random mutagenesis and linker mutagenesis (Binkowski et al., 2011). This led to drastic improvements in the sensitivity, dynamic range, and signal fold-change of the sensor, which improved its performance as a screening tool. To date, these sensors exhibit the largest signal fold-changes of any single-chain CSL-type biosensors (~3500-fold in vitro). Due to a reliance on ATP, however, FLuc is generally a less attractive choice for the development of biosensors, as ATP consumption can lead to unwanted effects in the system under study. Accordingly, CSL sensors based on coelenterazine-utilizing luciferases have also been developed. The first such example was a bioluminescent sensor for Ca^{2+} based on split RLuc (Kaihara et al., 2008). In this system, calmodulin (CaM) and the M13 peptide are inserted within RLuc at the 91/92 position, and the calcium-induced interaction between CaM and M13 leads to a reconstitution of RLuc activity.

A subclass of CSL-type sensors based on Nano-lantern scaffolds have also been reported. In these CSL-BRET sensors the luciferase domain is split with a binding domain, as in CSL-type sensors, but an FP acceptor is also added to the N-terminus of the luciferase. While these sensors contain a FP acceptor and thus technically produce a BRET signal, the signal change produced by ligand binding is intensity-based, not ratiometric. However, as a result of high BRET efficiency in the YNL scaffold, the intensity of the signal produced is higher than standard split RLuc biosensors, making these sensors more amenable to single cell imaging applications. The first Nano-lantern-based sensors were developed from the YNL scaffold by splitting RLuc with different ligand binding domains (Saito et al., 2012). YNL-sensors were developed for Ca^{2+}, cAMP, and ATP that produced up 4-fold increases in signal intensity upon ligand binding and were used for imaging in HeLa cells, *Dictyostelium discoideum* cells, and *Arabidopsis* plant leaves, respectively. A slightly modified version of the Ca^{2+} sensor was also used for monitoring drug effects in cardiomyocytes, which serve as a valuable model for pharmacological toxicity testing (Suzuki et al., 2018). Compared to fluorescence imaging in the same cells, there were no adverse effects due to phototoxicity or photobleaching.

Second generation NL sensors for imaging Ca^{2+} were also developed based on the enhanced Nano-lantern scaffold (Suzuki et al., 2016). These sensors use split NLuc

rather than RLuc, and thus produce a higher intensity signal compared to the original YNL-based sensors. By using green, cyan, and orange emitting versions of these sensors with different affinities, Ca^{2+} dynamics could be simultaneously imaged in three distinct organelles in HeLa cells (Hossain et al., 2018). Due to the loss of signal that occurs as luminescent substrate is depleted, however, dynamics could only be monitored for up to three minutes. As seen in these examples, the bright signal and easily changeable emission wavelength of CSL-BRET designs have proven useful for single cell imaging in a variety of biological contexts. However, because the signal of CSL and CSL-BRET based sensors is based on a single emission, measurements are highly affected by the concentration of biosensor and luminescent substrate available, which makes quantitative, long-term measurements difficult. BRET-based biosensors, due to their ratiometric signal, help alleviate these issues, making quantitative, long-term, real-time imaging possible.

One of the first small molecule BRET sensors was developed for cAMP by inserting the human cAMP binding protein hEpac1 between a yellow FP, Citrine, and RLuc (Jiang et al., 2007). This sensor produced a ~70% change in BRET ratio in response to cAMP and was used for quantitative, real-time measurements of cAMP dynamics in eukaryotic cells. The first BRET sensor for Ca^{2+} was similarly developed by inserting the Ca^{2+}-binding CaM-M13 motif between the yellow FP, Venus, and RLuc (Saito et al., 2010). This sensor was optimized by altering the position of the donor and acceptor moieties in the scaffold and using circularly permuted variants of Venus, with the best construct exhibiting a 60% change in BRET ratio in response to Ca^{2+}. This sensor was used to image Ca^{2+} dynamics in HeLa cells and in the plant pathogen, *Pseudomonas syringae*, within *Arabidopsis* plant tissue, showcasing the ability to image in highly autofluorescent samples.

More recently, several BRET sensors have been developed that utilize the bright signal and high stability of NLuc. The first published example of this was in the development of dual readout BRET/FRET sensors for measuring Zn^{2+} (Aper et al., 2016). These sensors took advantage of previously engineered FRET sensors for Zn^{2+} which utilize a cyan FP (Cerulean) and yellow FP (Citrine) pair. By fusing NLuc to the Cerulean donor domain, sensors were generated that can produce a BRET signal in addition to their FRET signal, with BRET signal changes up 50%. These sensors allow for BRET-based monitoring of Zn^{2+} cells in plate reader-based assays and in single cells in real time, and additionally allow for the flexibility of using a FRET readout when desired. BRET-based sensors utilizing NLuc were developed for Ca^{2+} by inserting the Ca^{2+}-sensitive troponin-C (TnC) sequence between Venus and NLuc (Yang et al., 2016). By testing a library of circularly permuted Venus and NLuc variants, the CalfluxVTN sensor was developed that exhibits a remarkable 1100% change in BRET ratio in response to Ca^{2+} when tested *in vitro*. Taking advantage of the BRET signal, this sensor was used to image Ca^{2+} fluxes in cultured cells after optogenetic stimulation of channelrhodopsins. These types of optogenetic experiments are difficult to perform with fluorescence-based probes due to cross-excitation that can occur between the fluorophore and optogenetic probe which leads to undesired perturbation of the process under study.

The most recently developed BRET sensor utilizing NLuc, although not for small molecule sensing, is for monitoring membrane voltage (Inagaki et al., 2017). This sensor,

LOTUS-V, was developed by inserting a voltage sensing protein domain between NLuc and Venus which results in a ~23% change in BRET ratio upon membrane depolarization. This sensor was able to be used in combination with optogenetic tools to monitor changes in membrane voltage in cardiomyocytes. Remarkably, this sensor was applied to simultaneously imaging local brain activity in multiple interacting, moving mice (Inagaki et al., 2019).

These examples showcase how bioluminescent sensor systems have advanced to allow for quantitative, real-time imaging of cellular signaling pathways in complex biological samples. As the capabilities of these systems have improved over the years, experimental setups have moved from purely *in vitro* to a variety of biological samples, including tissue culture, single cells, plant tissue, and freely moving mice. Importantly, however, these advancements in BLI have focused almost exclusively on eukaryotic signaling pathways, most notably cAMP and Ca^{2+} signaling. Bacteria contain many equally complex signaling pathways that would benefit from further biosensor development. Accordingly, many fluorescent sensor systems have been developed and applied to understand bacterial signaling systems. However, bacteria naturally colonize highly diverse and complex environments, from gastrointestinal tracts to soil and plant surfaces, where fluorescent biosensors are not applicable. *To allow for the study of bacterial signaling within these more complex environments, new bioluminescent tools developed specifically for bacterial signaling are needed.*

Cyclic di-nucleotide signaling

The bacterial signaling pathways that are of most interest to our lab are cyclic di-nucleotide (CDN) signaling pathways. CDNs are a class of second messenger molecules formed by the cyclization of two nucleotide triphosphates (NTPs) to produce a cyclic, dimeric product of nucleotide monophosphates. Different combinations of NTPs produce different CDNs, which each have different biological roles and distinct signaling pathways (Krasteva and Sondermann, 2017). The three canonical CDNs present in bacteria are cyclic di-GMP (c-di-GMP), cyclic di-AMP (c-di-AMP), and cyclic AMP-GMP (cGAMP) (Figure 1.4), although additional CDNs containing pyrimidine nucleotides have recently been discovered (Whiteley et al., 2019). Recent work has also found that CDN signaling networks can be interconnected with other nucleotide signaling in certain bacteria (Wright et al., 2019), but it is unclear whether this is generalizable to all bacteria and CDN signaling pathways. To interrogate these complex signaling networks in bacteria, several genetically encoded tools have been developed (Table 1.1).

The first genetically encoded tools for studying CDNs were reporter-based. In these systems, increased levels of CDN drive the production of a reporter gene that is under the control of a CDN-responsive transcription factor or RNA element (riboswitch). One benefit of these systems is that the reporter gene can be altered to produce different outputs, including LacZ activity, fluorescence, or bioluminescence. The downside, however, is that reporter systems are generally unable to monitor CDN dynamics at the fast time scale that signaling events take place, which is typically on the order of seconds to minutes. Once CDN levels have built up enough to “turn on” production of the reporter gene, it still takes time for the reporter to be translated and build up to high enough levels to produce an observable signal. The commonly used reporter gene superfolder GFP

(sfGFP), for example, takes ~15 minutes to mature after being translated (Balleza et al., 2018). Additionally, even after CDN levels have decreased, the signal from the reporter remains until the cellular machinery degrades it, which takes at least 15-30 minutes even for “destabilized” reporters. Accordingly, any dynamics that occur on the timescale faster than these events are not able to be observed with reporters.

To allow for the analysis of rapid signaling dynamics, several fluorescent biosensor systems have been developed for CDNs. For c-di-GMP in particular, these include protein-based FRET biosensors that have been used in *Escherichia coli* (Ho et al., 2013), *Caulobacter crescentus*, *Salmonella typhimurium*, and *Pseudomonas aeruginosa* (Christen et al., 2010) as well as RNA-based fluorescent (RBF) biosensors that have been used in *E. coli* and allow for the first time the ability to image c-di-GMP under anaerobic conditions (Wang et al., 2016). The rapid response of optimized RBF sensors ($t_{1/2}$ ~ 1 min) further allowed for the analysis of changes in c-di-GMP in *E. coli* in response to changes in extracellular zinc in real time (Yeo et al., 2017). Similar RBF sensors have also been developed for c-di-AMP and cGAMP. One drawback of fluorescent biosensors, however, is that due to a reliance on external illumination, these systems are incompatible with imaging in plant or animal tissue due to autofluorescence, and in long-term experiments due to phototoxicity. Accordingly, to allow for the analysis of CDN dynamics in more complex systems, new bioluminescent sensor systems are required.

Of the currently known CDNs, our understanding of c-di-GMP would likely benefit the most from bioluminescent sensor development. C-di-GMP is a key regulator of bacterial physiology and behavior, coordinating diverse processes such as motility, biofilm formation, and virulence (Figure 1.5). First discovered as a stimulator of cellulose synthesis (Ross et al., 1987), c-di-GMP has since been found to be nearly ubiquitous in bacteria, with c-di-GMP signaling pathways often integrated with other global regulatory systems, such as phosphorylation networks and quorum sensing pathways (Jenal et al., 2017; Romling et al., 2013). The intracellular levels of c-di-GMP are tightly regulated by diguanylate cyclase (DGC) and phosphodiesterase (PDE) enzymes that synthesize and degrade c-di-GMP, respectively. Many bacteria have an abundance of predicted DGC and PDE genes, suggesting unique c-di-GMP regulatory circuits are activated in response to different environmental cues, such as O_2, metal ions, or light. Most notably, c-di-GMP signaling networks play critical roles in the pathogenicity of many bacteria, allowing them to adapt to and survive in the changing environmental conditions that are experienced during the infection of a host (Hall and Lee, 2018). To interrogate these complex c-di-GMP signaling networks within bacteria in their natural environments, such as within an infected host, bioluminescent sensor systems such as those described for mammalian signaling earlier in this chapter would be valuable.

The PilZ domain as a c-di-GMP receptor

To develop a bioluminescent sensor system for any signaling molecule, some sort of sensor/receptor domain for that molecule is required. As described previously, many bioluminescent sensor systems were developed for cAMP and Ca^{2+} which utilized natural and engineered protein sequences that selectively bind to cAMP and Ca^{2+}. Importantly, these receptor domains must undergo large conformational changes upon binding to their target, which ultimately produces the signal change of the biosensor. Accordingly, to

develop a bioluminescent sensor system for c-di-GMP, a sensor domain is required that binds with high affinity and selectivity to c-di-GMP and undergoes a large conformational change upon binding. The c-di-GMP sensor domain that fits these criteria is the PilZ domain (Cheang et al., 2019; Chou and Galperin, 2016).

The PilZ domain was first discovered as a c-di-GMP receptor after characterization of the YcgR protein from *E. coli* (*Ec*YcgR) (Ryjenkov et al., 2006). *Ec*YcgR is a 28 kDa protein that contains an N-terminal β-barrel domain ($YcgR_N$ domain) and a C-terminal PilZ domain. The PilZ domain is named after the type IV pilus control protein first identified in *Pseudomonas aeruginosa,* which is essential for type IV pilus biosynthesis (Alm et al., 1996). Important to note, the PilZ protein from *P. aeruginosa* does not actually bind to c-di-GMP, as it lacks the conserved c-di-GMP binding motifs. The PilZ domain structure itself is characterized by a β-barrel structure with a flexible N-terminal loop. *Ec*YcgR exists as a monomer and binds to two molecules of c-di-GMP with an apparent affinity of ~840 nM, with two highly conserved motifs (RxxxR and D/NxSxxG) in the PilZ domain contributing to binding. Importantly, it was found that c-di-GMP binding led to a large conformational change in the protein that caused it to migrate differently during size exclusion chromatography. This conformational change exerts a biological effect, as it was later discovered that *Ec*YcgR interacts with flagellar machinery and acts as a "backstop brake" in response to increased c-di-GMP levels, leading to a suppression of motility (Paul et al., 2010). YcgR-like proteins (defined as having a $YcgR_N$-PilZ domain architecture) are present in many bacteria and have similarly been found to interact with motor proteins, producing c-di-GMP dependent effects on flagellar motor output (Cheang et al., 2019). To determine the molecular mechanism of this conformational change, numerous structural studies of YcgR-like proteins have been performed.

The first crystal structure of a PilZ-domain containing protein was of the YcgR-like protein PlzD (also VCA0042) from *Vibrio cholerae* (Benach et al., 2007). PlzD has a similar domain architecture to *Ec*YcgR, containing a $YcgR_N$ domain and a C-terminal PilZ domain, and was crystallized as a homodimer. Structures of both the c-di-GMP bound (holo) and unbound (apo) protein were solved which revealed that a major change in interdomain interactions occurs upon ligand binding. In the apo structure, the C-terminal PilZ domain is essentially detached from the $YcgR_N$ domain, making no substantial interdomain contacts. In the holo structure, however, the two domains are found in much closer proximity, with c-di-GMP packed at the domain interface. This conformational change involves a 123° rotation of the PilZ domain toward the $YcgR_N$ domain, and converts the extended apo form to a much more compact holo form (Figure 1.6a). Structures of the YcgR-like protein PP4397 from *Pseudomonas putida* showed a very similar structural change upon c-di-GMP binding, suggesting that this conformational switching mechanism is conserved in YcgR-like proteins of this type (Ko et al., 2010). The key c-di-GMP:protein interactions in these proteins occur in the conserved RxxxR and D/NxSxxG motifs.

The RxxxR motif is present at the N-terminal region of the PilZ domain, which serves as an inter-domain linker with the $YcgR_N$ domain, while the D/NxSxxG motif is present on a β-sheet platform ~30-40 residues away within the PilZ domain. In all structures of YcgR-like proteins, the side chains of conserved residues in these motifs make direct H-bonding interactions with c-di-GMP (Benach et al., 2007; Ko et al., 2010;

Subramanian et al., 2017). The conserved Arg in the RxxxR motif are particularly essential for c-di-GMP selectivity, as they make extensive H-bonding contacts and possible cation-π interactions with the guanine bases themselves (Figure 1.6b).

Interestingly, PlzD was crystallized binding to a single molecule of c-di-GMP, whereas PP4397 and the YcgR-like protein DgrA from *Bacillus subtilis* were crystallized binding to an intercalated dimer of c-di-GMP. This difference appears to be controlled by the identity of the residue immediately prior to the RxxxR motif, termed "position-X". In PlzD, this residue is a Leu, while in PP4397 and DgrA this residue is an Arg. The presence of a Leu or another small hydrophobic residue appears to sterically occlude the 2nd c-di-GMP molecule from entering the binding pocket, while the presence of an Arg promotes an "arginine-fork" interaction with a 2nd molecule of c-di-GMP. Accordingly, mutation of position-X from Arg to Leu in PP4397 (R122L) coverts the binding stoichiometry from two to one, while mutation from Leu to Arg in PlzD (L135R) leads to an increased binding stoichiometry (not exactly one to two) (Ko et al., 2010). Unexpectedly, the crystal structure of the c-di-GMP-bound PlzD (L135R) mutant shows a completely different domain orientation compared to the wild-type. This change appears to be caused mainly by differences in the inter-dimer interactions, which highlights how a single residue change can produce significant changes in global structure.

While YcgR-like proteins have been among the most well-studied PilZ-domain containing proteins, there is a large diversity in length and domain composition of PilZ-domain containing proteins, including a large number of small, single-domain PilZ proteins as well as much larger multi-domain proteins (Cheang et al., 2019). The underlying theme, however, is that the c-di-GMP-induced conformational switching of PilZ proteins allows for them to serve as regulatory domains with diverse outputs, which ultimately enables c-di-GMP to control the activity of many different cellular targets. Looking forward, it will be interesting to discover whether there are equivalent, undiscovered PilZ-like domains for other CDNs. Ultimately, the unique characteristics of the PilZ domain, in YcgR-like proteins in particular, makes them an attractive choice for use in the design of bioluminescent sensors for c-di-GMP.

Outlook

When starting my thesis work, I sought to develop a bioluminescent sensor system for c-di-GMP that would serve as a complementary technology to the RBF sensors that had already been developed in the lab, with the long term goal of enabling c-di-GMP imaging within mammalian tissues. My first foray into this led to the development and optimization of Nano-lantern-based sensors for c-di-GMP, which is described in Chapter 2. In this work, I learned a lot about the complications of luminescence imaging, especially in bacteria, and the limitations of intensity-based biosensors. The phylogenetic screen of YcgR variants performed in collaboration with the Joint Genome Institute (JGI) produced some amazing results, however, that were invaluable to the further development of these biosensors.

Inspired by the development of NLuc and other BRET-based sensors in the literature, I next sought to develop a ratiometric, luminescent sensor system for c-di-GMP, which is described in Chapter 3. Gratifyingly, I found that this design alleviates a lot of the issues in the original YNL-based sensors, even showing as a proof-of-concept that these

sensors work robustly for long-term imaging (at least 1 hour) within an animal tissue model, and require only ~10^3–10^4 bacterial cells to produce a visible signal. My hope is that our collaborators and other biologists will use these tools to study the c-di-GMP dynamics of bacteria over the different stages of host infection. Additionally, the ratiometric biosensor work unexpectedly led to the first luminescent sensors that respond to (3'3')-cGAMP (and maybe (2'3')-cGAMP), which should hopefully be applied to studying these CDN signals in the near future.

Finally, as had long been a research goal of mine, I sought to evolve a YcgR-like protein to bind to new CDN targets. This work, described in Chapter 4, encountered numerous issues along the way that are not all described here. Although we did not get a clear "winner" at the end of this process, the research led to the development of a very robust screening methodology that I feel will give the desired results in the future, with careful consideration of the lessons learned here. This directed evolution should ultimately allow for the development of biosensors (both fluorescent and bioluminescent) for new CDN targets. A protein-based sensor for (2'3')-cGAMP, in particular, would be extremely useful, as a lack of available tools has limited our understanding of the spatiotemporal dynamics of this signal. This sensor could be applied, for example, to studying the activation of cGAS in response to HIV infection.

FIGURES

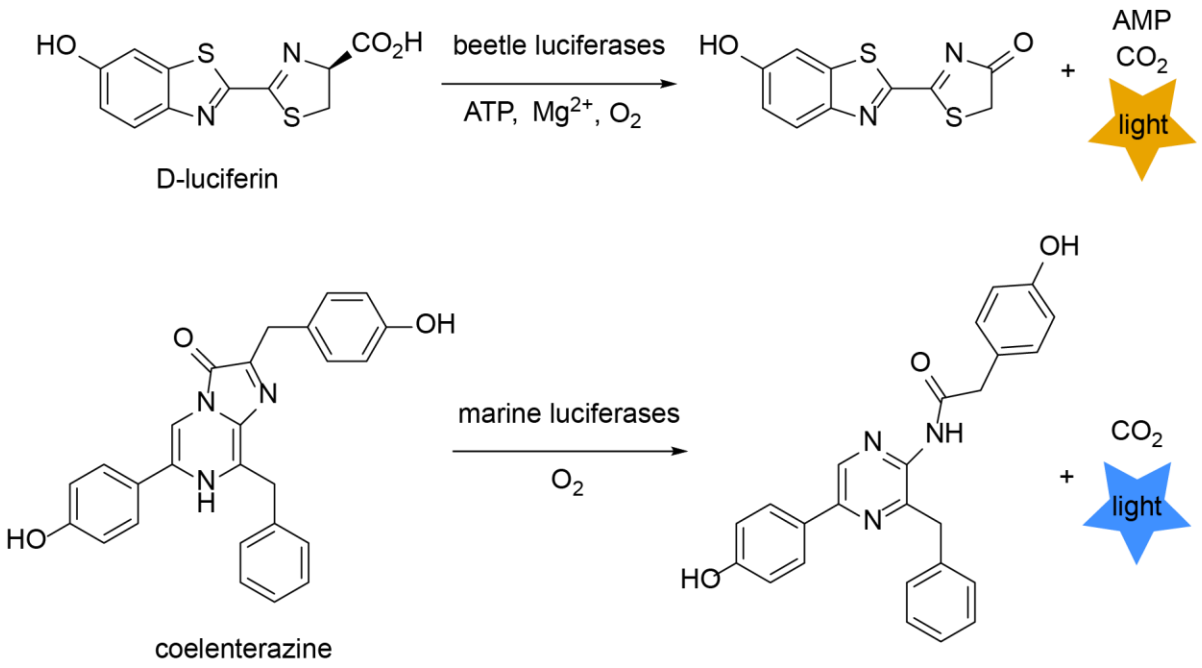

Figure 1.1 Natural bioluminescent systems. Chemical structures and reaction schemes for the well-studied beetle and marine luciferases.

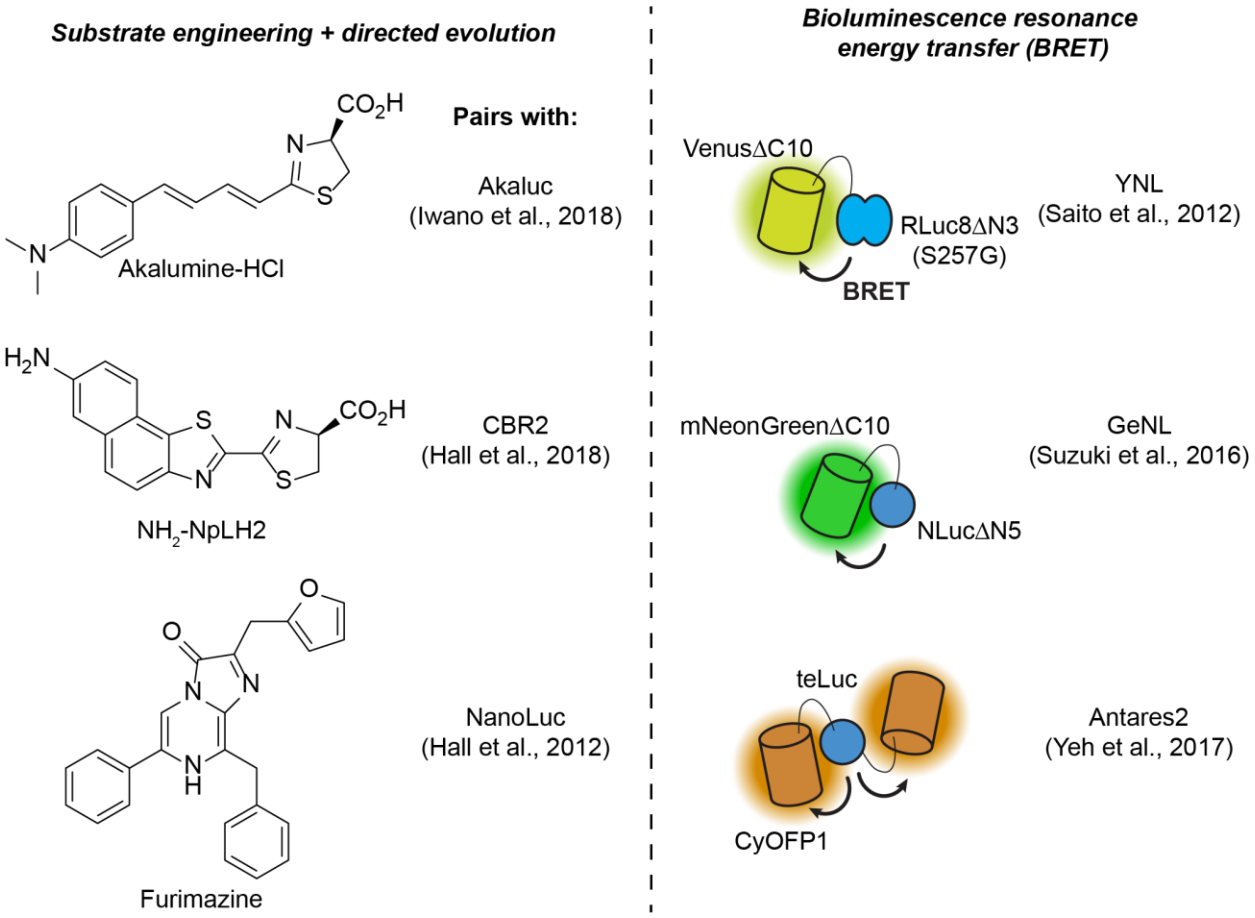

Figure 1.2 Engineered bioluminescent systems. Selected examples of new bioluminescent systems that have been developed via substrate engineering + directed evolution (left) and/or the use of bioluminescence resonance energy transfer (right).

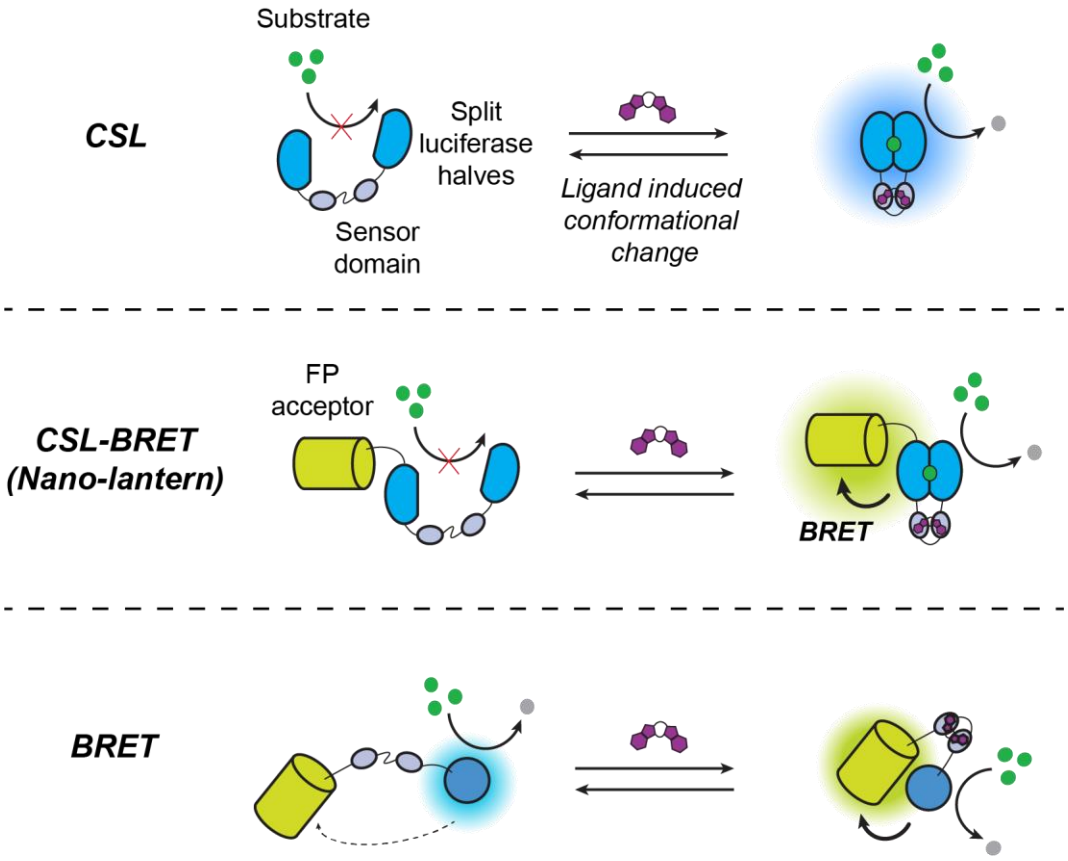

Figure 1.3 Approaches for the development of luciferase-based bioluminescent sensor systems. Schematics of the three main categories of luciferase-based bioluminescent sensor systems.

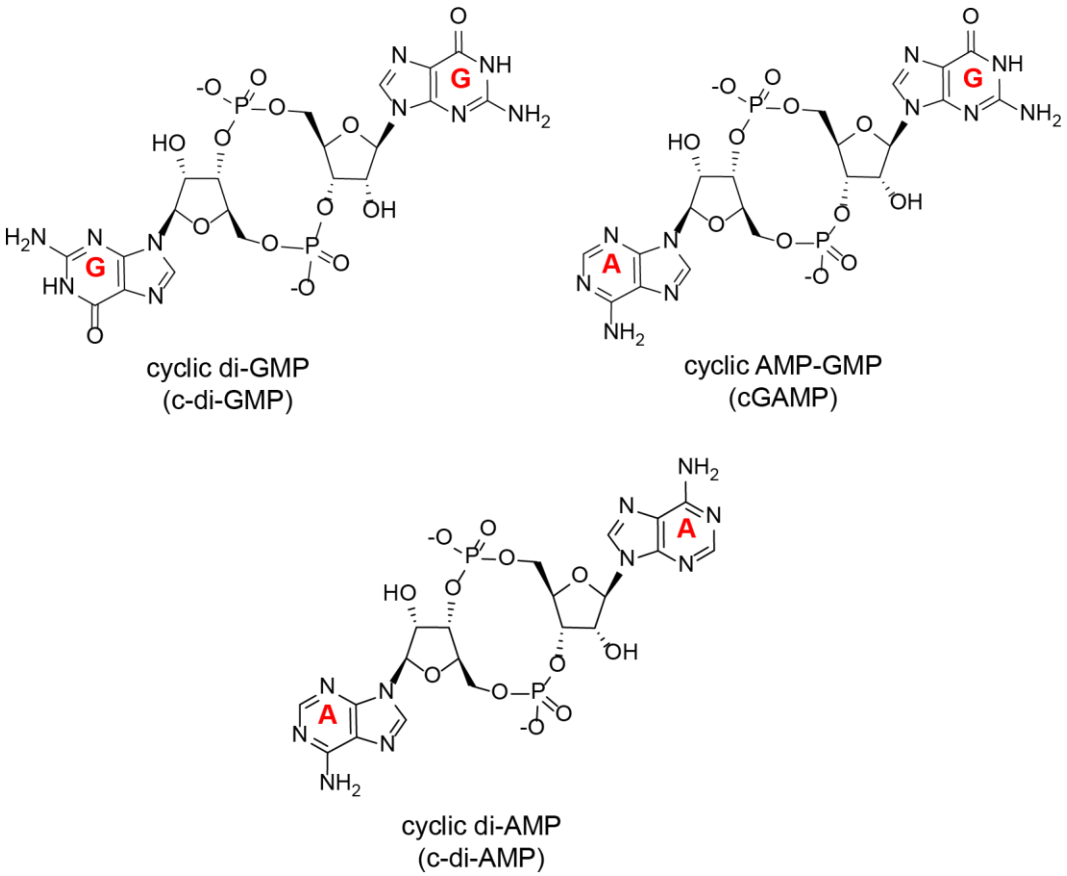

Figure 1.4 Bacterial cyclic di-nucleotides. Chemical structures of the three canonical cyclic di-nucleotides found in bacteria.

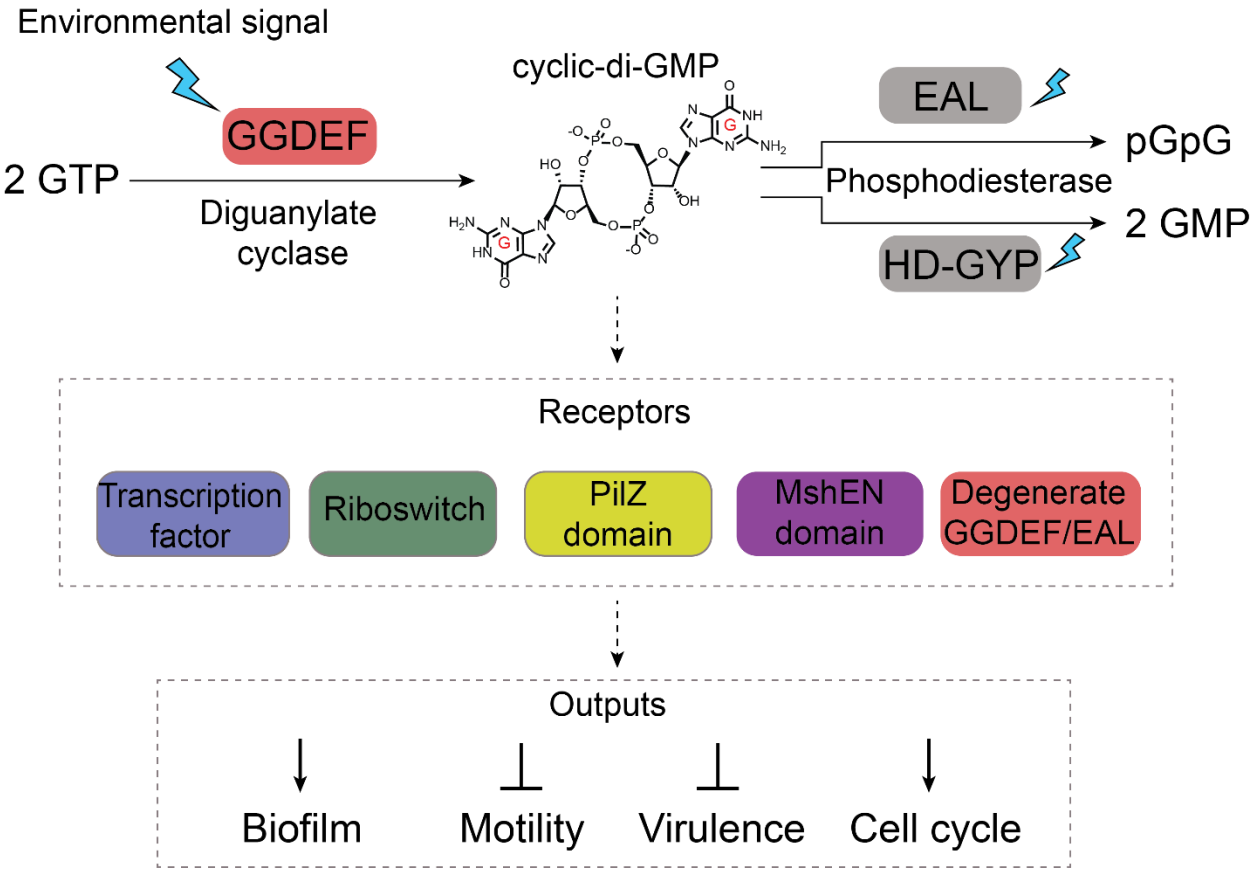

Figure 1.5 Cyclic di-GMP signaling in bacteria. Overall pathway for canonical c-di-GMP signaling in bacteria.

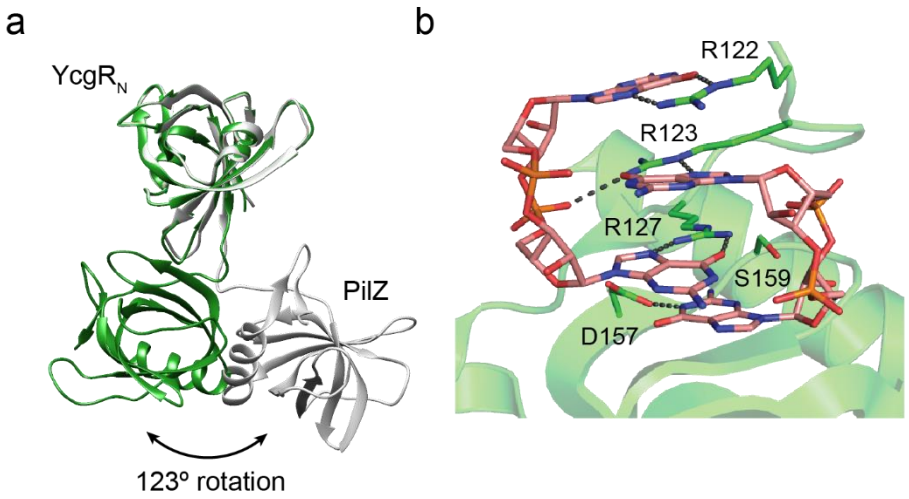

Figure 1.6 PilZ domain proteins as receptors for c-di-GMP. (a) Crystal structures of PlzD from *V. cholerae* in the apo (silver; PDB 1YLN) and holo (green; PDB 2RDE) states showing the large conformational change that occurs upon c-di-GMP binding. (b) Crystal structure of PP4397 from *P. putida* (PDB 3KYF) showing the key H-bonding interactions between conserved residues and c-di-GMP.

TABLES

Table 1.1 Genetically encodable tools for analysis of CDN signaling

[a]RS = riboswitch, TF = transcription factor.

[b]Citations refer to initial work and noteworthy applications/improvements.

CDN	Category[a]	Readout	Organism(s)[b]
cyclic di-GMP	RS-based biosensor	Fluorescence	*Escherichia coli* (Kellenberger et al., 2013; Wang et al., 2016)
	RS-based reporter	LacZ activity	*Bacillus subtilis* (Sudarsan et al., 2008) *Escherichia coli* (Zhou et al., 2016)
		Fluorescence	*Bacillus subtilis* (Gao et al., 2014) *Escherichia coli* (Zhou et al., 2016)
		Luminescence	*Geobacter sulfurreducens* (Hallberg et al., 2019)
	PilZ-based biosensor	FRET	*Caulobacter crescentus* (Christen et al., 2010) *Pseudomonas aeruginosa* PAO1 (Christen et al., 2010) *Klebsiella pneumoniae* (Christen et al., 2010) *Salmonella* Typhimurium (Christen et al., 2010; Mills et al., 2015) *Escherichia coli* (Ho et al., 2013)
		CSL-BRET	*Escherichia coli* **(see Chapter 2)** *(Dippel et al., 2018)*
		BRET	*Escherichia coli* in tissue model system **(see Chapter 3)**
	TF-based reporter	Fluorescence	*Pseudomonas aeruginosa* (Rybtke et al., 2012)
		Luminescence	*Pseudomonas aeruginosa* (Irie et al., 2012; Pawar et al., 2016) *Vibrio cholerae* (Koestler and Waters, 2014; Srivastava et al., 2011)
cGAMP	RS-based biosensor	Fluorescence	*Escherichia coli* (Kellenberger et al., 2015a)
	RS-based reporter	Luminescence	*Geobacter sulfurreducens* (Hallberg et al., 2019)
cyclic di-AMP	RS-based biosensor	Fluorescence	*Escherichia coli* (Kellenberger et al., 2015b) *Listeria monocytogenes* (Kellenberger et al., 2015b)
	RS-based reporter	LacZ activity	*Bacillus subtilis* (Nelson et al., 2013)

REFERENCES

Alm, R., Bodero, A., Free, P., and Mattick, J. (1996). Identification of a novel gene, pilZ, essential for type 4 fimbrial biogenesis in Pseudomonas aeruginosa. J. Bacteriol. *178*, 46.

Aper, S.J.A., Dierickx, P., and Merkx, M. (2016). Dual readout BRET/FRET-sensors for measuring intracellular zinc. ACS Chem. Biol. *11*, 2854–2864.

Balleza, E., Kim, J.M., and Cluzel, P. (2018). Systematic characterization of maturation time of fluorescent proteins in living cells. Nat. Methods *15*, 47–51.

Benach, J., Swaminathan, S.S., Tamayo, R., Handelman, S.K., Folta-Stogniew, E., Ramos, J.E., Forouhar, F., Neely, H., Seetharaman, J., Camilli, A., et al. (2007). The structural basis of cyclic diguanylate signal transduction by PilZ domains. EMBO J. *26*, 5153–5166.

Bhaumik, S., Lewis, X.Z., and Gambhir, S.S. (2004). Optical imaging of Renilla luciferase, synthetic Renilla luciferase, and firefly luciferase reporter gene expression in living mice. J. Biomed. Opt. *9*, 578.

Binkowski, B.F., Butler, B.L., Stecha, P.F., Eggers, C.T., Otto, P., Zimmerman, K., Vidugiris, G., Wood, M.G., Encell, L.P., Fan, F., et al. (2011). A luminescent biosensor with increased dynamic range for intracellular cAMP. ACS Chem. Biol. *6*, 1193–1197.

Brakemann, T., Weber, G., Andresen, M., Groenhof, G., Stiel, A.C., Trowitzsch, S., Eggeling, C., Grubmüller, H., Hell, S.W., Wahl, M.C., et al. (2019). Aequorea victoria's secrets. BioXriv 1–14.

Cheang, Q.W., Xin, L., Yuen, R., and Chea, F. (2019). Emerging paradigms for PilZ domain-mediated C-di-GMP signaling. Biochem Soc Trans. 1–8.

Chou, S., and Galperin, M.Y. (2016). Diversity of Cyclic Di-GMP-Binding Proteins and Mechanisms. J. Bacteriol. *198*, 32–46.

Christen, M., Kulasekara, H.D., Christen, B., Kulasekara, B.R., Hoffman, L.R., and Miller, S.I. (2010). Asymmetrical distribution of the second messenger c-di-GMP upon bacterial cell division. Science *328*, 1295–1297.

Chu, J., Oh, Y., Sens, A., Ataie, N., Dana, H., Macklin, J.J., Laviv, T., Welf, E.S., Dean, K.M., Zhang, F., et al. (2016). A bright cyan-excitable orange fluorescent protein facilitates dual-emission microscopy and enhances bioluminescence imaging in vivo. Nat. Biotechnol. *34*, 760–767.

Conley, N.R., Dragulescu-Andrasi, A., Rao, J., and Moerner, W.E. (2012). A selenium analogue of firefly D-luciferin with red-shifted bioluminescence emission. Angew. Chemie - Int. Ed. *51*, 3350–3353.

Contag, P.R., Nick Olomu, I., Stevenson, D.K., and Contag, C.H. (1998). Bioluminescent indicators in living mammals. Nat. Med. *4*, 245–247.

Dippel, A.B., Anderson, W.A., Evans, R.S., Deutsch, S., and Hammond, M.C. (2018).

Chemiluminescent Biosensors for Detection of Second Messenger Cyclic di-GMP. ACS Chem. Biol. *13*, 1872–1879.

Dragulescu-Andrasi, A., Chan, C.T., De, A., Massoud, T.F., and Gambhir, S.S. (2011). Bioluminescence resonance energy transfer (BRET) imaging of protein-protein interactions within deep tissues of living subjects. Proc. Natl. Acad. Sci. U. S. A. *108*, 12060–12065.

England, C.G., Ehlerding, E.B., and Cai, W. (2016). NanoLuc: A Small Luciferase Is Brightening Up the Field of Bioluminescence. Bioconjug. Chem. *27*, 1175–1187.

Evans, M.S., Chaurette, J.P., Adams, S.T., Reddy, G.R., Paley, M. a, Aronin, N., Prescher, J. a, and Miller, S.C. (2014). A synthetic luciferin improves bioluminescence imaging in live mice. Nat. Methods *11*, 393–395.

Fadero, T.C., Gerbich, T.M., Rana, K., Suzuki, A., DiSalvo, M., Schaefer, K.N., Heppert, J.K., Boothby, T.C., Goldstein, B., Peifer, M., et al. (2018). LITE microscopy: Tilted light-sheet excitation of model organisms offers high resolution and low photobleaching. J. Cell Biol. *217*, 1869–1882.

Fan, F., Binkowski, B.F., Butler, B.L., Stecha, P.F., Lewis, M.K., and Wood, K. V. (2008). Novel genetically encoded biosensors using firefly luciferase. ACS Chem. Biol. *3*, 346–351.

Gao, X., Dong, X., Subramanian, S., Matthews, P.M., Cooper, C.A., Kearns, D.B., and Dann, C.E. (2014). Engineering of Bacillus subtilis strains to allow rapid characterization of heterologous diguanylate cyclases and phosphodiesterases. Appl. Environ. Microbiol. *80*, 6167–6174.

Hall, C.L., and Lee, V.T. (2018). Cyclic-di-GMP regulation of virulence in bacterial pathogens. Wiley Interdiscip. Rev. RNA *9*, 1–19.

Hall, M.P., Unch, J., Binkowski, B.F., Valley, M.P., Butler, B.L., Wood, M.G., Otto, P., Zimmerman, K., Vidugiris, G., MacHleidt, T., et al. (2012). Engineered luciferase reporter from a deep sea shrimp utilizing a novel imidazopyrazinone substrate. ACS Chem. Biol. *7*, 1848–1857.

Hall, M.P., Woodroofe, C.C., Wood, M.G., Que, I., Van'T Root, M., Ridwan, Y., Shi, C., Kirkland, T.A., Encell, L.P., Wood, K. V., et al. (2018). Click beetle luciferase mutant and near infrared naphthyl-luciferins for improved bioluminescence imaging. Nat. Commun. *9*.

Hallberg, Z.F., Chan, C.H., Wright, T.A., Kranzusch, P.J., Doxzen, K.W., Park, J.J., Bond, D.R., and Hammond, M.C. (2019). Structure and mechanism of a Hypr GGDEF enzyme that activates cGAMP signaling to control extracellular metal respiration. Elife *8*, 1–36.

Ho, C.L., Chong, K.S.J., Oppong, J.A., Chuah, M.L.C., Tan, S.M., and Liang, Z.X. (2013). Visualizing the perturbation of cellular cyclic di-GMP levels in bacterial cells. J. Am. Chem. Soc. *135*, 566–569.

Hosoya, T., Iimori, R., Yoshida, S., Sumida, Y., Sahara-Miura, Y., Sato, J.I., and Inouye,

S. (2015). Concise Synthesis of v-Coelenterazines. Org. Lett. *17*, 3888–3891.

Hossain, M.N., Suzuki, K., Iwano, M., Matsuda, T., and Nagai, T. (2018). Bioluminescent Low-Affinity Ca $^{2+}$ Indicator for ER with Multicolor Calcium Imaging in Single Living Cells. ACS Chem. Biol. acschembio.7b01014.

Icha, J., Weber, M., Waters, J.C., and Norden, C. (2017). Phototoxicity in live fluorescence microscopy, and how to avoid it. BioEssays *39*, 1–15.

Inagaki, S., Tsutsui, H., Suzuki, K., Agetsuma, M., Arai, Y., Jinno, Y., Bai, G., Daniels, M.J., Okamura, Y., Matsuda, T., et al. (2017). Genetically encoded bioluminescent voltage indicator for multi-purpose use in wide range of bioimaging. Sci. Rep. *7*, 1–11.

Inagaki, S., Agetsuma, M., Ohara, S., Iijima, T., and Yokota, H. (2019). Imaging local brain activity of multiple freely moving mice sharing the same environment. Sci. Rep. *9*.

Irie, Y., Borlee, B.R., O'Connor, J.R., Hill, P.J., Harwood, C.S., Wozniak, D.J., and Parsek, M.R. (2012). Self-produced exopolysaccharide is a signal that stimulates biofilm formation in Pseudomonas aeruginosa. Proc. Natl. Acad. Sci. *109*, 20632–20636.

Iwano, S., Sugiyama, M., Hama, H., Watakabe, A., Hasegawa, N., Kuchimaru, T., Tanaka, K.Z., Takahashi, M., Ishida, Y., Hata, J., et al. (2018). Single-cell bioluminescence imaging of deep tissue in freely moving animals. Science *939*, 935–939.

Jenal, U., Reinders, A., and Lori, C. (2017). Cyclic di-GMP: Second messenger extraordinaire. Nat. Rev. Microbiol. *15*, 271–284.

Jiang, L.I., Collins, J., Davis, R., Lin, K.M., DeCamp, D., Roach, T., Hsueh, R., Rebres, R.A., Ross, E.M., Taussig, R., et al. (2007). Use of a cAMP BRET sensor to characterize a novel regulation of cAMP by the sphingosine 1-phosphate/G13 pathway. J. Biol. Chem. *282*, 10576–10584.

Jones, K.A., Porterfield, W.B., Rathbun, C.M., Mccutcheon, C., Paley, M.A., and Prescher, J.A. (2017). Orthogonal luciferase-luciferin pairs for bioluminescence imaging. J. Am. Chem. Soc.

Kaihara, A., Umezawa, Y., and Furukawa, T. (2008). Bioluminescent indicators for Ca2+ based on split Renilla luciferase complementation in living cells. Anal. Sci. *24*, 1405–1408.

Kaskova, Z.M., Tsarkova, A.S., and Yampolsky, I. V. (2016). 1001 Lights: Luciferins, Luciferases, Their Mechanisms of Action and Applications in Chemical Analysis, Biology and Medicine. Chem. Soc. Rev. *45*, 6048–6077.

Kellenberger, C.A., Wilson, S.C., Sales-Lee, J., and Hammond, M.C. (2013). RNA-Based Fluorescent Biosensors for Live Cell Imaging of Second Messengers Cyclic di-GMP and Cyclic AMP-GMP. J. Am. Chem. Soc. *135*, 4906–4909.

Kellenberger, C.A., Wilson, S.C., Hickey, S.F., Gonzalez, T.L., Su, Y., Hallberg, Z.F., Brewer, T.F., Iavarone, A.T., Carlson, H.K., Hsieh, Y.-F., et al. (2015a). GEMM-I riboswitches from Geobacter sense the bacterial second messenger cyclic AMP-GMP.

Proc. Natl. Acad. Sci. U. S. A. *112*, 5383–5388.

Kellenberger, C.A., Chen, C., Whiteley, A.T., Portnoy, D.A., and Hammond, M.C. (2015b). RNA-Based Fluorescent Biosensors for Live Cell Imaging of Second Messenger Cyclic di-AMP. J. Am. Chem. Soc. *137*, 6432–6435.

Ko, J., Ryu, K.S., Kim, H., Shin, J.S., Lee, J.O., Cheong, C., and Choi, B.S. (2010). Structure of PP4397 reveals the molecular basis for different c-di-GMP binding modes by pilz domain proteins. J. Mol. Biol. *398*, 97–110.

Koestler, B.J., and Waters, C.M. (2014). Bile acids and bicarbonate inversely regulate intracellular cyclic di-GMP in vibrio cholerae. Infect. Immun. *82*, 3002–3014.

Krasteva, P.V., and Sondermann, H. (2017). Versatile modes of cellular regulation via cyclic dinucleotides. Nat. Chem. Biol. *13*, 350–359.

Kuchimaru, T., Iwano, S., Kiyama, M., Mitsumata, S., Kadonosono, T., Niwa, H., Maki, S., and Kizaka-Kondoh, S. (2016). A luciferin analogue generating near-infrared bioluminescence achieves highly sensitive deep-tissue imaging. Nat. Commun. *7*, 1–8.

Li, J. Bin, Liu, H.W., Fu, T., Wang, R., Zhang, X.B., and Tan, W. (2019). Recent Progress in Small-Molecule Near-IR Probes for Bioimaging. Trends Chem. *1*, 224–234.

Loening, A.M., Fenn, T.D., Wu, A.M., and Gambhir, S.S. (2006). Consensus guided mutagenesis of Renilla luciferase yields enhanced stability and light output. Protein Eng. Des. Sel. *19*, 391–400.

Loening, A.M., Wu, A.M., and Gambhir, S.S. (2007). Red-shifted Renilla reniformis luciferase variants for imaging in living subjects. Nat. Methods *4*, 641–643.

Matthews, J.C., Hori, K., and Cormier, M.J. (1977). Purification and properties of Renilla reniformis Luciferase. Biochemistry *16*, 85–91.

Miller, D.R., Jarrett, J.W., Hassan, A.M., and Dunn, A.K. (2017). Deep tissue imaging with multiphoton fluorescence microscopy. Curr. Opin. Biomed. Eng. *4*, 32–39.

Mills, E., Petersen, E., Kulasekara, B.R., and Miller, S.I. (2015). A direct screen for c-di-GMP modulators reveals a Salmonella Typhimurium periplasmic L -arginine – sensing pathway. Sci. Signal. *8*, 1–12.

Miloud, T., Henrich, C., and Hämmerling, G.J. (2007). Quantitative comparison of click beetle and firefly luciferases for in vivo bioluminescence imaging. J. Biomed. Opt. *12*, 054018.

Mofford, D.M., Reddy, G.R., and Miller, S.C. (2014). Aminoluciferins extend firefly luciferase bioluminescence into the near-infrared and can be preferred substrates over d-luciferin. J. Am. Chem. Soc. *136*, 13277–13282.

Monici, M. (2005). Cell and tissue autofluorescence research and diagnostic applications. Biotechnol. Annu. Rev. *11*, 227–256.

Nelson, J.W., Sudarsan, N., Furukawa, K., Weinberg, Z., Wang, J.X., and Breaker, R.R. (2013). Riboswitches in eubacteria sense the second messenger c-di-AMP. Nat. Chem.

Biol. *9*, 834–839.

Nishihara, R., Suzuki, H., Hoshino, E., Suganuma, S., Sato, M., Saitoh, T., Nishiyama, S., Iwasawa, N., Citterio, D., and Suzuki, K. (2015). Bioluminescent coelenterazine derivatives with imidazopyrazinone C-6 extended substitution. Chem. Commun. *51*, 391–394.

Ouzounov, D.G., Wang, T., Wang, M., Feng, D.D., Horton, N.G., Cruz-Hernández, J.C., Cheng, Y.T., Reimer, J., Tolias, A.S., Nishimura, N., et al. (2017). In vivo three-photon imaging of activity of GcamP6-labeled neurons deep in intact mouse brain. Nat. Methods *14*, 388–390.

Paul, K., Nieto, V., Carlquist, W.C., Blair, D.F., and Harshey, R.M. (2010). The c-di-GMP Binding Protein YcgR Controls Flagellar Motor Direction and Speed to Affect Chemotaxis by a “Backstop Brake” Mechanism. Mol. Cell *38*, 128–139.

Pawar, S.V., Messina, M., Rinaldo, S., Cutruzzolà, F., Kaever, V., Rampioni, G., and Leoni, L. (2016). Novel genetic tools to tackle c-di-GMP-dependent signalling in Pseudomonas aeruginosa. J. Appl. Microbiol. *120*, 205–217.

Power, R.M., and Huisken, J. (2017). A guide to light-sheet fluorescence microscopy for multiscale imaging. Nat. Methods *14*, 360–373.

Pozzo, T., Akter, F., Nomura, Y., Louie, A.Y., and Yokobayashi, Y. (2018). Firefly Luciferase Mutant with Enhanced Activity and Thermostability. ACS Omega *3*, 2628–2633.

Prescher, J.A., and Contag, C.H. (2010). Guided by the light: visualizing biomolecular processes in living animals with bioluminescence. Curr. Opin. Chem. Biol. *14*, 80–89.

Rathbun, C.M., and Prescher, J.A. (2017). Bioluminescent Probes for Imaging Biology beyond the Culture Dish. Biochemistry *56*, 5178–5184.

Rathbun, C.M., Porterfield, W.B., Jones, K.A., Sagoe, M.J., Reyes, M.R., Hua, C.T., and Prescher, J.A. (2017). Parallel Screening for Rapid Identification of Orthogonal Bioluminescent Tools. ACS Cent. Sci. acscentsci.7b00394.

Rodriguez, E.A., Campbell, R.E., Lin, J.Y., Lin, M.Z., Miyawaki, A., Palmer, A.E., Shu, X., Zhang, J., and Tsien, R.Y. (2017). The Growing and Glowing Toolbox of Fluorescent and Photoactive Proteins. Trends Biochem. Sci. *42*, 111–129.

Romling, U., Galperin, M.Y., and Gomelsky, M. (2013). Cyclic di-GMP: the first 25 years of a universal bacterial second messenger. Microbiol. Mol. Biol. Rev. *77*, 1–52.

Ross, P., Weinhouse, H., Aloni, Y., Michaeli, D., Weinberger-Ohana, P., Mayer, R., Braun, S., de Vroom, E., van der Marel, G.A., van Boom, J.H., et al. (1987). Regulation of cellulose synthesis in Acetobacter xylinum by cyclic diguanylic acid. Nature *325*, 279–281.

Rybtke, M.T., Borlee, B.R., Murakami, K., Irie, Y., Hentzer, M., Nielsen, T.E., Givskov, M., Parsek, M.R., and Tolker-Nielsen, T. (2012). Fluorescence-based reporter for gauging cyclic Di-GMP levels in Pseudomonas aeruginosa. Appl. Environ. Microbiol. *78*,

5060–5069.

Ryjenkov, D.A., Simm, R., Römling, U., and Gomelsky, M. (2006). The PilZ domain is a receptor for the second messenger c-di-GMP: The PilZ domain protein YcgR controls motility in enterobacteria. J. Biol. Chem. *281*, 30310–30314.

Saito, K., Hatsugai, N., Horikawa, K., Kobayashi, K., Matsu-Ura, T., Mikoshiba, K., and Nagai, T. (2010). Auto-luminescent genetically-encoded ratiometric indicator for real-time Ca2+ imaging at the single cell level. PLoS One *5*, e9935.

Saito, K., Chang, Y.-F., Horikawa, K., Hatsugai, N., Higuchi, Y., Hashida, M., Yoshida, Y., Matsuda, T., Arai, Y., and Nagai, T. (2012). Luminescent proteins for high-speed single-cell and whole-body imaging. Nat. Commun. *3*, 1262.

Santos, E.B., Yeh, R., Lee, J., Nikhamin, Y., Punzalan, B., Punzalan, B., Perle, K. La, Larson, S.M., Sadelain, M., and Brentjens, R.J. (2009). Sensitive in vivo imaging of T cells using a membrane-bound Gaussia princeps luciferase. Nat. Med. *15*, 338–344.

Shen, Y., Dana, H., Abdelfattah, A.S., Patel, R., Shea, J., Molina, R.S., Rawal, B., Rancic, V., Chang, Y.F., Wu, L., et al. (2018). A genetically encoded Ca 2+ indicator based on circularly permutated sea anemone red fluorescent protein eqFP578. BMC Biol. *16*, 1–16.

Srivastava, D., Harris, R.C., and Waters, C.M. (2011). Integration of Cyclic di-GMP and Quorum Sensing in the Control of vpsT and aphA in Vibrio cholerae. J. Bacteriol. *193*, 6331–6341.

Subramanian, S., Gao, X., Dann, C.E., and Kearns, D.B. (2017). MotI (DgrA) acts as a molecular clutch on the flagellar stator protein MotA in Bacillus subtilis . Proc. Natl. Acad. Sci. *114*, 13537–13542.

Sudarsan, N., Lee, E.R., Weinberg, Z., Moy, R.H., Kim, J.N., Link, K.H., and Breaker, R.R. (2008). Riboswitches in Eubacteria Sense the Second Messneger Cyclic Di-GMP. Science (80-.). *321*, 411–413.

Suzuki, K., Kimura, T., Shinoda, H., Bai, G., Daniels, M.J., Arai, Y., Nakano, M., and Nagai, T. (2016). Five colour variants of bright luminescent protein for real-time multicolour bioimaging. Nat. Commun. *7*, 13718.

Suzuki, K., Onishi, T., Nakada, C., Takei, S., Daniels, M.J., Nakano, M., Matsuda, T., and Nagai, T. (2018). Uninterrupted monitoring of drug effects in human-induced pluripotent stem cell-derived cardiomyocytes with bioluminescence Ca2+ microscopy. BMC Res. Notes *11*, 1–6.

Takai, A., Nakano, M., Saito, K., Haruno, R., Watanabe, T.M., Ohyanagi, T., Jin, T., Okada, Y., and Nagai, T. (2015). Expanded palette of Nano-lanterns for real-time multicolor luminescence imaging. Proc. Natl. Acad. Sci. *112*, 4352–4356.

Tannous, B.A., Kim, D.E., Fernandez, J.L., Weissleder, R., and Breakefield, X.O. (2005). Codon-optimized gaussia luciferase cDNA for mammalian gene expression in culture and in vivo. Mol. Ther. *11*, 435–443.

Tsien, R.Y. (1998). the Green Fluorescent Protein. Annu. Rev. Biochem. *67*, 509–544.

Wang, X.C., Wilson, S.C., and Hammond, M.C. (2016). Next-generation fluorescent RNA biosensors enable anaerobic detection of cyclic di-GMP. Nucleic Acids Res. *44*, e139.

Weissleder, R., and Ntziachristos, V. (2003). Shedding light onto live molecular targets. Nat. Med. *9*, 123–128.

Whiteley, A.T., Eaglesham, J.B., de Oliveira Mann, C.C., Morehouse, B.R., Lowey, B., Nieminen, E.A., Danilchanka, O., King, D.S., Lee, A.S.Y., Mekalanos, J.J., et al. (2019). Bacterial cGAS-like enzymes synthesize diverse nucleotide signals. Nature.

Wietek, J., and Prigge, M. (2016). Enhancing Channelrhodopsins: An Overview. In Optogenetics: Methods and Protocols, pp. 141–165.

Wright, T.A., Jiang, L., Park, J.J., Anderson, W.A., and Chen, G. (2019). Second messengers and divergent HD-GYP enzymes. BioRxiv.

Yang, J., Cumberbatch, D., Centanni, S., Shi, S., Winder, D., Webb, D., and Johnson, C.H. (2016). Coupling optogenetic stimulation with NanoLuc-based luminescence (BRET) Ca++ sensing. Nat. Commun. *7*, 13268.

Yao, Z., Zhang, B.S., and Prescher, J.A. (2018). Advances in bioluminescence imaging: new probes from old recipes. Curr. Opin. Chem. Biol. *45*, 148–156.

Yeh, H.W., Karmach, O., Ji, A., Carter, D., Martins-Green, M.M., and Ai, H.W. (2017). Red-shifted luciferase-luciferin pairs for enhanced bioluminescence imaging. Nat. Methods *14*, 971–974.

Yeh, H.W., Wu, T., Chen, M., and Ai, H.W. (2019a). Identification of Factors Complicating Bioluminescence Imaging. Biochemistry *58*, 1689–1697.

Yeh, H.W., Xiong, Y., Wu, T., Chen, M., Ji, A., Li, X., and Ai, H.W. (2019b). ATP-Independent Bioluminescent Reporter Variants to Improve in Vivo Imaging. ACS Chem. Biol. *14*, 959–965.

Yeo, J., Dippel, A.B., Wang, X.C., and Hammond, M.C. (2017). In Vivo Biochemistry: Single-cell dynamics of cyclic di-GMP in E. coli in response to zinc overload. Biochemistry *57*, 108–116.

Zhao, H., Doyle, T.C., Wong, R.J., Cao, Y., Stevenson, D.K., Piwnica-Worms, D., and Contag, C.H. (2004). Characterization of coelenterazine analogs for measurements of renilla luciferase activity in live cells and living animals. Mol. Imaging *3*, 43–54.

Zhao, H., Doyle, T.C., Coquoz, O., Kalish, F., Rice, B.W., and Contag, C.H. (2005). Emission spectra of bioluminescent reporters and interaction with mammalian tissue determine the sensitivity of detection in vivo. J. Biomed. Opt. *10*, 41210.

Zhou, H., Zheng, C., Su, J., Chen, B., Fu, Y., Xie, Y., Tang, Q., Chou, S.H., and He, J. (2016). Characterization of a natural triple-tandem c-di-GMP riboswitch and application of the riboswitch-based dual-fluorescence reporter. Sci. Rep. *6*, 1–13.

Zipfel, W.R., Williams, R.M., Christie, R., Nikitin, A.Y., Hyman, B.T., and Webb, W.W. (2003). Live tissue intrinsic emission microscopy using multiphoton-excited native fluorescence and second harmonic generation. Proc. Natl. Acad. Sci. *100*, 7075–7080.

Chapter Two

Chemiluminescent biosensors for detection of second messenger cyclic di-GMP

Portions of this chapter have been published in:

Dippel, A. B., Anderson, W. A., Evans, R. S., Deutsch, S., Hammond, M.C. "Chemiluminescent biosensors for detection of second messenger cyclic di-GMP." ACS Chem Bio (2018) *13*, 1872-1879.

ABSTRACT

Bacteria colonize highly diverse and complex environments, from gastrointestinal tracts, to soil and plant surfaces. This colonization process is controlled in part by the intracellular signal cyclic di-GMP, which regulates bacterial motility and biofilm formation. To interrogate cyclic di-GMP signaling networks, a variety of fluorescent biosensors for live cell imaging of cyclic di-GMP have been developed. However, the need for external illumination precludes the use of these tools for imaging bacteria in their natural environments, including in deep tissues of whole organisms and in samples that are highly autofluorescent or photosensitive. The need for genetic encoding also complicates the analysis of clinical isolates and environmental samples. Toward expanding the study of bacterial signaling to these systems, we have developed the first chemiluminescent biosensors for cyclic di-GMP. The biosensor design combines the complementation of split luciferase (CSL) and bioluminescence resonance energy transfer (BRET) approaches. Furthermore, we developed a lysate-based assay for biosensor activity that enabled reliable high-throughput screening of a phylogenetic library of 92 biosensor variants. The screen identified biosensors with very large signal changes (~40 and 90-fold) as well as biosensors with high affinities for cyclic di-GMP (K_D <50 nM). These chemiluminescent biosensors then were applied to measure cyclic di-GMP levels in *E. coli*. The cellular experiments revealed an unexpected challenge for chemiluminescent imaging in Gram negative bacteria, but showed promising application in lysates. Taken together, this work establishes the first chemiluminescent biosensors for studying cyclic di-GMP signaling, and provides a foundation for using these biosensors in more complex systems.

INTRODUCTION

The second messenger 3',5'-cyclic di-guanosine monophosphate (c-di-GMP) is the first discovered cyclic dinucleotide signaling molecule and has been found to be nearly ubiquitous in bacteria (Romling et al., 2013; Ross et al., 1987). Within cells, c-di-GMP levels are controlled by complex networks of diguanylate cyclases (DGCs) and c-di-GMP phosphodiesterases (PDEs) that work to tightly regulate the cellular concentration of this second messenger, often in response to extracellular signals (Hengge, 2009; Sarenko et al., 2017). These signaling networks coordinate a multitude of fundamental cellular functions, including the transition from sessile to motile states, virulence, and cell cycle control. To interrogate the dynamics of c-di-GMP within these complex signaling networks, we and others have developed biosensors for live cell imaging of c-di-GMP. These include protein-based FRET biosensors that have been used in *E. coli* (Ho et al., 2013), *C. crescentus*, *S. typhimurium,* and *P. aeruginosa* (Christen et al., 2010; Mills et al., 2015), as well as RNA-based fluorescent biosensors that have been used in *E. coli* and allow for the first time the ability to image c-di-GMP under anaerobic conditions (Wang et al., 2016).

One long-term goal in the field is to analyze c-di-GMP signaling in more complex settings, including bacteria colonizing the gut, and in clinical isolates, mixed cultures, or environmental samples (Koestler and Waters, 2014; Rossi et al., 2017). None of these applications have been shown with the fluorescent biosensor tools currently available. Due to its reliance on external illumination, fluorescent imaging is often incompatible with

imaging in deep tissues of animals and in long-term experiments due to phototoxicity. Additionally, fluorescent biosensors are difficult to apply to clinical isolates, mixed cultures, and environmental samples, because they haven't been shown to work in complex lysates that exhibit increased autofluorescence and decreased signal due to sample dilution. One alternative technique that does not require external illumination to produce a signal is chemiluminescence imaging (Prescher and Contag, 2010). Thus, to expand the study of c-di-GMP signaling networks to these more complex systems, we sought to develop the first chemiluminescent biosensors for c-di-GMP.

Chemiluminescent biosensors generally utilize luciferases, enzymes which catalyze the oxidation of small molecule luciferin substrates to produce light (Saito and Nagai, 2015). Luciferase-based biosensors typically fall into one of two categories: complementation of split luciferase (CSL) or bioluminescence resonance energy transfer (BRET)-based biosensors. In CSL systems, a sensor domain is used to split the luciferase protein into two non-functional halves, such that analyte binding results in a conformational change that reconstitutes the luciferase to produce a change in signal intensity (Fan et al., 2008; Hattori et al., 2013; Kaihara et al., 2008; Takenouchi et al., 2016; Zhang et al., 2007). In BRET systems, the sensor domain is inserted between a fluorescent protein acceptor on one side and an intact luciferase donor on the other side, and analyte binding leads to a change in BRET efficiency between donor and acceptor (Biswas et al., 2008; Jiang et al., 2007; Saito et al., 2010; Yang et al., 2016). CSL biosensors generally produce large signal changes, however their signal intensity is often low due to poor reconstitution of luciferase activity. BRET biosensors generally have high signal intensity and are ratiometric, however their signal change upon analyte binding is typically small. To overcome these drawbacks, the Nagai lab combined the CSL and BRET approaches and used Nano-lantern (NL) or enhanced Nano-lantern (eNL) scaffolds to produce chemiluminescent biosensors with large signal changes (up to 4-fold with original NL and 6-fold with eNL) and good signal intensity for imaging (Saito et al., 2012; Suzuki et al., 2016; Takai et al., 2015). They used these biosensors to perform single-cell imaging of Ca^{2+}, cyclic AMP, and ATP in HeLa cells, *D. discoideum* cells, and *Arabidopsis* plant leaves, respectively (Saito et al., 2012).

In this work, we applied the CSL-BRET strategy to develop the first chemiluminescent biosensors for c-di-GMP. First, an insertion site for the *E. coli* c-di-GMP binding protein YcgR (*Ec*YcgR) within the NL scaffold was found that generated a functional biosensor. Next, we mined sequence databases for diverse YcgR homologs and selected a set of 92 proteins for functional characterization within the biosensor scaffold. These phylogenetic variants were synthesized as codon optimized sequences for cloning into the NL scaffold. The resulting phylogenetic biosensor library was expressed and rapidly screened in a lysate-based assay for response to c-di-GMP. A large number of biosensors were identified with improved affinity, signal change, and stability compared to the initial *Ec*YcgR biosensor. This new collection of chemiluminescent biosensors includes ones with the highest affinity for a protein-based c-di-GMP biosensor (<50 nM) and others with the largest signal change for a CSL-BRET biosensor (up to 90-fold). These biosensors were applied to measure c-di-GMP levels in live *E. coli*, and revealed challenges for chemiluminescence imaging in Gram-negative bacteria. Subsequently, we developed a bacterial lysate assay for diguanylate cyclase

activity using the biosensors. This work provides the first chemiluminescent biosensors for measuring c-di-GMP levels in bacteria and lays the groundwork for live cell imaging of c-di-GMP dynamics without external illumination.

RESULTS

Design of chemiluminescent biosensor for cyclic di-GMP. PilZ domain-containing proteins bind c-di-GMP and have previously been used to generate genetically encoded FRET biosensors for c-di-GMP (Christen et al., 2010; Ho et al., 2013; Pultz et al., 2012). For the initial design, the PilZ domain-containing protein YcgR from *E. coli* (*Ec*YcgR) was chosen as the sensor domain to insert into the yellow Nano-lantern (YNL) scaffold, which is an NL scaffold that uses Venus as the fluorescent acceptor (Figure 2.1a). *Ec*YcgR has previously been shown to bind to c-di-GMP with an affinity of ~800 nM and undergo a large conformational change upon binding (Ryjenkov et al., 2006).

Four biosensors were designed that differed in either the split site of RLuc8 (91/92 or 228/229) or the deletion/retention of a flexible N-terminal region of RLuc8 (1.0 or 1.1 scaffold) (Figure 2.1b). These designs were chosen based on previously developed NL sensors (Saito et al., 2012). The four biosensors were constructed, expressed, and purified from *E. coli*, then tested for response to c-di-GMP. While all of the biosensors produced a chemiluminescent signal, only biosensors with *Ec*YcgR inserted at the 91/92 site of RLuc8 produced a c-di-GMP-dependent change in signal (Figure 2.1c). For further characterization, the biosensors were expressed and purified from *E. coli* co-expressing the c-di-GMP-specific phosphodiesterase PdeH (also called YhjH) to ensure that minimal to no c-di-GMP remain bound. The EcYcgR-91 biosensor has a dissociation constant (K_D) for c-di-GMP of 615 ± 115 nM and gives a 2.6-fold change in chemiluminescent signal intensity upon binding (Figure 2.1d). The measured affinity for the biosensor is slightly improved compared to previously reported affinity values for *Ec*YcgR alone (Ryjenkov et al., 2006) and the signal change and intensity are comparable to previously developed NL biosensors (Saito et al., 2012). Additional *in vitro* binding tests with related compounds showed that the biosensor is highly specific for c-di-GMP (Figure 2.1d).

Lysate-based assay of biosensor performance. One of the benefits of chemiluminescent biosensors compared to fluorescent or FRET-based biosensors is that because external illumination is not required, output signal is not compromised by solution autofluorescence. Accordingly, we find that biosensor activity can be reliably assayed in lysates of cells grown in complex media with no further purification. Growth and assay procedures were optimized to permit the use of small culture volumes and to produce consistent growth between wells, which led to the development of a 96-well plate format lysate activity assay for biosensor constructs (Figure 2.2). Importantly, by measuring in lysates rather than whole cells, new biosensor designs can be rapidly and reliably screened with any analyte of interest at a set concentration, including non-cell permeable compounds like c-di-GMP.

Using this assay workflow, various mutants of *Ec*YcgR were tested (Figure 2.3a). These mutations have been characterized in other YcgR proteins, and are predicted to alter the binding stoichiometry to c-di-GMP (M1; R113L mutant) (Ko et al., 2010) abolish binding to c-di-GMP (M2, R118D), or improve affinity for c-di-GMP (M3; S147A mutant) (Ryjenkov et al., 2006). A double mutant combination of M1 and M3 mutations (M4;

R113L, S147A) was also tested. While M2 severely reduced binding affinity as expected, the other mutations also led to decreased affinity or signal change (Figure 2.3b, c; Supplemental Notes). In addition, a small library of biosensors with different linkers flanking *Ec*YcgR was analyzed using the lysate-based screen. It is well known that linker length and composition can produce large changes in the affinity and/or signal change of both CSL and BRET-type biosensors (Fan et al., 2008; Thestrup et al., 2014) but to our knowledge, this had not yet been tested in NL biosensors. Six different linker designs were tested spanning a length of 2–5 residues on either side of *Ec*YcgR that were designed to be either flexible or rigid (Figure 2.3a). However, none of the new linker designs produced signal changes better than the original linkers used (Figure 2.3d; Supplemental Notes).

This 96-well format lysate-based activity assay enables biosensor constructs to be rapidly assessed without individually purifying each protein. A small library of *Ec*YcgR mutants and linker variants was tested, but none showed improved biosensor performance. While a larger randomized library-based approach could lead to improved affinity or signal change, the biosensor would remain limited by the characteristics of the sensor domain, *Ec*YcgR. Thus, we instead decided to focus on altering the sensor domain itself in the next round of optimization.

Phylogenetic screen for improved c-di-GMP binding domains. Our lab has previously used phylogenetic libraries in the development of RNA-based fluorescent biosensors, and we have found that such an approach can lead to rapid improvements in biosensor characteristics (Su et al., 2016; Wang et al., 2016). A small number of YcgR proteins have been tested in FRET-based biosensors for c-di-GMP, with the best design exhibiting a –60.6% signal change and 195 nM affinity (Christen et al., 2010; Mills et al., 2015). For a wider screen, all PilZ-containing proteins with domain architectures similar to *Ec*YcgR (YcgR-PilZ and YcgR_2-PilZ) were obtained from the Pfam database. From this set of 840 sequences resulting from the bioinformatic query, 92 sequences were synthesized and cloned into the NL scaffold (Table 2.3) using the design found to work best with the *Ec*YcgR sensor domain (91/92 insertion site, 1.0 scaffold). This set included 34 sequences chosen from the genomes of candidate thermophilic bacteria, as we hypothesized that these would produce more stably folded biosensors. Additionally, c-di-GMP binding to PilZ domains has been found to be largely entropically driven (Benach et al., 2007) so we expected that sensor domains from thermophiles may bind with higher affinity to c-di-GMP than those from mesophiles. Of the remaining 58 sequences, at least three were previously characterized YcgR proteins (Benach et al., 2007; Ko et al., 2010; Paul et al., 2010) and the remainder were chosen from a large variety of different bacterial genomes.

All sequences were codon optimized for *E. coli* expression to aid screening. In addition, an mCherry fluorescent tag (Shaner et al., 2004) was introduced at the C-terminus to measure the relative folding stability of each biosensor variant. During purification of *Ec*YcgR biosensors, it was found that truncated proteins were produced at appreciable levels during expression, suggesting the degradation of improperly folded biosensors (Figure 2.4a). In contrast, the purified YNL had little-to-no truncated products. Thus, the ratio of mCherry fluorescence (C-terminal) to Venus fluorescence (N-terminal) provides a proxy for the relative amount of full-length biosensor in cells and can be

determined in a high-throughput manner via flow cytometry. This ratio for each phylogenetic variant was normalized to the ratio for the *Ec*YcgR biosensor (mCh/Venus = 1). Library members with mCherry/Venus fluorescence ratios above 1 were considered more well-folded than *Ec*YcgR, while library members with fluorescence ratios lower than 1 were considered less well-folded (Figure 2.4b). The mCherry-tagged version of the *Ec*YcgR biosensor was tested in the lysate-based assay and showed that the mCherry tag had little-to-no effect on biosensor performance (Figure 2.4c).

To determine signal change and relative affinity for c-di-GMP, all candidate biosensors were tested in the lysate-based assay with two different concentrations of c-di-GMP (Figure 2.5, 2.6a). Less than 10% (8 sequences) were inactive and produced low chemilumescent signal, likely due to poor expression and/or misfolding. Of the sequences that were active, over 40% (34 sequences) showed signal changes better than *Ec*YcgR in response to 20 µM c-di-GMP (~1.86-fold). Two constructs showed signal changes of ~17-fold and ~28-fold, which are larger than signal changes for previously developed NL biosensors (Saito et al., 2012; Suzuki et al., 2016). Interestingly, while the large majority of these variants all showed signal changes in the positive direction, 3 sequences showed signal changes in the negative direction, suggesting that they may undergo a different sort of structural rearrangement upon binding to c-di-GMP. Of all tested constructs, over 60% (56 sequences) showed relative folding stability better than the *Ec*YcgR biosensor, and 6 showed greater stability than the YNL scaffold itself. Out of the 31 thermophilic variants that were active, 25 showed better folding stability than *Ec*YcgR, supporting the hypothesis that thermophilic sensor domains produce more well-folded biosensors in the NL scaffold. Taken together, this lysate-based screen of a large phylogenetic library of YcgR sensor domains resulted in multiple biosensors that exhibit the largest signal changes of any NL biosensors to date, as well as many biosensors that are more well-folded and have larger signal change than the original *Ec*YcgR biosensor.

***In vitro* characterization of phylogenetic biosensor variants.** From the screening panel, a subset of biosensors that displayed either increased affinity, large signal change, or rare negative signal change were chosen for re-screening and further analysis. For in vitro characterization, all phylogenetic biosensor variants were recloned without the mCherry tag and expressed, then purified from cells co-expressing PdeH to ensure that minimal to no c-di-GMP remain bound. Biosensors that showed maximal signal in response to 1 µM c-di-GMP in the original screen were predicted to have increased affinity; we further selected only biosensors that displayed positive signal change of at least 2.5-fold. Out of the 31 sequences with positive signal changes greater than *Ec*YcgR, 9 met these criteria. Re-screening in the lysate-based assay with lower concentrations of c-di-GMP confirmed that all 9 sequences had affinities better than or equal to *Ec*YcgR, while 7 of the sequences appeared to have affinities <200 nM (Figure 2.6b). As purified proteins, these 7 sequences span a range of affinities, all <200 nM, with 5 of the sequences exhibiting affinities <50 nM (Table 2.1). Interestingly, the *Cb*YcgR biosensor showed a decrease in signal intensity at high concentrations of c-di-GMP, suggesting a secondary binding site (Figure 2.7a).

The two biosensor variants that showed large signal changes in the lysate-based screen, *Dn*Ycgr and *To*YcgR, demonstrated signal changes of ~40-fold and ~25-fold as purified proteins, respectively (Table 2.1; Figure 2.7a). These signal changes are about

10x higher than those seen in any previously developed NL biosensors. To our knowledge, the largest signal change reported for any rationally designed, single chain CSL-type biosensor was a 70-fold change for a cAMP biosensor (Fan et al., 2008). Interestingly, the largest signal change we characterized was for *Bt*YcgR, which exhibited negative signal change and showed ~90-fold maximal decrease in chemiluminesence activity in response to c-di-GMP (Figure 2.7a). *Bt*YcgR was among the most poorly folded variants as measured by the mCh/Venus fluorescence ratio, which may contribute to its large signal change. Of the other 2 biosensor sequences with negative signal changes, *Pt*YcgR recapitulated the lysate-based results, while *Nt*YcgR did not. The biosensors with negative signal changes could be useful for measuring decreases in c-di-GMP, for example, due to phosphodiesterase activity.

The ligand selectivities for three of the high affinity biosensors were tested, and all retained high selectivity for c-di-GMP versus (3'3')-cAG and pGpG (Figure 2.8a). Both *Cp*YcgR and *Tb*YcgR biosensors showed >100-fold selectivity against (3'3')-cAG and no appreciable binding to pGpG. *Tu*YcgR also showed >100-fold selectivity against (3'3')-cAG, but was slightly less selective against pGpG than the other biosensors were. Interestingly, our lab has shown that riboswitch-based biosensors for c-di-GMP have exquisitely selectivity against other cyclic di-nucleotides, with no appreciable binding, but ~2000-fold selectivity against pGpG (Wang et al., 2016), which is the opposite trend to what is observed for these protein-based biosensors.

Another key characteristic of these biosensors is signal intensity. CSL-type biosensors rely on the complementation of a split enzyme to produce signal, so their signal intensity is often only a fraction of the brightness of the non-split protein. In previously developed NL biosensors, for example, the brightest design achieved 35% of the intact YNL signal and was sufficient for single cell imaging experiments (Saito et al., 2012). Two of our highest affinity biosensors variants, *Tu*YcgR and *Cp*YcgR, gave maximal signal intensities of ~40% and 30%, respectively, of the intact YNL signal (Figure 2.8b). However, while total protein concentration was the same for each sample based on Venus domain absorbance (Nagai et al., 2002), the biosensor samples contained visible amounts of a truncated product including Venus, whereas the YNL sample was a single protein band (Figure 2.7b). Thus, the relative chemiluminescence intensities we measured likely underestimate the actual brightness of the biosensors.

Finally, we measured the response time for one of the best-performing biosensors, *Cp*YcgR. To test the kinetics of biosensor activation, c-di-GMP was co-injected with chemiluminescent substrate at time 0 into solutions containing the biosensor. To provide comparison to prebound or unbound controls, the *Cp*YcgR biosensor was pre-incubated with or without c-di-GMP before substrate was injected at time 0. The $t_{1/2}$ value for the co-injected sample was 9-9.5 sec compared to the $t_{1/2}$ value of 0.2 sec for prebound biosensor (Figure 2.8c). This experiment shows that the CSL-BRET biosensor undergoes a c-di-GMP-dependent conformational change that activates chemiluminescence in less than one minute, which is similar to the results for YcgR-based FRET biosensors used for live cell imaging (Christen et al., 2010).

Taken together, in vitro characterization of phylogenetic variants revealed a set of biosensors with good signal changes that span a range of affinities for c-di-GMP,

including several incorporating novel YcgR proteins that have <50 nM K_D values. One biosensor showed positive signal changes of ~40-fold and another showed negative signal changes of ~90-fold, which are among the largest signal changes observed for any CSL-type biosensors. Finally, the biosensors showed strong signal intensities and fast activation in response to c-di-GMP.

Measuring cellular levels of c-di-GMP with chemiluminescent biosensors. As an initial test of our new NL biosensors for measuring c-di-GMP in live cells, we co-expressed a subset of the mCherry-tagged biosensors in *E. coli* along with a diguanylate cyclase (WspR-D70E) or a phosphodiesterase (PdeH) to generate high or low levels of c-di-GMP, respectively. After overnight growth in autoinduction media, cells were pelleted and washed with PBS, then chemiluminescent substrate was added and total signal was measured in a plate reader. The mCherry fluorescence signal of the cells was also measured so that chemiluminescent signal intensity could be normalized to the amount of full-length biosensor (LUM/mCherry FL). However, to our surprise, the majority of biosensors did not show the expected signal increase with WspR-D70E (Figure 2.9a). Instead, several of them showed decreases in total signal when comparing WspR-D70E versus PdeH overexpressing cells, which was also observed for YNL alone.

The result for YNL suggested that WspR-D70E overexpression could be decreasing substrate diffusion into cells due to increased biofilm formation, which is a phenotypic consequence of high c-di-GMP levels. Thus, we repeated the experiment but lysed the cells using the same protocol as the lysate-based assay before adding the chemiluminescent substrate. With no barriers to substrate diffusion, all the biosensors except for *Tu*YcgR showed signal increases with WspR-D70E lysates versus PdeH lysates, whereas YNL showed no significant difference (Figure 2.9b). In addition, the normalized signal intensities were also much larger in cell lysates compared to live cells, which is consistent with substrate diffusion affecting the signal in intact cells.

Thus, we revised the plan to develop a rapid assay for measuring c-di-GMP levels in cell lysates instead. In this assay, the purified *Cp*YcgR biosensor is added directly to lysed cells and signal is measured after addition of chemiluminescent substrate in a plate reader (Figure 2.9c). Due to *E. coli* having low endogenous levels of c-di-GMP (Sarenko et al., 2017) we could not detect differences in c-di-GMP lysate levels between cells expressing inactive enzyme (WspR-G249A, i.e. endogenous levels) or expressing a c-di-GMP specific phosphodiesterase (PdeH). However, from these data we were able to observe clear differences in c-di-GMP lysate levels between cells expressing active diguanylate cyclases (WspR-WT, WspR-D70E, and PleD) and control cells containing empty vector. Notably, the signal strength and fold-change of the *Cp*YcgR biosensor was almost identical in cell lysates and in buffer alone.

DISCUSSION AND FUTURE DIRECTIONS

This work represents, to our knowledge, the development of the first chemiluminescent biosensors for c-di-GMP. After initial validation of the NL biosensor design, a phylogenetic library of YcgR-like proteins was rapidly screened in a lysate-based assay to identify variants with improved biosensor characteristics. The two key benefits of this lysate-based assay are that the biosensors can be screened without purification and for binding to any ligand of interest. We envision that a similar approach can be used to screen YcgR

mutants in a high-throughput manner to generate chemiluminescent biosensors for other cyclic dinucleotides, such as c-di-AMP, (2',3')-cGAMP, and (3',3')-cGAMP (Danilchanka and Mekalanos, 2013; Krasteva and Sondermann, 2017).

The screen identified a panel of biosensor variants with improved affinity, signal change, folding stability, and signal intensity compared to the initial *Ec*YcgR biosensor and other protein-based biosensors for c-di-GMP. While Nano-lantern-based biosensors have been used to make live cell measurements in eukaryotic systems, to our knowledge, they had not been applied in bacterial systems prior to this study. Our results suggest that changes in diffusion of the chemiluminescent substrate, coelenterazine-h, due to increased biofilm formation may be an issue for live cell experiments in bacteria, which can be overcome in part by performing measurements with the biosensors in cell lysates. Thus, we developed a rapid plate reader-based assay for measuring diguanylate cyclase activity in cell lysates, which could be applied to other types of complex samples, such as clinical isolates or microbial co-cultures. Future work will focus on developing ratiometric, rather than intensity-based, chemiluminescent biosensors using the panel of sensor domains discovered here to overcome limitations in bioavailability of substrate. An encouraging precedent is a ratiometric BRET system that has been employed to monitor chemotaxis receptor kinase activity in live *E. coli* (Shimizu et al., 2006). Ultimately, we aim to study c-di-GMP dynamics in biological systems for which fluorescent biosensors are less useful, such as in plant-pathogen interactions or intestinal bacteria in the gut.

FIGURES

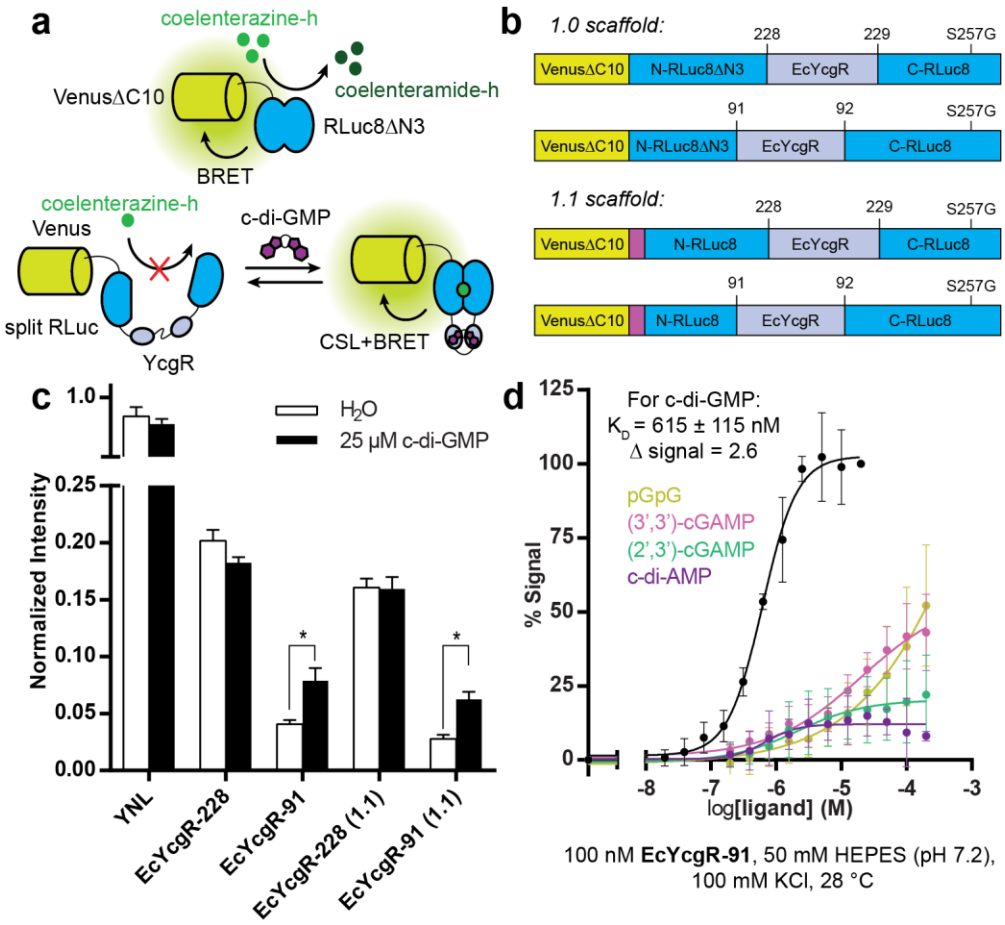

Figure 2.1 Initial design and characterization of *Ec*YcgR biosensors. (a) BRET and CSL-BRET mechanism for the yellow Nano-lantern (YNL) scaffold (top) and for NL sensors for c-di-GMP, respectively (bottom). (b) Schematic of the domain structures of *Ec*YcgR sensors. (c) Relative chemiluminescent signal intensity of *Ec*YcgR sensors with or without c-di-GMP. Data are from at least 4 replicates represented as mean ± SD. (d) Biosensor binding affinity measurements for *Ec*YcgR-91. Data are from 3 replicates represented as mean ± SD.

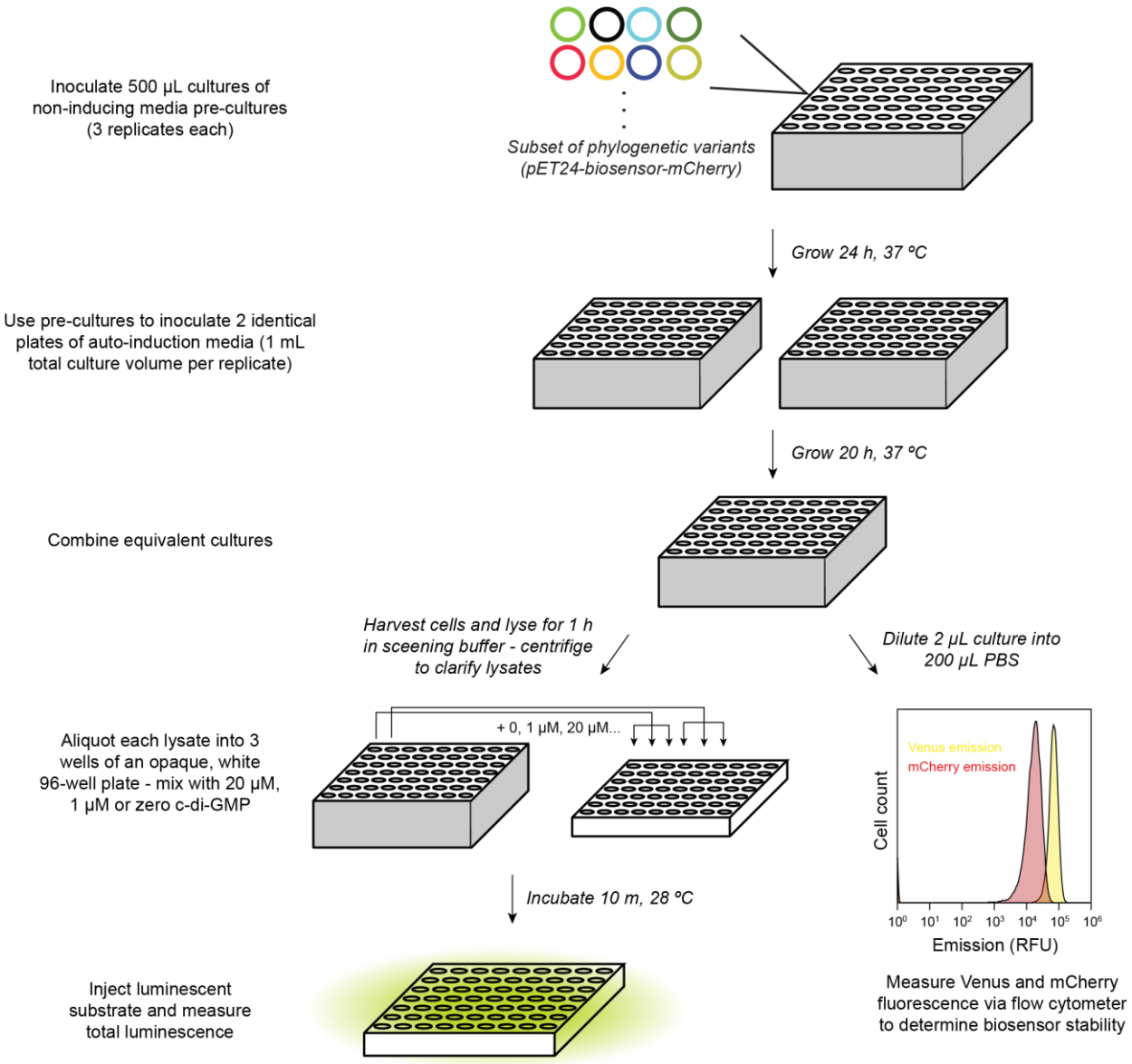

Figure 2.2 Workflow for lysate-based biosensor assay. *E. coli* transformed with biosensor variants are grown in non-inducing media in deep-well plates to generate pre-cultures. The following day, pre-cultures are used to inoculate auto-induction media and cultures are grown overnight. The next day, a small aliquot of cells is analyzed via flow cytometry to determine relative biosensor expression and stability. The remaining cells are harvested and lysed in screening buffer. Clarified lysates are mixed with c-di-GMP in an opaque white, 96-well plate, chemiluminescent substrate is added, and total chemiluminescent signal is measured to determine signal fold-changes.

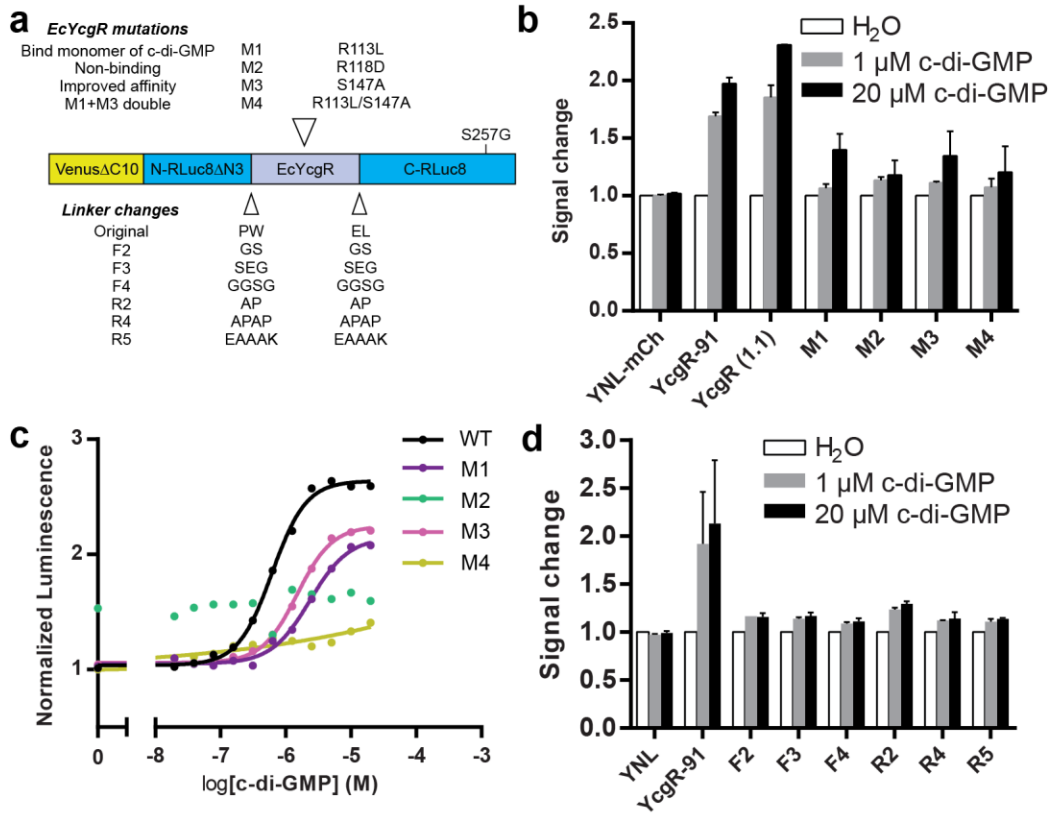

Figure 2.3 Lysate-based screen of *Ec*YcgR biosensor mutant and linker variants. (a) Schematic of *Ec*YcgR-91 biosensor showing different mutations to *Ec*YcgR and the different linkers tested. (b) Signal change for *Ec*YcgR-91 biosensors and mutants in the lysate-based assay. Data are from 2 biological replicates represented as mean ± SD. (c) Biosensor binding affinity measurements with purified *Ec*YcgR-91 mutants. Data are presented as mean of 3 replicates. Error bars are omitted for clarity. (d) Signal change for *Ec*YcgR-91 linker variants in the lysate-based assay. Data are from 2 biological replicates represented as mean ± SD.

Supplemental Notes:

***Ec*YcgR mutations.** The R113L mutation (M1) in YNL-EcYcgR was predicted to change the c-di-GMP binding stoichiometry from 2:1 to 1:1 as well as reduce affinity for c-di-GMP based on analysis of the corresponding mutant in the YcgR protein PP4397 from *P. putida* (Ko et al., 2010). As expected, M1 showed reduced affinity in the lysate-based assay (Figure 2.3b). Measurements with purified protein confirmed the reduced affinity and showed that binding stoichiometry was very slightly reduced compared to WT (Figure 2.3c). The oligomeric states of c-di-GMP are dependent on the ions present, with potassium (present at 100 mM in the binding assay buffer) promoting the formation of higher order oligomeric complexes, which may have complicated measurements of the binding stoichiometry (Ko et al., 2010; Zhang et al., 2006).

The R118D mutation (M2) in YNL-EcYcgR was predicted to knock out binding for c-di-GMP, as this residue should make key interactions with the phosphate linkage of c-di-GMP. This mutation effectively ablated binding to c-di-GMP, as expected.

The S147A mutation (M3) in the YNL-EcYcgR scaffold was predicted to modestly improve affinity for c-di-GMP based on literature measurements (Ryjenkov *et al*. reported a K_D change from 0.84 ± 0.16 μM to 0.69 μM for full-length EcYcgR (Ryjenkov et al., 2006)), but our lysate-based measurements showed slightly reduced affinity instead. This discrepancy may be due to differences in the protein constructs, the assay methods (Ryjenkov *et al*. used equilibrium dialysis with purified protein), and buffer conditions. Interestingly, the corresponding mutant in PP4397 has a 4-fold reduced affinity as measured by ITC, which is in line with our result (Ko et al., 2010).

Due to additive effects, the S147A/R113L double mutation (M4) showed poorer affinity than either M1 or M3 mutation alone.

M1, M3, and M4 mutations to YNL-EcYcgR unexpectedly led to decreased signal changes (Figure 2.3c). These mutations to the c-di-GMP binding pocket may subtly alter the conformation of the bound or unbound state of the sensor domain.

Linker screen. The different linker regions tested in YNL-EcYcgR all showed decreased signal changes compared to the original linker sequence used (Figure 2.3d). While no crystal structure is available for EcYcgR that would allow for a rational design of the linker regions, crystal structures of the homologous YcgR protein PP4397 from *P. putida* provide some degree of insight into the relative distance and orientation of the N- and C-termini in YcgR proteins. PP4397 was analyzed in the phylogenetic screen (sequence 2 in Figure 2.6a) and was found to behave very similarly to EcYcgR, which suggests that their overall structures are likely similar. In the apo x-ray crystal structure of full length PP4397 (PDB ID: 2GJG), the distance between Cα atoms of the N- and C-termini is ~25.7 Å. This distance appears to be too long to be bridged by the original linker that gave a functional YNL-EcYcgR biosensor, which was 2 residues. However, we note that the first ~11 N-terminal residues and the last ~3 C-terminal residues are largely unstructured, so may serve as flexible linkers on their own.

Prior to this structural analysis, we had designed new linkers to be either flexible or rigid with varying lengths from 2 to 5 residues. All of the linkers tested showed similarly decreased signal changes compared to the original linker, which suggests that they led to increased interaction of RLuc halves in the unbound state. These results indicate that shortening the linkers or truncating the YcgR protein may lead to improved signal change and/or brightness for YNL-EcYcgR, but these changes are unlikely to be directly translatable to other phylogenetic variants, which are of different lengths. Since the original linkers were applied successfully to YNL-EcYcgR and other Nano-lantern-based biosensors (Saito et al., 2012), they were carried forward to the phylogenetic screen.

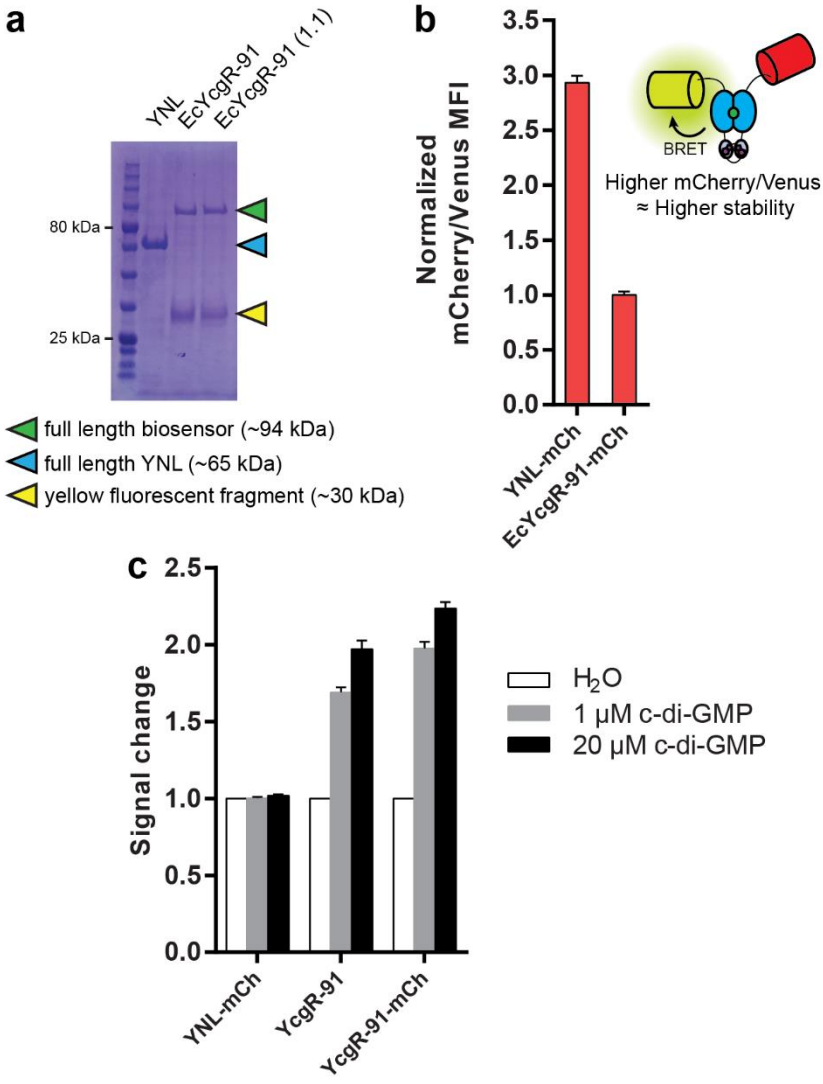

Figure 2.4 Analysis of mCherry tag as measure of biosensor stability. (a) SDS-PAGE of purified proteins showing presence of truncated protein products for NL biosensor constructs. (b) Normalized mCherry/Venus MFI ratios of cells expressing mCherry tagged NL constructs as measured by flow cytometry. Ratios are normalized to the ratio for EcYcgR-91-mCh and show that the ratio correlates with relative protein stability. Data are from 3 biological replicates represented as mean ± SD. (c) Signal change for NL constructs in the lysate-based assay show the mCherry tag has no negative effect on biosensor performance. Data are from 2 biological replicates represented as mean ± SD.

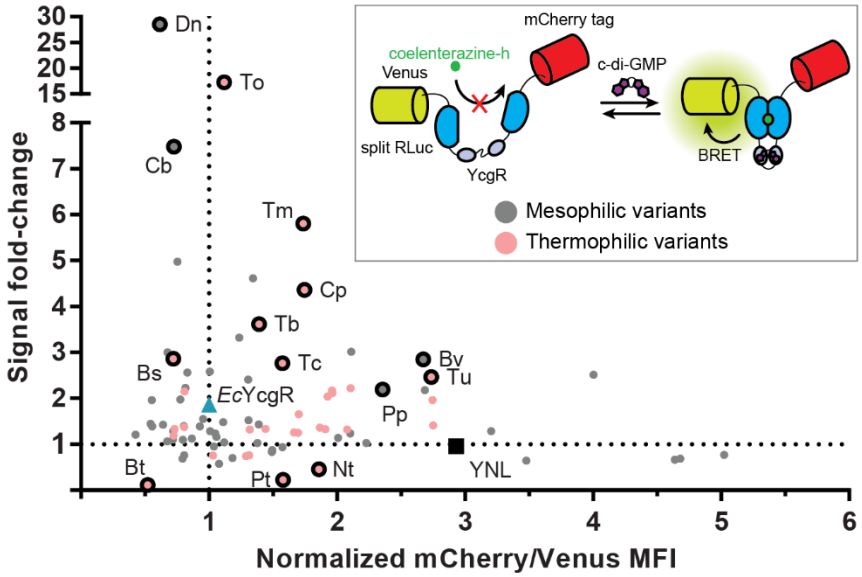

Figure 2.5 Lysate-based screen of phylogenetic biosensor variants identifies a panel of improved biosensor variants. Signal fold-change, defined as ratio of signal with 20 μM c-di-GMP to no c-di-GMP, was plotted with respect to biosensor stability (*x*-axis), defined as ratio of mCherry/Venus mean fluorescence intensities (MFIs) normalized to the valuye for the *Ec*YcgR biosensor. Pink data points correspond to sequence variants from thermophilic organisms, and gray data points correspond to sequence variants from mesophilic organisms. The original *Ec*YcgR biosensor (blue triangle) and YNL (black square) are labeled for comparison. Circled data points correspond to variants chosen for further characterization. Inset: General scheme for biosensor variants showing the mCherry-tagged constructs used in the screen.

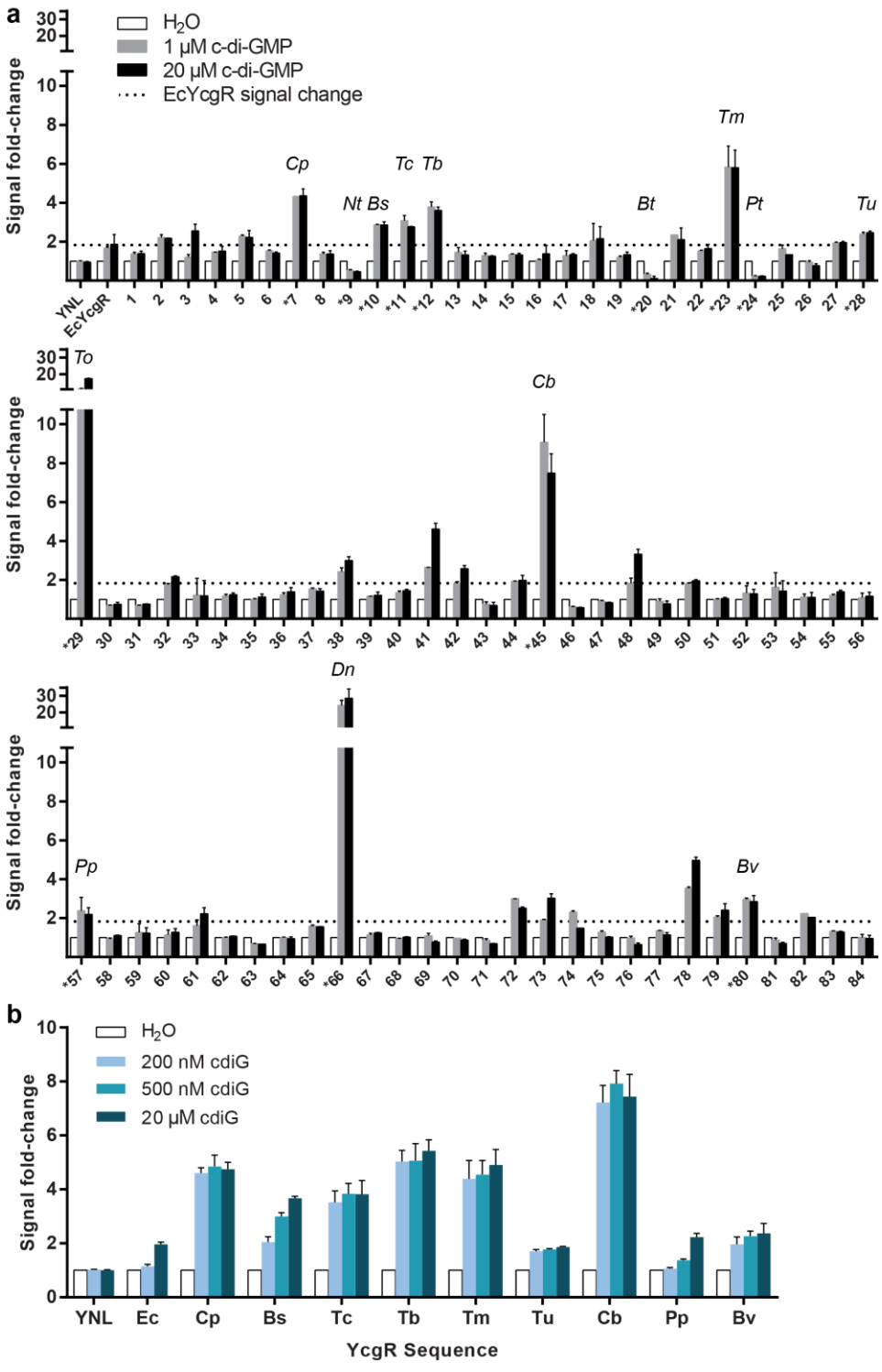
a
H2O
1 μM c-di-GMP
20 μM c-di-GMP
EcYcgR signal change
Signal fold-change
YNL
EcYcgR
Cp
Nt Bs
Tc Tb
Tm
Bt
Pt
Tu
To
Cb
Dn
Pp
Bv
b
H2O
200 nM cdiG
500 nM cdiG
20 μM cdiG
Signal fold-change
YNL Ec Cp Bs Tc Tb Tm Tu Cb Pp Bv
YcgR Sequence

Figure 2.6 Lysate-based screen of phylogenetic library variants. (a) Signal fold-change for the 84 active phylogenetic biosensor variants. Labeled sequences were chosen for further characterization due to apparent high affinity, large signal change, or negative signal change. See Table 2.3 for numbering. Data are from 2 biological replicates represented as mean ± SD. (b) Signal fold-change for selected high affinity variants. Selected variants were re-screened in the lysate-based assay with lower concentrations of c-di-GMP. Data are from 3 biological replicates represented as mean ± SD.

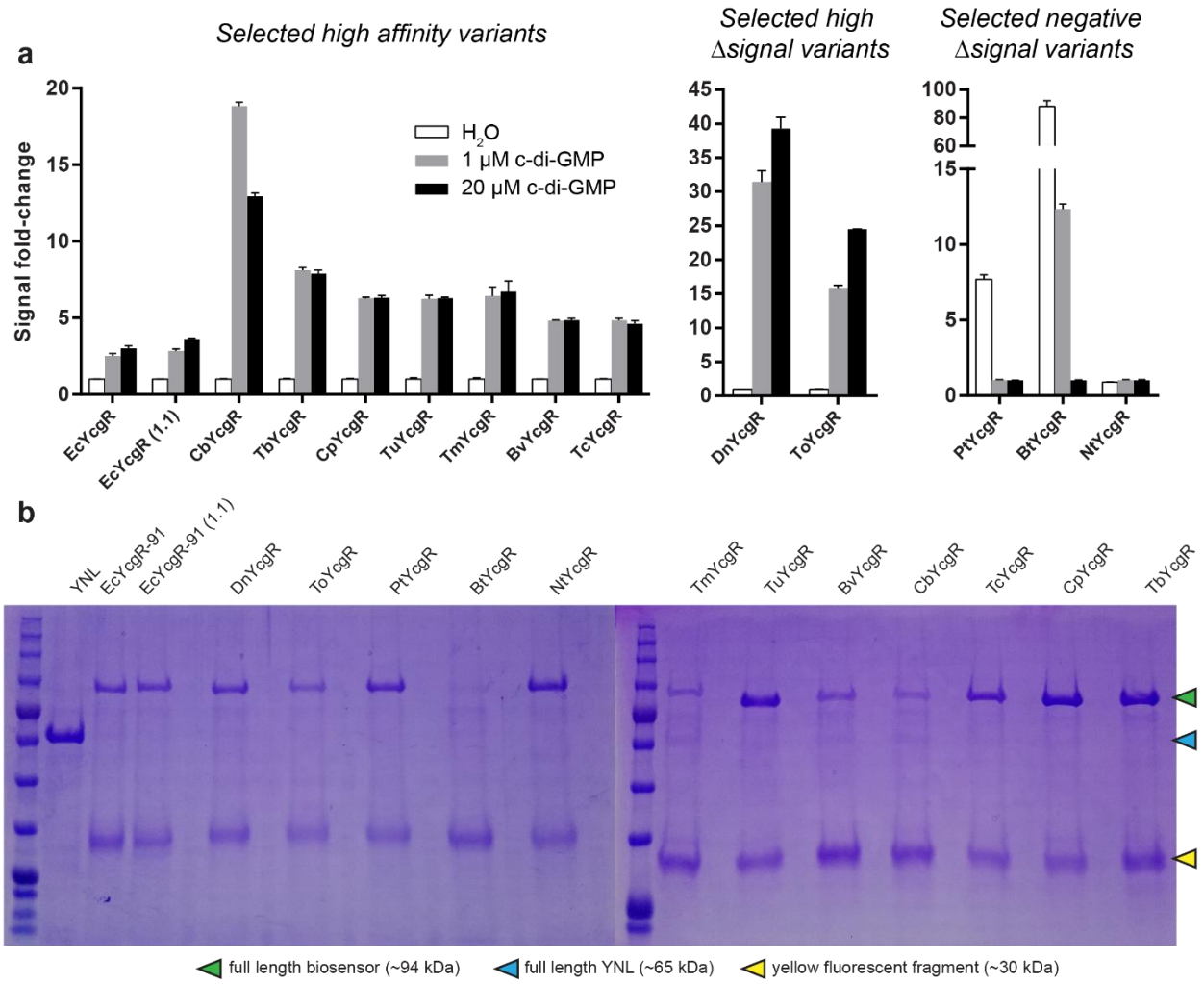

Figure 2.7 In vitro characterization of biosensor variants. (a) Same data as in Figure 3b, but presented as signal fold-change. Values are normalized to no c-di-GMP for selected high affinity and high Δsignal variants, and values are normalized to 20 μM c-di-GMP for negative Δsignal variants. Signal change data is summarized in Table 2.1. Data are from 3 replicates represented as mean ± SD. (b) SDS-PAGE of all purified biosensor variants used for in vitro characterization showing the presence of a truncated protein product that is fluorescent.

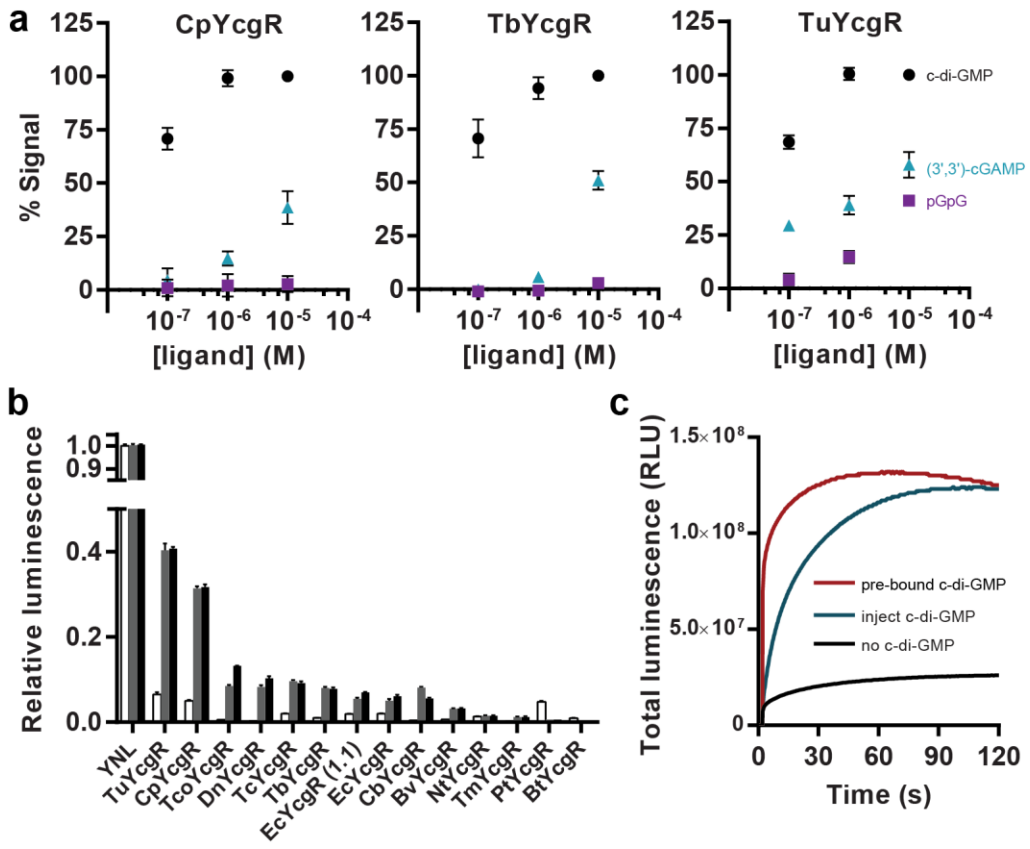

Figure 2.8 *In vitro* characterization of biosensor variants, continued. (a) Analysis of selectivity for high affinity biosensor variants. Data are from 3 replicates represented as mean ± SD. (b) Relative brightness of purified NL biosensors with or without c-di-GMP normalized to YNL. Data are from 3 replicates represented as mean ± SD. (c) Signal turn-on kinetics of *Cp*YcgR biosensor. Chemiluminescence intensity traces are from one representative measurement.

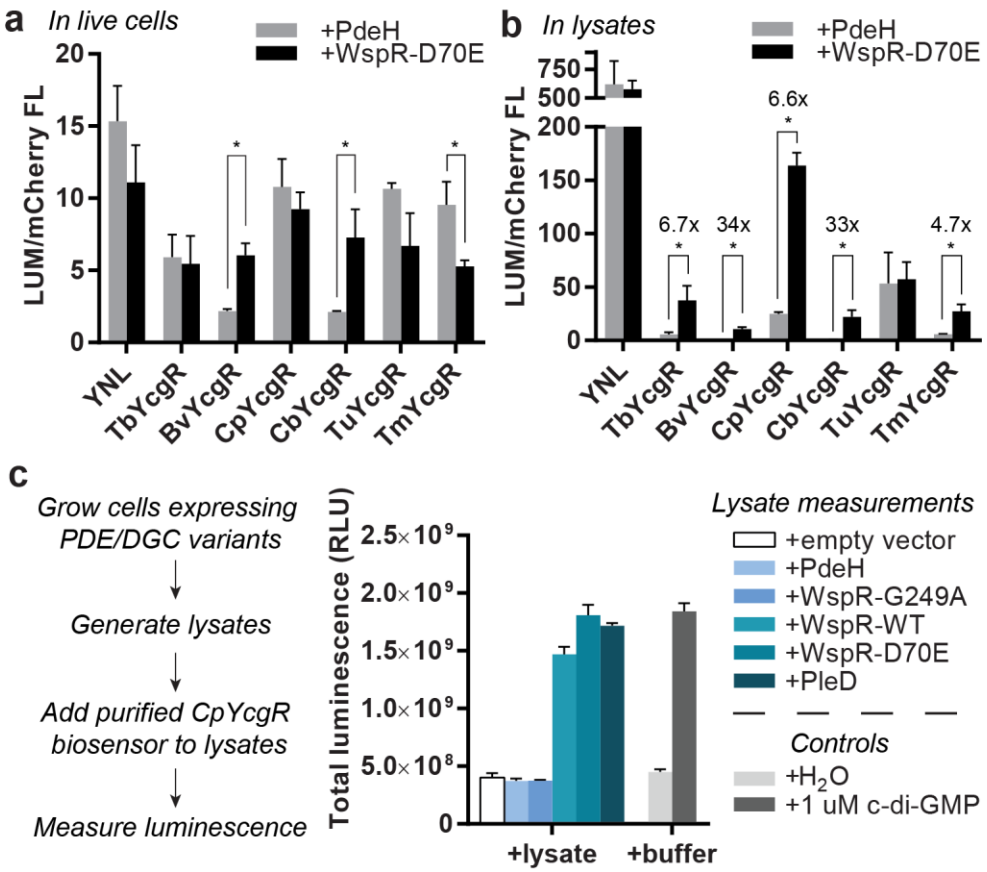

Figure 2.9 Applying selected biosensors to detect cellular c-di-GMP levels. (a) Chemiluminescent signal intensities of live cells coexpressing mCherry-tagged NL biosensors and PdeH or WspR- D70E normalized to mCherry fluorescent signal. Data are from 3 biological replicates represented as mean ± SD. (b) Chemiluminescent signal intensities of lysates of cells coexpressing mCherry-tagged NL biosensors and PdeH or WspR-D70E normalized to mCherry fluorescent signal. Data are from 3 biological replicates represented as mean ± SD. (c) Measuring c-di-GMP levels by addition of CpYcgR to cell lysates. Cells are expressing various PDE or DGC enzymes. Data are from 3 biological replicates represented as mean ± SD.

MATERIALS AND METHODS

General reagents and oligonucleotides. Cyclic dinucleotides were purchased from Axxora, LLC. Coelenterazine-h was purchased from NanoLight Technologies and stored as a ~6.15 mM stock in EtOH at –80 °C. Oligonucleotides used in molecular cloning were purchased from Elim Biopharmaceuticals.

Molecular cloning. The pRSET$_B$-Nano-lantern plasmid was a gift from Takeharu Nagai (Addgene plasmid # 51969). Plasmids encoding YhjH, WspR alleles, and PleD were available in our lab. For expression and purification, all biosensor constructs were cloned into the pRSET$_B$ plasmid between the NdeI and EcoRI sites with an N-terminal His-tag. Overlap-extension PCR was used to add the three N-terminal residues back to RLuc8 to create pRSET$_B$-Nano-lantern (1.1). All NL biosensor constructs using *Ec*YcgR were cloned into pRSET$_B$ using Gibson Assembly(Gibson et al., 2009) in which both linear backbone and insert fragments were amplified by PCR. The *Ec*YcgR sequence was amplified from BL21 Star genomic DNA and mutant alleles were generated using site-directed mutagenesis. For lysate or live-cell based experiments, YNL and *Ec*YcgR biosensor constructs were amplified by PCR and ligated into pET21 and/or pET24 plasmids between NdeI and HindIII sites and included a C-terminal His-tag. To create mCherry tagged versions of these plasmids, mCherry was amplified by PCR to add a flexible linker (GSGGSGGS) at the N-terminus then ligated between BamHI and HindIII sites of the empty plasmid to generate pET21-linker-mCherry and pET24-linker-mCherry. YNL and *Ec*YcgR biosensor constructs were then amplified by PCR and ligated into the pET21- or pET24-linker-mCherry plasmid between NdeI and BamHI sites.

Protein purification. *E. coli* BL21 (DE3) Star cells (Life Technologies) were transformed with the pRSET$_B$ vector encoding N-terminally His-tagged NL biosensor variants. Transformants were cultured in 2xYT medium at 37 °C until OD reached ~0.8–1.0, followed by induction of protein expression with 0.1 mM IPTG for 20 h at 20 °C. Cells were collected and lysed by sonication in lysis buffer [50 mM Tris (pH 7.5), 150 mM NaCl, 20 mM imidazole, 5% (v/v) glycerol] with 300 µg/mL lysozyme and 1 mM PMSF added. Clarified lysate was bound to Ni-NTA agarose (Thermo Scientific), and resin was washed with lysis buffer supplemented with 500 mM NaCl prior to elution with lysis buffer supplemented with 300 mM imidazole. Using Amicon Ultra-15 Centrifugal Filter Units (molecular weight cutoff 10 kDa; Millipore), the elution fractions were concentrated and dialyzed to storage buffer [50 mM HEPES (pH 7.2), 100 mM KCl, 10% (v/v) glycerol]. Concentrated protein was flash frozen in liquid nitrogen then stored at -80 °C in small aliquots to prevent repetitive freeze-thaw cycles. Protein concentrations were determined using the absorption of Venus at 515 nm (extinction coefficient = 92200 M^{-1} cm^{-1}). In stated cases, cells were co-transformed with the pCOLA-PdeH plasmid lacking a His-tag to enable purification of the biosensor without c-di-GMP bound.

Phylogenetic library generation. YcgR sequence variants employed were selected using the Pfam database. Briefly, Pfam was searched for all PilZ-domain containing proteins with a domain architecture similar to EcYcgR (YcgR-PilZ), which were presumed to undergo conformational changes upon binding c-di-GMP. The query resulted in 840 total sequences (258 sequences with YcgR-PilZ, 582 sequences with YcgR_2-PilZ), then a subset of 92 sequences were chosen for synthesis and cloning into

the biosensor scaffold (pET21- and pET24-biosensor-mCherry). All sequences from suspected thermophilic organisms were given priority, and all remaining sequences were chosen from a large variety of bacterial genomes. The selected genes were codon optimized and 'polished' to remove DNA synthesis constraints using BOOST (Oberortner et al., 2017). Double stranded DNA was obtained from Gen9 (Gingko Bioworks). For cloning into the pET21 and pET24 derived vectors using Gibson cloning (Gibson et al., 2009), 25 bp linkers at the beginning and end of the sequences were included. Eight colonies per construct were sequenced verified using PACBIO RSII system (Pacific Biosciences), and variant calling was performed using the GATK software package (McKenna et al., 2010).

Chemiluminescence measurements. All chemiluminescence measurements were performed in opaque white, 96-well LUMITRAC 600 plates (Grenier). Briefly, proteins and ligands were added to assay buffer [50 mM HEPES (pH 7.2), 100 mM KCl, 10 mM DTT, 0.1% BSA] to the given final concentrations in 100 µL reaction volume, then incubated at 28 °C for at least 10 min to reach binding equilibrium. Unless otherwise noted, all affinity and kinetics measurements were made using 50 nM protein, and all signal change, brightness, and selectivity measurements were made using 100 nM protein. Chemiluminescent substrate was prepared by diluting coelenterazine-h to 60 µM in reagent buffer [50 mM HEPES (pH 7.2), 100 mM KCl, 300 mM ascorbate], and allowing the solution to equilibrate to RT for at least 30 min. For equilibrated biosensor measurements, chemiluminescence at 28 °C was measured on a SpectraMax i3x platereader (Molecular Devices) by injecting 20 µL of chemiluminescent substrate, then integrating total chemiluminescent signal for 10 sec after a 3 sec delay. For biosensor kinetics measurements, chemiluminescence at 28 °C was measured over 3 min in 200 ms intervals with 100 ms integration times starting at substrate injection. For c-di-GMP binding kinetics, c-di-GMP was co-injected with substrate for a final concentration of 2 µM c-di-GMP.

Lysate-based assay for biosensor activity. Single colonies of BL21(DE3) star *E. coli* cells transformed with pET24-biosensor-mCherry plasmids were resuspended in 500 µL of P-0.5G non-inducing media [0.5% glucose, 25 mM $(NH_4)_2SO_4$, 50 mM KH_2PO_4, 50 mM Na_2HPO_4, 1 mM $MgSO_4$] (Studier, 2005) supplemented with 100 µg/mL kanamycin in 2.2 mL 96-well deep well plates (VWR), then grown at 37 °C, 325 rpm, for 24 h to generate pre-cultures. A 5 µL aliquot of each pre-culture was used to inoculate 500 µL of ZYP-5052 auto-induction media [25 mM $(NH_4)_2SO_4$, 50 mM KH_2PO_4, 50 mM Na_2HPO_4, 1 mM $MgSO_4$, 0.5% (v/v) glycerol, 0.05% glucose, 0.2% α-lactose, 1% tryptone, and 0.5% yeast extract] (Studier, 2005) supplemented with 100 µg/mL kanamycin in deep well plates. Two identical plates of auto-induction media were inoculated to permit aeration with shaking and to yield 1 mL of combined culture for each sample. Plates were grown at 37 °C, 325 rpm, for 20 h for biosensor expression. After 20 h of growth, equivalent cultures were combined into a single plate.

For flow cytometry analysis of biosensor expression and stability, 2 µL of each culture was added to 200 µL of phosphate-buffered saline (PBS) [137 mM NaCl, 2.7 mM KCl, 10 mM Na_2HPO_4, 1.8 mM KH_2PO_4, pH 7.4]. The mean fluorescence intensities were analyzed on an Attune NxT flow cytometer (Life Technologies). Venus fluorescence was measured with a 488 nm laser for excitiation and a 530/30 filter for emission. mCherry

fluorescence was measured with a 561 nm laser for excitation and a 620/15 filter for emission.

For chemiluminescence measurements, the remaining culture was harvested in the deep-well plate by centrifugation at 4700 rpm for 10 min at 4 °C. Supernatant media was removed and each cell pellet was resuspended in 360 µL screening buffer [50 mM Tris (pH 7.5), 100 mM KCl, 5% glycerol, 2 mM EDTA, 300 µg/mL lysozyme, 1 mM PMSF]. Cells were gently lysed for 1 h at 4 °C and lysates were clarified by centrifugation at 4700 rpm for 40 min at 4 °C. To obtain three samples, 90 µL aliquots of clarified lysates were pipetted into three wells of opaque white, 96-well LUMITRAC 600 plates (Grenier), being careful not to disturb the pelleted cell debris. Each aliquot was mixed with 10 µL of either buffer, 10 µM c-di-GMP, or 200 µM c-di-GMP [in 50 mM HEPES (pH 7.2), 100 mM KCl] to produce final concentrations of 0, 1 µM or 20 µM c-di-GMP. Mixtures were incubated at 28 °C for at least 10 min to allow binding to occur, then chemiluminescence was measured as described above. Signal fold-changes were calculated for at least two biological replicates by dividing the total chemiluminescence signal with added c-di-GMP by the total signal without added c-di-GMP.

Cellular c-di-GMP measurements with biosensor co-expression. Single colonies of BL21(DE3) star *E. coli* cells co-transformed with pET21-biosensor-mCherry plasmids and pCOLA-PdeH or pCOLA-WspR-D70E were resuspended in 500 µL of P-0.5G non-inducing media [0.5% glucose, 25 mM $(NH_4)_2SO_4$, 50 mM KH_2PO_4, 50 mM Na_2HPO_4, 1 mM $MgSO_4$] (Studier, 2005) supplemented with 100 µg/mL kanamycin and 50 µg/mL carbenicillin in 2.2 mL 96-well deep well plates (VWR), then grown at 37 °C, 325 rpm, for 24 h to generate pre-cultures. A 5 µL aliquot of each pre-culture was used to inoculate 500 µL of ZYP-5052 auto-induction media [25 mM $(NH_4)_2SO_4$, 50 mM KH_2PO_4, 50 mM Na_2HPO_4, 1 mM $MgSO_4$, 0.5% (v/v) glycerol, 0.05% glucose, 0.2% α-lactose, 1% tryptone, and 0.5% yeast extract] (Studier, 2005) supplemented with 100 µg/mL kanamycin and 50 µg/mL carbenicillin in a deep well plate and grown at 37 °C, 325 rpm, for 20 h to allow for protein expression. For live cell measurements, cultures were harvested by centrifugation, media was removed, and cell pellets were resuspended in 500 µL PBS. A 100 µL aliquot of each culture was transferred to an opaque white 96-well plate, and the plate was incubated at 28 °C for 10 min. The mCherry fluorescence intensity was measured for each well, 20 µL chemiluminescent substrate was added manually to each well, and then total chemiluminescence was monitored over 10 min. Luminescent signal was calculated as the total chemiluminescence at 10 min divided by the mCherry fluorescence intensity to normalize differences in biosensor expression between biological replicates.

For lysate measurements, cultures were harvested and clarified lysates were prepared as described for the lysate-based assay for biosensor activity, except each culture was resuspended in 240 µL screening buffer. A 100 µL aliquot of each clarified lysate was carefully pipetted into an opaque white 96-well plate, and the plate was incubated at 28 °C for 10 min. The mCherry fluorescence intensity was measured for each well, then chemiluminescent substrate was injected and chemiluminescence was measured as described in the lysate-based assay. Luminescent signal was calculated as the total chemiluminescence divided by the mCherry fluorescence intensity to normalize differences in biosensor expression between biological replicates.

Cellular c-di-GMP measurements with biosensor addition. Single colonies of BL21(DE3) star *E. coli* cells transformed with pCOLA plasmids encoding c-di-GMP-related enzymes were resuspended in 500 µL of P-0.5G non-inducing media supplemented with 100 µg/mL kanamycin in 2.2 mL 96-well deep well plates (VWR), then grown at 37 °C, 325 rpm, for 24 h to generate pre-cultures. A 5 µL aliquot of each pre-culture was used to inoculate 500 µL of ZYP-5052 auto-induction media supplemented with 100 µg/mL kanamycin in a deep well plate and grown at 37 °C, 325 rpm, for 20 h to allow for protein expression. Cultures were harvested and clarified lysates were prepared as described for the lysate-based assay, except each culture was resuspended in 120 µL screening buffer. For +lysate samples, a 50 µL aliquot of each clarified lysate was mixed with 50 µL of 100 nM biosensor in 2x assay buffer in an opaque white 96-well plate, and the plate was incubated at 28 °C for 10 min. Chemiluminescent substrate was injected and chemiluminesce was measured as described above. For +buffer samples, 50 µL of screening buffer was added instead of the lysate.

TABLES

Table 2.1 Characteristics of selected biosensor variants

Sequence	K_D *(nM)*[a]	*Δ signal*[b]	*Hill coefficient*[a]	*mCh/Venus*[c]
*Ec*YcgR[d]	354 ± 18	3	2.3 ± 0.23	1
Selected for high affinity				
*Tm*YcgR	< 50	6.1	1.5 ± 0.04	1.7
*Tu*YcgR	< 50	6.3	1.4 ± 0.04	2.7
*Tb*YcgR	< 50	7.9	1.6 ± 0.1	1.4
*Cp*YcgR	< 50	6.3	1.9 ± 0.1	1.7
*Cb*YcgR	< 50	18.8	1.2 ± 0.04	0.73
*Tc*YcgR	59 ± 2	4.6	1.7 ± 0.1	1.6
*Bv*YcgR	105 ± 2	4.9	1.9 ± 0.05	2.7
Selected for high signal change				
*Dn*YcgR	303 ± 15	39.3	1.8 ± 0.1	0.61
*To*YcgR	379 ± 23	24.5	2.2 ± 0.2	1.1
Selected for negative signal change				
*Pt*YcgR	< 50	–7.7	–1.8 ± 0.1	1.6
*Bt*YcgR	286 ± 17	–89	–2 ± 0.2	0.52

[a]Data are from 3 independent replicates represented as mean ± standard error. [b]Data are the mean maximal signal change from 3 independent replicates; data presented in Figure S5a. [c]Data are mean mCherry/Venus ratios normalized to *Ec*YcgR from 3 biological replicates as measured in the lysate-based assay. [d]Improved K_D and Δsignal compared to Figure 1d due to changes in buffer.

Table 2.2 Oligonucleotides used in this study

Name	Sequence (5' to 3')
REV-RLuc228-YcgR-insert	ACGATCTGCACCACGTCGGGCTTGCCGAGCTCGTCGCGCACTTTGTCCGC
FWD-RLuc228-YcgR-insert	GATCCCCCTGGTGAAGGGCCCATGGATGAGTCATTACCATGAGCAGTTCC
REV-RLuc228-YcgR-vector	AACTGCTCATGGTAATGACTCATCCATGGGCCCTTCACCAGGGGGATCTC
FWD-RLuc228-YcgR-vector	GGGAAAAAGCGGACAAAGTGCGCGACGAGCTCGGCAAGCCCGACGTGGTG
FWD-RLuc91-YcgR-insert	AGAGCGGCAACGGCAGCccatggATGagtcattaccatgagcagttcctg
REV-RLuc91-YcgR-insert	GTACTTGTAGTGGTCCAGCAGCCTGTAgagctcgtcgcgcactttgtccg
FWD-RLuc91-YcgR-vector	ggacaaagtgcgcgacgagctcTACAGGCTGCTGGACCACTACAAGTACC
REV-RLuc91-YcgR-vector	aggaactgctcatggtaatgactCATccatggGCTGCCGTTGCCGCTCTT
FWD-Venus (-C10)-BamHi	gtagtagGgatccgATGGTGAGCAAGG
REV-Venus (-C10)-add RLuc N3	CCTTGCTGGCCATggtaccCCCGGCGG
FWD-RLuc-add RLuc N3	ggtaccATGGCCAGCAAGGTGTACGACCCCGAGC
REV-RLuc-EcoRI	gtagtagGAATTcTTACTGCTCGTTCTTCAGCA
FWD-Rluc91-YcgR-GS-insert	AGAGCGGCAACGGCAGCggcagcATGagtcattaccatgagcagttcctg
REV-Rluc91-ycgr-GS-insert	GTACTTGTAGTGGTCCAGCAGCCTGTAgctgccgtcgcgcactttgtccg
REV-Rluc91-ycgr-GS-vector	aggaactgctcatggtaatgactCATgctgccGCTGCCGTTGCCGCTCTT
FWD-Rluc91-ycgr-GS-vector	ggacaaagtgcgcgacggcagcTACAGGCTGCTGGACCACTACAAGTACC
FWD-Rluc91-ycgr-SEG-insert	GCGGCAACGGCAGCagcgagggcATGagtcattaccatgagcagttcctg
REV-Rluc91-ycgr-SEG-insert	CTTGTAGTGGTCCAGCAGCCTGTAgccctcgctgtcgcgcactttgtccg
REV-Rluc91-ycgr-SEG-vector	aactgctcatggtaatgactCATgccctcgctGCTGCCGTTGCCGCTCTT
FWD-Rluc91-ycgr-SEG-vector	caaagtgcgcgacagcgagggcTACAGGCTGCTGGACCACTACAAGTACC
FWD-Rluc91-ycgr-GGSG-insert	GCAACGGCAGCggcggcagcggcATGagtcattaccatgagcagttcctg
REV-Rluc91-ycgr-GGSG-insert	GTAGTGGTCCAGCAGCCTGTAgccgctgccgccgtcgcgcactttgtccg
REV-Rluc91-ycgr-GGSG-vector	tgctcatggtaatgactCATgccgctgccgccGCTGCCGTTGCCGCTCTT
FWD-Rluc91-ycgr-GGSG-vector	agtgcgcgacggcggcagcggcTACAGGCTGCTGGACCACTACAAGTACC
FWD-Rluc91-ycgr-AP-insert	AGAGCGGCAACGGCAGCgcccccATGagtcattaccatgagcagttcctg
REV-Rluc91-ycgr-AP-insert	GTACTTGTAGTGGTCCAGCAGCCTGTAgggggcgtcgcgcactttgtccg
FWD-Rluc91-ycgr-AP-vector	ggacaaagtgcgcgacgcccccTACAGGCTGCTGGACCACTACAAGTACC
REV-Rluc91-ycgr-AP-vector	aggaactgctcatggtaatgactCATgggggcGCTGCCGTTGCCGCTCTT
FWD-Rluc91-ycgr-APAP-insert	GCAACGGCAGCgccccgccccccATGagtcattaccatgagcagttcctg
REV-Rluc91-ycgr-APAP-insert	GTAGTGGTCCAGCAGCCTGTAgggggcgggggcgtcgcgcactttgtccg
REV-Rluc91-ycgr-APAP-vector	tgctcatggtaatgactCATgggggcgggggcGCTGCCGTTGCCGCTCTT
FWD-Rluc91-ycgr-APAP-vector	agtgcgcgacgcccccgccccccTACAGGCTGCTGGACCACTACAAGTACC
FWD-Rluc91-ycgr-EAAAK-insert	ACGGCAGCgaggccgccgccaagATGagtcattaccatgagcagttcctg
REV-Rluc91-ycgr-EAAAK-insert	GTGGTCCAGCAGCCTGTActtggcggcggcctcgtcgcgcactttgtccg
REV-Rluc91-ycgr-EAAAK-vector	tcatggtaatgactCATcttggcggcggcctcGCTGCCGTTGCCGCTCTT
FWD-Rluc91-ycgr-EAAAK-vector	gcgcgacgaggccgccgccaagTACAGGCTGCTGGACCACTACAAGTACC
FWD-YcgR-R113L quikchange	caccttatggtttgtacaactacgccgatatttccg
REV-YcgR-R113L quikchange	cggaaatatcggcgtagttgtacaaaccataaggtg
FWD-YcgR-R118D-rth	GAcatctccgccccactcc

REV-YcgR-R118D-rth	gaaatatcggcgtcgttgtacaaacc
FWD-YcgR-S147A-rth	Gcgttaggcggcatggg
REV-YcgR-S147A-rth	caaatcatacaggcggaaacg
FWD-YNL-NdeI	tattcacatATGGTGAGCAAGGGCGAGG
REV-YNL-HindIII (no stop)	cgtaagcttCTGCTCGTTCTTCAGCACTCTCTC
REV-YNL-BamHI (no stop)	ataggatccCTGCTCGTTCTTCAGCACTCTCTC
FWD-mCherry w/ linker-BamHI	ataggatccggcggcagcggcggcagcATGGTGAGCAAGGGCGA
REV-mCherry-HindIII (no stop)	tataagcttCTTGTACAGCTCGTCCATGCC
FWD-YNL-pRSET insert	GACGATGACGATAAGgatccgATGGTGAGCAAGGGCGAG
REV-YNL-pRSET insert	CCGGATCAAGCTTCGAATTcTTACTGCTCGTTCTTCAGCACTCTC

Table 2.3 Phylogenetic sequence variants. Orange highlighted organism names are predicted thermophiles. Any sequence without a number label (numbering used in Figure 2.6) produced very low luminescence activity in the lysate-based screen and was not included in any data shown.

UniProt accession	Description	Organism	Domain arch	Length	Number	Name
YCGRL_VIBCH	Cyclic di-GMP binding protein VCA0042	Vibrio cholerae serotype O1 (strain ATCC 39315 / El Tor Inaba N16961)	YcgR2-PilZ	252	1	
YCGR_PSEPK	Flagellar brake protein YcgR	Pseudomonas putida (strain KT2440)	YcgR-PilZ	247	2	
YCGR_SALTY	Flagellar brake protein YcgR	Salmonella typhimurium (strain LT2 / SGSC1412 / ATCC 700720)	YcgR-PilZ	244	3	
Q9HYP3_PSEAE	Uncharacterized protein	Pseudomonas aeruginosa (strain ATCC 15692 / DSM 22644 / CIP 104116 / JCM 14847 / LMG 12228 / 1C / PRS 101 / PAO1)	YcgR-PilZ	263	4	
Q67PC2_SYMTH	Putative uncharacterized protein	Symbiobacterium thermophilum (strain T / IAM 14863)	YcgR2-PilZ	234	5	
R7RRU9_9CLOT	Flagellar protein	Thermobrachium celere DSM 8682	YcgR2-PilZ	223	6	
B5Y7A9_COPPD	Type IV pilus assembly protein PilZ	Coprothermobacter proteolyticus (strain ATCC 35245 / DSM 5265 / BT)	YcgR2-PilZ	233	7	Cp
G0GFW8_SPITZ	Type IV pilus assembly PilZ	Spirochaeta thermophila (strain ATCC 700085 / DSM 6578 / Z-1203)	YcgR2-PilZ	369		
M1E4L7_9FIRM	Type IV pilus assembly PilZ	Thermodesulfobium narugense DSM 14796	YcgR2-PilZ	246	8	
G0GFW8_SPITZ	Type IV pilus assembly PilZ	Spirochaeta thermophila (strain ATCC 700085 / DSM 6578 / Z-1203)	YcgR2-PilZ	357		
B7GHM9_ANOFW	Predicted glycosyltransferase	Anoxybacillus flavithermus (strain DSM 21510 / WK1)	YcgR2-PilZ	239		
B2A369_NATTJ	Type IV pilus assembly PilZ	Natranaerobius thermophilus (strain ATCC BAA-1301 / DSM 18059 / JW/NM-WN-LF)	YcgR2-PilZ	225	9	Nt
A0A150LBE3_9BACI	Uncharacterized protein	Bacillus sporothermodurans	YcgR2-PilZ	216	10	Bs
A1HN17_9FIRM	Type IV pilus assembly PilZ	Thermosinus carboxydivorans Nor1	YcgR2-PilZ	211	11	Tc
A0A124FJ12_9FIRM	Type IV pilus assembly PilZ	Thermoanaerobacterales bacterium 50_218	YcgR2-PilZ	220	12	Tb
D5XFF1_THEPJ	Type IV pilus assembly PilZ	Thermincola potens (strain JR)	YcgR2-PilZ	219	13	
A0A0S3QVC2_9AQUI	Type IV pilus assembly PilZ	Thermosulfidibacter takaii ABI70S6	YcgR2-PilZ	242	14	
B8CYP6_HALOH	Type IV pilus assembly PilZ	Halothermothrix orenii (strain H 168 / OCM 544 / DSM 9562)	YcgR2-PilZ	216	15	
D7CM20_SYNLT	Type IV pilus assembly PilZ	Syntrophothermus lipocalidus (strain DSM 12680 / TGB-C1)	YcgR2-PilZ	216	16	
B0K9S5_THEP3	Type IV pilus assembly PilZ	Thermoanaerobacter pseudethanolicus (strain ATCC 33223 / 39E)	YcgR2-PilZ	209	17	

I3VWB4_THESW	Type IV pilus assembly PilZ	Thermoanaerobacterium saccharolyticum (strain DSM 8691 / JW/SL-YS485)	YcgR2-PilZ	209	18	
K8EBV6_9FIRM	Type IV pilus assembly PilZ	Desulfotomaculum hydrothermale Lam5 = DSM 18033	YcgR2-PilZ	227	19	
A0A090IV04_9BACI	Glycosyltransferase	Bacillus thermoamylovorans	YcgR2-PilZ	220	20	Bt
A8F4V2_PSELT	Type IV pilus assembly PilZ	Pseudothermotoga lettingae (strain ATCC BAA-301 / DSM 14385 / NBRC 107922 / TMO)	YcgR2-PilZ	234	21	
F7YXY9_9THEM	Type IV pilus assembly PilZ	Pseudothermotoga thermarum DSM 5069	YcgR2-PilZ	227	22	
Q9X007_THEMA	Flagellar protein	Thermotoga maritima (strain ATCC 43589 / MSB8 / DSM 3109 / JCM 10099)	YcgR2-PilZ	229	23	Tm
A5D0H5_PELTS	Glycosyltransferase	Pelotomaculum thermopropionicum (strain DSM 13744 / JCM 10971 / SI)	YcgR2-PilZ	219	24	Pt
D9S3A4_THEOJ	Type IV pilus assembly PilZ	Thermosediminibacter oceani (strain ATCC BAA-1034 / DSM 16646 / JW/IW-1228P)	YcgR2-PilZ	212	25	
K4LH04_THEPS	Type IV pilus assembly PilZ	Thermacetogenium phaeum (strain ATCC BAA-254 / DSM 12270 / PB)	YcgR2-PilZ	220	26	
A6LMY0_THEM4	Type IV pilus assembly PilZ	Thermosipho melanesiensis (strain DSM 12029 / CIP 104789 / BI429)	YcgR2-PilZ	220	27	
A0A101EVB1_9THEM	Type IV pilus assembly PilZ	Thermotoga sp. 50_1627	YcgR2-PilZ	227	28	Tu
L0EE96_THECK	Putative glycosyltransferase	Thermobacillus composti (strain DSM 18247 / JCM 13945 / KWC4)	YcgR2-PilZ	217	29	To
A3DCP7_CLOTH	Type IV pilus assembly PilZ	Clostridium thermocellum (strain ATCC 27405 / DSM 1237 / NBRC 103400 / NCIMB 10682 / NRRL B-4536 / VPI 7372)	YcgR2-PilZ	224	30	
E6SJP9_THEM7	Type IV pilus assembly PilZ	Thermaerobacter marianensis (strain ATCC 700841 / DSM 12885 / JCM 10246 / 7p75a)	YcgR2-PilZ	220	31	
Q2RKC8_MOOTA	Glycosyltransferase-like protein	Moorella thermoacetica (strain ATCC 39073 / JCM 9320)	YcgR2-PilZ	219	32	
D1B6A2_THEAS	Type IV pilus assembly PilZ	Thermanaerovibrio acidaminovorans (strain ATCC 49978 / DSM 6589 / Su883)	YcgR2-PilZ	227	33	
K8EH43_9FIRM	Type IV pilus assembly PilZ	Desulfotomaculum hydrothermale Lam5 = DSM 18033	YcgR2-PilZ	208	34	
H2INW0_RAHAC	Flagellar brake protein YcgR	Rahnella aquatilis (strain ATCC 33071 / DSM 4594 / JCM 1683 / NBRC 105701 / NCIMB 13365 / CIP 78.65)	YcgR-PilZ	248	35	
A0A080M6H4_9PROT	Flagellar brake protein YcgR	Candidatus Accumulibacter sp. SK-02	YcgR-PilZ	266	36	
A0A0R0ARV1_9GAMM	Flagellar brake protein YcgR	Stenotrophomonas panacihumi	YcgR-PilZ	265	37	
A0A063BEK1_9BURK	Flagellar brake protein YcgR	Burkholderia sp. lig30	YcgR-PilZ	251	38	

Q7CK58_YERPE	Flagellar brake protein YcgR	Yersinia pestis	YcgR-PilZ	252	39	
H8GFW9_METAL	Flagellar brake protein YcgR	Methylomicrobium album BG8	YcgR-PilZ	239	40	
B4E8L7_BURCJ	Flagellar brake protein YcgR	Burkholderia cenocepacia (strain ATCC BAA-245 / DSM 16553 / LMG 16656 / NCTC 13227 / J2315 / CF5610)	YcgR-PilZ	251	41	
S6B8T9_9PROT	Flagellar brake protein YcgR	Sulfuricella denitrificans skB26	YcgR-PilZ	257	42	
A0A0D5V569_9BURK	Flagellar brake protein YcgR	Paraburkholderia fungorum	YcgR-PilZ	263	43	
YCGR_LARHH	Flagellar brake protein YcgR	Laribacter hongkongensis (strain HLHK9)	YcgR-PilZ	271	44	
H1SBM0_9BURK	Flagellar brake protein YcgR	Cupriavidus basilensis OR16	YcgR-PilZ	233	45	Cb
E1TCJ5_BURSG	Flagellar brake protein YcgR	Burkholderia sp. (strain CCGE1003)	YcgR-PilZ	263	46	
D8IT03_HERSS	Flagellar brake protein YcgR	Herbaspirillum seropedicae (strain SmR1)	YcgR-PilZ	251	47	
C5AEG4_BURGB	Flagellar brake protein YcgR	Burkholderia glumae (strain BGR1)	YcgR-PilZ	250	48	
YCGR_NITEC	Flagellar brake protein YcgR	Nitrosomonas eutropha (strain C91)	YcgR-PilZ	269		
YCGR_THIDA	Flagellar brake protein YcgR	Thiobacillus denitrificans (strain ATCC 25259)	YcgR-PilZ	255	49	
A0A126T293_9GAMM	Flagellar brake protein YcgR	Methylomonas denitrificans	YcgR-PilZ	249	50	
H5V7W3_ESCHE	Flagellar brake protein YcgR	Escherichia hermannii NBRC 105704	YcgR-PilZ	243	51	
YCGR1_DECAR	Flagellar brake protein YcgR 1	Dechloromonas aromatica (strain RCB)	YcgR-PilZ	264	52	
A9MP65_SALAR	Flagellar brake protein YcgR	Salmonella arizonae (strain ATCC BAA-731 / CDC346-86 / RSK2980)	YcgR-PilZ	244	53	
E6WB98_PANSA	Flagellar brake protein YcgR	Pantoea sp. (strain At-9b)	YcgR-PilZ	244	54	
S6ALU3_PSERE	Flagellar brake protein	Pseudomonas resinovorans NBRC 106553	YcgR-PilZ	264	55	
YCGR_METML	Flagellar brake protein YcgR	Methylotenera mobilis (strain JLW8 / ATCC BAA-1282 / DSM 17540)	YcgR-PilZ	253	56	
L1LXK9_PSEPU	Uncharacterized protein	Pseudomonas putida CSV86	YcgR-PilZ	247	57	Pp
A0A080MAN3_9PROT	Flagellar brake protein YcgR	Candidatus Accumulibacter sp. BA-91	YcgR-PilZ	259	58	
A0A0L0GIP1_9ENTR	Flagellar brake protein YcgR	Trabulsiella odontotermitis	YcgR-PilZ	243	59	
A0A0K1K509_9BURK	Flagellar brake protein YcgR	Massilia sp. NR 4-1	YcgR-PilZ	253	60	
A0A024HEU5_PSEKB	Flagellar brake protein YcgR	Pseudomonas knackmussii (strain DSM 6978 / LMG 23759 / B13)	YcgR-PilZ	249	61	
A0A0S8DMJ3_9GAMM	Flagellar brake protein YcgR	Gammaproteobacteria bacterium SG8_47	YcgR-PilZ	252	62	

Q97H69_CLOAB	Uncharacterized protein, YPFA B.subtilis ortholog	Clostridium acetobutylicum (strain ATCC 824 / DSM 792 / JCM 1419 / LMG 5710 / VKM B-1787)	YcgR2-PilZ	222	63	
A0A0U9HJ89_9THEO	C-di-GMP-binding flagellar brake protein YcgR	Tepidanaerobacter syntrophicus	YcgR2-PilZ	213	64	
A0A140LAQ7_9THEO	Flagellar brake protein YcgR	Fervidicola ferrireducens	YcgR2-PilZ	212	65	
D4H107_DENA2	Type IV pilus assembly PilZ	Denitrovibrio acetiphilus (strain DSM 12809 / N2460)	YcgR2-PilZ	219	66	Dn
D3PCV1_DEFDS	Type IV pilus assembly protein PilZ	Deferribacter desulfuricans (strain DSM 14783 / JCM 11476 / NBRC 101012 / SSM1)	YcgR2-PilZ	223	67	
A8FEM7_BACP2	Pilus assembly protein PilZ	Bacillus pumilus (strain SAFR-032)	YcgR2-PilZ	215	68	
W6N5K7_CLOTY	Flagellar protein	Clostridium tyrobutyricum DIVETGP	YcgR2-PilZ	216	69	
A4J746_DESRM	Type IV pilus assembly PilZ	Desulfotomaculum reducens (strain MI-1)	YcgR2-PilZ	221	70	
A0A151B6Q5_9CLOT	Flagellar protein YcgR	Clostridium tepidiprofundi DSM 19306	YcgR2-PilZ	217	71	
C6C102_DESAD	Type IV pilus assembly PilZ	Desulfovibrio salexigens (strain ATCC 14822 / DSM 2638 / NCIB 8403 / VKM B-1763)	YcgR2-PilZ	229		
A6M180_CLOB8	Type IV pilus assembly PilZ	Clostridium beijerinckii (strain ATCC 51743 / NCIMB 8052)	YcgR2-PilZ	213		
R1AST9_9CLOT	Flagellar protein	Caldisalinibacter kiritimatiensis	YcgR2-PilZ	222	72	
F7NL64_9FIRM	Type IV pilus assembly PilZ	Acetonema longum DSM 6540	YcgR2-PilZ	215	73	
L0FC86_DESDL	Putative glycosyltransferase	Desulfitobacterium dichloroeliminans (strain LMG P-21439 / DCA1)	YcgR2-PilZ	214	74	
R7C6C4_9CLOT	Type IV pilus assembly PilZ	Clostridium sp. CAG:62	YcgR2-PilZ	236	75	
A0A139D977_9FIRM	Flagellar protein	Halanaerobium sp. T82-1	YcgR2-PilZ	213	76	
R7R388_9FIRM	Flagellar protein	Roseburia sp. CAG:100	YcgR2-PilZ	255	77	
A0A0E3W3A0_9FIRM	PilZ domain	Syntrophomonas zehnderi OL-4	YcgR2-PilZ	216	78	
D5CSE9_SIDLE	Type IV pilus assembly PilZ	Sideroxydans lithotrophicus (strain ES-1)	YcgR2-PilZ	311		
I8RFB4_9FIRM	Type IV pilus assembly PilZ	Pelosinus fermentans B4	YcgR2-PilZ	215	79	
Q24T82_DESHY	Putative uncharacterized protein	Desulfitobacterium hafniense (strain Y51)	YcgR2-PilZ	200		
W1SJT3_9BACI	Type iv pilus assembly pilz	Bacillus vireti LMG 21834	YcgR2-PilZ	207	80	Bv
A3WPA0_9GAMM	Predicted glycosyltransferase	Idiomarina baltica OS145	YcgR2-PilZ	233	81	
K8DYS2_9FIRM	Putative Type IV pilus assembly PilZ	Desulfotomaculum hydrothermale Lam5 = DSM 18033	YcgR2-PilZ	209	82	
W0JLH8_DESAE	Uncharacterized protein	Desulfurella acetivorans A63	YcgR2-PilZ	224	83	
A0A0E4HD84_9BACL	Type IV pilus assembly protein PilZ	Paenibacillus riograndensis SBR5	YcgR2-PilZ	186	84	

Table 2.4 Amino acid sequences of biosensor plasmids.

pRSET-YNL-EcYcgR-91	MRGSHHHHHHGMASMTGGQQMGRDLYDDDDKDPMVSKGEELFTGVVPILVELDGDVNGHKFSVSGEGEGD ATYGKLTLKLICTTGKLPVPWPTLVTTLGYGLQCFARYPDHMKQHDFFKSAMPEGYVQERTIFFKDDGNY KTRAEVKFEGDTLVNRIELKGIDFKEDGNILGHKLEYNYNSHNVYITADKQKNGIKANFKIRHNIEDGGV QLADHYQQNTPIGDGPVLLPDNHYLSYQSKLSKDPNEKRDHMVLLEFVTAAGGTKVYDPEQRKRMITGPQ WWARCKQMNVLDSFINYYDSEKHAENAVIFLHGNATSSYLWRHVVPHIEPVARCIIPDLIGMGKSGKSGN GSPWMSHYHEQFLKQNPLAVLGVLRDLHKAAIPLRLSWNGGQLISKLLAITPDKLVLDFGSQAEDNIAVL KAQHITITAETQGAKVEFTVEQLQQSEYLQLPAFITVPPPTLWFVQRRRYFRISAPLHPPYFCQTKLADN STLRFRLYDLSLGGMGALLETAKPAELQEGMRFAQIEVNMGQWGVFHFDAQLISISERKVIDGKNETITT PRLSFRFLNVSPTVERQLQRIIFSLEREAREKADKVRDELYRLLDHYKYLTAWFELLNLPKKIIFVGHDW GAALAFHYAYEHQDRIKAIVHMESVVDVIESWDEWPDIEEDIALIKSEEGEKMVLENNFFVETVLPSKIM RKLEPEEFAAYLEPFKEKGEVRRPTLSWPREIPLVKGGKPDVVQIVRNYNAYLRASDDLPKLFIEGDPGF FSNAIVEGAKKFPNTEFVKVKGLHFLQEDAPDEMGKYIKSFVERVLKNEQ*stop
pET21/24-YNL-EcYcgR-91	MVSKGEELFTGVVPILVELDGDVNGHKFSVSGEGEGDATYGKLTLKLICTTGKLPVPWPTLVTTLGYGLQ CFARYPDHMKQHDFFKSAMPEGYVQERTIFFKDDGNYKTRAEVKFEGDTLVNRIELKGIDFKEDGNILGH KLEYNYNSHNVYITADKQKNGIKANFKIRHNIEDGGVQLADHYQQNTPIGDGPVLLPDNHYLSYQSKLSK DPNEKRDHMVLLEFVTAAGGTKVYDPEQRKRMITGPQWWARCKQMNVLDSFINYYDSEKHAENAVIFLHG NATSSYLWRHVVPHIEPVARCIIPDLIGMGKSGKSGNGSPWMSHYHEQFLKQNPLAVLGVLRDLHKAAIP LRLSWNGGQLISKLLAITPDKLVLDFGSQAEDNIAVLKAQHITITAETQGAKVEFTVEQLQQSEYLQLPA FITVPPPTLWFVQRRRYFRISAPLHPPYFCQTKLADNSTLRFRLYDLSLGGMGALLETAKPAELQEGMRF AQIEVNMGQWGVFHFDAQLISISERKVIDGKNETITTPRLSFRFLNVSPTVERQLQRIIFSLEREAREKA DKVRDELYRLLDHYKYLTAWFELLNLPKKIIFVGHDWGAALAFHYAYEHQDRIKAIVHMESVVDVIESWD EWPDIEEDIALIKSEEGEKMVLENNFFVETVLPSKIMRKLEPEEFAAYLEPFKEKGEVRRPTLSWPREIP LVKGGKPDVVQIVRNYNAYLRASDDLPKLFIEGDPGFFSNAIVEGAKKFPNTEFVKVKGLHFLQEDAPDE MGKYIKSFVERVLKNEQKLAAALEHHHHHH*stop
pET21/24-YNL-EcYcgR-91-mCherry	MVSKGEELFTGVVPILVELDGDVNGHKFSVSGEGEGDATYGKLTLKLICTTGKLPVPWPTLVTTLGYGLQ CFARYPDHMKQHDFFKSAMPEGYVQERTIFFKDDGNYKTRAEVKFEGDTLVNRIELKGIDFKEDGNILGH KLEYNYNSHNVYITADKQKNGIKANFKIRHNIEDGGVQLADHYQQNTPIGDGPVLLPDNHYLSYQSKLSK DPNEKRDHMVLLEFVTAAGGTKVYDPEQRKRMITGPQWWARCKQMNVLDSFINYYDSEKHAENAVIFLHG NATSSYLWRHVVPHIEPVARCIIPDLIGMGKSGKSGNGSPWMSHYHEQFLKQNPLAVLGVLRDLHKAAIP LRLSWNGGQLISKLLAITPDKLVLDFGSQAEDNIAVLKAQHITITAETQGAKVEFTVEQLQQSEYLQLPA FITVPPPTLWFVQRRRYFRISAPLHPPYFCQTKLADNSTLRFRLYDLSLGGMGALLETAKPAELQEGMRF AQIEVNMGQWGVFHFDAQLISISERKVIDGKNETITTPRLSFRFLNVSPTVERQLQRIIFSLEREAREKA DKVRDELYRLLDHYKYLTAWFELLNLPKKIIFVGHDWGAALAFHYAYEHQDRIKAIVHMESVVDVIESWD EWPDIEEDIALIKSEEGEKMVLENNFFVETVLPSKIMRKLEPEEFAAYLEPFKEKGEVRRPTLSWPREIP LVKGGKPDVVQIVRNYNAYLRASDDLPKLFIEGDPGFFSNAIVEGAKKFPNTEFVKVKGLHFLQEDAPDE MGKYIKSFVERVLKNEQGGSGGSMVSKGEEDNMAIIKEFMRFKVHMEGSVNGHEFEIEGEGEGRPYEGTQ TAKLKVTKGGPLPFAWDILSPQFMYGSKAYVKHPADIPDYLKLSFPEGFKWERVMNFEDGGVVTVTQDSS LQDGEFIYKVKLRGTNFPSDGPVMQKKTMGWEASSERMYPEDGALKGEIKQRLKLKDGGHYDAEVKTTYK AKKPVQLPGAYNVNIKLDITSHNEDYTIVEQYERAEGRHSTGGMDELYKKLAAALEHHHHHH*stop

Notes: His-tag, Venus ΔC10, RLuc8 (4-91), EcYcgR, RLuc8 (92-311), mCherry tag; phylogenetic biosensor variants use the same sequences, except the phylogenetic variant is used in place of EcYcgR.

Table 2.5 Nucleotide sequences of biosensor plasmids. Corresponding nucleotide sequences of amino acid sequences presented in Table 2.4.

pRSET-YNL-EcYcgR-91	ATGCGGGGTTCTCATCATCATCATCATCATGGTATGGCTAGCATGACTGGTGGACAGCAAATGGGTCGGGA TCTGTACGACGATGACGATAAGgatccgATGGTGAGCAAGGGCGAGGAGCTGTTCACCGGGGTGGTGCCCA TCCTGGTCGAGCTGGACGGCGACGTAAACGGCCACAAGTTCAGCGTGTCCGGCGAGGGCGAGGGCGATGCC ACCTACGGCAAGCTGACCCTGAAGCTGATCTGCACCACCGGCAAGCTGCCCGTGCCCTGGCCCACCCTCGT GACCACCCTGGGCTACGGCCTGCAGTGCTTCGCCCGCTACCCCGACCACATGAAGCAGCACGACTTCTTCA AGTCCGCCATGCCCGAAGGCTACGTCCAGGAGCGCACCATCTTCTTCAAGGACGACGGCAACTACAAGACC CGCGCCGAGGTGAAGTTCGAGGGCGACACCCTGGTGAACCGCATCGAGCTGAAGGGCATCGACTTCAAGGA GGACGGCAACATCCTGGGGCACAAGCTGGAGTACAACTACAACAGCCACAACGTCTATATCACCGCCGACA AGCAGAAGAACGGCATCAAGGCCAACTTCAAGATCCGCCACAACATCGAGGACGGCGGCGTGCAGCTCGCC GACCACTACCAGCAGAACACCCCCATCGGCGACGGCCCCGTGCTGCTGCCCGACAACCACTACCTGAGCTA CCAGTCCAAGCTGAGCAAAGACCCCAACGAGAAGCGCGATCACATGGTCCTGCTGGAGTTCGTGACCGCCG CCGGGggtaccAAGGTGTACGACCCCGAGCAGAGGAAGAGGATGATCACCGGCCCCCAGTGGTGGGCCAGG TGCAAGCAGATGAACGTGCTGGACAGCTTCATCAACTACTACGACAGCGAGAAGCACGCCGAGAACGCCGT GATCTTCCTGCACGGCAACGCCaCTAGCAGCTACCTGTGGAGGCACGTGGTGCCCCACATCGAGCCCGTGG CCAGGTGCATCATCCCCGATCTGATCGGCATGGGCAAGAGCGGCAAGAGCGGCAACGGCAGCccatggATG agtcattaccatgagcagttcctgaaacaaaatccgttagccgtcctgggcgtgttacgcgatttgcacaa agccgcaattcctttgcgtctcagttggaatggcgggcagctgatcagcaaattactggcaataaccccgg ataaactggtgctggatttcggcagtcaagccgaagacaacatcgccgtgctaaaggcacagcacattacc attaccgccgaaactcagggtgcgaaagtcgagtttactgttgaacaactacagcagagtgaatacttgca gcttccggcatttattaccgtaccgcctcccaccttatggtttgtacaacgacgccgatatttccgcatct ccgccccactccatccgccttatttttgccagaccaaactggcggataacagtacgttacgtttccgcctg tatgatttgtcgttaggcggcatgggcgcattactggaaacagcaaagcctgccgaattacaagaaggcat gcgcttcgctcagattgaagtcaacatggggcaatggggtgtttttcactttgacgcccagttaatctcca tcagcgagcgcaaagtgattgatggcaagaatgaaaccatcaccactccccgtctgagcttccgttttctt aacgtcagcccgacggtggagcggcaattacagcggattattttctctctcgagcgagaagcccgggaaaa agcggacaaagtgcgcgacgagctcTACAGGCTGCTGGACCACTACAAGTACCTGACCGCCTGGTTCGAGC TCCTGAACCTGCCCAAGAAGATCATCTTCGTGGGCCACGACTGGGGCGCCgcCCTGGCCTTCCACTACgcC TACGAGCACCAGGACAgGATCAAGGCCATCGTGCACatgGAGAGCGTGGTGGACGTGATCGAGAGCTGGGA CGAGTGGCCAGACATCGAGGAGGACATCGCCCTGATCAAGAGCGAGGAGGGCGAGAAGATGGTGCTGGAGA ACAACTTCTTCGTGGAGACCgTGCTGCCCAGCAAGATCATGAGAAAGCTGGAGCCCGAGGAGTTCGCCGCC TACCTGGAGCCCTTCAAGGAGAAGGGCGAGGTGAGAAGACCCACCCTGAGCTGGCCCAGAGAGATCCCCCT GGTGAAGGGCGGCAAGCCCGACGTGGTGCAGATCGTGAGAAACTACAACGCCTACCTGAGAGCCAGCGACG ACCTGCCCAAGcTGTTCATCGAGggcGACCCCGGCTTCTTCAGCAACGCCATCGTGGAGGGCGCCAAGAAG TTCCCCAACACCGAGTTCGTGAAGGTGAAGGGCCTGCACTTCctCCAGGAGGACGCCCCCGACGAGATGGG CAAGTACATCAAGAGCTTCGTGGAGAGAGTGCTGAAGAACGAGCAGTAA
pET21/24-YNL-EcYcgR-91	ATGGTGAGCAAGGGCGAGGAGCTGTTCACCGGGGTGGTGCCCATCCTGGTCGAGCTGGACGGCGACGTAAA CGGCCACAAGTTCAGCGTGTCCGGCGAGGGCGAGGGCGATGCCACCTACGGCAAGCTGACCCTGAAGCTGA TCTGCACCACCGGCAAGCTGCCCGTGCCCTGGCCCACCCTCGTGACCACCCTGGGCTACGGCCTGCAGTGC TTCGCCCGCTACCCCGACCACATGAAGCAGCACGACTTCTTCAAGTCCGCCATGCCCGAAGGCTACGTCCA GGAGCGCACCATCTTCTTCAAGGACGACGGCAACTACAAGACCCGCGCCGAGGTGAAGTTCGAGGGCGACA CCCTGGTGAACCGCATCGAGCTGAAGGGCATCGACTTCAAGGAGGACGGCAACATCCTGGGGCACAAGCTG GAGTACAACTACAACAGCCACAACGTCTATATCACCGCCGACAAGCAGAAGAACGGCATCAAGGCCAACTT CAAGATCCGCCACAACATCGAGGACGGCGGCGTGCAGCTCGCCGACCACTACCAGCAGAACACCCCCATCG GCGACGGCCCCGTGCTGCTGCCCGACAACCACTACCTGAGCTACCAGTCCAAGCTGAGCAAAGACCCCAAC GAGAAGCGCGATCACATGGTCCTGCTGGAGTTCGTGACCGCCGCCGGGggtaccAAGGTGTACGACCCCGA GCAGAGGAAGAGGATGATCACCGGCCCCCAGTGGTGGGCCAGGTGCAAGCAGATGAACGTGCTGGACAGCT TCATCAACTACTACGACAGCGAGAAGCACGCCGAGAACGCCGTGATCTTCCTGCACGGCAACGCCaCTAGC AGCTACCTGTGGAGGCACGTGGTGCCCCACATCGAGCCCGTGGCCAGGTGCATCATCCCCGATCTGATCGG CATGGGCAAGAGCGGCAAGAGCGGCAACGGCAGCccatggATGagtcattaccatgagcagttcctgaaac aaaatccgttagccgtcctgggcgtgttacgcgatttgcacaaagccgcaattcctttgcgtctcagttgg aatggcgggcagctgatcagcaaattactggcaataaccccggataaactggtgctggatttcggcagtca agccgaagacaacatcgccgtgctaaaggcacagcacattaccattaccgccgaaactcagggtgcgaaag tcgagtttactgttgaacaactacagcagagtgaatacttgcagcttccggcatttattaccgtaccgcct cccaccttatggtttgtacaacgacgccgatatttccgcatctccgccccactccatccgccttatttttg ccagaccaaactggcggataacagtacgttacgtttccgcctgtatgatttgtcgttaggcggcatgggcg cattactggaaacagcaaagcctgccgaattacaagaaggcatgcgcttcgctcagattgaagtcaacatg gggcaatggggtgtttttcactttgacgcccagttaatctccatcagcgagcgcaaagtgattgatggcaa gaatgaaaccatcaccactccccgtctgagcttccgttttcttaacgtcagcccgacggtggagcggcaat tacagcggattattttctctctcgagcgagaagcccgggaaaaagcggacaaagtgcgcgacgagctcTAC

	AGGCTGCTGGACCACTACAAGTACCTGACCGCCTGGTTCGAGCTCCTGAACCTGCCCAAGAAGATCATCTT CGTGGGCCACGACTGGGGCGCCgcCCTGGCCTTCCACTACgcCTACGAGCACCAGGACAgGATCAAGGCCA TCGTGCACatgGAGAGCGTGGTGGACGTGATCGAGAGCTGGGACGAGTGGCCAGACATCGAGGAGGACATC GCCCTGATCAAGAGCGAGGAGGGCGAGAAGATGGTGCTGGAGAACAACTTCTTCGTGGAGACCgTGCTGCC CAGCAAGATCATGAGAAAGCTGGAGCCCGAGGAGTTCGCCGCCTACCTGGAGCCCTTCAAGGAGAAGGGCG AGGTGAGAAGACCCACCCTGAGCTGGCCCAGAGAGATCCCCCTGGTGAAGGGCGGCAAGCCCGACGTGGTG CAGATCGTGAGAAACTACAACGCCTACCTGAGAGCCAGCGACGACCTGCCCAAGcTGTTCATCGAGggcGA CCCCGGCTTCTTCAGCAACGCCATCGTGGAGGGCGCCAAGAAGTTCCCCAACACCGAGTTCGTGAAGGTGA AGGGCCTGCACTTCctCCAGGAGGACGCCCCCGACGAGATGGGCAAGTACATCAAGAGCTTCGTGGAGAGA GTGCTGAAGAACGAGCAGaagcttgcggccgcactcgagcaccaccaccaccaccactga
pET21/24-YNL-EcYcgR-91-mCherry	ATGGTGAGCAAGGGCGAGGAGCTGTTCACCGGGGTGGTGCCCATCCTGGTCGAGCTGGACGGCGACGTAAA CGGCCACAAGTTCAGCGTGTCCGGCGAGGGCGAGGGCGATGCCACCTACGGCAAGCTGACCCTGAAGCTGA TCTGCACCACCGGCAAGCTGCCCGTGCCCTGGCCCACCCTCGTGACCACCCTGGGCTACGGCCTGCAGTGC TTCGCCCGCTACCCCGACCACATGAAGCAGCACGACTTCTTCAAGTCCGCCATGCCCGAAGGCTACGTCCA GGAGCGCACCATCTTCTTCAAGGACGACGGCAACTACAAGACCCGCGCCGAGGTGAAGTTCGAGGGCGACA CCCTGGTGAACCGCATCGAGCTGAAGGGCATCGACTTCAAGGAGGACGGCAACATCCTGGGGCACAAGCTG GAGTACAACTACAACAGCCACAACGTCTATATCACCGCCGACAAGCAGAAGAACGGCATCAAGGCCAACTT CAAGATCCGCCACAACATCGAGGACGGCGGCGTGCAGCTCGCCGACCACTACCAGCAGAACACCCCCATCG GCGACGGCCCCGTGCTGCTGCCCGACAACCACTACCTGAGCTACCAGTCCAAGCTGAGCAAAGACCCCAAC GAGAAGCGCGATCACATGGTCCTGCTGGAGTTCGTGACCGCCGCCGGGgtaccAAGGTGTACGACCCCGA GCAGAGGAAGAGGATGATCACCGGCCCCCAGTGGTGGGCCAGGTGCAAGCAGATGAACGTGCTGGACAGCT TCATCAACTACTACGACAGCGAGAAGCACGCCGAGAACGCCGTGATCTTCCTGCACGGCAACGCCaCTAGC AGCTACCTGTGGAGGCACGTGGTGCCCCACATCGAGCCCGTGGCCAGGTGCATCATCCCCGATCTGATCGG CATGGGCAAGAGCGGCAAGAGCGGCAACGGCAGCccatggATGagtcattaccatgagcagttcctgaaac aaaatccgttagccgtcctgggcgtgttacgcgatttgcacaaagccgcaattcctttgcgtctcagttgg aatggcgggcagctgatcagcaaattactggcaataaccccggataaactggtgctggatttcggcagtca agccgaagacaacatcgccgtgctaaaggcacagcacattaccattaccgccgaaactcagggtgcgaaag tcgagtttactgttgaacaactacagcagagtgaatacttgcagcttccggcatttattaccgtaccgcct cccaccttatggtttgtacaacgacgccgatatttccgcatctccgccccactccatccgccttatttttg ccagaccaaactggcggataacagtacgttacgtttccgcctgtatgatttgtcgttaggcggcatgggcg cattactggaaacagcaaagcctgccgaattacaagaaggcatgcgcttcgctcagattgaagtcaacatg gggcaatggggtgtttttcactttgacgcccagttaatctccatcagcgagcgcaaagtgattgatggcaa gaatgaaaccatcaccactccccgtctgagcttccgttttcttaacgtcagcccgacggtggagcggcaat tacagcggattattttctctctcgagcgagaagcccgggaaaaagcggacaaagtgcgcgacgagctcTAC AGGCTGCTGGACCACTACAAGTACCTGACCGCCTGGTTCGAGCTCCTGAACCTGCCCAAGAAGATCATCTT CGTGGGCCACGACTGGGGCGCCgcCCTGGCCTTCCACTACgcCTACGAGCACCAGGACAgGATCAAGGCCA TCGTGCACatgGAGAGCGTGGTGGACGTGATCGAGAGCTGGGACGAGTGGCCAGACATCGAGGAGGACATC GCCCTGATCAAGAGCGAGGAGGGCGAGAAGATGGTGCTGGAGAACAACTTCTTCGTGGAGACCgTGCTGCC CAGCAAGATCATGAGAAAGCTGGAGCCCGAGGAGTTCGCCGCCTACCTGGAGCCCTTCAAGGAGAAGGGCG AGGTGAGAAGACCCACCCTGAGCTGGCCCAGAGAGATCCCCCTGGTGAAGGGCGGCAAGCCCGACGTGGTG CAGATCGTGAGAAACTACAACGCCTACCTGAGAGCCAGCGACGACCTGCCCAAGcTGTTCATCGAGggcGA CCCCGGCTTCTTCAGCAACGCCATCGTGGAGGGCGCCAAGAAGTTCCCCAACACCGAGTTCGTGAAGGTGA AGGGCCTGCACTTCctCCAGGAGGACGCCCCCGACGAGATGGGCAAGTACATCAAGAGCTTCGTGGAGAGA GTGCTGAAGAACGAGCAGggatccggcggcagcggcggcagcATGGTGAGCAAGGGCGAGGAGGATAACAT GGCCATCATCAAGGAGTTCATGCGCTTCAAGGTGCACATGGAGGGCTCCGTGAACGGCCACGAGTTCGAGA TCGAGGGCGAGGGCGAGGGCCGCCCCTACGAGGGCACCCAGACCGCCAAGCTGAAGGTGACCAAGGGTGGC CCCCTGCCCTTCGCCTGGGACATCCTGTCCCCTCAGTTCATGTACGGCTCCAAGGCCTACGTGAAGCACCC CGCCGACATCCCCGACTACTTGAAGCTGTCCTTCCCCGAGGGCTTCAAGTGGGAGCGCGTGATGAACTTCG AGGACGGCGGCGTGGTGACCGTGACCCAGGACTCCTCCCTGCAGGACGGCGAGTTCATCTACAAGGTGAAG CTGCGCGGCACCAACTTCCCCTCCGACGGCCCCGTAATGCAGAAGAAGACCATGGGCTGGGAGGCCTCCTC CGAGCGGATGTACCCCGAGGACGGCGCCCTGAAGGGCGAGATCAAGCAGAGGCTGAAGCTGAAGGACGGCG GCCACTACGACGCTGAGGTCAAGACCACCTACAAGGCCAAGAAGCCCGTGCAGCTGCCCGGCGCCTACAAC GTCAACATCAAGTTGGACATCACCTCCCACAACGAGGACTACACCATCGTGGAACAGTACGAACGCGCCGA GGGCCGCCACTCCACCGGCGGCATGGACGAGCTGTACAAGaagcttgcggccgcactcgagcaccaccacc accaccactga

REFERENCES

Benach, J., Swaminathan, S.S., Tamayo, R., Handelman, S.K., Folta-Stogniew, E., Ramos, J.E., Forouhar, F., Neely, H., Seetharaman, J., Camilli, A., et al. (2007). The structural basis of cyclic diguanylate signal transduction by PilZ domains. EMBO J. *26*, 5153–5166.

Biswas, K.H., Sopory, S., and Visweswariah, S.S. (2008). The GAF domain of the cGMP-binding, cGMP-specific phosphodiesterase (PDE5) is a sensor and a sink for cGMP. Biochemistry *47*, 3534–3543.

Christen, M., Kulasekara, H.D., Christen, B., Kulasekara, B.R., Hoffman, L.R., and Miller, S.I. (2010). Asymmetrical distribution of the second messenger c-di-GMP upon bacterial cell division. Science *328*, 1295–1297.

Danilchanka, O., and Mekalanos, J.J. (2013). Cyclic dinucleotides and the innate immune response. Cell *154*, 962–970.

Fan, F., Binkowski, B.F., Butler, B.L., Stecha, P.F., Lewis, M.K., and Wood, K. V. (2008). Novel genetically encoded biosensors using firefly luciferase. ACS Chem. Biol. *3*, 346–351.

Gibson, D.G., Young, L., Chuang, R.Y., Venter, J.C., Hutchison, C.A., and Smith, H.O. (2009). Enzymatic assembly of DNA molecules up to several hundred kilobases. Nat. Methods *6*, 343–345.

Hattori, M., Haga, S., Takakura, H., Ozaki, M., and Ozawa, T. (2013). Sustained accurate recording of intracellular acidification in living tissues with a photo-controllable bioluminescent protein. Proc. Natl. Acad. Sci. *110*, 9332–9337.

Hengge, R. (2009). Principles of c-di-GMP signalling in bacteria. Nat. Rev. Microbiol. *7*, 263–273.

Ho, C.L., Chong, K.S.J., Oppong, J.A., Chuah, M.L.C., Tan, S.M., and Liang, Z.X. (2013). Visualizing the perturbation of cellular cyclic di-GMP levels in bacterial cells. J. Am. Chem. Soc. *135*, 566–569.

Jiang, L.I., Collins, J., Davis, R., Lin, K.M., DeCamp, D., Roach, T., Hsueh, R., Rebres, R.A., Ross, E.M., Taussig, R., et al. (2007). Use of a cAMP BRET sensor to characterize a novel regulation of cAMP by the sphingosine 1-phosphate/G13 pathway. J. Biol. Chem. *282*, 10576–10584.

Kaihara, A., Umezawa, Y., and Furukawa, T. (2008). Bioluminescent indicators for Ca2+ based on split Renilla luciferase complementation in living cells. Anal. Sci. *24*, 1405–1408.

Ko, J., Ryu, K.S., Kim, H., Shin, J.S., Lee, J.O., Cheong, C., and Choi, B.S. (2010). Structure of PP4397 reveals the molecular basis for different c-di-GMP binding modes by pilz domain proteins. J. Mol. Biol. *398*, 97–110.

Koestler, B.J., and Waters, C.M. (2014). Bile acids and bicarbonate inversely regulate intracellular cyclic di-GMP in vibrio cholerae. Infect. Immun. *82*, 3002–3014.

Krasteva, P.V., and Sondermann, H. (2017). Versatile modes of cellular regulation via cyclic dinucleotides. Nat. Chem. Biol. *13*, 350–359.

McKenna, A., Hanna, M., Banks, E., Sivachenko, A., Cibulskis, K., Kernytsky, A., Garimella, K., Altshuler, D., Gabriel, S., Daly, M., et al. (2010). The Genome Analysis Toolkit: A MapReduce framework for analyzing next-generation DNA sequencing data. Genome Res. *20*, 1297–1303.

Mills, E., Petersen, E., Kulasekara, B.R., and Miller, S.I. (2015). A direct screen for c-di-GMP modulators reveals a Salmonella Typhimurium periplasmic L -arginine – sensing pathway. Sci. Signal. *8*, 1–12.

Nagai, T., Ibata, K., Park, E.S., Kubota, M., Mikoshiba, K., and Miyawaki, A. (2002). A variant of yellow fluorescent protein with fast and efficient maturation for cell-biological applications. Nat. Biotechnol. *20*, 87–90.

Oberortner, E., Cheng, J.F., Hillson, N.J., and Deutsch, S. (2017). Streamlining the Design-to-Build Transition with Build-Optimization Software Tools. ACS Synth. Biol. *6*, 485–496.

Paul, K., Nieto, V., Carlquist, W.C., Blair, D.F., and Harshey, R.M. (2010). The c-di-GMP Binding Protein YcgR Controls Flagellar Motor Direction and Speed to Affect Chemotaxis by a “Backstop Brake” Mechanism. Mol. Cell *38*, 128–139.

Prescher, J.A., and Contag, C.H. (2010). Guided by the light: visualizing biomolecular processes in living animals with bioluminescence. Curr. Opin. Chem. Biol. *14*, 80–89.

Pultz, I.S., Christen, M., Kulasekara, H.D., Kennard, A., Kulasekara, B., and Miller, S.I. (2012). The response threshold of Salmonella PilZ domain proteins is determined by their binding affinities for c-di-GMP. Mol. Microbiol. *86*, 1424–1440.

Romling, U., Galperin, M.Y., and Gomelsky, M. (2013). Cyclic di-GMP: the first 25 years of a universal bacterial second messenger. Microbiol. Mol. Biol. Rev. *77*, 1–52.

Ross, P., Weinhouse, H., Aloni, Y., Michaeli, D., Weinberger-Ohana, P., Mayer, R., Braun, S., de Vroom, E., van der Marel, G.A., van Boom, J.H., et al. (1987). Regulation of cellulose synthesis in Acetobacter xylinum by cyclic dyguanylic acid. Nature *325*, 279–281.

Rossi, E., Cimdins, A., Lüthje, P., Brauner, A., Sjöling, Å., Landini, P., and Römling, U. (2017). “It’s a gut feeling” – *Escherichia coli* biofilm formation in the gastrointestinal tract environment. Crit. Rev. Microbiol. *7828*, 1–30.

Ryjenkov, D.A., Simm, R., Römling, U., and Gomelsky, M. (2006). The PilZ domain is a receptor for the second messenger c-di-GMP: The PilZ domain protein YcgR controls motility in enterobacteria. J. Biol. Chem. *281*, 30310–30314.

Saito, K., and Nagai, T. (2015). Recent progress in luminescent proteins development. Curr. Opin. Chem. Biol. *27*, 46–51.

Saito, K., Hatsugai, N., Horikawa, K., Kobayashi, K., Matsu-Ura, T., Mikoshiba, K., and Nagai, T. (2010). Auto-luminescent genetically-encoded ratiometric indicator for real-

time Ca2+ imaging at the single cell level. PLoS One *5*, e9935.

Saito, K., Chang, Y.-F., Horikawa, K., Hatsugai, N., Higuchi, Y., Hashida, M., Yoshida, Y., Matsuda, T., Arai, Y., and Nagai, T. (2012). Luminescent proteins for high-speed single-cell and whole-body imaging. Nat. Commun. *3*, 1262.

Sarenko, O., Klauck, G., Wilke, F.M., Pfiffer, V., Richter, A.M., Herbst, S., Kaever, V., and Hengge, R. (2017). More than Enzymes That Make or Break Cyclic Di-GMP — Local Signaling in the Interactome of GGDEF/EAL Domain Proteins of Escherichia coli. MBio *8*, e01639-17.

Shaner, N.C., Campbell, R.E., Steinbach, P.A., Giepmans, B.N.G., Palmer, A.E., and Tsien, R.Y. (2004). Improved monomeric red, orange and yellow fluorescent proteins derived from Discosoma sp. red fluorescent protein. Nat. Biotechnol. *22*, 1567–1572.

Shimizu, T.S., Delalez, N., Pichler, K., and Berg, H.C. (2006). Monitoring bacterial chemotaxis by using bioluminescence resonance energy transfer: Absence of feedback from the flagellar motors. Proc. Natl. Acad. Sci. *103*, 2093–2097.

Studier, F.W. (2005). Protein production by auto-induction in high-density shaking cultures. Protein Expr. Purif. *41*, 207–234.

Su, Y., Hickey, S.F., Keyser, S.G.L., and Hammond, M.C. (2016). In Vitro and in Vivo Enzyme Activity Screening via RNA-Based Fluorescent Biosensors for S-Adenosyl- l -homocysteine (SAH). J. Am. Chem. Soc. *138*, 7040–7047.

Suzuki, K., Kimura, T., Shinoda, H., Bai, G., Daniels, M.J., Arai, Y., Nakano, M., and Nagai, T. (2016). Five colour variants of bright luminescent protein for real-time multicolour bioimaging. Nat. Commun. *7*, 13718.

Takai, A., Nakano, M., Saito, K., Haruno, R., Watanabe, T.M., Ohyanagi, T., Jin, T., Okada, Y., and Nagai, T. (2015). Expanded palette of Nano-lanterns for real-time multicolor luminescence imaging. Proc. Natl. Acad. Sci. *112*, 4352–4356.

Takenouchi, O., Kanno, A., Takakura, H., Hattori, M., and Ozawa, T. (2016). Bioluminescent Indicator for Highly Sensitive Analysis of Estrogenic Activity in a Cell-Based Format. Bioconjug. Chem. *27*, 2689–2694.

Thestrup, T., Litzlbauer, J., Bartholomäus, I., Mues, M., Russo, L., Dana, H., Kovalchuk, Y., Liang, Y., Kalamakis, G., Laukat, Y., et al. (2014). Optimized ratiometric calcium sensors for functional in vivo imaging of neurons and T lymphocytes. Nat. Methods *11*, 175–182.

Wang, X.C., Wilson, S.C., and Hammond, M.C. (2016). Next-generation fluorescent RNA biosensors enable anaerobic detection of cyclic di-GMP. Nucleic Acids Res. *44*, e139.

Yang, J., Cumberbatch, D., Centanni, S., Shi, S., Winder, D., Webb, D., and Johnson, C.H. (2016). Coupling optogenetic stimulation with NanoLuc-based luminescence (BRET) Ca++ sensing. Nat. Commun. *7*, 13268.

Zhang, L., Lee, K.C., Bhojani, M.S., Khan, A.P., Shilman, A., Holland, E.C., Ross, B.D.,

and Rehemtulla, A. (2007). Molecular imaging of Akt kinase activity. Nat. Med. *13*, 1114–1119.

Zhang, Z., Kim, S., Gaffney, B.L., and Jones, R.A. (2006). Polymorphism of the signaling molecule c-di-GMP. J. Am. Chem. Soc. *128*, 7015–7024.

Chapter Three

Ratiometric chemiluminescent biosensors towards *in vivo* imaging of bacterial signaling

Portions of this chapter will be published in:

Dippel, A. B*, Anderson, W. A.*, Park, J., Yildiz, F. H., and Hammond, M.C. "Ratiometric Chemiluminescent Biosensors Towards *In Vivo* Imaging of Bacterial Signaling." Manuscript in prep. (*Authors contributed equally).

INTRODUCTION

The second messenger molecule cyclic di-GMP is a key regulator of bacterial physiology and behavior, coordinating diverse processes such as motility, biofilm formation, and virulence. First discovered as a stimulator of cellulose synthesis (Ross et al., 1987), c-di-GMP has since been found to be nearly ubiquitous in bacteria, with c-di-GMP signaling pathways often integrated with other global regulatory systems, such as phosphorylation networks and quorum sensing pathways (Jenal et al., 2017; Romling et al., 2013). The intracellular levels of c-di-GMP are tightly regulated by diguanylate cyclase (DGC) and phosphodiesterase (PDE) enzymes that synthesize and degrade c-di-GMP, respectively. Many bacteria have an abundance of predicted DGC and PDE genes, suggesting unique c-di-GMP regulatory circuits are activated in response to different environmental cues. In many bacterial pathogens, including *Pseudomonas aeruginosa*, *Clostridium difficile*, *Vibrio cholerae*, and pathogenic strains of *Escherichia coli*, these complex c-di-GMP signaling networks allow the bacteria to adapt to and survive in the changing environmental conditions that are experienced during infection of a mammalian host (Hall and Lee, 2018). While multiple studies have examined the effects of c-di-GMP levels on virulence in these pathogens, there currently are no tools available that allow for the quantification of c-di-GMP in bacteria during stages of mammalian host infection. To interrogate these complex c-di-GMP signaling networks in bacteria over the course of the infection process, new analytical tools and needed for quantifying and imaging intracellular c-di-GMP levels within tissue over extended time frames.

Commonly used tools for analyzing intracellular c-di-GMP levels include phenotypic screens and mass spectrometry (MS) analysis of bacterial cell extracts. Phenotypic screens for motility and biofilm formation can serve as proxies for measuring intracellular c-di-GMP levels (O'Toole et al., 1999; Wolfe and Berg, 1989). These assays can be high throughput and are useful in screening genetic knockouts, however they have low sensitivity and provide indirect measurement of c-di-GMP that can be complicated by pleiotropic effects. MS-based analysis of c-di-GMP from bacterial cell extracts is highly sensitive and quantitative, however the multi-step sample preparation and long analysis time required leads to reduced throughput (Burhenne and Kaever, 2013; Petrova and Sauer, 2017; Spangler et al., 2010). In addition, neither phenotypic assays nor mass spectrometry-based analysis can provide real-time, dynamic measurements of c-di-GMP in cells. To overcome these issues, our lab and others have developed several genetically encodable fluorescent biosensors that can report on single-cell dynamics of c-di-GMP using fluorescence microscopy or flow cytometry (Christen et al., 2010; Ho et al., 2013; Wang et al., 2016). These tools are sensitive, can provide real-time measurements of c-di-GMP dynamics, and are amenable to high throughput screening. Notable examples include protein-based FRET biosensors that have been used to image c-di-GMP dynamics during asymmetric cell division in *Caulobacter crescentus* (Christen et al., 2010) and RNA-based fluorescent sensors that were used to visualize c-di-GMP changes in *E. coli* in direct response to an environmental signal, zinc (Yeo et al., 2017).

One drawback of fluorescent biosensors, however, is that due to a reliance on external illumination, these systems are incompatible with imaging in deep tissues of animals and in long-term experiments due to phototoxicity and/or photobleaching. In a preliminary effort to expand the capabilities of genetically encodable tools for quantifying

c-di-GMP levels to overcome these issues, our lab developed the first chemiluminescent biosensors for c-di-GMP (Dippel et al., 2018) based on the yellow Nano-lantern (YNL) scaffold and a CSL-BRET mechanism (Saito et al., 2012). These YNL-YcgR biosensors provide nanomolar sensitivity for c-di-GMP with high selectivity, large signal changes, and a luminescent signal that is produced without external illumination. The sensors were used to develop a rapid, plate-reader based assay for measuring diguanylate cyclase activity in bacterial lysates. The intensity-based signal of these sensors is useful for in vitro activity assays with lysates or purified enzymes where biosensor and luminescent substrate levels can be controlled. However, in long-term imaging experiments and/or situations where luminescent substrate availability differs between samples, signal quantitation becomes complicated for intensity-based sensors. Accordingly, we encountered issues when applying the YNL sensors to live cell measurements of c-di-GMP in bacteria (Dippel et al., 2018).

This current study tests our hypothesis that altering the biosensor scaffold to produce a ratiometric rather than intensity-based signal would enable long-term, quantitative, live cell imaging of c-di-GMP in bacteria. Ratiometric BRET sensors using the engineered marine luciferase NanoLuc (NLuc) (Hall et al., 2012) have recently been developed for imaging Ca^{2+} (Yang et al., 2016), Zn^{2+} (Aper et al., 2016) and membrane voltage (Inagaki et al., 2017), however to our knowledge no sensors of this type have been applied to imaging in bacteria to date. In this work, we generate the first BRET biosensor scaffold that selectively responds to c-di-GMP and produces a ratiometric signal change. By engineering the biosensor scaffold, a suite of Venus-YcgR-NLuc (VYN) sensors is generated that provide extremely high sensitivity (K_D < 300 pM) and large BRET signal changes (up to 109%). The tVYN-TmΔ biosensor was applied to develop a plate reader-based assay to quantify c-di-GMP levels in bacterial extracts with sensitivity comparable to MS-based methods (LOD = 30 fmol). This assay is used to analyze *V. cholerae* extracts grown under a variety of conditions that mimic the infection cycle and reveal changes in c-di-GMP in response to changes in growth conditions.

Finally, the VYN sensors are applied as genetically encodable tools for live cell measurements of c-di-GMP in *E. coli*, using both a plate reader and an IVIS small animal imaging system. As a proof-of-concept that VYN biosensors can image c-di-GMP levels during host infection, we show that the VYN biosensors also function in the context of a tissue phantom model. In this model, the tVYN-NtΔ sensor produces measurable changes in BRET ratio between high and low c-di-GMP conditions with only ~10^3-10^4 biosensor-expressing cells required for the measurement. Furthermore, the BRET signal remains stable for at least one hour after luminescent substrate addition, suggesting that VYN sensors could be used for long-term imaging of c-di-GMP dynamics during host infection. The VYN sensors developed here can serve as robust *in vitro* diagnostic tools for high throughput screening, as well as genetically encodable tools for monitoring the dynamics of c-di-GMP in live cells, and lay the groundwork for live cell imaging of c-di-GMP dynamics in bacteria during host infection, and other complex environments.

RESULTS

Design of BRET sensor for cyclic di-GMP. The starting BRET scaffold, V-NLuc, pairs the newly developed marine luciferase, NanoLuc (NLuc), with a truncation of the

monomeric yellow fluorescent protein, Venus, as the donor and acceptor moieties, respectively, similar to the previously developed YeNL (Suzuki et al., 2016). NLuc produces a glow-type luminescence with an emission maximum at 460 nm and an overall luminescent output ~100-150x that of the commonly used Renilla or firefly luciferases (Hall et al., 2012). Compared to the intensity-based yellow Nano-lantern (YNL) sensors for c-di-GMP previously designed by our lab that use a mutated version of Renilla luciferase as the donor moiety, the substitution of NLuc should produce significantly higher signal intensity, improved thermodynamic stability, and increased signal stability over time. Combined with the benefits of a ratiometric signal compared to an intensity-based signal, these improvements should allow for imaging in more complex biological systems, including within tissues of live animals. The emission of NLuc overlaps well with the excitation of Venus, producing an efficient energy transfer in V-NLuc, as measured by the BRET ratio (530/460 nm) (Figure 3.1a).

To design a c-di-GMP sensor from the V-NLuc scaffold, a c-di-GMP-binding YcgR protein is inserted between Venus and NLuc (Figure 3.1b). YcgR-like proteins contain the c-di-GMP-binding PilZ domain at their C-terminus (Benach et al., 2007; Ko et al., 2010; Ryjenkov et al., 2006). These proteins typically undergo large conformational changes upon c-di-GMP binding (Benach et al., 2007), which can be harnessed for the generation of genetically encoded sensors for c-di-GMP (Christen et al., 2010; Dippel et al., 2018; Ho et al., 2013; Pultz et al., 2012). We predicted that the binding of c-di-GMP to this Venus-YcgR-NLuc (VYN) sensor would produce a change in energy transfer efficiency between Venus and NLuc, which could be measured by a change in the BRET ratio. Depending on the conformational state of the unbound sensor, the change could be from low to high BRET ratio upon binding, or vice versa, thereby producing positive or negative signal changes, respectively (Figure 3.1b).

For initial testing of the sensor design, the full-length YcgR protein from *Escherichia coli* (*Ec*YcgR) was inserted into the BRET scaffold with 3 amino acid linkers on either side to generate VYN-Ec. The sensor was purified from *E. coli* after co-expression with the c-di-GMP-specific phosphodiesterase (PDE) PdeH to ensure the sensor did not co-purify with any endogenous c-di-GMP bound. Initial testing of the purified sensor showed that c-di-GMP binding induced a change from high to low BRET state, which corresponds to a negative change in BRET ratio (Figure 3.1c). In accordance with the ratiometric nature of the sensor, the BRET ratio of un-bound VYN-Ec remained stable even as overall signal intensity decreased due to consumption of luminescent substrate (Figure 3.2a, b). Further testing of purified VYN-Ec showed that it binds to two molecules of c-di-GMP with an apparent affinity (K_D) of ~50 nM and a BRET signal change of -48% (Figure 3.1d). The sensor retains selectivity for c-di-GMP over structurally related CDNs (Figure 3.2c, d).

This initial VYN-Ec design successfully produced a BRET biosensor that binds with high affinity and selectivity to c-di-GMP and produces a significant signal change upon binding. The inclusion of NLuc in the scaffold results in the production of a bright and stable signal, and the ratiometric nature of the biosensor allows for long-term measurements compared to previous intensity-based YNL-YcgR sensors. These properties alone suggest that the VYN biosensor scaffold will prove to be useful for long-term imaging of c-di-GMP dynamics in complex biological systems. Interestingly, the

affinity of the VYN-Ec sensor (K_D~50 nM) is significantly higher compared to what was measured in the equivalent YNL-EcYcgR sensor (K_D~350 nM) (Dippel et al., 2018) and previously reported affinity values for *Ec*YcgR (K_D~800 nM) (Ryjenkov et al., 2006). Since c-di-GMP binding to PilZ domains has been found to be largely entropically driven (Benach et al., 2007), this finding suggests that the VYN scaffold itself may be providing a degree of additional stability that results in a decreased entropic cost of binding c-di-GMP, leading to increased binding affinity. Encouraged by the VYN-Ec results, we sought to further improve the properties of the sensor via phylogenetic screening and semi-rational protein engineering.

Optimization of VYN biosensors. Our lab has previously shown that using a phylogenetic screening approach in biosensor development can lead to rapid improvements in biosensor characteristics (Dippel et al., 2018; Su et al., 2016; Wang et al., 2016). More specifically, we have observed that swapping to different phylogenetic YcgR variants within the YNL scaffold produced drastic changes and improvements in the affinity, signal change, and stability of NL-based sensors for c-di-GMP (Dippel et al., 2018). To examine the effects of these changes in the ratiometric VYN scaffold, four phylogenetic YcgR variants previously characterized in the YNL scaffold were selected for testing in the VYN scaffold. These YcgR variants were chosen because in the YNL scaffold they displayed high affinity, high stability, and large positive signal changes (*Tm*YcgR, *Cp*YcgR, and *Tb*YcgR), or a moderate affinity and a moderate negative signal change (*Nt*YcgR). Purified VYN sensors with *Tm*YcgR, *Nt*YcgR, and *Tb*YcgR exhibited c-di-GMP dependent changes in BRET, while the VYN-Cp sensor appeared non-responsive (Figure 3.3a). As expected, the functional sensors displayed higher affinities for c-di-GMP compared to VYN-Ec. While the success of three out of the four phylogenetic variants was promising, we sought to further improve the dynamic range of these sensors through semi-rational engineering of the VYN scaffold itself.

Two routes were used to alter the signal change of the VYN sensors: composite linker truncation and circular permutation of Venus. Both strategies are commonly used to improve signal change in the development of ratiometric sensors (FRET and BRET), but it is difficult to predict the effects these changes will have on the resulting sensor (Deuschle et al., 2005; van Rosmalen et al., 2017). Accordingly, a small library of VYN variants was generated to screen for sensors with improved properties (Figure 3.3b). For linker truncation, rather than reduce the length of the already short 3 amino acid linkers in the original VYN scaffold, the “composite linkers” (defined as the N- and C-terminal residues of Venus, YcgR, and NLuc that are not necessary for fluorescence, ligand binding, or luminescence) were truncated. For the truncated VYN (tVYN) scaffold, 2 additional C-terminal residues from Venus and 4 N-terminal residues from NLuc were removed (Suzuki et al., 2016). For YcgRΔ variants, the secondary structure prediction software SABLE was used to predict unstructured N- and C-terminal residues for removal (Table 3.3). For circular permutations of Venus, five variants were chosen that previously were shown to not disrupt Venus fluorescence (Table 3.4) (Nagai et al., 2004).

A library of 39 VYN variants was constructed and tested in a lysate-based assay to determine biosensor performance in response to increasing concentrations of c-di-GMP (0, 50 nM, and 5 µM). In this assay each individual sensor is co-expressed in *E. coli* with PdeH, cells are lysed, c-di-GMP is added to the lysate at specified concentrations,

and BRET ratios are measured. This assay allows for biosensor performance to be rapidly assessed without the need for protein purification. In Figure 3.3c, the $\log_2$(signal fold-change) values for each sensor are reported to simplify the comparison of positive and negative signal change sensors. While no clear trends could be drawn between designs, the small set of linker truncations and circular permutations tested produced at least one BRET sensor for each YcgR protein with a signal change -30% or +50%, which should prove useful for quantitative measurements of c-di-GMP (Figure 3.4). For example, while the original VYN-Cp design showed no detectable signal change, the Vcp157-Cp sensor produced a reasonable -30% signal change. Interestingly, this screen also revealed that seemingly small alterations in the scaffold can produce large differences in the resulting signal fold-change. The switch from tVYN-Nt to tVYN-NtΔ, for example, produced a sensor with the same relative signal fold-change, but flipped from a positive to negative change in BRET ratios (Figure 3.1b).

A subset of the sensors from the library was purified for further characterization in vitro (Table 3.1). The different sensors were found to span a range of affinities from < 300 pM up to ~100 nM. The tVYN-TmΔ sensor, to our knowledge, exhibits the highest affinity CDN:protein interaction ever measured. The binding of c-di-GMP to PilZ-domain containing proteins has been shown to be largely entropically driven (Benach et al., 2007), and therefore the affinity is highly temperature dependent. All of the YcgR variants tested aside from *Ec*YcgR come from predicted thermophilic organisms, so we expect that these proteins may be evolved to bind with nanomolar to micromolar affinity at the elevated temperatures of the organisms' natural environments.

For certain sensors, the signal change measured in lysates differs from that measured using purified protein. The most dramatic example of this is for tVYN-TmΔ, which shows a -28% change in the lysate screen and much improved -56% change as purified protein. We investigated this discrepancy and found that the difference likely arises due to two reasons: the extremely high affinity of the sensor, and the generation of luminescent signal from truncated protein products. First, given the extremely high affinity of the sensor, it may be pre-bound to endogenous c-di-GMP present in lysates regardless of the co-expression of PdeH, thereby masking the full signal change. Accordingly, when performing the lysate assay without the co-expression of PdeH, the signal change values are suppressed even further (Figure 3.5a). Second, we observe different BRET ratios when testing sensor purified with an N-terminal versus a C-terminal affinity tag (Figure 3.5b). When using a C-terminal affinity tag, truncated protein products containing NLuc are co-purified along with full length biosensor (Figure 3.5c) These protein products, which are also present in unpurified lysates, produce a high background of "non-specific" luminescent signal at 460 nm. This produces a corresponding decrease in BRET ratio that is independent of the c-di-GMP concentration, partially masking the signal change. Accordingly, when using an N-terminal affinity tag, these truncated protein products are not co-purified, resulting in generally larger BRET ratios and signal change. This finding highlights the fact that for these types of ratiometric sensors, increased "stability" of the scaffold is a highly desirable trait.

By screening a library of VYN sensors containing phylogenetic YcgR variants and altered sensor scaffolds, we discovered multiple BRET sensors for c-di-GMP with improved signal change and affinity compared to the starting VYN-Ec sensor. Moreover,

we showed that for an individual YcgR sequence, only a small panel (6 to 9) of sensor scaffolds needs to be tested to generate at least one with useful properties. Combined with the lysate-based screening method, we predict that this approach could be used to easily generate additional BRET-based sensors where the affinity of the YcgR protein is tailored to the system under study. While we focused on high affinity YcgR variants here, lower affinity variants could prove to be useful for analysis of c-di-GMP in certain situations. Further characterization of selected sensors revealed extremely high affinity interactions with c-di-GMP and highlighted how the overall stability of the sensors must be taken into account when comparing data from the lysate screen to that from purified proteins.

Quantification of c-di-GMP in *Vibrio cholerae* cell extracts. The quantification of intracellular c-di-GMP levels is routinely performed using mass spectrometry (MS)-based analysis of bacterial cell extracts. These methods are highly sensitive and allow for the quantitation of c-di-GMP in the picomolar or femtomolar range, depending on the detection method used (Burhenne and Kaever, 2013; Petrova and Sauer, 2017; Spangler et al., 2010). However, the sample preparations steps, long analysis time, and expertise required to perform MS-based analysis of cell extracts has limited the accessibility of these types of experiments for many researchers and high-throughput screening projects. Given the extremely high affinity of the VYN sensors for c-di-GMP, we predicted that it would be possible to develop a simple and robust plate reader-based assay for quantification of c-di-GMP with sensitivity comparable to that of MS-based methods. In comparison to our YNL-YcgR sensors for c-di-GMP (Dippel et al., 2018), the ~100-fold increases in affinity should allow for analysis in sample-limited situations (e.g. clinical isolates), and in cells with very low c-di-GMP levels. This assay should allow for quantification of c-di-GMP levels in any type of bacterial cell extract that is typically analyzed via MS-based methods, and significantly reduce the cost and time required for analysis, making these types of experiments more readily accessible to the community.

The tVYN-TmΔ sensor was selected for the development of this assay because it showed the highest affinity (<300 pM) and largest magnitude signal change (Δ ratio of –1.04) out of all tested sensors in vitro. While the sensitivity was highest using 300 pM biosensor (Figure 3.6a), the extract quantitation assay was performed with 3 nM biosensor due to improved signal intensity and stability. Under these conditions, the limit of detection (signal-to-noise ratio 3:1) of the tVYN-TmΔ sensor was measured to be 30 fmol, which is comparable to the most sensitive established LC-MS/MS-based methods (Figure 3.6b) (Burhenne and Kaever, 2013; Petrova and Sauer, 2017). One drawback of the biosensor assay is the limited linear range (~30 fmol to 400 fmol), however this can be alleviated by diluting any samples that fall outside of this range or using more biosensor.

To directly compare the performance of our plate reader-based protocol to established LC-MS/MS methods, cell extract samples from *V. cholerae* were analyzed using both methods. Cell extracts were generated from three different strains of *V. cholerae* – wild-type (SWT), wild-type lacking six DGCs (SΔ6DGC), and rugose (RΔvpsI/II) – that were expected to produce endogenous, low, and high levels of c-di-GMP respectively. Cells were grown under standard conditions in LB broth (see Materials & Methods) and extracts were generated to analyze total c-di-GMP content. Cell extracts

were analyzed with the biosensor and the expected differences in c-di-GMP were observed between the three strains (Figure 3.6c; Figure 3.7). The same samples were sent for analysis via LC-MS/MS and are results are pending.

Encouraged by these results, we decided to analyze the c-di-GMP content of *V. cholerae* grown under a variety of different conditions that have either been shown to affect or are predicted to affect endogenous c-di-GMP signaling networks within the bacterium. These conditions include changes in media (LB vs. AKI), salinity (0 vs. 0.1 vs. 0.3 M NaCl), pH (7 vs. 4), temperature (25 °C vs. 37 °C), O_2 content (+/- O_2), iron content (+/- bipyridyl), and the presence of mucin. Cells were grown under the specified conditions (see Materials & Methods for details), extracts were generated, and analyzed with the tVYN-TmΔ sensor to quantify total c-di-GMP content (Figure 3.6d; Figure 3.8). There were significant differences observed as a result of changes in media, salinity, pH, and O_2 content.

Utilizing the extremely high affinity (K_D<300 pM) and selectivity of the tVYN-TmΔ biosensor, we developed a robust plate reader based assay for sensitive quantification of c-di-GMP in different sample types. The assay in its current form was optimized using a 3 nM biosensor concentration, which provided an LOD of 30 fmol using pure c-di-GMP as a standard. The use of a lower concentration of biosensor leads to improved sensitivity, however the signal brightness and stability is reduced. The LOD of the biosensor assay is comparable to the most sensitive established LC-MS/MS methods, but is plate-based and significantly more rapid, which makes it more amenable to HTS applications. Theoretically, the biosensor signal could even be analyzed using a digital camera, which drastically reduces the cost of c-di-GMP quantification compared to MS-based methods (Johnsson et al., 2018). When applied to analysis of *V. cholerae* extracts, the biosensor assay was able to quantify changes in c-di-GMP concentration in response to changes in growth conditions. These results suggest that the biosensor assay will be generally applicable to the study of c-di-GMP in complex bacterial extract samples, including clinical isolates and mixed cultures.

Live-cell measurements of c-di-GMP. In the prior development of YNL-based sensors for c-di-GMP we encountered difficulties in making live cell measurements, presumably due to changes in luminescent substrate availability and biosensor expression between different conditions that made normalization of the intensity-based signal not possible (Figure 3.9) (Dippel et al., 2018). We predicted that the ratiometric nature of the signal produced by the VYN sensors would alleviate these issues. To test VYN biosensor performance in live cells, a subset of sensors were co-expressed in BL21 Star (DE3) *E. coli* with a PDE (PdeH – low c-di-GMP), an inactive diguanylate cyclase (DGC) as a control (WspR-G249A – endogenous c-di-GMP), or a constitutively active DGC (WspR-D70E – elevated c-di-GMP). After overnight growth in auto-induction media, the cells were pelleted, resuspended in PBS, luminescent substrate was added, and BRET ratios were measured in a plate reader (Figure 3.10). Encouragingly, many of the tested sensors showed significant changes in BRET ratio between low or endogenous c-di-GMP conditions versus elevated c-di-GMP conditions, as expected. These results confirm that switching from an intensity-based signal to a ratiometric signal allows the sensors to work in a live cell context.

Given the promising live cell measurements obtained in a plate reader, we sought to determine if the VYN sensors could function in an instrument routinely used for small animal imaging (Xenogen IVIS 100). One long-term goal is to be able to monitor c-di-GMP levels of bacterial cells in real time during infection of an animal host. Our initial proof-of-concept experiment was to validate the signal intensity and BRET signal changes of our sensors using this instrumentation with conventional filter sets and settings. Selected sensors were co-expressed in BL21 (DE3) Star *E. coli* cells with WspR-G249A or WspR-D70E to produce endogenous or elevated c-di-GMP levels, respectively. After overnight growth in auto-induction media, the cells were prepared in the same manner as for plate reader experiments. Luminescent substrate was added, then images were captured sequentially using no emission filter and the available 500 and 540 nm emission filters on the IVIS. The total flux (photons/sec) from each well in the 540 nm and 500 nm filter images was used to calculate BRET ratios for each culture (Figure 3.11a).

The raw BRET ratio values are different between IVIS and plate reader instruments, most likely due to the different emission filters, which are less optimal for the biosensor on the IVIS. However, the changes in BRET ratio between endogenous and elevated c-di-GMP conditions were faithfully reproduced for VYN-Ec and tVYN-NtΔ (Figure 3.11a). Luminescent signal was measurable with serial dilutions of cells down to 20,000-fold dilution, however, in highly diluted samples the VYN-Ec sensor no longer exhibited the expected change in BRET ratio (Figure 3.12a). The tVYN-NtΔ sensor, however, exhibited robust BRET ratio changes in all cases, although the magnitude of the signal change was decreased in more diluted samples. It was unclear exactly what caused this effect, but the increasing dilutions appeared to subtly change the observed BRET ratio. This points to the fact that although the percent change in BRET ratio is similar between these two sensors, the larger magnitude of the BRET change in tVYN-NtΔ is useful for overcoming any c-di-GMP-independent effects that may partially mask the full signal change under certain conditions.

Live-cell measurements of c-di-GMP in a tissue-like phantom model. To further extend the proof-of-concept, tissue-like phantom materials were utilized to mimic the light absorption and scattering of living tissue (De Grand et al., 2006). Thus, plates containing the bacterial cells were covered with 1.5 mm thick tissue phantoms prior to image capture (Figure 3.13). Encouragingly, luminescent signal was detected for all samples, and measurable changes in BRET ratio were observed for VYN-Ec and tVYN-NtΔ, as before (Figure 3.11b). BRET ratios were in general found to be lower due to the absorption of hemoglobin in the tissue-like phantom. Luminescent signal was detected with serial dilutions of cells down to 20,000-fold dilution, but with significantly reduced intensity compared to uncovered (Figure 3.12b). In highly diluted samples the VYN-Ec sensor no longer exhibited a measurable change in BRET ratio, but significant BRET ratio changes still were observed for the tVYN-NtΔ sensor in all cases (Figure 3.11c).

Given these promising results, we sought to determine if the VYN sensors would also be useful for long term imaging of c-di-GMP within the tissue phantom model. For the 200-fold cell dilutions, luminescence was monitored for an hour after the initial addition of luminescent substrate (Figure 3.12c). While the signal intensity reduced over time as luminescent substrate was consumed, the BRET ratios remained remarkably constant over the entire time course.

To determine whether the amount of bacteria that were being monitored in the IVIS experiments is biologically relevant, the number of colony-forming units (CFUs) was measured for representative cultures co-expressing the tVYN-NtΔ biosensor and WspR-G249A or WspR-D70E. Cells were prepared as before and then spotted onto LB/Agar plates containing no antibiotic, carbenicillin (Carb), kanamycin (Kan), or both Carb and Kan to determine if any plasmid loss occurred during growth (Figure 3.14). Results from the no antibiotic plates suggest that there are ~10^8 *E. coli* in each well for 2-fold diluted cultures, and down to ~10^6 and ~10^4 cells in the 200-fold and 20,000-fold diluted cultures, respectively. Results from antibiotic plates show that ~90% of cells have lost both the biosensor and WspR expression plasmids after overnight growth under these conditions. Thus, the actual number of bacteria producing luminescent signal in the IVIS is only 10% of the total. Given the signal observed 20,000-fold diluted cultures, the tVYN-NtΔ sensor is capable of imaging c-di-GMP levels in as few as ~10^3 biosensor-expression bacterial cells in a tissue-like model.

These co-expression experiments demonstrate that VYN sensors can function as genetically encodable tools for monitoring c-di-GMP levels in live bacterial cells, as measured in both a plate reader and a conventional small animal imaging system. Additionally, as a proof-of-concept for future *in vivo* studies, we show that the VYN sensors can report on c-di-GMP levels in live *E. coli* when used in the context of a tissue phantom model. Furthermore, the BRET signal produced was remarkably stable for at least 1 hour after luminescent substrate addition, suggesting that VYN sensors could be used for long-term imaging of c-di-GMP dynamics during infection of animal hosts. Finally, we determined based on CFU measurements that the tVYN-NtΔ sensor is capable of imaging c-di-GMP levels in as few as ~10^3 biosensor-expression bacterial cells in our tissue-like model. It has been shown in a *V. cholerae* infection model of infant mice that there are 10^4 to 10^5 bacteria in the small intestine after infection, which suggests that the tVYN-NtΔ sensor could be useful for analyzing c-di-GMP dynamics in this system (Tamayo et al., 2010).

DISCUSSION AND FUTURE DIRECTIONS

Cyclic di-GMP signaling networks are key regulators of bacterial behavior, coordinating motility, biofilm formation, and virulence. In many bacterial pathogens, c-di-GMP networks allow the bacteria to adapt to and survive the changing conditions that are experienced during infection of a mammalian host. In recent years, the development of genetically encodable sensors specific for c-di-GMP has advanced our knowledge of c-di-GMP signaling networks. However, it has not been possible to monitor c-di-GMP levels in bacteria during host infection, which has hindered our understanding of how c-di-GMP affects virulence under medically relevant conditions. In pursuit of this goal, the VYN sensors developed here are, to our knowledge, the first ratiometric, luminescent sensors of their kind for analyzing c-di-GMP signaling, and should allow for quantitative imaging of c-di-GMP in bacteria during host infection.

After initial validation of the VYN sensor scaffold, screening of a small library designed around phylogenetic variant YcgR proteins and semi-rational engineering of the biosensor scaffold resulted in a panel of biosensors that exhibit high affinity and large signal changes in response to c-di-GMP. We predict that the design strategies used here

should be generally applicable to the development of new VYN sensors using any desired YcgR-like protein sequence, allowing one to tailor the affinity of the VYN biosensor to a specific system under study. The highest affinity sensor identified here, tVYN-TmΔ, was used to develop a robust plate reader-based assay for quantification of c-di-GMP in cell extracts, with sensitivity comparable to that of established MS-based methods. While the linear range of the biosensor is reduced compared to LC/MS methods, we believe that the speed and ease of the plate reader-based measurements should make these types of cell extract experiments more accessible to the community. Beyond cell extracts, the VYN sensors should also be generally useful for any quantitative *in vitro* measurements of c-di-GMP, such as in monitoring enzyme kinetics or high throughput screening of activators/inhibitors of DGCs and PDEs (Opoku-Temeng et al., 2016; Sambanthamoorthy et al., 2012).

When applied as genetically encoded tools, the VYN sensors exhibited significant changes in BRET ratio between endogenous and elevated c-di-GMP conditions in *E. coli*. These results confirm that switching from an intensity-based luminescent signal to a ratiometric luminescent signal cancels out variations in biosensor expression and/or luminescent substrate availability between samples, which simplifies signal quantitation. Finally, as a proof-of-concept that VYN biosensors can image c-di-GMP levels during host infection, we show that the VYN biosensors function in the context of a tissue phantom model. These types of tissue phantoms have recently been used as a benchmark to compare photon output of luminescent protein systems within deep tissues (Chu et al., 2016). Importantly, we performed all experiments with the VYN scaffold using coelenterazine-h as the luminescent substrate, as opposed to furimazine, which is the preferred substrate for NLuc. Furimazine has been well characterized to produce higher luminescent output than coelenterzine-h (Hall et al., 2012). While the tissue phantom model used here does not account for *in vivo* substrate availability, previous reports have used NLuc and furimazine effectively to study the spread of pathogens in mice in real time, suggesting that substrate availability should not be a limitation in these experiments (Caine and Osorio, 2017; Silberstein et al., 2018; Sun et al., 2014; Tran et al., 2013). Additionally, BRET signal from the biosensor was found to be very stable for at least 1 hour after the initial administration of luminescent substrate, which should prove useful for examining c-di-GMP dynamics on this time scale. More long-term experiments (days, weeks, etc.) could also be carried out by using repeated administration of luminescent substrate at the desired times, which would allow for the monitoring of c-di-GMP dynamics over the extended time scale of infection.

In conclusion, the work here presents, to our knowledge, the first ratiometric, luminescent biosensors made specifically for studying bacterial signaling, as opposed to eukaryotic signaling. Rather than merely providing a luminescent readout for the presence of bacteria, the biosensors developed here should allow for the study of bacterial signaling pathways in biological systems in which fluorescent biosensors are less useful. Ultimately, we hope that the VYN biosensors developed here will serve as easy-to-use diagnostic tools for analyzing c-di-GMP in vitro, as well as useful genetically encodable tools for studying c-di-GMP dynamics in bacterial pathogens during host infection.

FIGURES

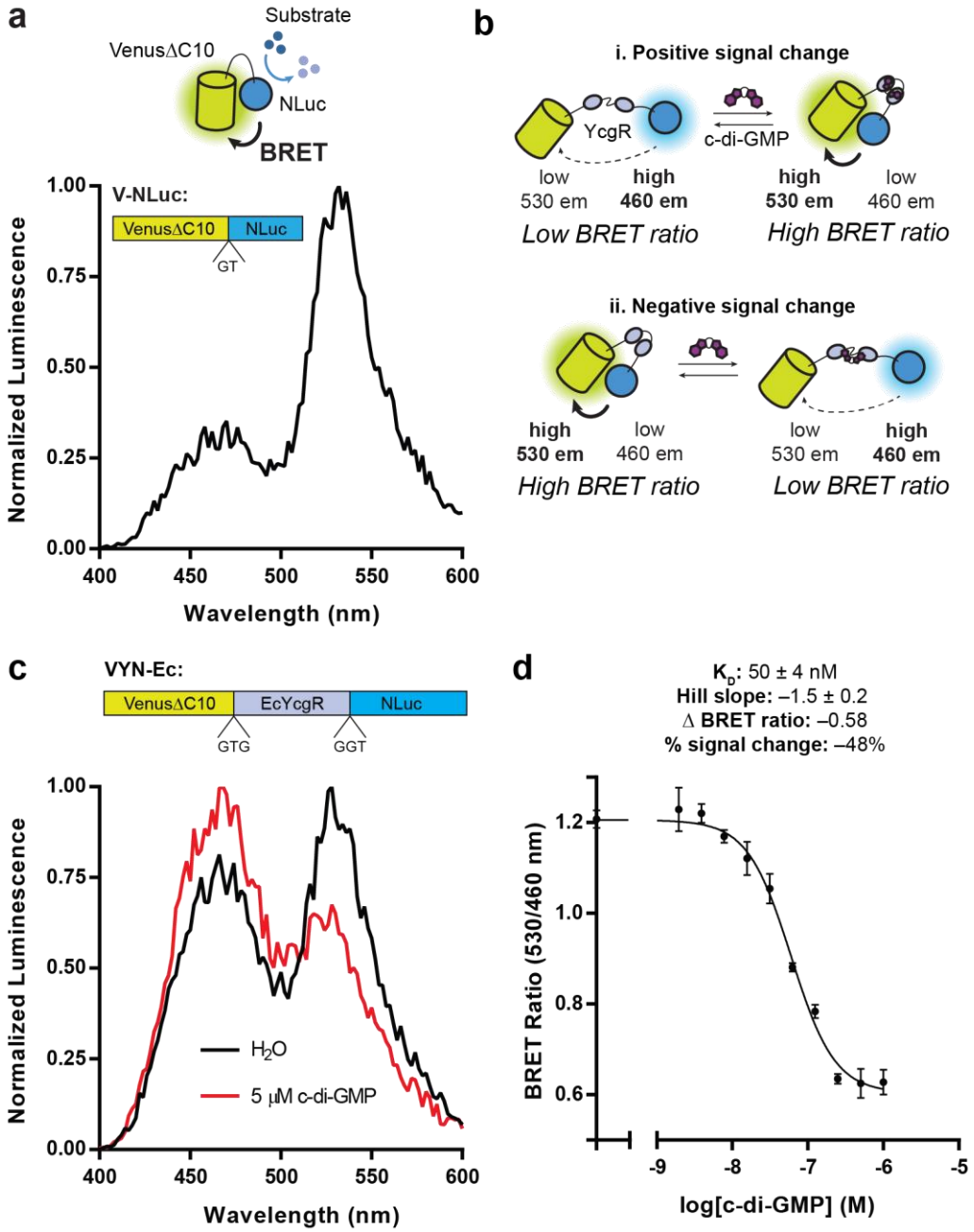

Figure 3.1 Design and characterization of ratiometric VYN biosensors. (a) Schematic for BRET mechanism of V-NLuc scaffold and the domain structure of the protein. Normalized luminescence emission spectra of purified V-NLuc. Data from one representative measurement. (b) Two potential mechanisms for modulation of BRET ratios by c-di-GMP binding to VYN sensors. Schematic of VYN-Ec sensor shown below. (c) Normalized luminescence emission spectra of purified VYN-Ec in the presence and absence of c-di-GMP. Data from one representative measurement shows the biosensor follows mechanism ii. (d) Binding affinity measurements for purified VYN-Ec. Data are from 3 replicates represented as mean +/- SD.

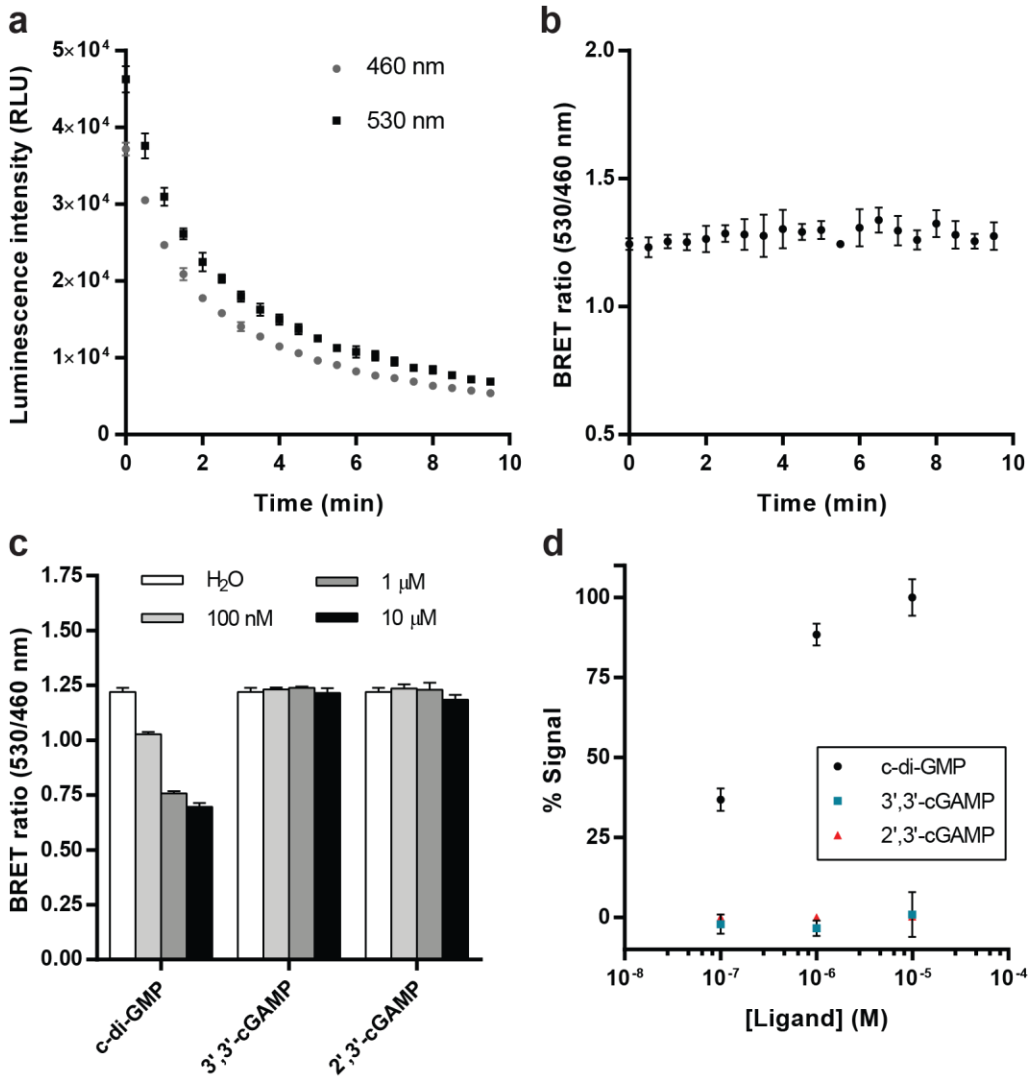

Figure 3.2 Additional characterization of VYN-Ec sensor. (a) Luminescence signal intensity of VYN-Ec sensor over time. Luminescent substrate was added just prior to beginning of measurement. Data are from 3 replicates represented as mean +/- SD. (b) BRET ratio calculated from data shown in part (a). Data are from 3 replicates represented as mean +/- SD. (c) BRET ratios of VYN-Ec sensor in response to different cyclic di-nucleotides. Data are from 3 replicates represented as mean +/- SD. (d) Percent signal calculated from part (c). Data are from 3 replicates represented as mean +/- SD.

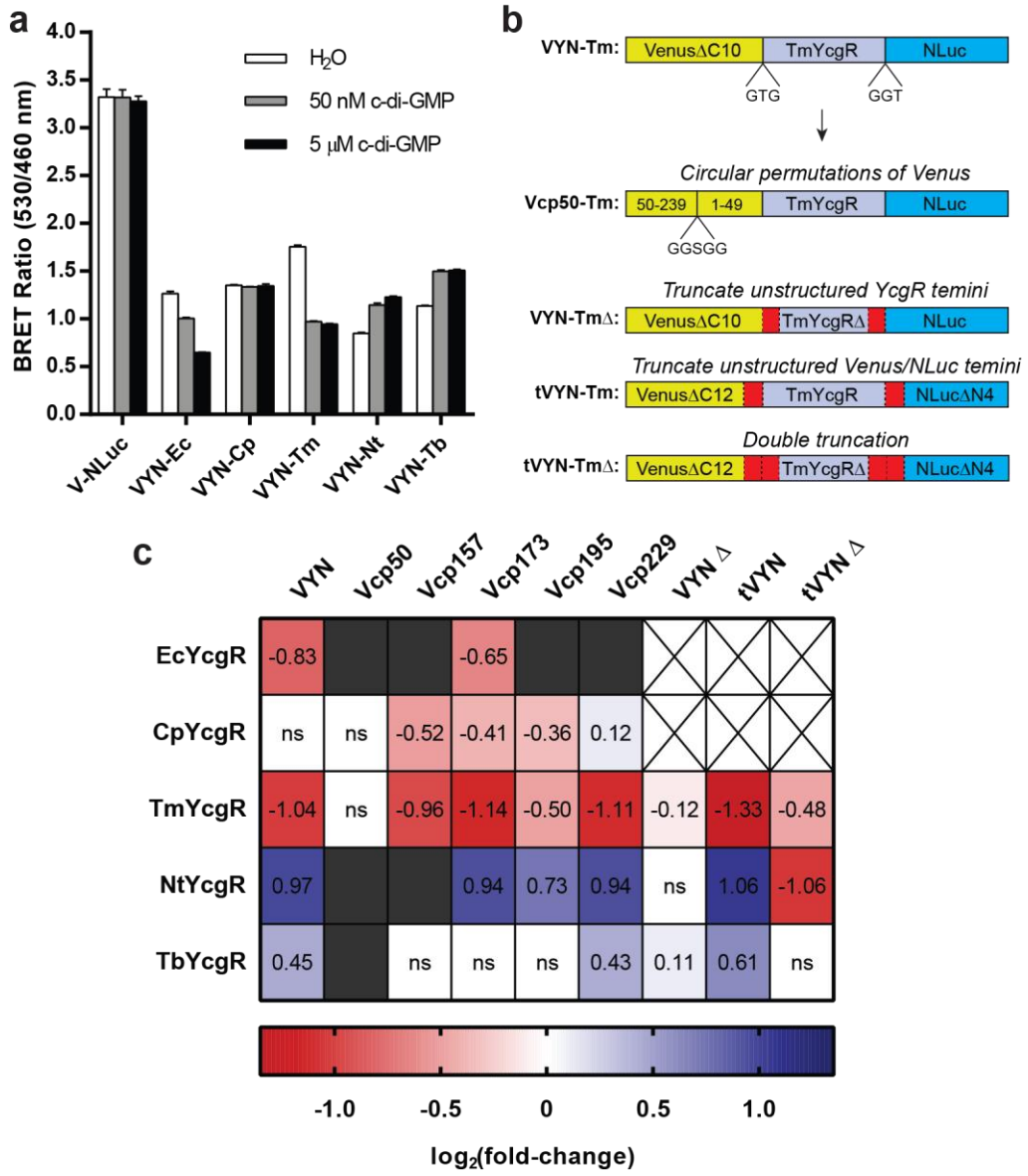

Figure 3.3 Optimization of VYN sensors for c-di-GMP. (a) BRET ratios of purified VYN sensors containing phylogenetic variant YcgR proteins in response to varying levels of c-di-GMP. Data are from 3 replicates represented as mean +/- SD. (b) Schematic representations of the domain architectures of altered VYN scaffolds, using TmYcgR as an example. Red regions highlight where truncations were made. (c) Signal fold-change (defined as BRET ratio with 5 μM c-di-GMP added divided by BRET ratio with buffer added and plotted as $\log_2$(fold-change)) of VYN sensor library screened in lysates. Grayed boxes = dim signal; crossed-out boxes = not tested; ns = no significant signal fold-change ($P > 0.05$ determined by Student's t-test). Data are from 4 biological replicates represented as the mean.

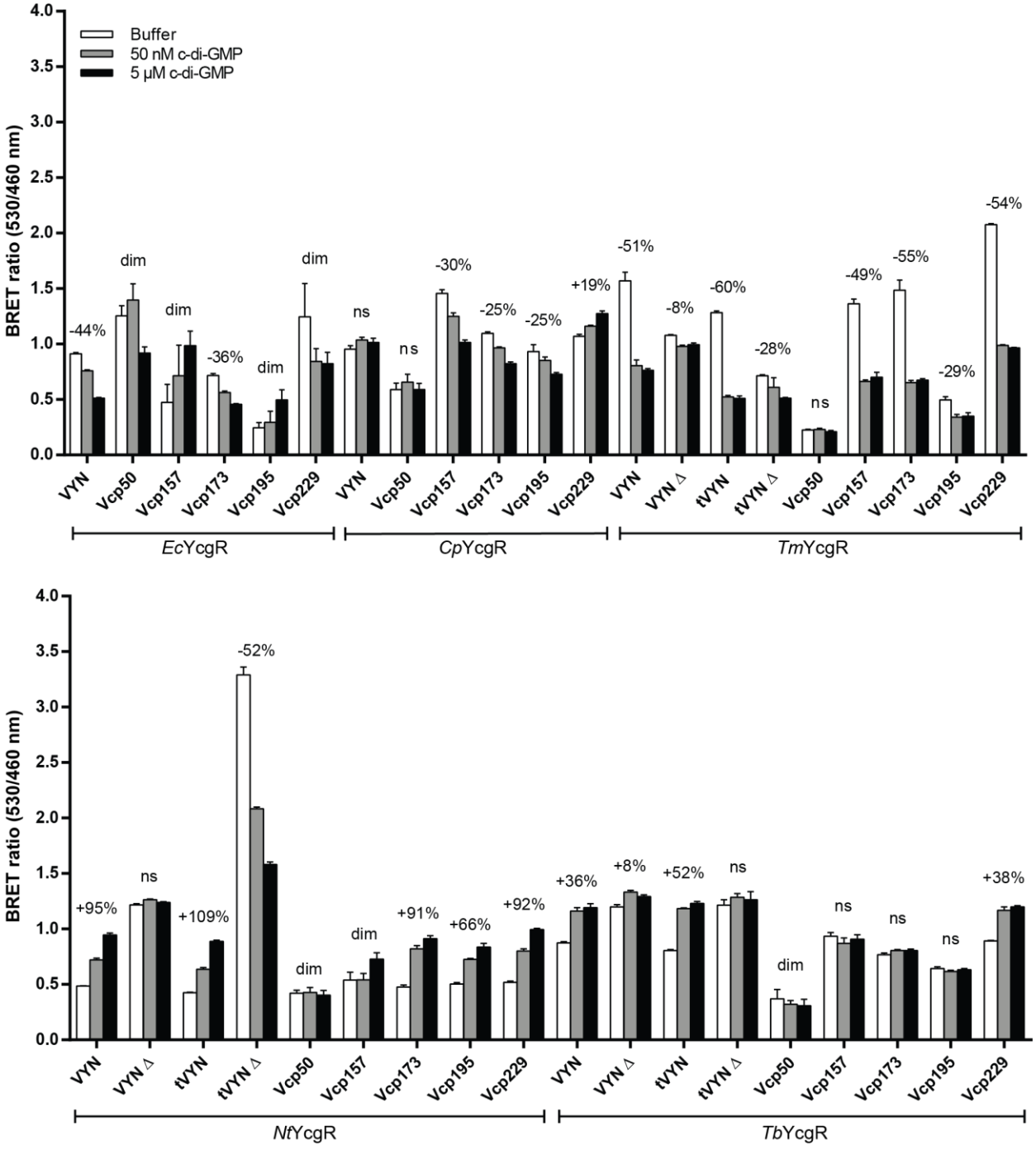

Figure 3.4 Lysate-based screen of VYN biosensor library. BRET value measurements from VYN library lysate screening in response to c-di-GMP (data summarized in Figure 3.3c). Percent signal change values (comparing buffer to 5 µM c-di-GMP conditions) shown for variants that exhibited significant changes in BRET ($P < 0.05$ determined by Student's t-test). Data are from 4 biological replicates represented as the mean +/- SD.

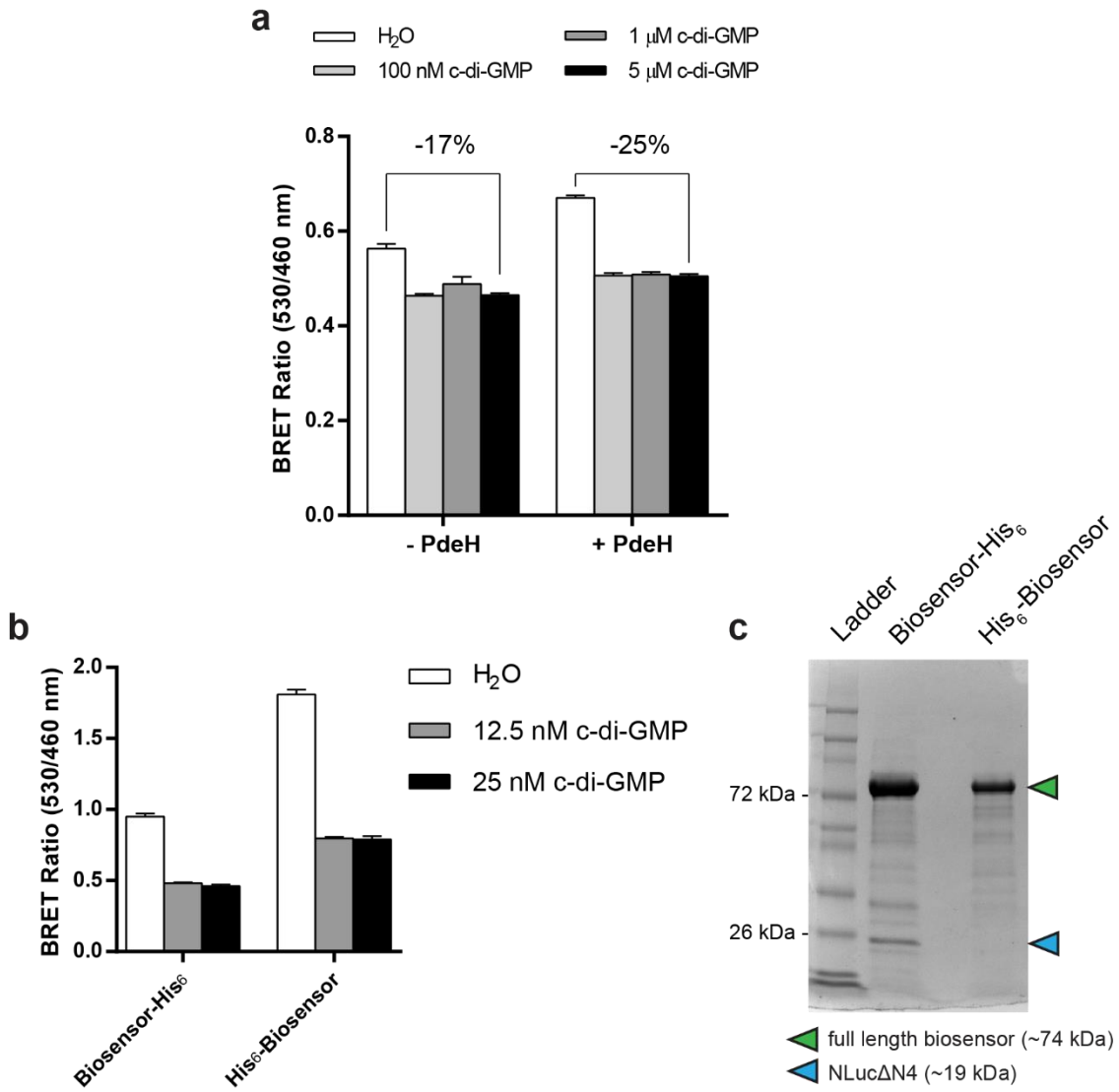

Figure 3.5 Additional characterization of tVYN-TmΔ biosensor. (a) BRET values from the tVYN-TmΔ biosensor in the lysate-based assay with or without the co-expression of the c-di-GMP specific phosphodiesterase, PdeH. Data are from 9 biological replicates represented as the mean +/- SD. (b) BRET values of tVYN-TmΔ in vitro after purification with a C-terminal or N-terminal His_6 tag. Data are from 3 replicates represented as mean +/- SD. (c) SDS-PAGE of the tVYN-TmΔ biosensor purified with a C-terminal or N-terminal His_6 tag, showing the presence of truncated NLuc protein products.

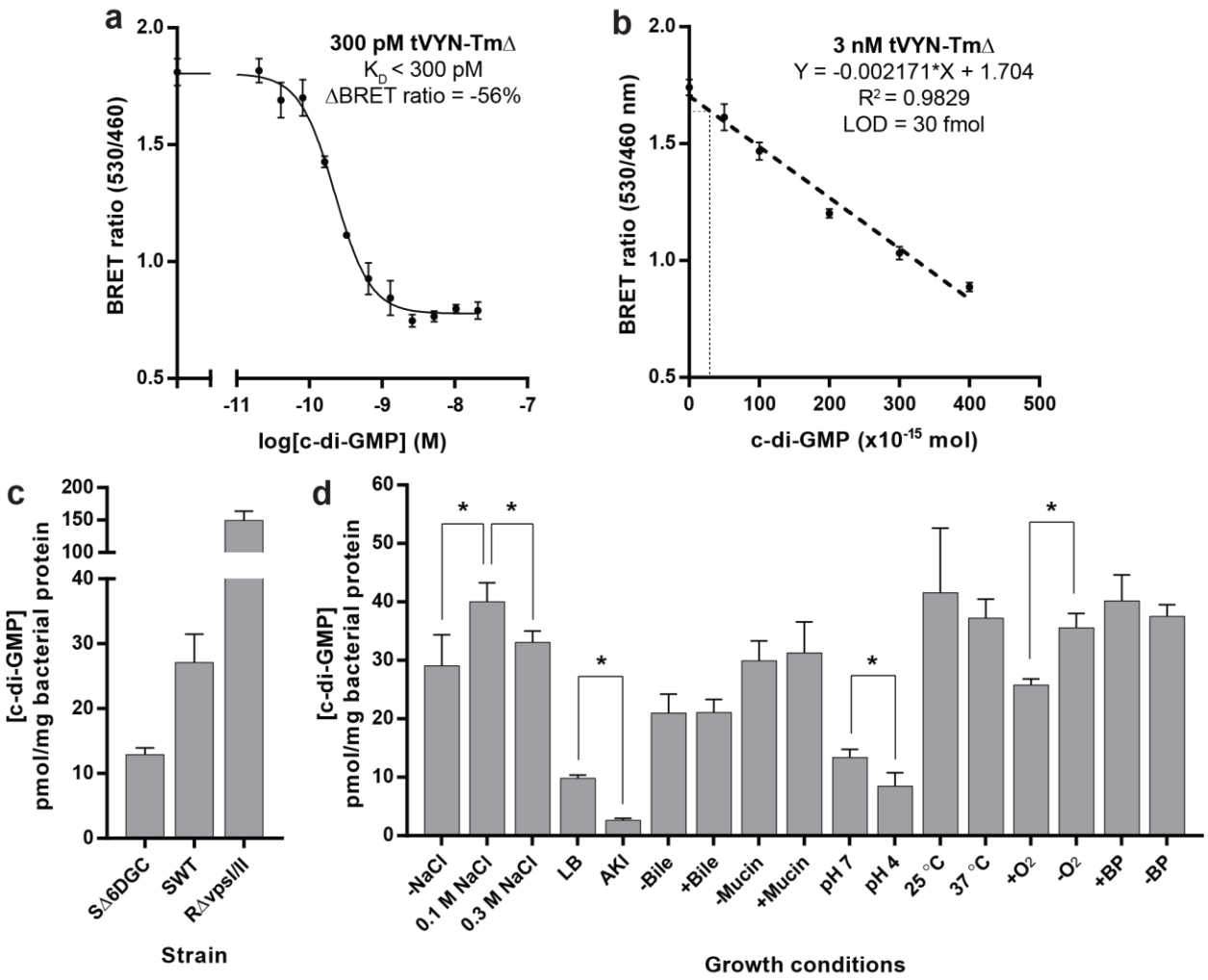

Figure 3.6 Quantitation of c-di-GMP using tVYN-TmΔ biosensor. (a) Binding affinity measurements for purified tVYN-TmΔ using decreased biosensor concentration. Data are from 3 replicates represented as mean +/- SD. (b) Standard curve for c-di-GMP quantitation using purified tVYN-TmΔ. Data are from 6 replicates represented as mean +/- SD. (c) Quantitation of c-di-GMP in cell extracts of 3 different strains of *V. cholerae* using the tVYN-TmΔ biosensor. Data are from 3 biological replicates represented as the mean +/- SD. (d) Quantitation of c-di-GMP in cell extracts of SWT *V. cholerae* grown under different conditions using the tVYN-TmΔ biosensor. Asterisks (*) denote significant changes in c-di-GMP between growth conditions ($P < 0.05$ determined by Student's t-test). Data are from 3 biological replicates represented as the mean +/- SD.

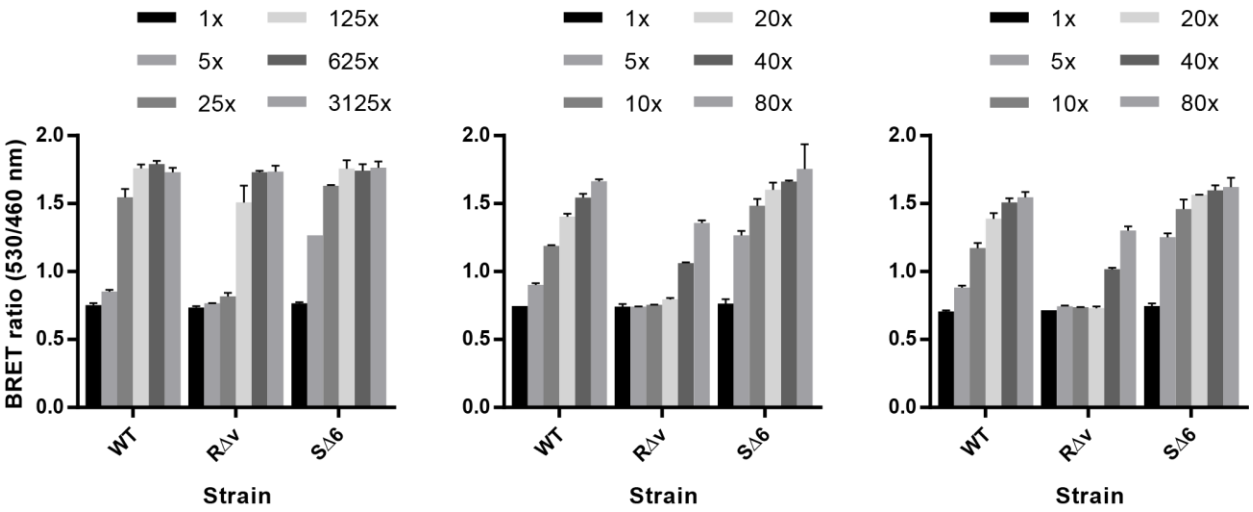

Figure 3.7 Biosensor analysis of *V. cholerae* reference strains. BRET ratios measured in serial dilutions of *V. cholerae* extract using the tVYN-TmΔ biosensor, with each panel representing a separate biological replicate. Note differences in dilution factor for replicate 1 (left) compared to replicates 2 and 3 (middle and right). Data are from 2 technical replicates represented as the mean +/- SD.

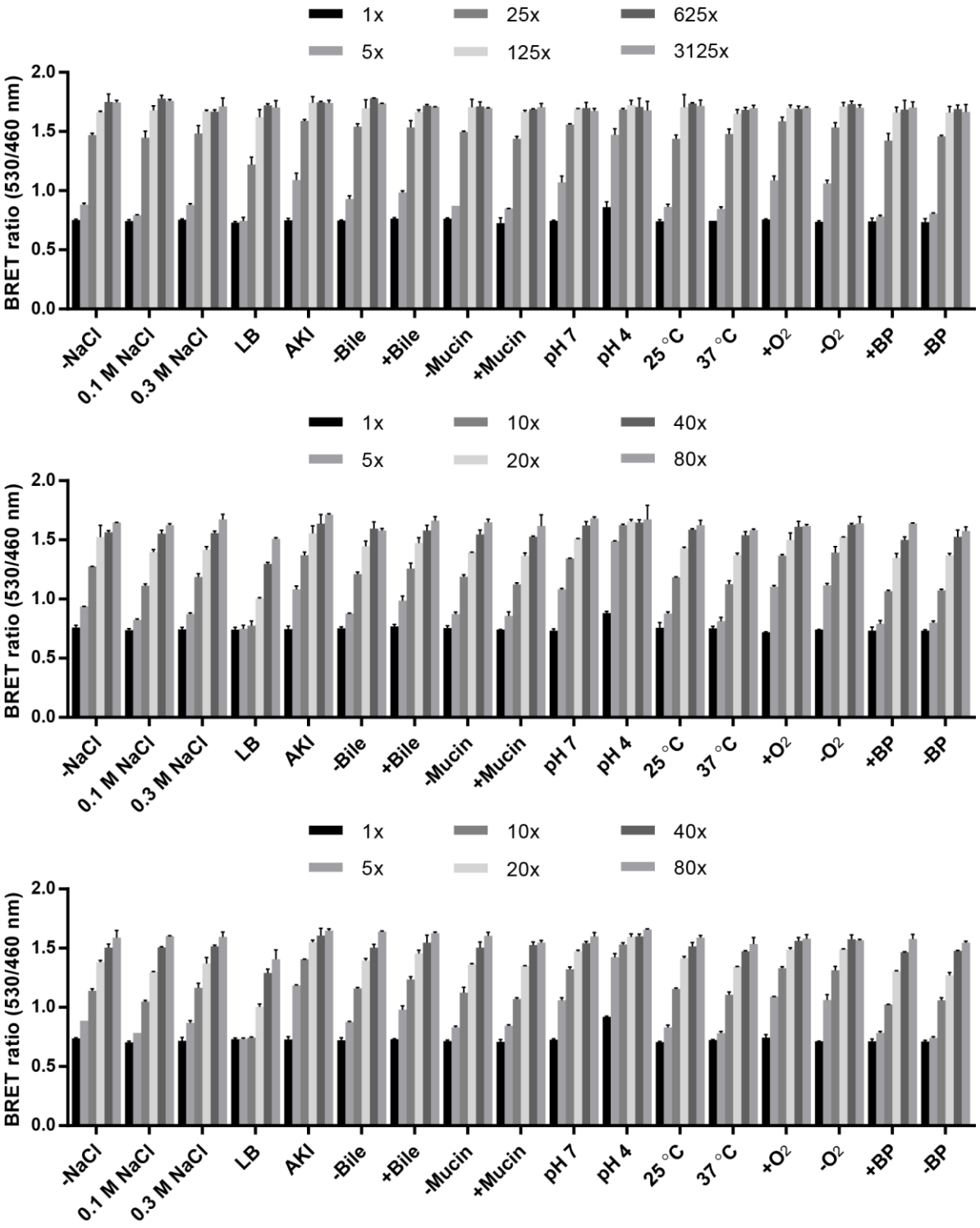

Figure 3.8 Biosensor analysis of *V. cholerae* under different growth conditions. BRET ratios measured in serial dilutions of *V. cholerae* extract using the tVYN-TmΔ biosensor, with each panel representing a separate biological replicate. Note differences in dilution factor for replicate 1 (top) compared to replicates 2 and 3 (bottom). Data are from 2 technical replicates represented as the mean +/- SD.

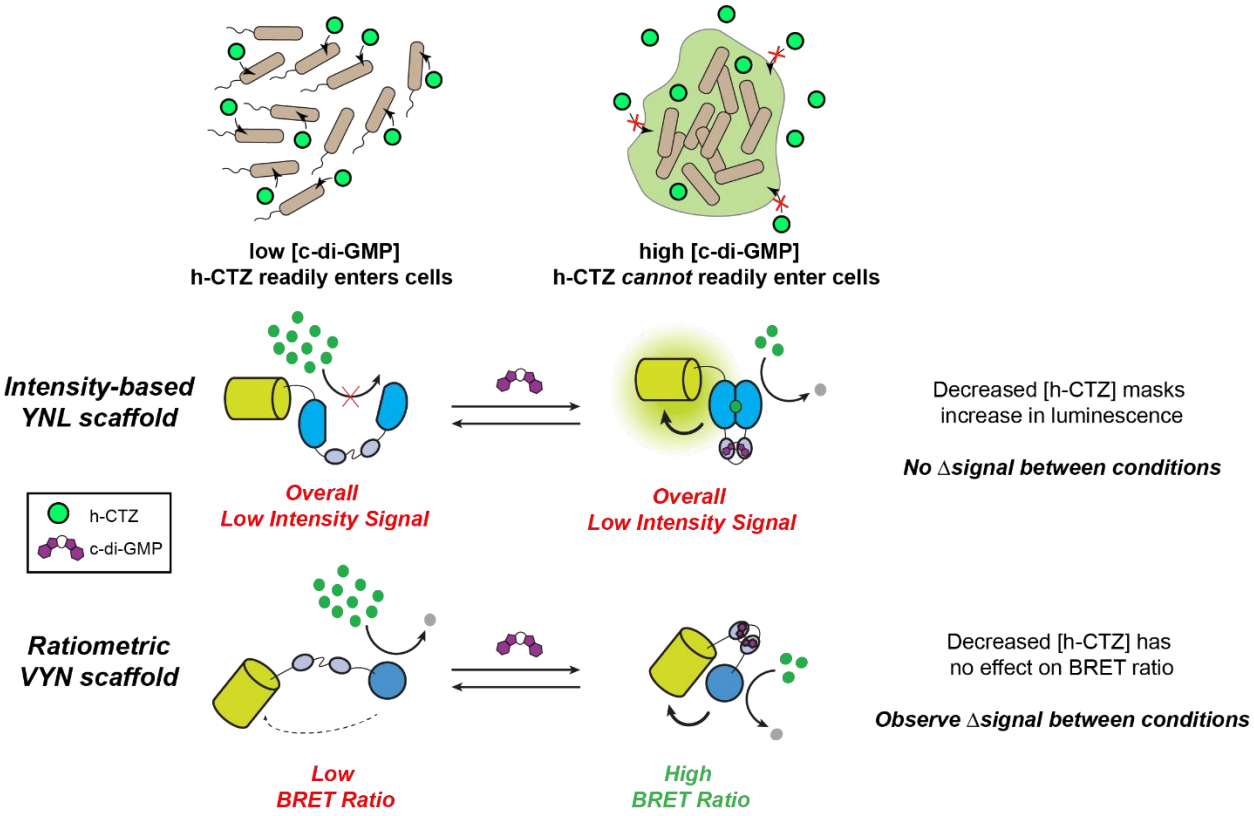

Figure 3.9 Live cell imaging with luminescent biosensors. Schematic showing the difficulties encountered making live cell measurements using the intensity-based YNL scaffold, compared to the ratiometric VYN scaffold.

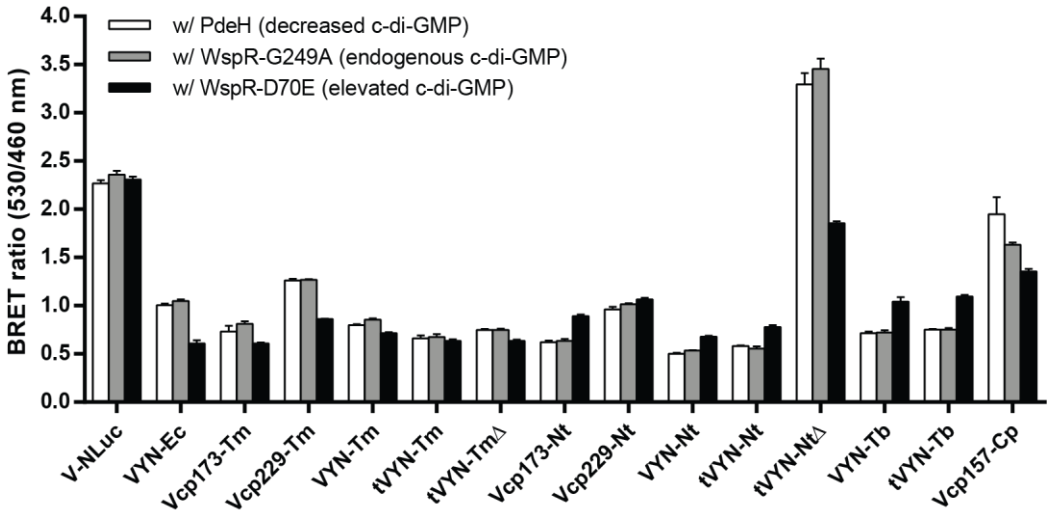

Figure 3.10 Live cell measurements of c-di-GMP using VYN sensors. BRET ratios of *E. coli* cells co-expressing VYN biosensors with PdeH, WspR-G249A, or WspR-D70E. Data are from 4 biological replicates represented as mean +/- SD.

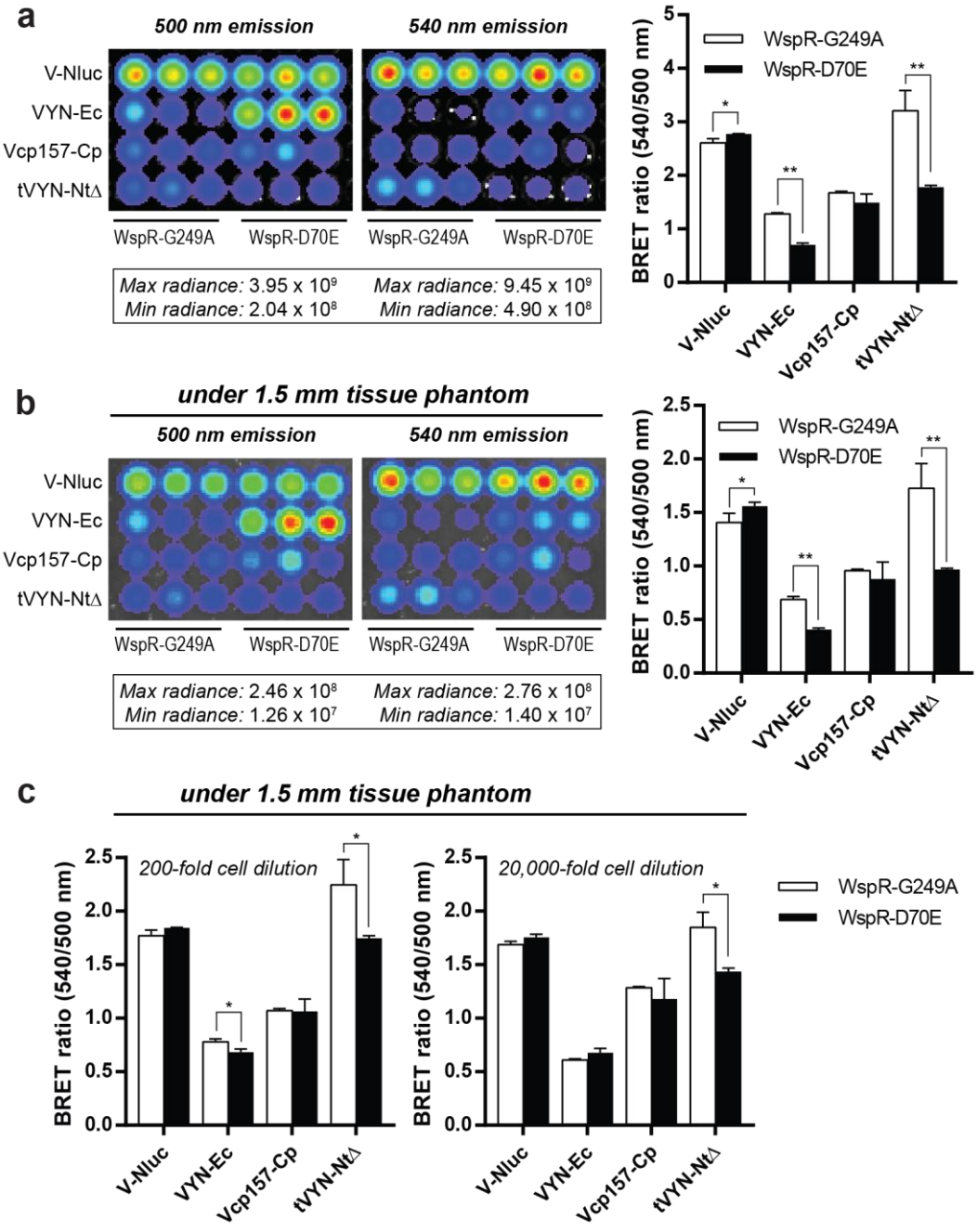

Figure 3.11 Live cell measurements of c-di-GMP using a tissue phantom model. (a) Luminescent images of 2-fold diluted *E. coli* cultures co-expressing VYN biosensors with WspR-G249A or WspR-D70E captured by an IVIS Spectrum, and the BRET values calculated from the radiance each well. Maximum and minimum radiance values (photons/sec/cm^2/steradian) captured for each image are shown. (b) Same as part (a), except plate was covered with a 1.5 mm thick tissue phantom prior to image capture. (c) BRET ratios of serially diluted *E. coli* cultures co-expressing VYN biosensors with WspR-G249A or WspR-D70E calculated from the radiance of each well. Plate was covered with a 1.5 mm thick tissue phantom prior to image capture. For all graphs, data are from 3 biological replicates represented as mean +/- SD. Asterisks (*) denote significant changes in BRET ratio (*P < 0.05, **P < 0.005 determined by Student's t-test).

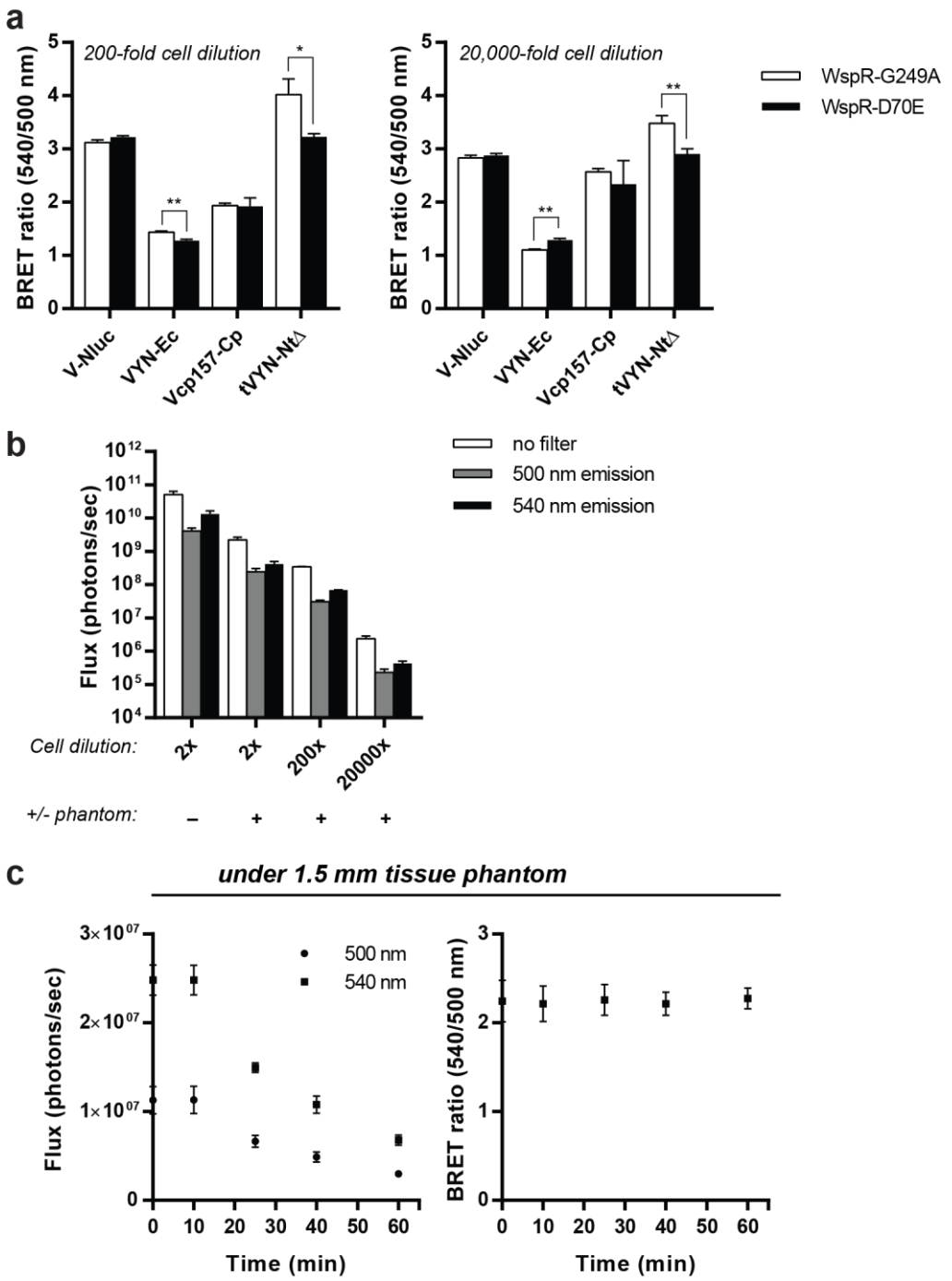

Figure 3.12 Additional data for live cell measurements of c-di-GMP using a tissue phantom model. (a) BRET ratios of serially diluted *E. coli* cultures co-expressing VYN biosensors with WspR-G249A or WspR-D70E calculated from the radiance of each well. Images captured without a phantom cover. Asterisks (*) denote significant changes in BRET ratio (*P < 0.05, **P < 0.005 determined by Student's t-test). (b) Total flux of *E. coli* cultures co-expressing the tVYN-NtΔ biosensor with WspR-G249A at various dilutions with or without the added tissue phantom. (c) (Left) Radiance and (right) corresponding BRET ratios of 200-fold diluted *E. coli* cultures co-expressing the tVYN-NtΔ biosensor with WspR-G249A over time. Luminescent substrate was added at time zero. For all graphs, data are from 3 biological replicates represented as mean +/- SD.

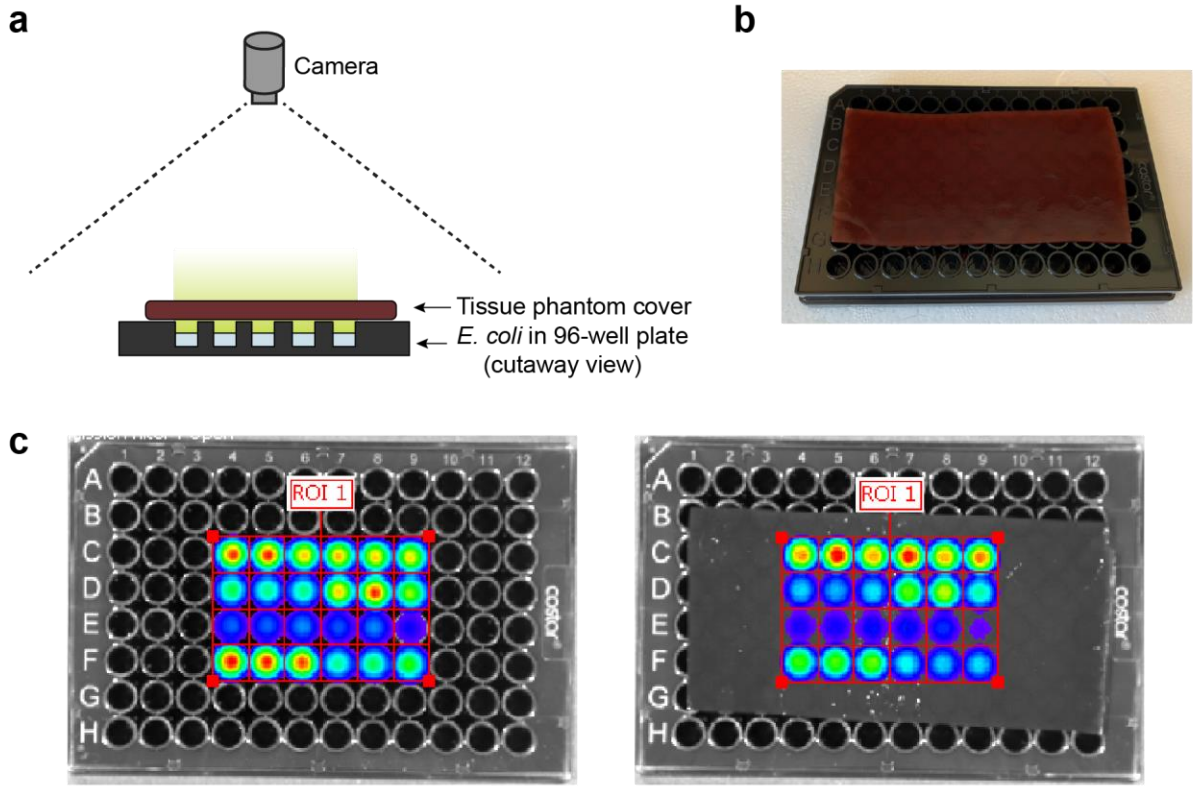

Figure 3.13 Tissue phantom imaging setup. (a) Schematic for imaging with a tissue phantom cover in the IVIS. (b) Representative photograph of plate covered with tissue phantom prior to imaging. (c) Representative images captured by the IVIS showing the ROI grids used for calculating total flux in each well.

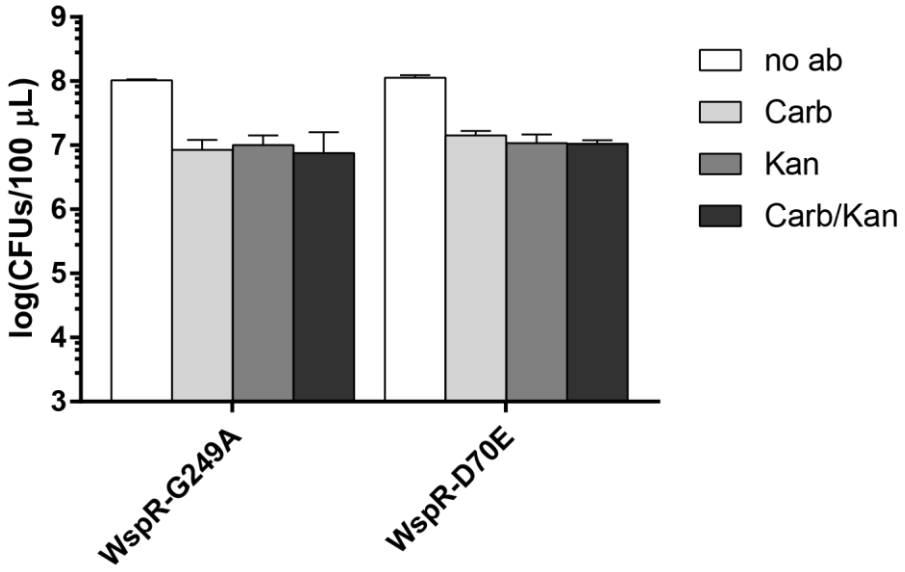

Figure 3.14 CFUs in live-cell measurements of c-di-GMP. CFUs measured for *E. coli* co-expressing the tVYN-NtΔ biosensor with WspR-G249A or WspR-D70E after overnight growth in auto-induction media. Data are from 2 biological replicates shown as the mean +/- SD.

MATERIALS AND METHODS

General reagents and oligonucleotides. Cyclic dinucleotides were purchased from Axxora, LLC. Coelenterazine-h was purchased from NanoLight Technologies and stored as a ~6.15 mM stock in EtOH at -80 °C. Oligonucleotides used in molecular cloning were purchased from Elim Biopharaceuticals or the University of Utah HSC Core facility.

Molecular cloning. The pNL(1.1) plasmid was obtained from Promega. Plasmids encoding PdeH, WspR alleles, and phylogenetic YcgR variants were previously available in the lab. The V-NLuc base scaffold was generated in the $pRSET_B$ plasmid using Gibson assembly (Gibson, 2011) with a pRSET-VenusΔC10 backbone and a NanoLuc insert amplified from pNL(1.1). The final vector was designed to contain a KpnI cut site between VenusΔC10 and NanoLuc and include an N-terminal His-tag. Base scaffolds were similarly generated in the pET21 plasmid containing a C-terminal His-tag. Biosensor constructs in $pRSET_B$ or pET21 were generated via Gibson assembly using KpnI digested base scaffolds and PCR amplified YcgR inserts. In general, pET24-YNL-YcgR biosensor plasmids previously generated in the lab (Dippel et al., 2018) were used as template for PCR amplification of YcgR sequences. Truncated biosensors (tVYN and YcgRΔ modifications) were created from the full-length scaffolds using 'Round-the-horn' mutagenesis and Gibson assembly, respectively. Venus circular permutations were created from the base V-NLuc scaffold via three-piece Gibson assembly ligations.

Protein purification. Biosensors were purified as described previously, with minor modifications (Dippel et al., 2018). Biosensors were purified from either the $pRSET_B$ or the pET21 plasmid after co-transforming the sensor plasmid and the pCOLA-PdeH plasmid in *E. coli* BL21 Star (DE3) cells (QB3 MacroLab). Transformants were cultured in 2xYT media at 37 ºC to OD ~ 1.0 and protein expression was induced for 20 h at 18 ºC with IPTG (0.1 mM IPTG for $pRSET_B$ plasmids or 0.5 mM IPTG for pET21 plasmids). Lysates were prepared and the biosensors were purified via Ni-NTA affinity chromatography as previously described (Dippel et al., 2018). Elution fractions were concentrated and dialyzed to storage buffer [50 mM HEPES (pH 7.2), 100 mM KCl, 10% (v/v) glycerol] using Amicon Ultra-15 Centrifugal Filter Units (10K MWCO; Millipore), and then flash frozen in liquid nitrogen and stored at -80 ºC. Final protein concentrations were determined using the absorption of Venus at 515 nm (extinction coefficient = 92200 M^{-1} cm^{-1}). All proteins were analyzed via SDS-PAGE to confirm purity.

Chemiluminescence measurements with purified protein. Briefly, proteins and ligands were prepared in opaque white 96-well LUMITRAC 600 plates (Grenier) in assay buffer [50 mM HEPES (pH 7.2), 100 mM KCl, 10 mM DTT, 0.1% BSA]. Unless otherwise noted, all measurements using purified protein were made using 3 nM sensor in 100 µL total reaction volume, then incubated at 28 ºC for at least 10 min to reach binding equilibrium. Chemiluminescent substrate was prepared by diluting coelenterazine-h to 60 µM in reagent buffer [50 mM HEPES (pH 7.2), 100 mM KCl, 300 mM ascorbate], and equilibrating the solution at RT for at least 30 min. Unless otherwise noted, all biosensor measurements were taken at 28 ºC in a SpectraMax i3x plate reader (Molecular Devices)

after manually adding 20 µL of chemiluminescent substrate. Emission intensities were measured at 460 and 530 nm for (200 ms integration) at 30 s intervals for 10 min after chemiluminescent substrate addition. In general, BRET ratios were calculated using emission values obtained 2 min after substrate addition. For emission spectrum measurements, emission intensities were measured over the range of 400-600 nm in steps of 2 nm.

Lysate-based assay for biosensor activity. The lysate-based assay was carried out as previously described, with minor modifications (Dippel et al., 2018). Single colonies of BL21 Star (DE3) *E. coli* cells co-transformed with pET21-biosensor and pCOLA-PdeH plasmids were resuspended in 500 µL of P-0.5G non-inducing media [0.5% glucose, 25 mM $(NH_4)_2SO_4$, 50 mM KH_2PO_4, 50 mM Na_2HPO_4, 1 mM $MgSO_4$] (Studier, 2005) supplemented with 50 µg/mL carbenicillin and 100 µg/mL kanamycin in 2.2 mL 96-well deep-well plates (VWR). Precultures were grown at 37 ºC, 340 rpm for 24 h at which point 5 µL of each was used to inoculate 500 µL of ZYP-5052 autoinduction media [25 mM $(NH_4)_2SO_4$, 50 mM KH_2PO_4, 50 mM Na_2HPO_4, 1 mM $MgSO_4$, 0.5% (v/v) glycerol, 0.05% glucose, 0.2% α-lactose, 1% tryptone, and 0.5% yeast extract] (Studier, 2005) supplemented with 50 µg/mL carbenicillin and 100 µg/mL kanamycin. Cultures were grown in ZYP-5052 autoinduction media at 37 ºC, 340 rpm for 20 h to express the biosensors, then harvested by centrifugation at 4700 rpm for 10 minutes at 4 ºC. Lysates were prepared by removing the supernatant media and resuspending cell pellets in 500 µL of screening buffer [50 mM Tris (pH 7.5), 100 mM KCl, 5% glycerol, 2 mM EDTA, 300 µg/mL lysozyme, 1 mM PMSF]. Cells were incubated for 1 h at 4 ºC to gently lyse, and total lysates were centrifuged for 40 min at 4700 rpm at 4 ºC to generate clarified lysates.

For chemiluminescence measurements, 5 µL of clarified lysate was mixed with 85 µL screening buffer (-lysozyme, -PMSF) and 10 µL of either buffer, 500 nM c-di-GMP, or 50 µM c-di-GMP [in screening buffer (-lysozyme, -PMSF)] in opaque white 96-well LUMITRAC 600 plates (Greiner) to generate final concentrations of 0, 50 nM, or 5 µM c-di-GMP. Chemiluminescence was measured using the same method described for purified protein, except BRET ratios were calculated using emission values obtained 1 min after substrate addition.

Live cell measurements with biosensor co-expression. Single colonies of of BL21 Star (DE3) *E. coli* cells co-transformed with pET21-biosensor and pCOLA-PdeH, pCOLA-WspR-G249A, or pCOLA-WspR-D70E plasmids were resuspended and grown in the same manner as previously described for the lysate-based assay. After growth in ZYP-5052 autoinduction media, cells were centrifuged, supernatant media was removed, and cell pellets were resuspended in 500 µL PBS [137 mM NaCl, 2.7 mM KCl, 10 mM Na_2HPO_4, 1.8 mM KH_2PO_4 (pH 7.4)]. For chemiluminescence measurements, cells were diluted 2-fold with PBS in an opaque 96-well LUMITRAC 600 plate (Greiner) to a final volume of 100 µL. Chemiluminescent substrate was added and emission intensities were measured in the same way as described for purified protein. BRET ratios were calculated using emission values obtained 5 min after substrate addition.

Live cell measurements in tissue-like phantom model. Tissue-like phantoms were prepared as described previously.(De Grand et al., 2006) Briefly, the phantom solution mixture was prepared with 10% gelatin, 170 µM bovine hemoglobin, and 1% intralipid in TBS-azide buffer [50 mM Tris-HCl (pH 7.4), 150 mM NaCl, 0.1% NaN_3]. Phantoms were poured to the desired thickness of 1.5 mm between glass plates to ensure uniformity, then stored at 4 °C.

Chemiluminescence measurements were carried out in a Xenogen IVIS 100 Bioluminescent Imager. Cells were grown and prepared in the same way as the live cell co-expression experiments but were diluted 2-fold, 200-fold, and 20,000-fold in PBS in opaque black 96-well assay plates (CoStar). To image the plates, 20 µL of chemiluminescent substrate was added to each well and plates were placed in the chamber. Luminescent images were captured sequentially using no filter, a 500 nm filter, and a 540 nm filter within a 13 cm field of view. The instrument was set to auto-adjust settings to ensure maximum signal for each image (exposure time of 0.5-60 s, binning of 1x-16x, f/stop of 1). For experiments with tissue-like phantoms, the wells were covered with a phantom immediately after addition of chemiluminescent substrate, and luminescent images were captured as before. For image analysis, a 12x8 ROI grid was applied to each image and used to calculate the flux (photons/s) for each individual well. For time course images, the same plate was repeatedly imaged for up to an hour after the initial addition of chemiluminescent substrate.

To determine the total number of bacterial cells in the IVIS experiments, cells co-expressing pET21-tVYN-NtΔ and pCOLA-WspR-G249A or pCOLA-WspR-D70E were grown as described above. After growth in ZYP-5052 autoinduction media, cells were centrifuged, supernatant media was removed, and cell pellets were resuspended in 500 µL PBS. Resuspended cultures were serially diluted (10^{-4}, 10^{-5}, 10^{-6}, and 10^{-7}) with PBS and 10 µL of each serial dilution was spotted on LB/Agar plates containing no antibiotics, 50 µg/mL carbenicillin, 50 µg/mL kanamycin, or 50 µg/mL of both carbenicillin and kanamycin. Each serial dilution was spotted in duplicate, and two biological replicates were used for each culture. Plates were incubated at 37 °C overnight, and colonies were counted to determine total CFUs/mL.

***Vibrio cholerae* strains and growth conditions.** *Vibrio cholerae* O1 El Tor A1552 was used as our wild-type strain and two *V. cholerae* strains, Δ6DGC (Townsley and Yildiz, 2015) and RΔ*vps*I-II (Fong et al., 2010), were used as reference strains with low and high cellular c-di-GMP level, respectively. Strains were grown in Luria–Bertani (LB) medium [1% tryptone, 0.5% yeast extract, 0.2 M NaCl; pH 7.5] with constant shaking at 200 rpm at 37^{o}C unless otherwise indicated.

To test the effects of salt concentration, LB supplemented with different concentrations of NaCl (0, 0.1, and 0.3M) were used (Shikuma et al., 2013). To test the effects of different growth temperature (Townsley and Yildiz, 2015) and oxygen availability, the diluted cultures were grown at 25 and 37 ^{o}C to OD_{600} ~0.5 or aerobically

and anaerobically (in a Vinyl Anaerobic Airlock Chamber, Coy Laboratory Products) to OD_{600} ~0.3.

To test the effects of bile (Hung et al., 2006), mucin (Silva et al., 2003), and iron-depleted conditions (Rogers et al., 2000), overnight-grown cultures were inoculated in a 1:200 dilution in LB supplemented with different components [0.4% (w/v) of bovine bile (Sigma-Aldrich), 0.4% (w/v) of bovine submaxillary gland mucin (Sigma-Aldrich), or 200 μM of 2,2'-dipyridyl (Alfa Aesar), respectively] and grown to OD_{600} ~0.5.

To test virulence-inducing conditions, overnight-grown cultures were inoculated in a 1:200 dilution in LB and in a 1:100 dilution in AKI [1.5% Bacto peptone, 0.4% yeast extract, 0.5% NaCl, 0.3% $NaHCO_3$]. LB cultures were grown overnight with shaking at 220 rpm at 37 ºC. AKI cultures were grown statically at 37ºC for 4 hours followed by shaking at 220 rpm at 37 ºC overnight (Iwanaga et al., 1986).

To test the effect of acidic conditions, overnight-grown cultures were inoculated in a 1:200 dilution in LB (pH 7), grown to OD_{600} ~0.5, and centrifuged at 1500 x g for 7 minutes. Cell pellets were adapted by resuspending in LB (pH 5.7) and incubating for 1 hour. Adapted cells were centrifugated and resuspended in LB (pH 4) followed by 1 hour incubation (Merrell et al., 2002).

Bacterial cell extract analysis. C-di-GMP extraction was performed as previously described with minor modification (Jones et al., 2015). Briefly, 1.5 mL of *V. cholerae* culture was centrifuged at 1500 x g for 7 minutes. Cell pellets were allowed to dry briefly then re-suspended in 1 mL extraction solution [40% acetonitrile, 40% methanol, 20% water], and incubated on ice for 5 minutes. Samples were centrifuged at 16,000 x g for 5 minutes and 900 μL of supernatant was dried under vacuum and lyophilized. Samples were re-suspended in 100 μL of ddH_2O and analyzed using the tVYN-TmΔ biosensor or liquid chromatography-tandem mass spectrometry (LC-MS/MS) to determine intracellular c-di-GMP levels. Each extract analysis was performed with three biological replicates.

For biosensor analysis, the re-suspended extracts were serially diluted with ddH_2O and 20 μL of serially diluted extract was mixed with 80 μL of biosensor and assay buffer in opaque white 96-well LUMITRAC 600 plates (Grenier) to give final concentrations of 3 nM biosensor and 1x assay buffer [50 mM HEPES (pH 7.2), 100 mM KCl, 10 mM DTT, 0.1% BSA]. Samples were incubated at 28 ºC for at least 10 min to reach binding equilibrium and chemiluminescence was measured as described for purified protein. BRET values were calculated using emission values obtained 5 minutes after substrate addition and each biosensor measurement was performed with two technical replicates. Mean BRET values that fell within the linear range of the biosensor (as determined by a standard curve with pure c-di-GMP) were used to calculate the total amount of c-di-GMP in each sample, and c-di-GMP amounts were normalized to total protein content.

For LC-MS/MS analysis, NaCl was added to the resuspended samples to a final concentration of 184 mM. Samples were analyzed via LC-MS/MS on a Thermo-Electron Finnigan LTQ mass spectrometer coupled to a surveyor HPLC (Thermo Scientific). The

Synergi Hydro 4u Fusion-RP 80A column (150 mm x 2.00 mm diameter; 4-µm particle size) (Phenomenex) was used for reverse-phase liquid chromatography. Solvent A was 0.1% acetic acid in 10 mM ammonium acetate, solvent B was 0.1% formic acid in methanol. The gradient used was as follows: time (t) = 0–4 minutes, 98% solvent A, 2% solvent B; t = 10–15 minutes, 5% solvent A, 95% solvent B. The injection volume was 20 µL and the flow rate for chromatography was 200 µL/minute.

The amount of c-di-GMP in samples was calculated with a standard curve generated from pure c-di-GMP suspended in 184 mM NaCl. Concentrations used for standard curve generation were 50 nM, 100 nM, 500 nM, 2 µM, 3.5 µM, 5 µM, 7.5 µM, and 10 µM. The assay is linear from 50 nM to 10 µM with an R2 of 0.999. C-di-GMP levels were normalized to total protein content in each culture.

To determine total protein content, 1.5 mL from each culture was pelleted, the supernatant was removed, and cells were lysed in 1 ml of 2% sodium dodecyl sulfate. Total protein in the samples was estimated with the BCA assay (Pierce) using bovine serum albumin (BSA) as standards.

TABLES

Table 3.1 Characteristics of selected VYN sensor variants

Notes: [a]Data are from 3 replicates represented as mean ± SD. [b]Affinity measurements were made using 300 pM biosensor to determine K_D values <3 nM. [c]Biosensor constructs were purified using an N-terminal His_6 tag, as opposed to a C-terminal His_6 tag for all others.

Sensor	*Δ ratio*[a]	*% change*[a]	*K_D (nM)*[a]	*Hill coefficient*[a]
tVYN-TmΔ[b, c]	–1.04	–56%	<0.3	–1.7 ± 0.03
tVYN-Tm[b]	–0.47	–50%	0.8 ± 0.03	–1.7 ± 0.1
VYN-Tm[b, c]	–0.67	–42%	0.8 ± 0.2	–1.5 ± 0.4
Vcp229-Tm[b]	–0.41	–44%	2.0 ± 0.1	–1.5 ± 0.1
VYN-Tb[c]	0.38	33%	8.0 ± 0.4	2.4 ± 0.3
tVYN-Tb	0.18	38%	12 ± 1	2.0 ± 0.3
Vcp229-Nt	0.22	52%	14 ± 1	1.6 ± 0.1
VYN-Nt[c]	0.39	45%	14 ± 4	1.4 ± 0.4
Vcp173-Nt	0.04	17%	17 ± 4	2.0 ± 0.7
tVYN-Nt	0.24	56%	20 ± 1	1.6 ± 0.2
VYN-Ec[c]	–0.58	–48%	50 ± 4	–1.5 ± 0.2
tVYN-NtΔ	–1.01	–51%	54 ± 4	–1.7 ± 0.1
Vcp157-Cp	–0.39	–33%	96 ± 6	–1.9 ± 0.2

Table 3.2 Amino acid sequences of biosensor plasmids

Notes: His-tag, VenusΔC10, NLuc, YcgR; phylogenetic biosensor variants use the same sequences, except the YcgR variant is used in place of TmYcgR (see Table S#); for tVYN and Vcp variants, the corresponding Venus and NLuc sequences were used in place of VenusΔC10 and NLuc (see Table S#)

pRSET-VYN	MRGSHHHHHHGMASMTGGQQMGRDLYDDDDKDPMVSKGEELFTGVVPILVELDGDVNGHKFSVS GEGEGDATYGKLTLKLICTTGKLPVPWPTLVTTLGYGLQCFARYPDHMKQHDFFKSAMPEGYVQ ERTIFFKDDGNYKTRAEVKFEGDTLVNRIELKGIDFKEDGNILGHKLEYNYNSHNVYITADKQK NGIKANFKIRHNIEDGGVQLADHYQQNTPIGDGPVLLPDNHYLSYQSKLSKDPNEKRDHMVLLE FVTAAGGTMVFTLEDFVGDWRQTAGYNLDQVLEQGGVSSLFQNLGVSVTPIQRIVLSGENGLKI DIHVIIPYEGLSGDQMGQIEKIFKVVYPVDDHHFKVILHYGTLVIDGVTPNMIDYFGRPYEGIA VFDGKKITVTGTLWNGNKIIDERLINPDGSLLFRVTINGVTGWRLCERILA*stop
pRSET-VYN-Tm	MRGSHHHHHHGMASMTGGQQMGRDLYDDDDKDPMVSKGEELFTGVVPILVELDGDVNGHKFSVS GEGEGDATYGKLTLKLICTTGKLPVPWPTLVTTLGYGLQCFARYPDHMKQHDFFKSAMPEGYVQ ERTIFFKDDGNYKTRAEVKFEGDTLVNRIELKGIDFKEDGNILGHKLEYNYNSHNVYITADKQK NGIKANFKIRHNIEDGGVQLADHYQQNTPIGDGPVLLPDNHYLSYQSKLSKDPNEKRDHMVLLE FVTAAGGTGMEYYTELVNAKDVIRPGQNVIVEVSAPEDLEGQYKSSVHDVDFEKRVLTLSMPSF RGRLVPLPRGTRCTVMILDSSAIYVFRTSVLESGRDEDGFPVTKVPFPGRLRKIQRRRFKRIKI FLEGTYRVASRDEPPKRFVTRDFSAGGMLMVVEDILTPEQIIYVTLDLDEDLKLKDHPARVVRE AGALETGERMYGVEFLNVPPALERKLVSFVFKKEIEMRNKERSESEGGTMVFTLEDFVGDWRQT AGYNLDQVLEQGGVSSLFQNLGVSVTPIQRIVLSGENGLKIDIHVIIPYEGLSGDQMGQIEKIF KVVYPVDDHHFKVILHYGTLVIDGVTPNMIDYFGRPYEGIAVFDGKKITVTGTLWNGNKIIDER LINPDGSLLFRVTINGVTGWRLCERILA*stop
pET21-VYN	MVSKGEELFTGVVPILVELDGDVNGHKFSVSGEGEGDATYGKLTLKLICTTGKLPVPWPTLVTT LGYGLQCFARYPDHMKQHDFFKSAMPEGYVQERTIFFKDDGNYKTRAEVKFEGDTLVNRIELKG IDFKEDGNILGHKLEYNYNSHNVYITADKQKNGIKANFKIRHNIEDGGVQLADHYQQNTPIGDG PVLLPDNHYLSYQSKLSKDPNEKRDHMVLLEFVTAAGGTMVFTLEDFVGDWRQTAGYNLDQVLE QGGVSSLFQNLGVSVTPIQRIVLSGENGLKIDIHVIIPYEGLSGDQMGQIEKIFKVVYPVDDHH FKVILHYGTLVIDGVTPNMIDYFGRPYEGIAVFDGKKITVTGTLWNGNKIIDERLINPDGSLLF RVTINGVTGWRLCERILAKLAAALEHHHHHH*stop
pET21-VYN-Tm	MVSKGEELFTGVVPILVELDGDVNGHKFSVSGEGEGDATYGKLTLKLICTTGKLPVPWPTLVTT LGYGLQCFARYPDHMKQHDFFKSAMPEGYVQERTIFFKDDGNYKTRAEVKFEGDTLVNRIELKG IDFKEDGNILGHKLEYNYNSHNVYITADKQKNGIKANFKIRHNIEDGGVQLADHYQQNTPIGDG PVLLPDNHYLSYQSKLSKDPNEKRDHMVLLEFVTAAGGTGMEYYTELVNAKDVIRPGQNVIVEV SAPEDLEGQYKSSVHDVDFEKRVLTLSMPSFRGRLVPLPRGTRCTVMILDSSAIYVFRTSVLES GRDEDGFPVTKVPFPGRLRKIQRRRFKRIKIFLEGTYRVASRDEPPKRFVTRDFSAGGMLMVVE DILTPEQIIYVTLDLDEDLKLKDHPARVVREAGALETGERMYGVEFLNVPPALERKLVSFVFKK EIEMRNKERSESEGGTMVFTLEDFVGDWRQTAGYNLDQVLEQGGVSSLFQNLGVSVTPIQRIVL SGENGLKIDIHVIIPYEGLSGDQMGQIEKIFKVVYPVDDHHFKVILHYGTLVIDGVTPNMIDYF GRPYEGIAVFDGKKITVTGTLWNGNKIIDERLINPDGSLLFRVTINGVTGWRLCERILAKLAAA LEHHHHHH*stop

Table 3.3 Amino acid sequences of YcgR proteins

Notes: Highlighted residues were removed for YcgRΔ variants

EcYcgR	MSHYHEQFLKQNPLAVLGVLRDLHKAAIPLRLSWNGGQLISKLLAITPDKLVLDFGSQAEDNIA VLKAQHITITAETQGAKVEFTVEQLQQSEYLQLPAFITVPPPTLWFVQRRRYFRISAPLHPPYF CQTKLADNSTLRFRLYDLSLGGMGALLETAKPAELQEGMRFAQIEVNMGQWGVFHFDAQLISIS ERKVIDGKNETITTPRLSFRFLNVSPTVERQLQRIIFSLEREAREKADKVRD
CpYcgR	MAKRKEPKVGDRGILRVREPGETGVEYYSTRIEDVRDGLIACSQPMRGQVYVKILSSPVELTYL KGDSVFSLMCEVIEQGKGDPPLIVLKPISGIYRSDRREYVRVPWMLDAELLFVKTFPADVKKFW EDHSHESVRAVILDLSAGGCRLSLAEACMVGEKVLIRFTVPEPNPDTFLLPALIKRVEPGSEPG VTNVGLQFVDVKDVIRDKLCRSVFCRQRELIKKGFYELEEE
TmYcgR	MEYYTELVNAKDVIRPGQNVIVEVSAPEDLEGQYKSSVHDVDFEKRVLTLSMPSFRGRLVPLPR GTRCTVMILDSSAIYVFRTSVLESGRDEDGFPVTKVPFPGRLRKIQRRRFKRIKIFLEGTYRVA SRDEPPKRFVTRDFSAGGMLMVVEDILTPEQIIYVTLDLDEDLKLKDHPARVVREAGALETGER MYGVEFLNVPPALERKLVSFVFKKEIEMRNKERSESE
NtYcgR	MLKIGLSIKIRVDNKDYSSRIEDMDSDYLYISTPMEKGQLVHFSQGSKISVYIIVKGAVYNFEE KIKEQIKSPVPLLKISKPDKLKKIQRRQFFRLEKKLPVKYKILDDDCESELSDTKDAYALDISG GGLKLATQEIIPVNSFLELNFELNIDEGKNSNIHDIRCVGKIVRTQKVDTDRVSIYHYGVKFIS LPSEIQDTIVRFIFNEQRKLRLKGRFSHAKRES
TbYcgR	MIKKEELKINQKVEVQIPDGSYKGNYSSRVEEIHPDGSIVLAAPFKRGVLIPLRKGDTVIVNFW GQTAGYSFTTAVLETNYQDVPMIRVAAPSTVRRIQRRNFVRVPAWIPLVFSVSSDSDDPSEKKI YRTETVNVSGGGLLIKSPFKLSEGVCLEMEIHLPKRGPVNARGQVVRVEEKREQSPMYLIGVAF TEIAETDRTKIINFVFEKQREMRQKGLI

Table 3.4 Amino acid sequences for tVYN and Vcp variants

Notes: For Vcp variants, an additional starting Met and an artificial linker (GGSGG) fusing the original N- and C- termini is added (added start codon, N-terminal portion, C-terminal portion)

Vcp50 N: (50-239) C: (1-49)	MTTGKLPVPWPTLVTTLGYGLQCFARYPDHMKQHDFFKSAMPEGYVQERTIFFKDDGNYKTRAE VKFEGDTLVNRIELKGIDFKEDGNILGHKLEYNYNSHNVYITADKQKNGIKANFKIRHNIEDGG VQLADHYQQNTPIGDGPVLLPDNHYLSYQSKLSKDPNEKRDHMVLLEFVTAAGITLGMDELYKG GSGGMVSKGEELFTGVVPILVELDGDVNGHKFSVSGEGEGDATYGKLTLKLIC
Vcp157 N: (157-239) C: (1-156)	MKQKNGIKANFKIRHNIEDGGVQLADHYQQNTPIGDGPVLLPDNHYLSYQSKLSKDPNEKRDHM VLLEFVTAAGITLGMDELYKGGSGGMVSKGEELFTGVVPILVELDGDVNGHKFSVSGEGEGDAT YGKLTLKLICTTGKLPVPWPTLVTTLGYGLQCFARYPDHMKQHDFFKSAMPEGYVQERTIFFKD DGNYKTRAEVKFEGDTLVNRIELKGIDFKEDGNILGHKLEYNYNSHNVYITAD
Vcp173 N: (173-239) C: (1-172)	MEDGGVQLADHYQQNTPIGDGPVLLPDNHYLSYQSKLSKDPNEKRDHMVLLEFVTAAGITLGMD ELYKGGSGGMVSKGEELFTGVVPILVELDGDVNGHKFSVSGEGEGDATYGKLTLKLICTTGKLP VPWPTLVTTLGYGLQCFARYPDHMKQHDFFKSAMPEGYVQERTIFFKDDGNYKTRAEVKFEGDT LVNRIELKGIDFKEDGNILGHKLEYNYNSHNVYITADKQKNGIKANFKIRHNI
Vcp195 N: (195-239) C: (1-194)	MLLPDNHYLSYQSKLSKDPNEKRDHMVLLEFVTAAGITLGMDELYKGGSGGMVSKGEELFTGVV PILVELDGDVNGHKFSVSGEGEGDATYGKLTLKLICTTGKLPVPWPTLVTTLGYGLQCFARYPD HMKQHDFFKSAMPEGYVQERTIFFKDDGNYKTRAEVKFEGDTLVNRIELKGIDFKEDGNILGHK LEYNYNSHNVYITADKQKNGIKANFKIRHNIEDGGVQLADHYQQNTPIGDGPV
Vcp229 N: (229-239) C: (1-228)	MGITLGMDELYKGGSGGMVSKGEELFTGVVPILVELDGDVNGHKFSVSGEGEGDATYGKLTLKL ICTTGKLPVPWPTLVTTLGYGLQCFARYPDHMKQHDFFKSAMPEGYVQERTIFFKDDGNYKTRA EVKFEGDTLVNRIELKGIDFKEDGNILGHKLEYNYNSHNVYITADKQKNGIKANFKIRHNIEDG GVQLADHYQQNTPIGDGPVLLPDNHYLSYQSKLSKDPNEKRDHMVLLEFVTAA
VenusΔC12	MVSKGEELFTGVVPILVELDGDVNGHKFSVSGEGEGDATYGKLTLKLICTTGKLPVPWPTLVTT LGYGLQCFARYPDHMKQHDFFKSAMPEGYVQERTIFFKDDGNYKTRAEVKFEGDTLVNRIELKG IDFKEDGNILGHKLEYNYNSHNVYITADKQKNGIKANFKIRHNIEDGGVQLADHYQQNTPIGDG PVLLPDNHYLSYQSKLSKDPNEKRDHMVLLEFVTA
NLucΔN4	LEDFVGDWRQTAGYNLDQVLEQGGVSSLFQNLGVSVTPIQRIVLSGENGLKIDIHVIIPYEGLS GDQMGQIEKIFKVVYPVDDHHFKVILHYGTLVIDGVTPNMIDYFGRPYEGIAVFDGKKITVTGT LWNGNKIIDERLINPDGSLLFRVTINGVTGWRLCERILA

Table 3.5 Oligonucleotides used in this study

Name	Sequence
REV-Venus-Nluc-vector	CCAGTCCCCAACGAAATCTTCGAGTGTGAAGACCATggtaccCCCGGCGG
FWD-Venus-Nluc-insert	GTTCGTGACCGCCGCCGGGggtaccATGGTCTTCACACTCGAAGATTTCG
FWD-Venus-Nluc-vector	CGGCTGTGCGAACGCATTCTGGCGTAAgAATTCGAAGCTTGATCCGGCTG
REV-Venus-Nluc-insert	TTGTTAGCAGCCGGATCAAGCTTCGAATTcTTACGCCAGAATGCGTTCGC
REV-VYN-YcgR-vector	ttcaggaactgctcatggtaatgactCATccatggCCCGGCGGCGGTCAC
FWD-VYN-YcgR-insert	TCGTGACCGCCGCCGGGccatggATGagtcattaccatgagcagttcctg
REV-VYN-YcgR-insert	ACGAAATCTTCGAGTGTGAAGACCATgagctcgtcgcgcactttgtccgc
FWD-VYN-YcgR-vector	ggacaaagtgcgcgacgagctcATGGTCTTCACACTCGAAGATTTCGTTG
FWD-TmYcgR-VYN-insert	TGACCGCCGCCGGGggtacaggtATGGAATATTATACCGAACTGGTGAAC
REV-TmYcgR-VYN-insert	AAATCTTCGAGTGTGAAGACCATggtaccaccTTCGCTTTCGCTGCGTTC
FWD-CpYcgR-VYN-insert	GAGTTCGTGACCGCCGCCGGGggtacaggtATGGCGAAACGCAAAGAACC
REV-CpYcgR-VYN-insert	CGAGTGTGAAGACCATggtaccaccTTCTTCTTCCAGTTCATAAAAGCCT
FWD-TbYcgR-VYN-insert	CGCCGCCGGGggtacaggtATGATTAAAAAAGAAGAACTGAAAATTAACC
REV-TbYcgR-VYN-insert	AAATCTTCGAGTGTGAAGACCATggtaccaccAATCAGGCCTTTCTGGCG
FWD-VYN-Nt-YcgR-insert	GCCGCCGGGggtacaggtATGCTGAAAATTGGCCTGAGCATTAAAATTCG
REV-VYN-Nt-YcgR-insert	GAGTGTGAAGACCATggtaccaccagATTCGCGTTTCGCATGGCTAAAGC
FWD-tVYN-rth	CTCGAAGATTTCGTTGGGGACTG
REV-tVYN-rth	GGTaccGGCGGTCACGAACTCCA
FWD-tVYN-TmYcgR delta flex	CTGCTGGAGTTCGTGACCGCCGGTACaggtTATACCGAACTGGTGAACGC
REV-tVYN-TmYcgR delta flex	CCAACGAAATCTTCGAGggtaccaccTTCTTTGTTGCGCATTTCAATTTC
FWD-Venus-pET21 insert	TGTTTAACTTTAAGAAGGAGATATACATATGATGGTGAGCAAGGGCGAGG
REV-Nluc-pET21 insert	GTGCGGCCGCAAGCTTCGCCAGAATGCGT
REV-Nluc-pET21 insert 2	CGGCCGCAAGCTTCGCCAGAATGCGTTCGC
FWD-Tm-Nluc insert	AAGAAGGAGATATACATATGggtacaggtATGGAATATTATACCGAACTG
FWD-Venus-pET21 RTH	ATGGACGAGCTGTACAAGAAGCTTGCGGCCGCACTC
REV-Venus-pET21 RTH	GCCGAGAGTGATCCCGGCGGCGGTCAC
FWD-Tm-Nluc-RTH	ATGGAATATTATACCGAACTGGTGAAC
REV-Tm-Nluc-RTH	ATGTATATCTCCTTCTTAAAGTTAAACAAAATTATTTC
FWD-cp-linker	GGTGGTTCCGGTGGTATGGTGAGCAAGGGCGAGG
REV-cp-linker	ACCACCGGAACCACCCTTGTACAGCTCGTCCATGCC
FWD-vcp50	GTTTAACTTTAAGAAGGAGATATACATATGACCACCGGCAAGCTGCC
REV-vcp50	CCAGTTCGGTATAATATTCCATacctgtaccGCAGATCAGCTTCAGGGTCAGC
FWD-vcp157	GTTTAACTTTAAGAAGGAGATATACATATGAAGCAGAAGAACGGCATCAAGG
REV-vcp157	CCAGTTCGGTATAATATTCCATacctgtaccGTCGGCGGTGATATAGACGTTG

FWD-vcp173	GTTTAACTTTAAGAAGGAGATATACATATGGAGGACGGCGGCGTG
REV-vcp173	CCAGTTCGGTATAATATTCCATacctgtaccGATGTTGTGGCGGATCTTGAAG
FWD-vcp195	GTTTAACTTTAAGAAGGAGATATACATATGCTGCTGCCCGACAACCAC
REV-vcp195	CCAGTTCGGTATAATATTCCATacctgtaccCACGGGGCCGTCGC
FWD-vcp229	GTTTAACTTTAAGAAGGAGATATACATATGGGGATCACTCTCGGCATGG
REV-vcp229	CCAGTTCGGTATAATATTCCATacctgtaccGGCGGCGGTCACGAACTC
REV-Nluc-HisTag	CATAAGCTTCGCCAGAATGCGTTCGCA
FWD-vcp-Nluc	AAGCTGATCTGCggtaccATGGTCTTCACACTCGAAGATTTCG
REV-vcp50-Nluc	CGAGTGTGAAGACCATggtaccGCAGATCAGCTTCAGGGTCAGC
REV-vcp157-Nluc	TGTGAAGACCATggtaccGTCGGCGGTGATATAGACGTTGTGG
REV-vcp173-Nluc	GAGTGTGAAGACCATggtaccGATGTTGTGGCGGATCTTGAAG
REV-vcp195-Nluc	GAAATCTTCGAGTGTGAAGACCATggtaccCACGGGGCCGTCGC
REV-vcp229-Nluc	TTCGAGTGTGAAGACCATggtaccGGCGGCGGTCACGAACTC
REV-VYN-Histag	ATCTTCGAGTGTGAAGACCATggtaccCCCGGCGGCGGTCAC
FWD-Ec-no vcp	GCCGCCGGGggtacaggtATGagtcattaccatgagcagttc
FWD-Ec-vcp50	CCTGAAGCTGATCTGCggtacaggtATGagtcattaccatgagcagttc
FWD-Ec-vcp157	CTATATCACCGCCGACggtacaggtATGagtcattaccatgagcagttc
FWD-Ec-vcp173	TCCGCCACAACATCggtacaggtATGagtcattaccatgagcagttc
FWD-Ec-vcp195	ACGGCCCGTGggtacaggtATGagtcattaccatgagcagttc
FWD-Ec-vcp229	GACCGCCGCCggtacaggtATGagtcattaccatgagcagttc
REV-Ec-vcp	TCGAGTGTGAAGACCATggtaccaccgtcgcgcactttgtccg
FWD-Nt-no vcp	GCCGCCGGGggtacaggtATGCTGAAAATTGGCCTGAG
FWD-Nt-vcp50	CCTGAAGCTGATCTGCggtacaggtATGCTGAAAATTGGCCTGAG
FWD-Nt-vcp157	CTATATCACCGCCGACggtacaggtATGCTGAAAATTGGCCTGAG
FWD-Nt-vcp173	TCCGCCACAACATCggtacaggtATGCTGAAAATTGGCCTGAG
FWD-Nt-vcp195	ACGGCCCCGTGggtacaggtATGCTGAAAATTGGCCTGAG
FWD-Nt-vcp229	GACCGCCGCCggtacaggtATGCTGAAAATTGGCCTGAG
REV-Nt-vcp	TCGAGTGTGAAGACCATggtaccaccTTCGCGTTTCGCATGG
FWD-Tb-no vcp	GCCGCCGGGggtacaggtATGATTAAAAAAGAAGAACTGAAAATTAACC
FWD-Tb-vcp50	TGAAGCTGATCTGCggtacaggtATGATTAAAAAAGAAGAACTGAAAATTAACC
FWD-Tb-vcp157	CACCGCCGACggtacaggtATGATTAAAAAAGAAGAACTGAAAATTAACC
FWD-Tb-vcp173	CCACAACATCggtacaggtATGATTAAAAAAGAAGAACTGAAAATTAACC
FWD-Tb-vcp195	CGGCCCCGTGggtacaggtATGATTAAAAAAGAAGAACTGAAAATTAACC
FWD-Tb-vcp229	GACCGCCGCCggtacaggtATGATTAAAAAAGAAGAACTGAAAATTAACC
REV-Tb-vcp	TCGAGTGTGAAGACCATggtaccaccAATCAGGCCTTTCTGGCG
FWD-Cp-no vcp	GCCGCCGGGggtacaggtATGGCGAAACGCAAAGAAC
FWD-Cp-vcp50	CCTGAAGCTGATCTGCggtacaggtATGGCGAAACGCAAAGAAC
FWD-Cp-vcp157	CTATATCACCGCCGACggtacaggtATGGCGAAACGCAAAGAAC
FWD-Cp-vcp173	TCCGCCACAACATCggtacaggtATGGCGAAACGCAAAGAAC

FWD-Cp-vcp195	ACGGCCCCGTGggtacaggtATGGCGAAACGCAAAGAAC
FWD-Cp-vcp229	GACCGCCGCCggtacaggtATGGCGAAACGCAAAGAAC
REV-Cp-vcp	TCGAGTGTGAAGACCATggtaccaccTTCTTCTTCCAGTTCATAAAAGCC
FWD-VYN-His tag	TGTTTAACTTTAAGAAGGAGATATACATATGGTGAGCAAGGGCGAG
REV-VYN-His tag 2	GTGCGGCCGCAAGCTTCGCCAGAATGCGTTCGC
REV-Nt-VYN insert	GTGAAGACCATggtaccaccAGATTCGCGTTTCGCATG
FWD-tVYN Nt-insert	GACCGCCGGTACaggtATGCTGAAAATTGGCCTGAG
REV-tVYN Nt-insert	CGAAATCTTCGAGggtaccaccAGATTCGCGTTTCGCATG
FWD-tVYN Tb-insert	GTGACCGCCGGTACaggtATGATTAAAAAAGAAGAACTGAAAATTAACC
REV-tVYN Tb-insert	CAACGAAATCTTCGAGggtaccaccAATCAGGCCTTTCTGGCG
FWD-Nt delta-VYN insert	CCGCCGGGggtacaggtAGCATTAAAATTCGCGTGG
REV-Nt delta-VYN insert	TCGAGTGTGAAGACCATggtaccaccCAGGCGCAGTTTGCG
FWD-Tb delta-VYN insert	GCCGCCGGGggtacaggtAAAGTGGAAGTGCAGATTCCG
REV-Tb delta-VYN insert	TCGAGTGTGAAGACCATggtaccaccCTGGCGCATTTCGCG
FWD-Tm delta-vcp229	GACCGCCGCCggtacaggtTATACCGAACTGGTGAACGCG
REV-Tm delta-vcp229	GAGTGTGAAGACCATggtaccaccTTCTTTGTTGCGCATTTCAATTTC
FWD-Nt delta-vcp229	GACCGCCGCCggtacaggtAGCATTAAAATTCGCGTGGATAAC
REV-Nt delta-vcp229	CGAGTGTGAAGACCATggtaccaccCAGGCGCAGTTTGCG
FWD-Tb delta-vcp229	GACCGCCGCCggtacaggtAAAGTGGAAGTGCAGATTCCG
REV-Tb delta-vcp229	CGAGTGTGAAGACCATggtaccaccCTGGCGCATTTCGCG
FWD-Nt delta-vcp173	CCGCCACAACATCggtacaggtAGCATTAAAATTCGCGTGGATAAC
FWD-Nt delta-tVYN insert	CGTGACCGCCGGTACaggtAGCATTAAAATTCGCGTGG
REV-Nt delta-tVYN insert	CCAACGAAATCTTCGAGggtaccaccCAGGCGCAGTTTGCG
FWD-Tb delta-tVYN insert	TCGTGACCGCCGGTACaggtAAAGTGGAAGTGCAGATTCCG
REV-Tb delta-tVYN insert	CAACGAAATCTTCGAGggtaccaccCTGGCGCATTTCGCG
FWD-Tm delta-tVYN insert	TCGTGACCGCCGGTACaggtTATACCGAACTGGTGAACGC
REV-Tm delta-tVYN insert	CAACGAAATCTTCGAGggtaccaccTTCTTTGTTGCGCATTTCAATTTC
FWD-tVYN Tm-insert	TTCGTGACCGCCGGTACaggtATGGAATATTATACCGAACTGGTGAAC
REV-tVYN Tm-insert	CAACGAAATCTTCGAGggtaccaccTTCGCTTTCGCTGCGTTC
FWD-Tm delta-VYN insert	GCCGCCGGGggtacaggtTATACCGAACTGGTGAACGCG
REV-Tm delta-VYN insert	TCGAGTGTGAAGACCATggtaccaccTTCTTTGTTGCGCATTTCAATTTC

REFERENCES

Aper, S.J.A., Dierickx, P., and Merkx, M. (2016). Dual readout BRET/FRET-sensors for measuring intracellular zinc. ACS Chem. Biol.

Benach, J., Swaminathan, S.S., Tamayo, R., Handelman, S.K., Folta-Stogniew, E., Ramos, J.E., Forouhar, F., Neely, H., Seetharaman, J., Camilli, A., et al. (2007). The structural basis of cyclic diguanylate signal transduction by PilZ domains. EMBO J. *26*, 5153–5166.

Burhenne, H., and Kaever, V. (2013). Quantification of Cyclic Dinucleotides by Reversed-Phase LC-MS/MS. In Methods in Molecular Biology, pp. 27–37.

Caine, E.A., and Osorio, J.E. (2017). In Vivo Imaging with Bioluminescent Enterovirus 71 Allows for Real-Time Visualization of Tissue Tropism and Viral Spread . J. Virol. *91*, 1–16.

Christen, M., Kulasekara, H.D., Christen, B., Kulasekara, B.R., Hoffman, L.R., and Miller, S.I. (2010). Asymmetrical distribution of the second messenger c-di-GMP upon bacterial cell division. Science *328*, 1295–1297.

Chu, J., Oh, Y., Sens, A., Ataie, N., Dana, H., Macklin, J.J., Laviv, T., Welf, E.S., Dean, K.M., Zhang, F., et al. (2016). A bright cyan-excitable orange fluorescent protein facilitates dual-emission microscopy and enhances bioluminescence imaging in vivo. Nat. Biotechnol. *34*, 760–767.

Deuschle, K., Okumoto, S., Fehr, M., Looger, L.L., Kozhukh, L., and Frommer, W.B. (2005). Construction and optimization of a family of genetically encoded metabolite sensors by semirational protein engineering. Protein Sci. *14*, 2304–2314.

Dippel, A.B., Anderson, W.A., Evans, R.S., Deutsch, S., and Hammond, M.C. (2018). Chemiluminescent Biosensors for Detection of Second Messenger Cyclic di-GMP. ACS Chem. Biol. *13*, 1872–1879.

Fong, J.C.N., Syed, K.A., Klose, K.E., and Yildiz, F.H. (2010). Role of Vibrio polysaccharide (vps) genes in VPS production, biofilm formation and Vibrio cholerae pathogenesis. Microbiology *156*, 2757–2769.

Gibson, D.G. (2011). Enzymatic assembly of overlapping DNA fragments. Methods Enzymol. *498*, 349–361.

De Grand, A.M., Lomnes, S.J., Lee, D.S., Pietrzykowski, M., Ohnishi, S., Morgan, T.G., Gogbashian, A., Laurence, R.G., and Frangioni, J. V. (2006). Tissue-like phantoms for near-infrared fluorescence imaging system assessment and the training of surgeons. J. Biomed. Opt. *11*, 014007.

Hall, C.L., and Lee, V.T. (2018). Cyclic-di-GMP regulation of virulence in bacterial pathogens. Wiley Interdiscip. Rev. RNA *9*, 1–19.

Hall, M.P., Unch, J., Binkowski, B.F., Valley, M.P., Butler, B.L., Wood, M.G., Otto, P., Zimmerman, K., Vidugiris, G., MacHleidt, T., et al. (2012). Engineered luciferase reporter from a deep sea shrimp utilizing a novel imidazopyrazinone substrate. ACS

Chem. Biol. *7*, 1848–1857.

Ho, C.L., Chong, K.S.J., Oppong, J.A., Chuah, M.L.C., Tan, S.M., and Liang, Z.X. (2013). Visualizing the perturbation of cellular cyclic di-GMP levels in bacterial cells. J. Am. Chem. Soc. *135*, 566–569.

Hung, D.T., Zhu, J., Sturtevant, D., and Mekalanos, J.J. (2006). Bile acids stimulate biofilm formation in Vibrio cholerae. Mol. Microbiol. *59*, 193–201.

Inagaki, S., Tsutsui, H., Suzuki, K., Agetsuma, M., Arai, Y., Jinno, Y., Bai, G., Daniels, M.J., Okamura, Y., Matsuda, T., et al. (2017). Genetically encoded bioluminescent voltage indicator for multi-purpose use in wide range of bioimaging. Sci. Rep. *7*, 1–11.

Iwanaga, M., Yamamoto, K., Higa, N., Ichinose, Y., Nakasone, N., and Tanabe, M. (1986). Culture Conditions for Stimulating Cholera Toxin Production by Vibrio cholerae 01 El Tor. Microbiol. Immunol. *30*, 1075–1083.

Jenal, U., Reinders, A., and Lori, C. (2017). Cyclic di-GMP: Second messenger extraordinaire. Nat. Rev. Microbiol. *15*, 271–284.

Johnsson, K., Yu, Q., Binz, P.-A., Fabritz, S., Roux, C., Xue, L., Griss, R., Haas, D., Hiblot, J., and Okun, J.G. (2018). Semisynthetic sensor proteins enable metabolic assays at the point of care. Science *361*, 1122–1126.

Jones, C.J., Utada, A., Davis, K.R., Thongsomboon, W., Zamorano Sanchez, D., Banakar, V., Cegelski, L., Wong, G.C.L., and Yildiz, F.H. (2015). C-di-GMP Regulates Motile to Sessile Transition by Modulating MshA Pili Biogenesis and Near-Surface Motility Behavior in Vibrio cholerae. PLoS Pathog. *11*, 1–27.

Ko, J., Ryu, K.S., Kim, H., Shin, J.S., Lee, J.O., Cheong, C., and Choi, B.S. (2010). Structure of PP4397 reveals the molecular basis for different c-di-GMP binding modes by pilz domain proteins. J. Mol. Biol. *398*, 97–110.

Merrell, D.S., Hava, D.L., and Camilli, A. (2002). Identification of novel factors involved in colonization and acid tolerance of Vibrio cholerae. Mol. Microbiol. *43*, 1471–1491.

Nagai, T., Yamada, S., Tominaga, T., Ichikawa, M., and Miyawaki, A. (2004). Expanded dynamic range of fluorescent indicators for Ca2+ by circularly permuted yellow fluorescent proteins. Proc. Natl. Acad. Sci. *101*, 10554–10559.

O'Toole, G., Pratt, L., Watnick, P., Newman, D., Weaver, V., and Kolter, R. (1999). Genetic Approaches to Study of Biofilms. Methods Enzymol. *310*, 91–109.

Opoku-Temeng, C., Zhou, J., Zheng, Y., Su, J., and Sintim, H.O. (2016). Cyclic dinucleotide (c-di-GMP, c-di-AMP, and cGAMP) signalings have come of age to be inhibited by small molecules. Chem. Commun. *52*, 9327–9342.

Petrova, O.E., and Sauer, K. (2017). High-Performance Liquid Chromatography (HPLC)-Based Detection and Quantitation of Cellular c-di-GMP. In Methods in Molecular Biology, pp. 33–43.

Povolotsky, T.L., and Hengge, R. (2016). Genome-based comparison of cyclic di-GMP

signaling in pathogenic and commensal Escherichia coli strains. J. Bacteriol. *198*, 111–126.

Pultz, I.S., Christen, M., Kulasekara, H.D., Kennard, A., Kulasekara, B., and Miller, S.I. (2012). The response threshold of Salmonella PilZ domain proteins is determined by their binding affinities for c-di-GMP. Mol. Microbiol. *86*, 1424–1440.

Purcell, E.B., McKee, R.W., McBride, S.M., Waters, C.M., and Tamayo, R. (2012). Cyclic diguanylate inversely regulates motility and aggregation in clostridium difficile. J. Bacteriol. *194*, 3307–3316.

Richter, A.M., Povolotsky, T.L., Wieler, L.H., and Hengge, R. (2014). Cyclic-di-GMP signalling and biofilm-related properties of the Shiga toxin-producing 2011 German outbreak Escherichia coli O104:H4. EMBO Mol. Med. *6*, 1622–1637.

Rogers, M.B., Sexton, J.A., DeCastro, G.J., and Calderwood, S.B. (2000). Identification of an operon required for ferrichrome iron utilization in Vibrio cholerae. J. Bacteriol. *182*, 2350–2353.

Romling, U., Galperin, M.Y., and Gomelsky, M. (2013). Cyclic di-GMP: the first 25 years of a universal bacterial second messenger. Microbiol. Mol. Biol. Rev. *77*, 1–52.

van Rosmalen, M., Krom, M., and Merkx, M. (2017). Tuning the Flexibility of Glycine-Serine Linkers To Allow Rational Design of Multidomain Proteins. Biochemistry *56*, 6565–6574.

Ross, P., Weinhouse, H., Aloni, Y., Michaeli, D., Weinberger-Ohana, P., Mayer, R., Braun, S., de Vroom, E., van der Marel, G.A., van Boom, J.H., et al. (1987). Regulation of cellulose synthesis in Acetobacter xylinum by cyclic diguanylic acid. Nature *325*, 279–281.

Ryjenkov, D.A., Simm, R., Römling, U., and Gomelsky, M. (2006). The PilZ domain is a receptor for the second messenger c-di-GMP: The PilZ domain protein YcgR controls motility in enterobacteria. J. Biol. Chem. *281*, 30310–30314.

Saito, K., Chang, Y.-F., Horikawa, K., Hatsugai, N., Higuchi, Y., Hashida, M., Yoshida, Y., Matsuda, T., Arai, Y., and Nagai, T. (2012). Luminescent proteins for high-speed single-cell and whole-body imaging. Nat. Commun. *3*, 1262.

Sambanthamoorthy, K., Sloup, R.E., Parashar, V., Smith, J.M., Kim, E.E., Semmelhack, M.F., Neiditch, M.B., and Waters, C.M. (2012). Identification of Small Molecules That Antagonize Diguanylate Cyclase Enzymes To Inhibit Biofilm Formation. Antimicrob. Agents Chemother. *56*, 5202–5211.

Shikuma, N.J., Davis, K.R., Fong, J.N.C., and Yildiz, F.H. (2013). The transcriptional regulator, CosR, controls compatible solute biosynthesis and transport, motility and biofilm formation in Vibrio cholerae. Environ. Microbiol. *15*, 1387–1399.

Silberstein, E., Serna, C., Fragoso, S.P., Nagarkatti, R., and Debrabant, A. (2018). A novel nanoluciferase-based system to monitor Trypanosoma cruzi infection in mice by bioluminescence imaging. PLoS One *13*, 1–21.

Silva, A.J., Pham, K., and Benitez, J.A. (2003). Haemagglutinin/protease expression and mucin gel penetration in El Tor biotype Vibrio cholerae. Microbiology *149*, 1883–1891.

Spangler, C., Böhm, A., Jenal, U., Seifert, R., and Kaever, V. (2010). A liquid chromatography-coupled tandem mass spectrometry method for quantitation of cyclic di-guanosine monophosphate. J. Microbiol. Methods *81*, 226–231.

Studier, F.W. (2005). Protein production by auto-induction in high-density shaking cultures. Protein Expr. Purif. *41*, 207–234.

Su, Y., Hickey, S.F., Keyser, S.G.L., and Hammond, M.C. (2016). In Vitro and in Vivo Enzyme Activity Screening via RNA-Based Fluorescent Biosensors for S-Adenosyl- l -homocysteine (SAH). J. Am. Chem. Soc. *138*, 7040–7047.

Sun, C., Gardner, C.L., Watson, A.M., Ryman, K.D., and Klimstra, W.B. (2014). Stable, High-Level Expression of Reporter Proteins from Improved Alphavirus Expression Vectors To Track Replication and Dissemination during Encephalitic and Arthritogenic Disease. J. Virol. *88*, 2035–2046.

Suzuki, K., Kimura, T., Shinoda, H., Bai, G., Daniels, M.J., Arai, Y., Nakano, M., and Nagai, T. (2016). Five colour variants of bright luminescent protein for real-time multicolour bioimaging. Nat. Commun. *7*, 13718.

Tamayo, R., Patimalla, B., and Camilli, A. (2010). Growth in a biofilm induces a hyperinfectious phenotype in Vibrio cholerae. Infect. Immun. *78*, 3560–3569.

Townsley, L., and Yildiz, F.H. (2015). Temperature affects c-di-GMP signalling and biofilm formation in Vibrio cholerae. Environ. Microbiol. *17*, 4290–4305.

Tran, V., Moser, L.A., Poole, D.S., and Mehle, A. (2013). Highly Sensitive Real-Time In Vivo Imaging of an Influenza Reporter Virus Reveals Dynamics of Replication and Spread. J. Virol. *87*, 13321–13329.

Wang, X.C., Wilson, S.C., and Hammond, M.C. (2016). Next-generation fluorescent RNA biosensors enable anaerobic detection of cyclic di-GMP. Nucleic Acids Res. *44*, e139.

Wolfe, A.J., and Berg, H.C. (1989). Migration of bacteria in semisolid agar. Proc. Natl. Acad. Sci. *86*, 6973–6977.

Yang, J., Cumberbatch, D., Centanni, S., Shi, S., Winder, D., Webb, D., and Johnson, C.H. (2016). Coupling optogenetic stimulation with NanoLuc-based luminescence (BRET) Ca++ sensing. Nat. Commun. *7*, 13268.

Yeo, J., Dippel, A.B., Wang, X.C., and Hammond, M.C. (2017). In Vivo Biochemistry: Single-cell dynamics of cyclic di-GMP in E. coli in response to zinc overload. Biochemistry *57*, 108–116.

Chapter Four

Directed evolution of cGAMP-binding proteins

Portions of this chapter have been published in:

Dippel, A. B. and Hammond, M. C. (2019). A Poxin on Both of Your Houses: Poxviruses Degrade the Immune Signal cGAMP.” Biochemistry *58*, 2387-2388.

INTRODUCTION

It has long been known that cytosolic DNA serves as a potent immune stimulant, however it was only recently discovered that this response occurs through the activation of cyclic GMP-AMP synthase (cGAS) and production of the cyclic dinucleotide second messenger 2',3'-cyclic GMP-AMP ((2'3')-cGAMP) (Ablasser et al., 2013; Diner et al., 2013; Gao et al., 2013). Low nanomolar levels of (2'3')-cGAMP can bind to and activate the stimulator of interferon genes (STING) receptor, which initiates interferon (IFN) and NF-kB immune responses (Chen et al., 2016). In this way, the presence of any aberrant cytosolic dsDNA, whether it is host-derived (from nuclear or mitochondrial leakage) or pathogen-derived (from DNA viruses, retroviruses, or bacteria) triggers the innate immune response. Many recent studies have raised interesting questions about the dynamics and localization of cGAS-STING signaling in response to infection and other pathophysiological conditions (Eaglesham et al., 2019; Yoh et al., 2015). Given its central role in innate immune signaling, the cGAS-cGAMP-STING pathway has rapidly become an attractive target for the development of cancer immunotherapy and autoimmune disease treatments (Corrales et al., 2015; Ramanjulu et al., 2018).

Despite the deluge of studies seeking to further understand the basic biology of the cGAS-cGAMP-STING signaling pathway, to our knowledge there are no tools currently available that permit the imaging of (2'3')-cGAMP dynamics within live eukaryotic cells. Instead, luciferase reporters are commonly used that provide a luminescent readout based on the activation of STING and downstream production of IFN-β (Burdette et al., 2011; Kranzusch et al., 2013). The luciferase gene is placed under the control of an IFN-β promoter such that increased production of IFN-β leads to an increase in the production of luciferase. While these reporters have proven useful for fundamental studies of (2'3')-cGAMP signaling, they provide only an indirect measurement of (2'3')-cGAMP levels, are not quantitative, and do not report on the intracellular dynamics of (2'3')-cGAMP. Given the high interest of the cGAS-cGAMP-STING pathways as a drug target, we and others have also developed *in vitro* analytical tools that are amenable to high throughput screening of compounds that modulate the cGAS-cGAMP-STING pathway. These techniques include the RNA-based fluorescent biosensor developed by our lab (Bose et al., 2016), a RapidFire mass-spec-based assay (Vincent et al., 2017), a fluorescence polarization/antibody assay (Hepworth et al., 2017), and more recently a luminescence assay based on ATP substrate consumption (Lama et al., 2019). Based on our expertise with developing Nano-lantern (NL) type biosensors for c-di-GMP, we sought to develop a protein-based luminescent biosensor for (2'3')-cGAMP that we hoped would be useful as both a genetically encodable tool for live cell imaging as well as a robust *in vitro* tool for high throughput drug screening.

In NL-based biosensors, a ligand sensor domain is used to split a luciferase protein (RLuc) into two nonfunctional halves, such that ligand binding results in a conformational change that reconstitutes luciferase activity and produces a change in luminescence intensity (Saito et al., 2012). To develop an NL-based biosensor for (2'3')-cGAMP, a protein sensor domain was needed that binds with high affinity and selectivity to (2'3')-cGAMP and undergoes a conformational change upon binding. The only protein known to bind with high affinity and selectivity to (2'3')-cGAMP is STING (Kranzusch et al., 2015). STING, however, binds to (2'3')-cGAMP as a dimer or higher order oligomer, which

makes it not amenable to use in the NL-based scaffold (Shang et al., 2019). Inspired by a previous graduate student, Dr. Yichi Su's, work in mutating a natural c-di-GMP binding riboswitch aptamer to a (2'3')-cGAMP binding aptamer (Bose et al., 2016), we hypothesized that a similar approach could be applied to convert a natural c-di-GMP binding protein into a (2'3')-cGAMP binding protein. Thus, we sought to use a directed protein evolution approach to evolve (2'3')-cGAMP binding capabilities from a c-di-GMP binding YcgR protein. A benefit to this approach was that we could use the robust lysate-based screening method previously developed to analyze phylogenetic YNL-YcgR biosensor libraries (Dippel et al., 2018). In this screen, the change in luminescent signal intensity that occurs upon ligand binding to YNL-YcgR sensors would serve as a readout for selecting mutant proteins that bind to (2'3')-cGAMP. To our knowledge, this is the first example of using the signal change of a biosensor as a selection strategy for the directed evolution of novel binding capabilities in a protein.

This chapter describes the ongoing work towards the generation of mutant YcgR proteins that bind to (2'3')-cGAMP. Given the large number of clones that need to be assayed during library screening and accordingly the large amount of CDN ligands that are required for screening, a protocol was first optimized that allowed for the enzymatic synthesis and purification of CDN ligands on a large (tens of milligrams) scale. This protocol was found to work very well for natural CDNs, however it can also be applied to unnatural CDNs, albeit with reduced yields. A library cloning strategy was then optimized that allowed for the rapid generation of single site saturation mutagenesis (SSM) libraries. These libraries provide high diversity at the amino acid level with low codon redundancy, thereby decreasing the overall cost of library screening. The lysate-based biosensor screening process developed previously was further optimized for screening large numbers of clones (200+ clones/day) and then applied to screening 16 different SSM libraries of YNL-TbYcgR for binding to (3'3')-cGAMP, an intermediate ligand, in an interative saturation mutagenesis (ISM) process. After 2 rounds of screening, 11 mutants were purified and characterized *in vitro*. Unexpectedly, none of the purified mutants showed the expected increases in affinity for (3'3')-cGAMP. This appears to be due to surprising differences in signal fold-change observed between binding to c-di-GMP versus (3'3')-cGAMP. The work here lays the groundwork for future studies on using a biosensor-based approach for the directed evolution of novel binding capabilities in YcgR proteins.

RESULTS

Enzymatic synthesis and purification of CDNs. To generate the large quantities of CDN ligand that are necessary for library screening, target ligands were enzymatically synthesized and purified where possible, as this helps to reduce the overall cost of library screening. Using enzymatic methods, all of the canonical CDNs and a number of non-canonical CDNs can be generated (Launer-Felty and Strobel, 2018; Li et al., 2014; Rao et al., 2009). While the overall scale of enzymatic CDN synthesis is small compared to chemical synthesis (milligram versus gram scale, respectively) (Gaffney et al., 2010), the speed and ease provided by enzymatic synthesis was attractive.

Initial efforts for large-scale CDN synthesis and purification focused on the target (2'3')-cGAMP. Large-scale reactions of cGAS (~5-10 mL) were set up to generate (2'3')-

cGAMP, and the product was purified using a silica plug with 5 mM NH_4HCO_3/15% H_2O/85% EtOH as the mobile phase, following published protocols (Li et al., 2014). This method produced good yields of target (~76%) with reasonable purity (~90%). This product was used to determine the approximate affinity of the YNL-CpYcgR biosensor for (2'3')-cGAMP. The YNL-CpYcgR sensor was chosen in part because it binds with very high affinity to c-di-GMP, suggesting that it may also have some affinity for (2'3')-cGAMP. Surprisingly, the biosensor exhibited an unexpected decrease in signal intensity in the presence of large amounts of (2'3')-cGAMP (>250 uM) (Figure 4.1a), potentially due to residual solvent and/or impurities present in the silica plug purified product. In order to further purify the product, three additional purification steps were attempted: removal of volatile salts by repeated lyophilization, conversion to sodium salt via ion exchange resin, reversed-phase HPLC purification, or combinations of these routes. The purity of these products was compared to that of commercial product via testing with YNL-CpYcgR (Figure 4.1b). While repeated lyophilization alone did not alleviate the negative signal change effect, additional ion exchange or HPLC purification steps appeared to produce signal changes comparable to those observed with commercial product. Any differences between the purified products and the commercial product were likely due to error in the concentration calculation for the purified (2'3')-cGAMP products (LC/MS was not available at the time to assist with determining purity of samples). While the exact cause of this negative signal change effect was not made clear, it was most likely due to the presence of residual silica particles that carried through after the silica plug purification, which were removed by ion exchange or HPLC purification. To avoid any future issues and to ensure high product purity, HPLC purification alone was used as the purification scheme going forward.

Given the low affinity of the wild-type YcgR proteins for (2'3')-cGAMP (>>100 μM), we hypothesized it would be simpler to use an intermediate ligand on the path towards generating a YcgR mutant that binds to (2'3')-cGAMP (Figure 4.2a). Based on chemical structures, either (3'3')-cGAMP or (2'3')-c-di-GMP could likely serve as useful intermediates in the path from c-di-GMP binding to (2'3')-cGAMP binding, as they differ in only the nucleobase or linkage structure, and not both (Figure 4.2b). In this manner, a screen could be conducted to select for mutants that bind to a mixed linkage CDN (i.e. (2'3')-c-di-GMP), while in parallel, a screen could be conducted to select for mutants that bind to a mixed base CDN (i.e. (3'3')-cGAMP). These mutants could be combined and used as starting scaffolds to conduct a screen for mutants that bind to the desired ligand, (2'3')-cGAMP. After having optimized the method for enzymatic synthesis and purification of (2'3')-cGAMP, both (2'3')-c-di-GMP and (3'3')-cGAMP were targeted for synthesis and purification.

Given that (2'3')-c-di-GMP is not the preferred product of any known CDN synthases, conditions need to be optimized for enzymatic synthesis. Previous results have shown that human cGAS (hcGAS), which naturally produces (2'3')-cGAMP, will produce (2'3')-c-di-GMP when provided with only GTP as substrate, albeit with very low yields (Ablasser et al., 2013). Mouse cGAS (mcGAS) is generally more active, and accepts non-natural substrates such as dNTPs or phosphorothioate NTPs to produce a variety of mixed-linkage CDN products (Li et al., 2014). Given the increased promiscuity and enzymatic activity of mcGAS, it was chosen for synthesis of (2'3')-c-di-GMP rather

than hcGAS. Reaction conditions were optimized to promote the production of (2'3')-c-di-GMP (Figure 4.3). Elevated pH and the use of Mn^{2+} led to increased yields of (2'3')-c-di-GMP, although after HPLC purification the total isolated yields were very small (~5%).

To enzymatically produce (3'3')-cGAMP, the cyclic GMP-AMP synthase, DncV, from *Vibrio cholerae* was used (Launer-Felty and Strobel, 2018). Large-scale synthesis was performed following established protocols, and HPLC purification was carried out using the same conditions optimized for (2'3')-c-di-GMP, which provided good separation of the 3 CDN products produced by DncV. This method resulted in good isolated yields (~70%) with very high purity (>99%). Given the excellent yields possible for (3'3')-cGAMP, it was ultimately chosen as the first target for screening.

Selectivity of phylogenetic YcgR variants. To determine the ideal starting scaffold for directed evolution of (3'3')-cGAMP binding (and eventually (2'3')-cGAMP binding), the relative affinity and selectivity of four phylogenetic YcgR variants – CpYcgR, TmYcgR, TbYcgR, and CbYcgR – within the YNL biosensor scaffold was determined for different CDNs. These sensors all exhibit high affinity for c-di-GMP (<50 nM) with large signal fold-changes (>6-fold) and good stability (Dippel et al., 2018). We sought to determine which YcgR protein was *least selective* against mixed-base/mixed-linkage CDNs (i.e. most promiscuous binder), as we hypothesized that the most promiscuous starting scaffold would require fewer mutations to create a version that binds to (3'3')-cGAMP/(2'3')-cGAMP with high affinity. Theoretically, these mutations could then be transferred to the other YcgR proteins to create multiple sensors capable of binding cGAMP.

The relative affinity/selectivity of these sensors was tested using c-di-GMP, (2'3')-c-di-GMP, (3'3')-cGAMP, and (2'3')-cGAMP to see the effects of mixed bases and mixed linkages on binding (Figure 4.4, 4.5). Relative affinity data suggest that for all sensors, the mixed-linkage isomer of c-di-GMP [(2'3')-c-di-GMP] is more well tolerated than the mixed-base isomer [(3'3')-cGAMP], and that the additive effects of mixed-base and mixed-linkage lead to very high selectivity (>2000-fold) against (2'3')-cGAMP (Table 4.1). Accordingly, all sensors exhibited very poor affinity for (2'3')-cGAMP (K_D >>100 μM, the highest concentration tested). Gratifyingly, this confirmed our hypothesis that either (2'3')-c-di-GMP or (3'3')-cGAMP could serve as intermediates on the path towards (2'3')-cGAMP binding (Figure 4.2a). The four YcgR variants exhibited different relative selectivities towards the tested CDNs, with YNL-TbYcgR sensor being the least selective/most promiscuous binder overall. Based on these results, YNL-TbYcgR was chosen as the starting scaffold towards the evolution of improved cGAMP binding.

Generation of saturation mutagenesis libraries. Having chosen YNL-TbYcgR as the starting scaffold, a strategy was developed for the generation of mutant YcgR libraries. Given the throughput of the lysate-based screen (up to ~800 samples/day limited by manual loading of plates and plate reader read time), we decided to use a focused site saturation mutagenesis (SSM) approach, as it limits library size and the overall screening cost compared to using random mutagenesis. To maximize the probability of obtaining additive and/or cooperative mutations, genes from the initial SSM libraries that exhibited desired properties would then be used as templates for additional rounds of SSM library generation and screening (Reetz and Carballeira, 2007). This approach, known as

iterative saturation mutagenesis (ISM), has been shown to be an efficient strategy for directed evolution of enzymes with enhanced thermostability, enantioselectivity, or altered substrate profiles, but to our knowledge had not been applied to evolve new ligand binding in protein receptors (Reetz, 2011).

In choosing sites for the generation of SSM libraries within YNL-TbYcgR, the highly conserved residues of the PilZ domain were purposefully avoided, as mutations at these sites would likely ablate all CDN binding (Benach et al., 2007; Chou and Galperin, 2016; Ko et al., 2010; Ryjenkov et al., 2006). Instead, libraries were focused on the less well-conserved residues that surround the binding pocket and make contacts with c-di-GMP. This type of semi-rational library design process is known as CASTing (combinatorial active site saturation test) and results in the creation of smaller "smarter" libraries that reduces the cost of library screening (Chica et al., 2005; Reetz and Carballeira, 2007; Steiner and Schwab, 2012). We hypothesized that cGAMP was likely to bind as a monomer, so the structural model was based mainly on the crystal structure of VCA0042 bound to a monomer of c-di-GMP (Figure 4.6a) (Benach et al., 2007). One of the key mutations in YcgR-like proteins that appears to promote monomer binding over dimer binding is at "position X", which is the residue immediately prior to the highly conserved RxxxR motif. In VCA0042 this residue is a Leu (L135), while in many PilZ domain-containing proteins it is an Arg. Mutation to a Leu or other small hydrophobic residue appears to sterically occlude the 2nd c-di-GMP molecule from entering the binding pocket, while the presence of an Arg promotes an "arginine-fork" interaction with a 2nd molecule of c-di-GMP (Ko et al., 2010). It was unclear which orientation cGAMP would adopt in the binding pocket (adenine base on "top" or "bottom"), so SSM regions were chosen that would theoretically interact with the altered base at either position. With these considerations, eight total residues were chosen for SSM library creation (Figure 4.6b).

Given the throughput that is possible in the lysate-based screen (~800 samples/day), we had to carefully choose a method of SSM library creation that would allow for rapid screening of these 8 different sites as well as the future libraries needed for the ISM process (Reetz and Carballeira, 2007). In order to get sufficient library coverage at a single site (>95% coverage), approximately 3x the number of variants encoded in the library must be screened (Patrick et al., 2003) (Figure 4.7a). With this in mind, SSM libraries were generated using the 22c trick method, as it produces a library that encodes all 20 possible amino acids with very little redundancy (22 codons), thereby reducing the number of clones that need to be screened for good coverage (Acevedo-Rocha et al., 2015; Kille et al., 2013) (Figure 4.7b). The 22c trick method uses a defined mixture of three primers to create a degeneracy of 22 codons that encode all 20 amino acids. The Tang method was also considered as it produces a similar library diversity with zero redundancy (20 codons encoded), but it requires an additional primer per site and would not significantly reduce the screening effort required (Tang et al., 2012).

SSM libraries were generated at each of the 8 sites using an "around the horn" mutagenesis type approach. In this method, non-overlapping primers are used to amplify the entire plasmid via PCR, and mutations are encoded on only a single primer (5' end of the forward primer or the 3' end of the reverse primer). The linear PCR product is ligated to form circularized DNA which can then be transformed into cells. QuikChange mutagenesis, which is also commonly used for library creation, uses long, overlapping

primers and encodes the mutation on both primers. QuikChange additionally requires transformed cells to repair the nick is the PCR product, generally leading to reduced transformation efficiency. Using the around the horn approach rather than QuikChange allowed for the use of short oligo sequences and standard chemically competent cells in the transformations, which simplified the generation of the mutant libraries. Pooled libraries for each site were sequenced and characterized using the "Quick Quality Control" (QQC) method to determine the approximate quality of the library (Sullivan et al., 2013). This method provides a statistical value that represents how well the library diversity (as measured by peaks in a sequencing chromatogram) matches that of an "ideal" library, with a Q value close to 1 meaning better library diversity. In general, Q values >0.7 suggest that the library is of high enough quality for screening (Sullivan et al., 2013). In our hands, the cloning methods described here consistently produced libraries with Q values of 0.70-0.85, which are suitable for screening.

Lysate-based screening of TbYcgR 22c libraries. The 8 different SSM libraries were individually screened as mCherry-tagged biosensors in lysates with buffer, 1 µM c-di-GMP, or 5 µM (3'3')-cGAMP added. The mCherry tag was used so that the luminescent signal for each clone could be normalized to the mCherry fluorescence, thereby accounting for differences in biosensor expression/stability. The 1 µM c-di-GMP condition was included to provide a way to normalize to the fully saturated signal for each clone. The starting affinity wild-type YNL-TbYcgR for c-di-GMP is <50 nM, so it was hypothesized that 1 µM would always lead to a saturating signal, even for mutants with reduced c-di-GMP affinity. The 5 µM (3'3')-cGAMP concentration was chosen because this is the approximate affinity of wild-type YNL-TbYcgR for (3'3')-cGAMP (Figure 4.4, 4.5). Accordingly, WT controls would show ~50% signal with 5 µM (3'3')-cGAMP compared to the fully saturated c-di-GMP signal, while any clones with increased affinity would show >50% signal and any clones with decreased affinity would show <50% signal.

For each library, 90 mutant clones were screened alongside 6 WT controls to ensure sufficient library coverage and a measure of reproducibility. While only ~66 clones are needed for 95% coverage in these libraries, this assumes the absence of any frame shifts/indels that may have been produced during cloning that result in a truncated protein product. About 5-10% of all clones exhibited very low luminescent signal, suggesting these clones were producing truncated or mis-folded protein product. Accordingly, by oversampling and screening 90 clones per site, we ensure sufficient library coverage with minimal additional effort.

The max signal fold-change (Δsignal) for each clone was calculated based on the signal for 1 µM c-di-GMP compared to buffer (Figure 4.8). To determine relative affinities for (3'3')-cGAMP, the signal for 1 µM c-di-GMP was assumed to be saturating and used to calculate the % signal with (3'3')-cGAMP over c-di-GMP for each clone. The WT YNL-TbYcgR sensor exhibited a Δsignal max of ~5.2 and a % signal of ~64% with 5 µM (3'3')-cGAMP under the lysate screen conditions (average of 48 lysate measurements across multiple days/plates) (Figure 4.8a). Mutant clones exhibited signal fold-change and % signal values that varied significantly from site to site (Figure 4.8b). To remove any clones that had drastically reduced affinity for c-di-GMP from the analysis, % signal values were not calculated for any clones that showed Δsignal values for 1 µM c-di-GMP less than 2.

Additionally, clones exhibiting very low luminescent signal were completely excluded from analysis – the luminescent signal cutoff was defined as being <1% that of the WT.

Clones with significantly improved signal change (> ~10-fold) and/or improved % signal with (3'3')-cGAMP over c-di-GMP (> ~75%) were selected for re-screening. Most libraries showed only a few clones with % signal values >75%, however the R100 site library produced many clones with % signal values >100%, including some with >200% values (Figure 4.9, 4.10). These surprising results suggested that the affinity/selectivity in these clones was altered such that (3'3')-cGAMP was preferred over c-di-GMP (i.e. 1 μM c-di-GMP is not saturating but 5 μM cGAMP is), which was a desired outcome. An alternate explanation is that the mutants bind to c-di-GMP and cGAMP in a different manner, leading to different max Δsignal values depending on the ligand, which was an undesired outcome. From this first round of screening, 40 clones were selected that had improved % signal with (3'3')-cGAMP over c-di-GMP, and 22 clones were selected that had improved Δsignal values.

The 62 selected clones were subjected to re-screening under identical conditions, but with 4 biological replicates used for each measurement. All selected R100 site mutants were additionally screened against 10 μM c-di-GMP to determine if 1 μM c-di-GMP was saturating. For these clones the 1 μM c-di-GMP condition did indeed appear to be saturating, suggesting that the reason % signal values were >100% was due to differential binding/signal change between c-di-GMP and (3'3')-cGAMP. This unexpected property appeared to be unique to the R100 site mutants. All clones that showed statistically significant improvements for the desired properties were then isolated and sequenced. A total of 9 unique sequences were found that appeared to have improved properties (4 with improved Δsignal and 5 with improved % signal with (3'3')-cGAMP over c-di-GMP) (Figure 4.11, Table 4.2).

Following the first round of SSM library screening, two single mutant sequences that displayed favorable combinations of Δsignal and % signal (N102W and R100V) were then used as parent templates to generate additional SSM libraries (Table 4.2). SSM libraries were generated at sites R100 (for N102W template only), N102 (for R100V template only), V136, S137, and V174 as these sites produced mutants with improvements in Δsignal and % signal (Table 4.2). Sites G139, L142, and R175 were dropped at this round because these libraries produced few to no major improvements in the first round of SSM library screening. Double mutant libraries were screened in lysates as before, except the single mutant parent was used as the "WT" control in each case, and lysates were screened with 2.5 μM (3'3')-c-di-GMP added, rather than 5 μM, to increase the stringency of selection (Figure 4.12). Clones that showed improved % signal with (3'3')-cGAMP over c-di-GMP (> ~60%; 31 clones) and/or improved signal change (> ~15-fold; 14 clones) were subjected to re-screening with additional biological replicates. After re-screening, clones that showed statistically significant improvements for the desired properties were isolated and sequenced. A total of 11 unique sequences were found that appeared to have improved properties (Figure 4.13, Table 4.2). Double mutants that were generated from the N102W parent template exhibited increases in a single property compared to the parent (3 with improved % signal, 3 with improved Δsignal), whereas double mutants generated from the R100V parent template all exhibited increases in both properties compared to the parent sequence (5 clones).

Interestingly, four mutations that had appeared in the first round of screening appeared again here (R100M, N102R, V136Q, and S137Q) suggesting that these mutations are indeed having significant effects on % signal and Δsignal.

In vitro characterization of TbYcgR mutants. Two rounds of iterative saturation mutagenesis and screening identified 5 single and 8 double mutant sequences that exhibited improved % signal with (3'3')-cGAMP over c-di-GMP in the lysate-based screen. This property suggests these mutants were promising candidates for evolved (3'3')-cGAMP binding protein domains/biosensors. The relative (3'3')-cGAMP affinities of the 5 single mutants were first measured in lysates. The mutants were screened with varying concentrations of (3'3')-cGAMP and compared to the WT sequence (Figure 4.14). The N102W, R100V, R100L, and R100K mutants all showed increased % signal values for (3'3')-cGAMP compared to the WT sequence, suggesting that they had improved affinity for cGAMP, as expected. The R100M mutant exhibited % signal values for (3'3')-cGAMP over c-di-GMP >100%, suggesting that this mutation may lead to differential binding between (3'3')-cGAMP and c-di-GMP, which was not desired.

Selected mutants were re-cloned into the pRSET vector without the mCherry tag, expressed, and purified for in vitro characterization. Each protein was tested for binding to c-di-GMP (up to 1 μM) and (3'3')-cGAMP (up to 10 μM) to determine relative affinity and selectivity. To our surprise, the single mutants (N102W and R100V) that were isolated from the first round of library screening actually exhibited *poorer affinity* for (3'3')-cGAMP than the WT sequence, but similar affinity for c-di-GMP (Figure 4.15; Table 4.3; Table 4.4). These decreases in (3'3')-cGAMP affinity were completely unexpected, as the % signal with (3'3')-cGAMP over c-di-GMP for these mutants was greater than for the WT in the lysate screen. The reason this does not translate to an increase in (3'3')-cGAMP affinity, it appears, is that the mutants exhibit different max fold-change values for c-di-GMP compared to (3'3')-cGAMP, with (3'3')-cGAMP producing larger Δsignal values (Table 4.3; Table 4.4). The R100M mutant, as noted previously, is an extreme case of this differential binding, whereas the N102W and R100V mutants show more subtle differences. Also of note, the Hill slope of the R100V mutant is ~1, suggesting that the mutation to a small hydrophobic at this residue indeed promotes the binding of monomeric c-di-GMP in TbYcgR, as hypothesized.

Similar affinity results were observed in all the remaining double mutants, with no mutant showing significantly improved (3'3')-cGAMP affinity compared to wild-type (Figures 4.16, 4.17, 4.18). Unfortunately, these results suggest that because all (3'3')-cGAMP binding data was normalized to c-di-GMP signal, the screen inadvertently selected mutants that exhibited differences in Δsignal between the two ligands, rather than the desired improvements in (3'3')-cGAMP binding affinity.

DISCUSSION AND FUTURE DIRECTIONS

The work here represents, to our knowledge, the first attempts at evolving a YcgR protein to bind a new CDN ligand, with the ultimate goal being to develop protein-based biosensors for CDN targets that currently have no known receptors. Furthermore, to our knowledge, this represents the first example of using a biosensor scaffold as the readout for ligand binding in directed evolution library screening. It comes as no surprise then, that some unexpected difficulties were encountered along the way.

This library screening process taught us some valuable lessons about ligand binding to YcgR proteins and the complicating factors that arise when using conformational change (∆signal) as a readout for ligand binding. One of the most surprising aspects of the mutant YNL-TbYcgR library screening process was the profound effects that single mutations had on the behavior of the biosensors. For example, we observed that the S137Q mutation alone produced a biosensor with a 53-fold signal change (Table 4.2), compared to a ~5.2-fold signal change in the wild-type protein, albeit with reduced c-di-GMP binding affinity. Prior work characterizing the YcgR-like protein PlzD from *V. cholerae* showed that a single L135R mutation (at "position-X") produced a completely different inter-domain structure in the c-di-GMP bound state compared to the WT (Ko et al., 2010), which may be similar to the effects we observed in TbYcgR mutants. Early efforts in engineering CSL-type sensors for cAMP similarly found that global mutagenesis and directed evolution of the biosensor scaffold (including binding domain) could lead to dramatic improvements in signal change with only a few mutations (Binkowski et al., 2011), however that approach used random mutagenesis rather than targeted SSM. In future studies it would be interesting to see if the mutations that were discovered in TbYcgR (see also V136Y, V136Q) are transferrable to other YcgR proteins to produce similar effects, or if they are unique to TbYcgR. Additionally, it would be interesting to see if these TbYcgR mutants can be transferred to one of the ratiometric VYN biosensor scaffolds to produce improved changes in BRET ratio.

Equally surprising was the differences we observed in signal fold-change for mutant TbYcgR proteins binding to c-di-GMP versus (3'3')-c-di-GMP. When starting this screening process, it was assumed that because both ligands would likely bind to the same region of the protein, the ∆signal values would be similar for both binding events. While small differences could be expected, the magnitude of the differences that were observed in selected mutants was surprising. Small changes to protein sequence (R100M, N102W/R100G, N102W/R100T – see Figures 4.15 and 4.16) produced very large differences in ∆signal for the two ligands. Looking back at the initial selectivity screen, there were actually subtle differences in max ∆signal for c-di-GMP versus (2'3')-c-di-GMP, suggesting that these differences might be common in all YcgR proteins (Figure 4.4). This effect is likely due to subtle differences in binding interactions and reorganization of the binding pocket around the two different ligands, and potentially differences in the binding stoichiometry for the two different CDNs. Unfortunately, because all (3'3')-cGAMP binding data was normalized to c-di-GMP in this screen, we inadvertently selected for extreme cases of this phenomenon (you get what you screen for!). In future studies, this problem could potentially be solved by using an additional high concentration of (3'3')-cGAMP for normalization, as opposed to c-di-GMP.

Despite the outcome, the library generation and screening methods developed here have proven to be very robust. Using the cloning methods described, high quality SSM libraries can rapidly and cheaply be generated. The workflow for screening libraries was highly optimized (up to 800 samples/day), and screening 8 different SSM libraries took only ~2 weeks. Any clones subjected to re-screening consistently reproduced what was seen in the original screen. Additionally, the results observed under lysate screen conditions were replicated by the purified mutant constructs, suggesting the high quality of the lysate screen data, even with single replicates. These details emphasize the fact

that although this library screening campaign did not successfully produce mutants with the desired characteristics, this same methodology could be repeated with small changes to the protocol (i.e. different [CDNs] for normalization) on the same exact libraries, or slightly modified libraries (i.e. different YcgR, VYN scaffold), with minimal effort.

FIGURES

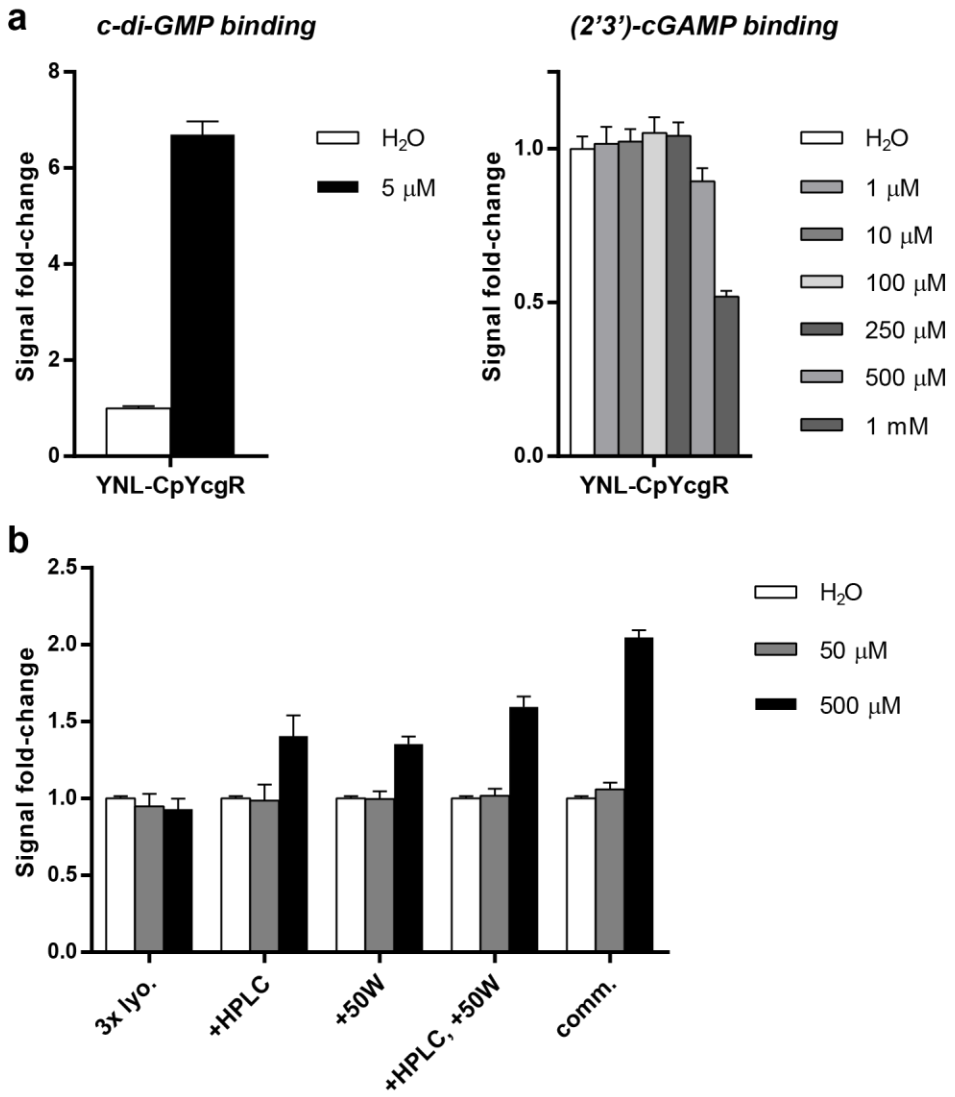

Figure 4.1 Binding measurements with enzymatically synthesized (2'3')-cGAMP. (a) Luminescence signal fold-changes of YNL-CpYcgR sensor in response to (left) commercial c-di-GMP stocks and (right) increasing concentrations of silica-plug purified (2'3')-cGAMP. Data are from 3 replicates represented as mean ± SD. (b) Luminescence response of YNL-CpYcgR sensor in response to (2'3')-cGAMP with increasing levels of purity. 3x lyo. = lyophilized three times, +HPLC = additionally purified via reverse-phase HPLC, +50W = additionally converted to Na^+ salt with ion exchange resin, comm. = commercial product. Data are from 3 replicates represented as mean ± SD.

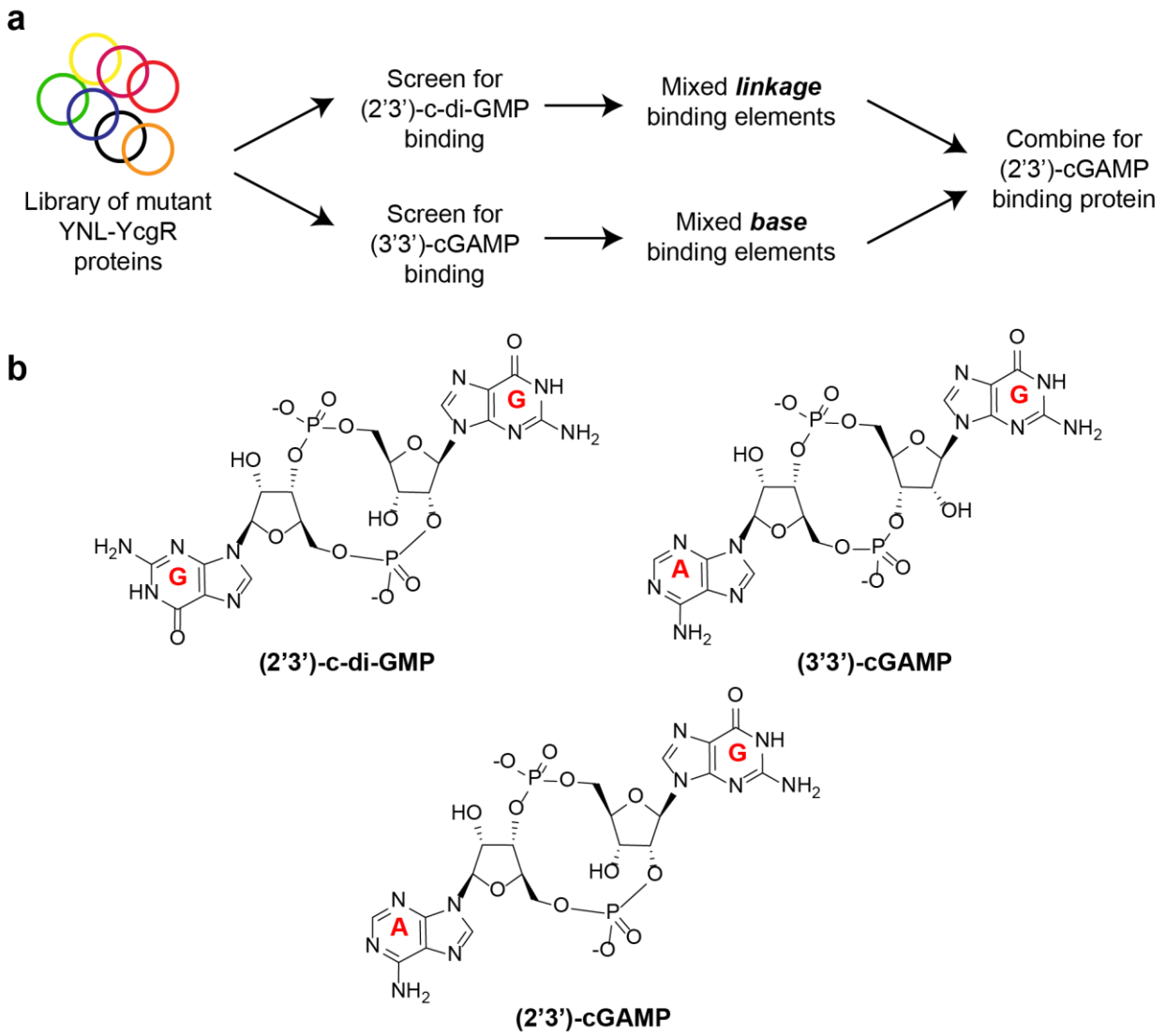

Figure 4.2 Intermediate target strategy for evolution of a (2'3')-cGAMP binding protein. (a) Schematic of the 2 potential routes to (2'3')-cGAMP binding using mixed-linkage [(2'3')-c-di-GMP] or mixed-base [(3'3')-cGAMP] CDNs as intermediates. (b) Chemical structures of the three CDNs.

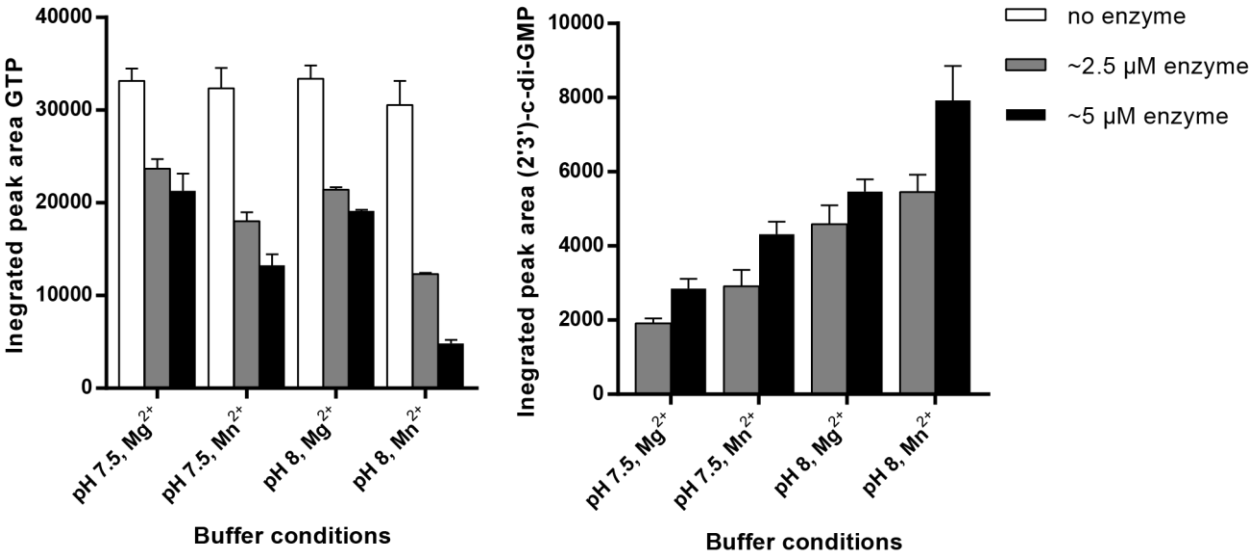

Figure 4.3 Optimization of (2'3')-c-di-GMP synthesis by mcGAS. Integrated peak areas (A_{254}) of GTP (left) and (2'3')-c-di-GMP (right) measured by LC-MS after overnight incubation with mcGAS under the specified conditions. Data are from 2 replicates represented as mean ± SD.

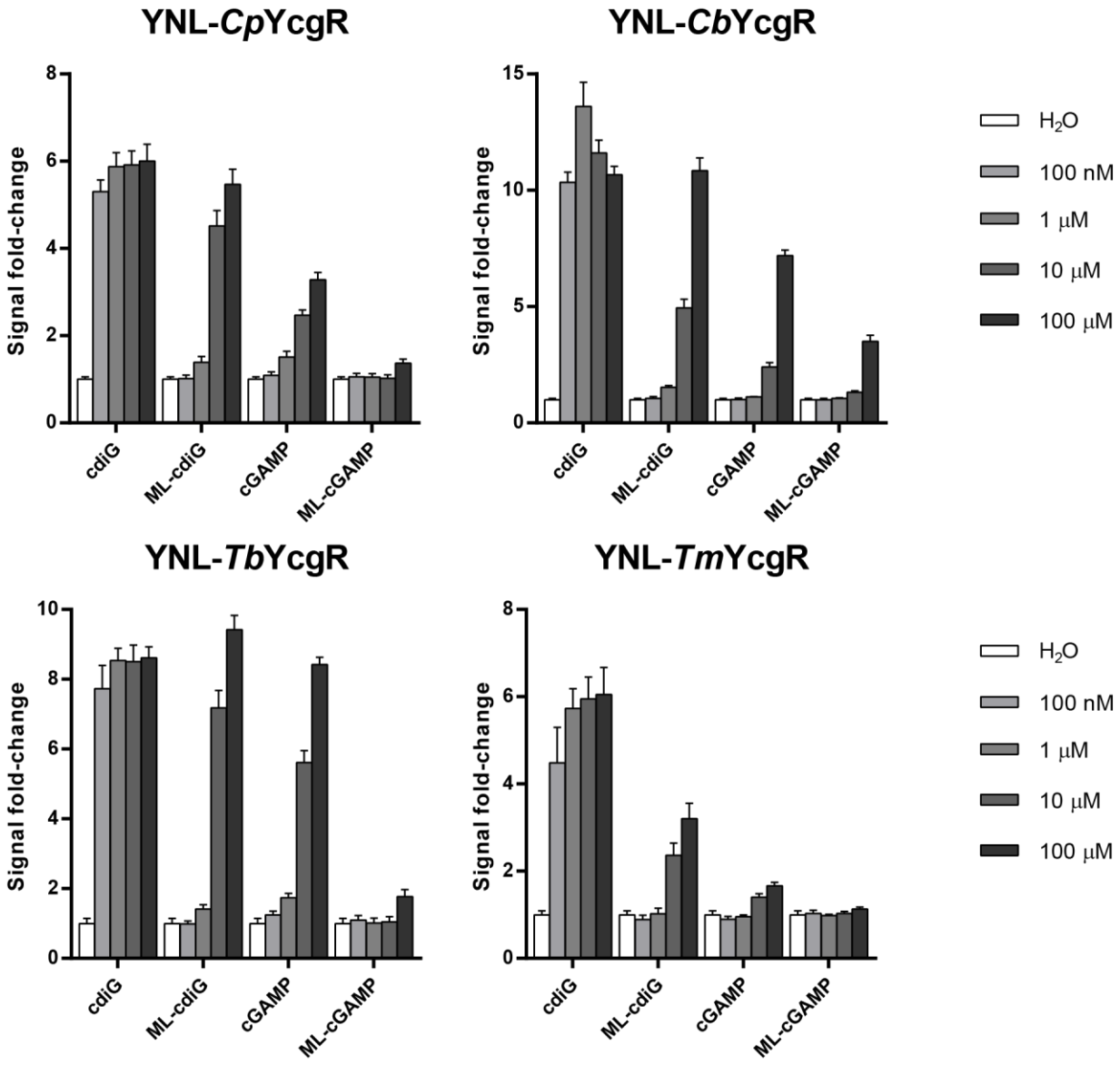

Figure 4.4 CDN selectivity of YNL-YcgR variants. Luminescence signal fold-changes of YNL-YcgR sensors in response to increasing concentrations of different CDNs. Data are from 3 replicates represented as mean ± SD.

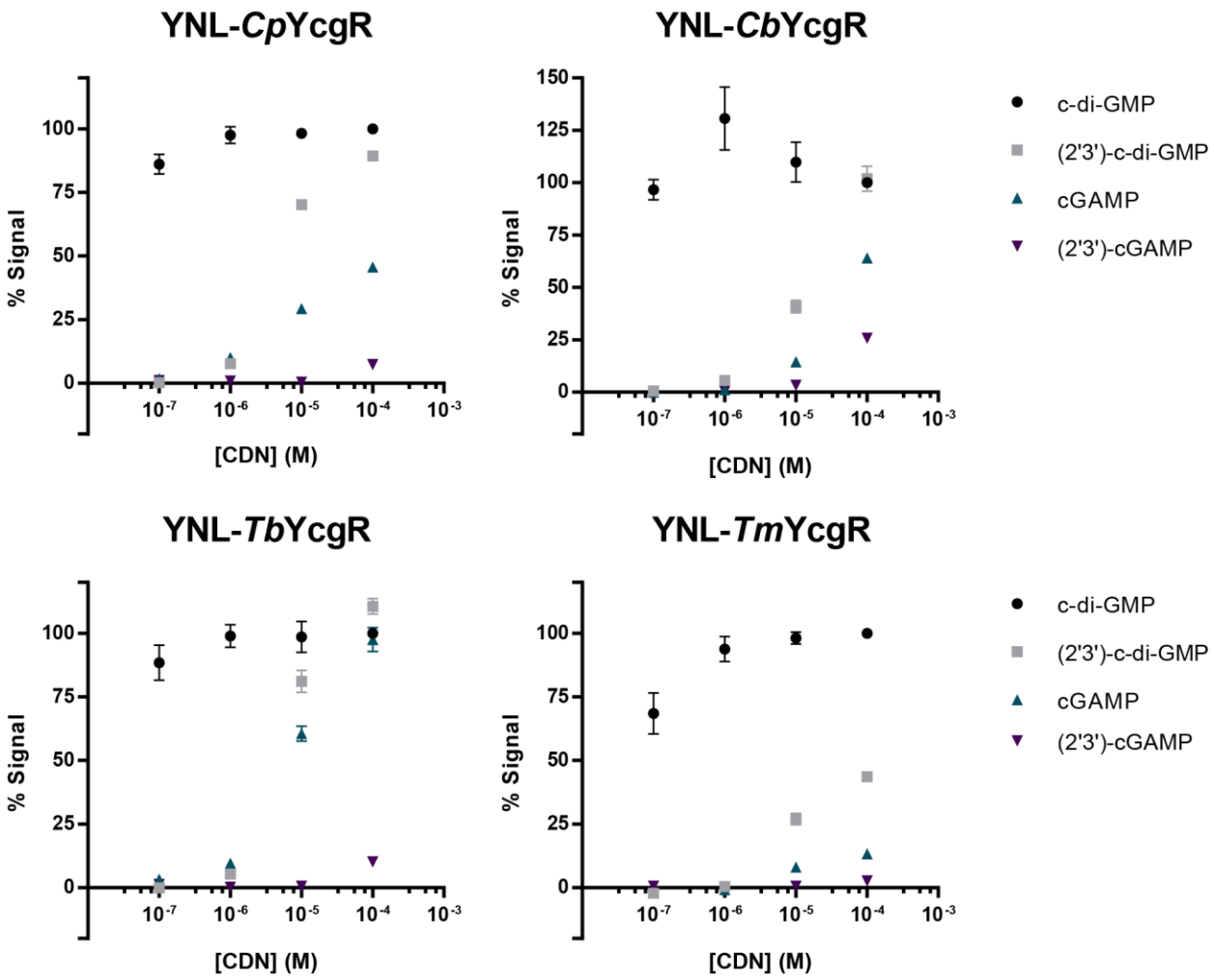

Figure 4.5 CDN selectivity of YNL-YcgR variants, continued. Data from Figure 4.4 represented as % Signal (compared to 100 µM c-di-GMP) instead of signal fold-change.

a

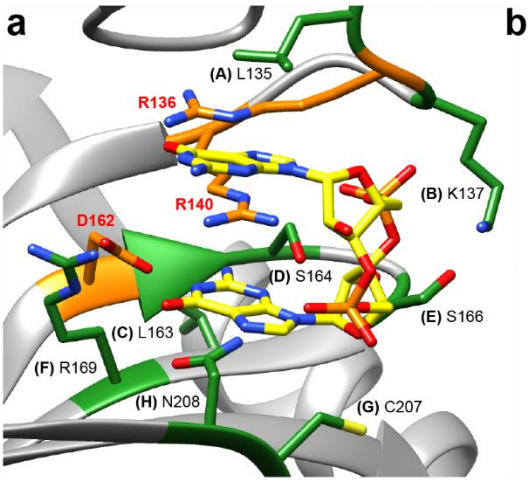

b

Label	VCA0042 numbering	*Tb*YcgR numbering
A	L135	R100
B	K137	N102
C	L163	V136
D	S164	S137
E	S166	G139
F	R169	L142
G	C207	V174
H	N208	R175

Figure 4.6 CASTing the c-di-GMP binding pocket of a PilZ domain. (a) Crystal structure of VCA0042 bound to c-di-GMP (PDB 2RDE). Orange colored residues represent highly conserved residues that are critical for c-di-GMP binding. Green colored residues represent regions that were targeted for mutagenesis. (b) Labeling scheme for saturation mutagenesis library creation based on VCA0042 numbering.

a

$$L = -V * \ln(1 - F)$$

L = number of samples screened
V = total number of possible variants (e.g. codons$^{\#\ of\ sites}$)
F = fractional library completedness

For 95% completeness (F = 0.95):

$$L = -V * \ln(0.95) \approx V * 3$$

b

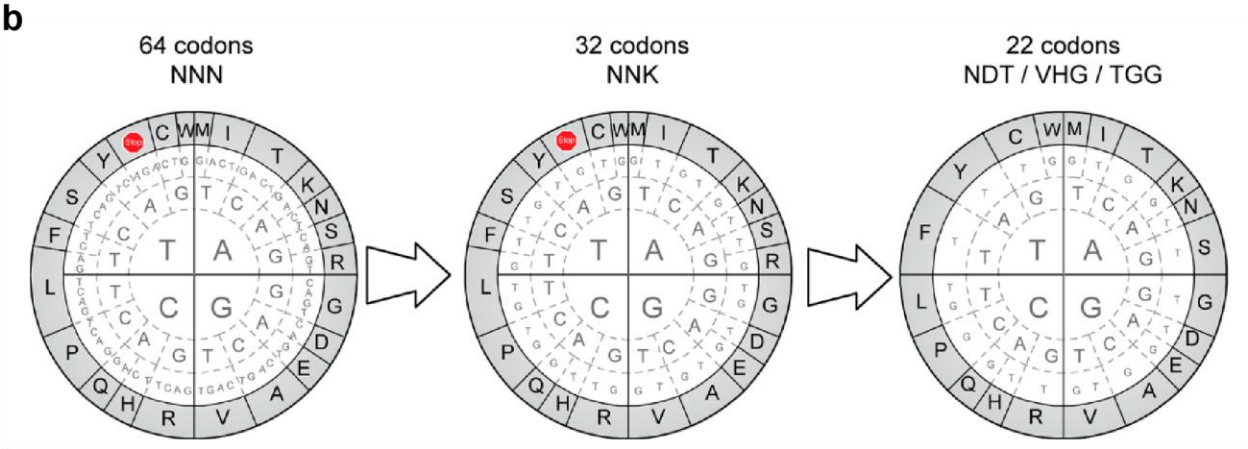

Figure 4.7 Considerations for saturation mutagenesis library creation. (a) Equation for estimating fractional library completeness (Patrick et al., 2003). (b) Schematic showing the reduced codon redundancy in the "22c trick" library. Reprinted with permission from Kille et al., 2013. Copyright 2013 American Chemical Society.

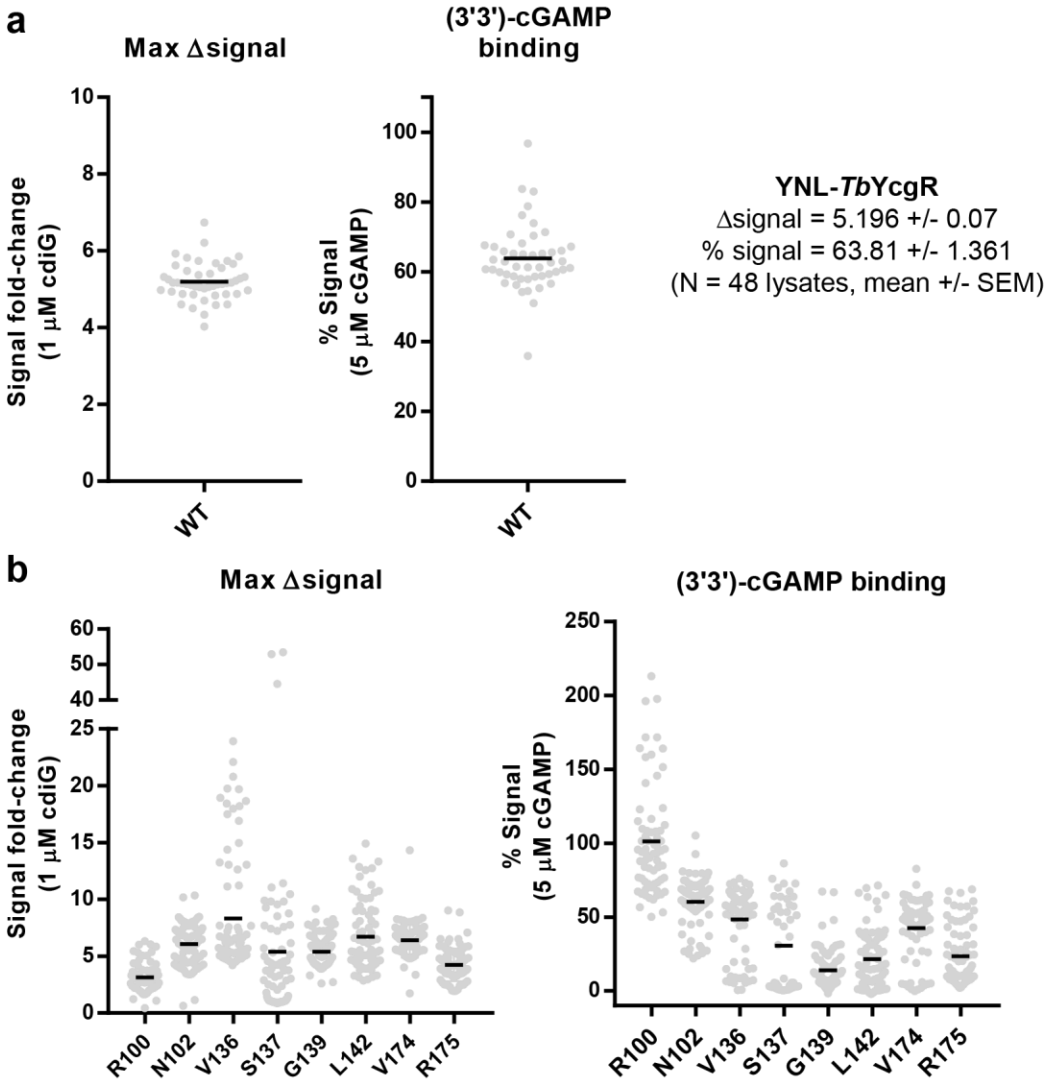

Figure 4.8 Lysate screening results of YNL-TbYcgR SSM libraries. (a) Luminescent signal fold-change and % signal measurements for wild-type YNL-TbYcgR during library screening. Each dot represents a single biological replicate (n = 48), black bars represent the mean of all replicates. Measurements were taken from multiple plates across multiple days of the library screening process. (b) Luminescent signal fold-change and % signal measurements for individual clones from the saturation mutagenesis libraries. Each dot represents a single clone (~90 per site), black bars represent the mean of all clones at that site.

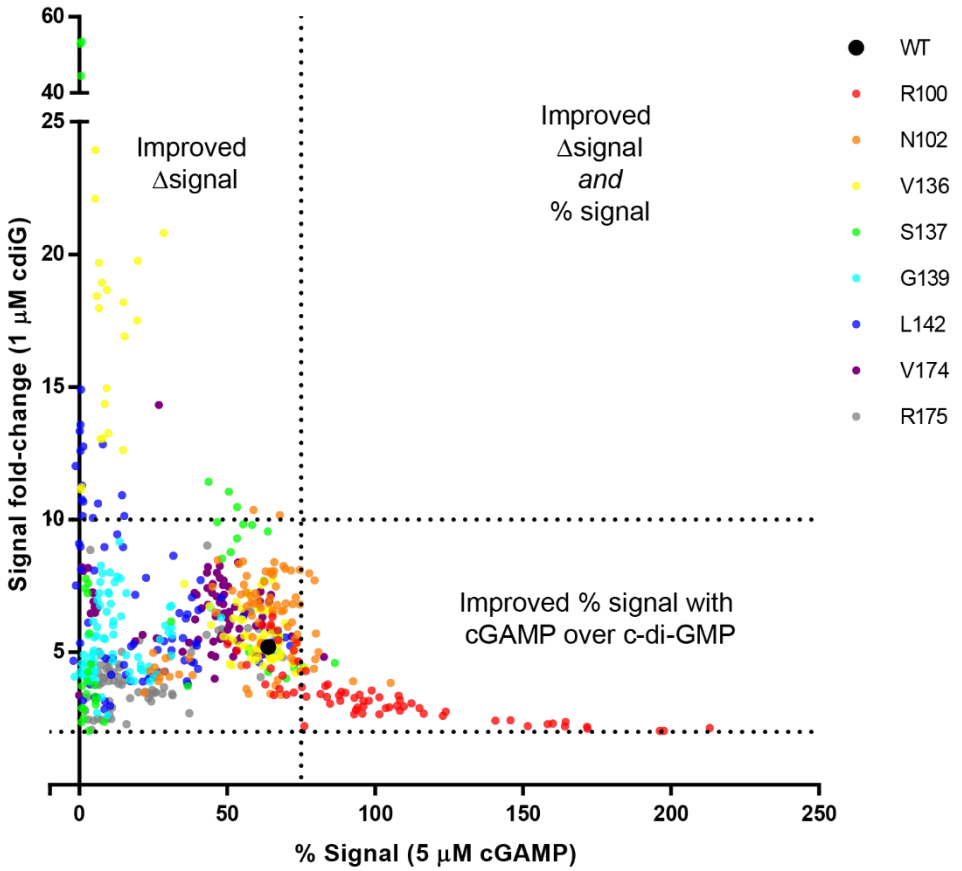

Figure 4.9 Percent signal with cGAMP over c-di-GMP versus signal fold-change of YNL-TbYcgR mutants. Lysate screening data from Figure 4.8 plotted as % signal vs. signal fold-change for individual clones.

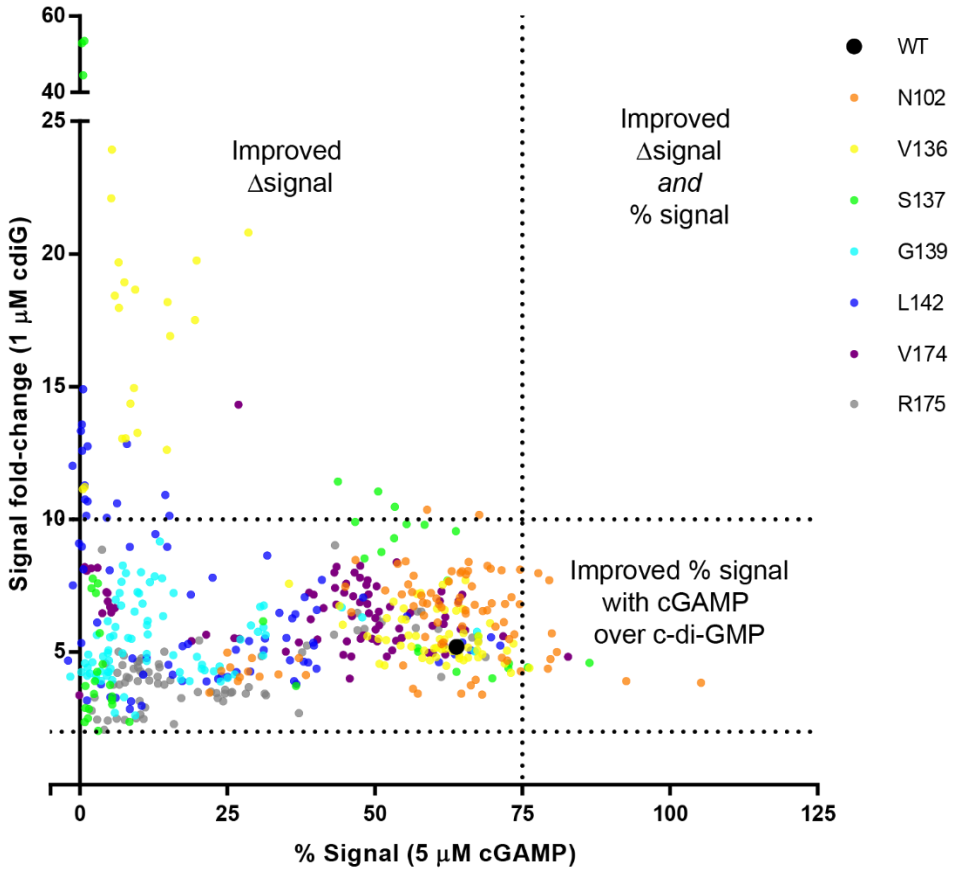

Figure 4.10 Percent signal with cGAMP over c-di-GMP versus signal fold-change of YNL-TbYcgR mutants, zoomed in. Plot from Figure 4.9 with R100 site data removed to more clearly show distribution of mutants.

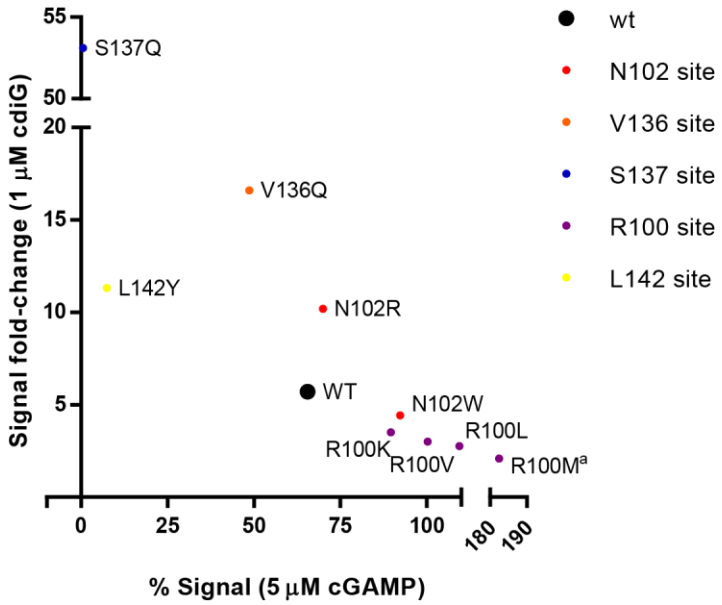

Figure 4.11 Percent signal with cGAMP over c-di-GMP versus signal change of sequenced YNL-TbYcgR mutants. Lysate screening data of sequenced YNL-TbYcgR mutants. Data are from 4 biological replicates represented as mean. [a]% signal value >100% are due to differences in signal fold-change for c-di-GMP versus (3'3')-cGAMP.

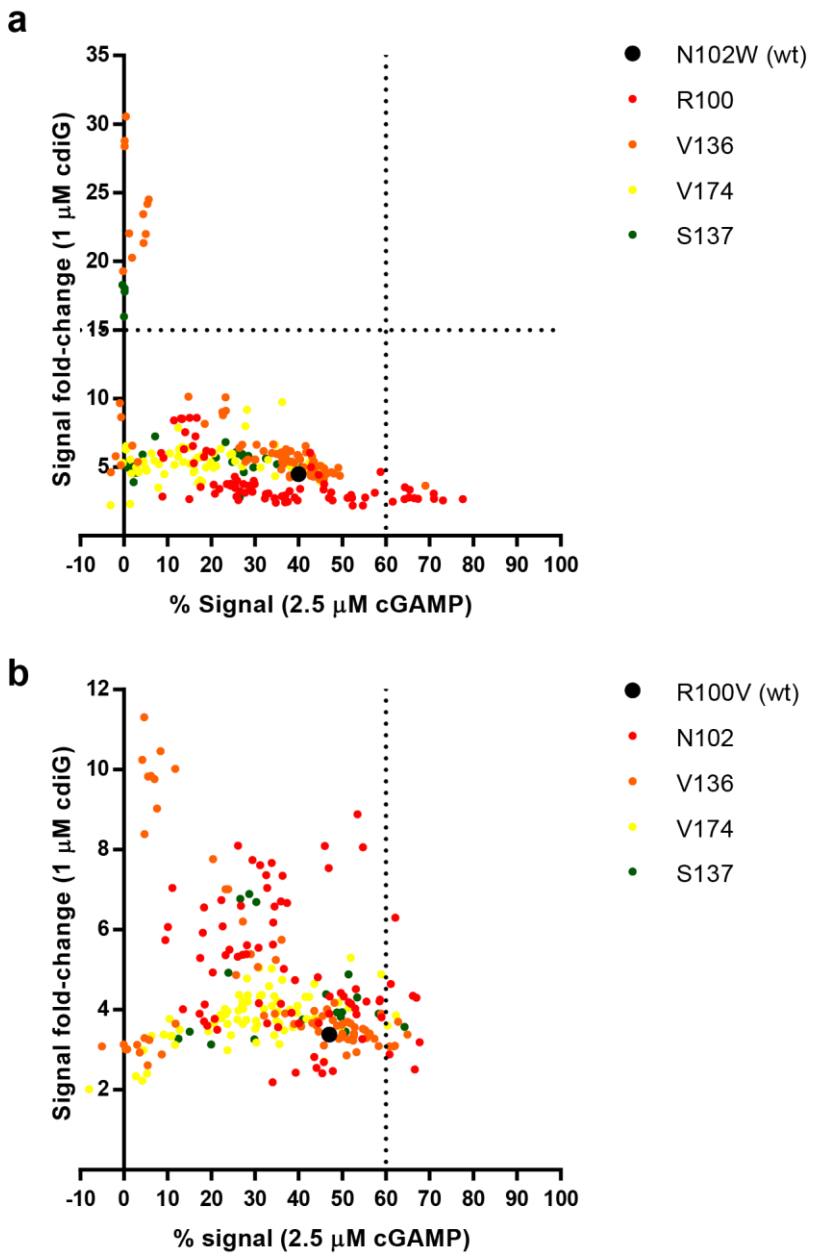

Figure 4.12 Percent signal with cGAMP over c-di-GMP versus signal change of double mutant YNL-TbYcgR libraries. (a) Lysate screening data of SSM libraries using N102W as the parent template. Each point represents data from a single clone. (b) Lysate screening data of SSM libraries using R100V as the parent template. Each point represents data from a single clone.

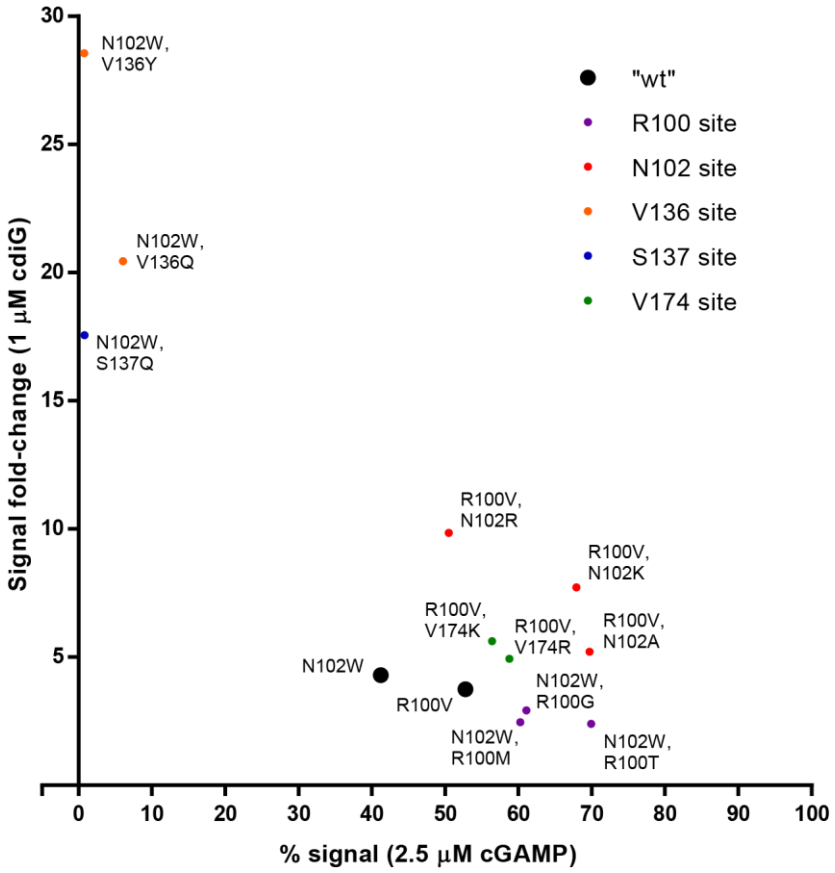

Figure 4.13 Percent signal with cGAMP over c-di-GMP versus signal change of sequenced YNL-TbYcgR double mutants. Lysate screening data of sequenced YNL-TbYcgR double mutants. Data are from 4 biological replicates represented as mean.

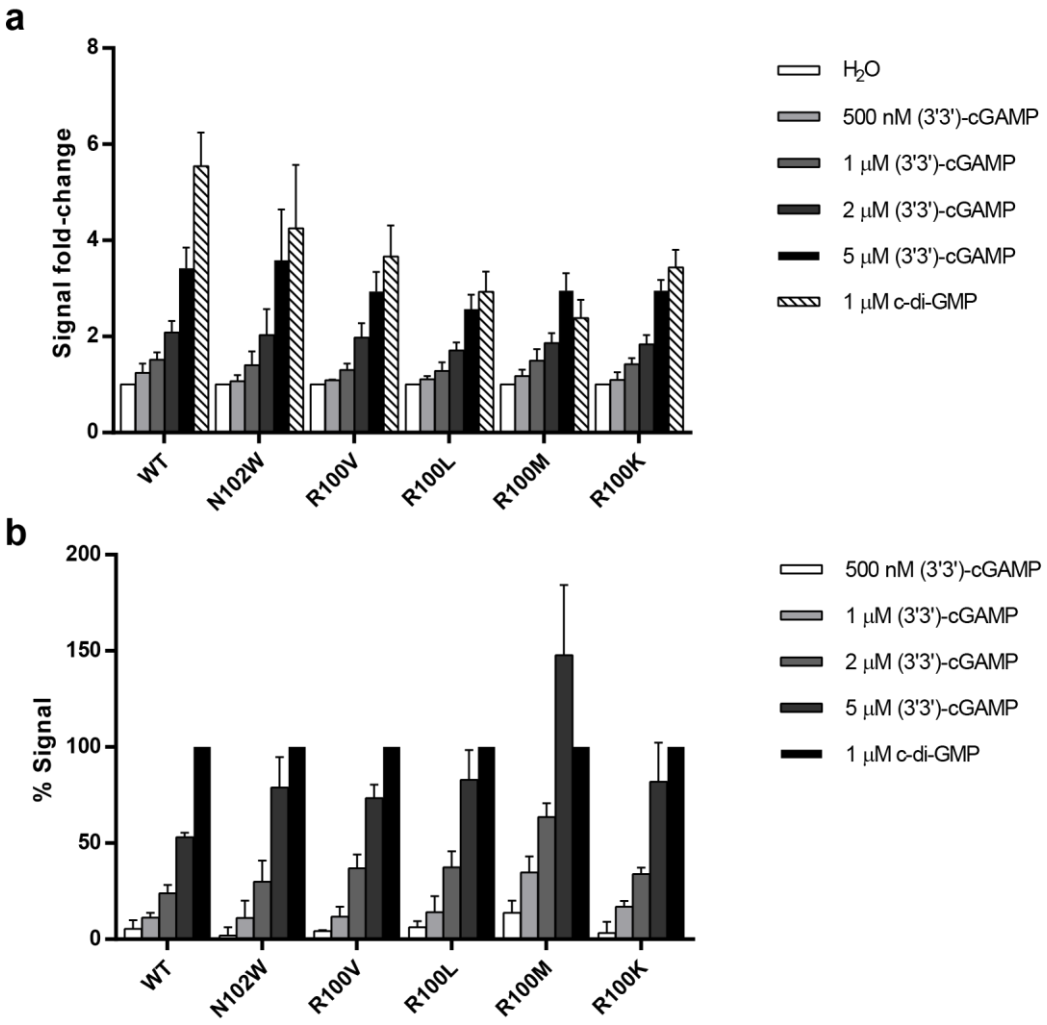

Figure 4.14 Relative (3’3’)-cGAMP affinity of selected YNL-TbYcgR mutants. (a) Luminescence signal fold-changes of YNL-TbYcgR mutants in response to (3’3’)-cGAMP and c-di-GMP, measured in lysates. Data are from 4 biological replicates represented as mean ± SD. (b) Percent signal of of YNL-TbYcgR mutants in response to (3’3’)-cGAMP, with 1 μM c-di-GMP signal normalized to 100%. Data are from 4 biological replicates represented as mean ± SD.

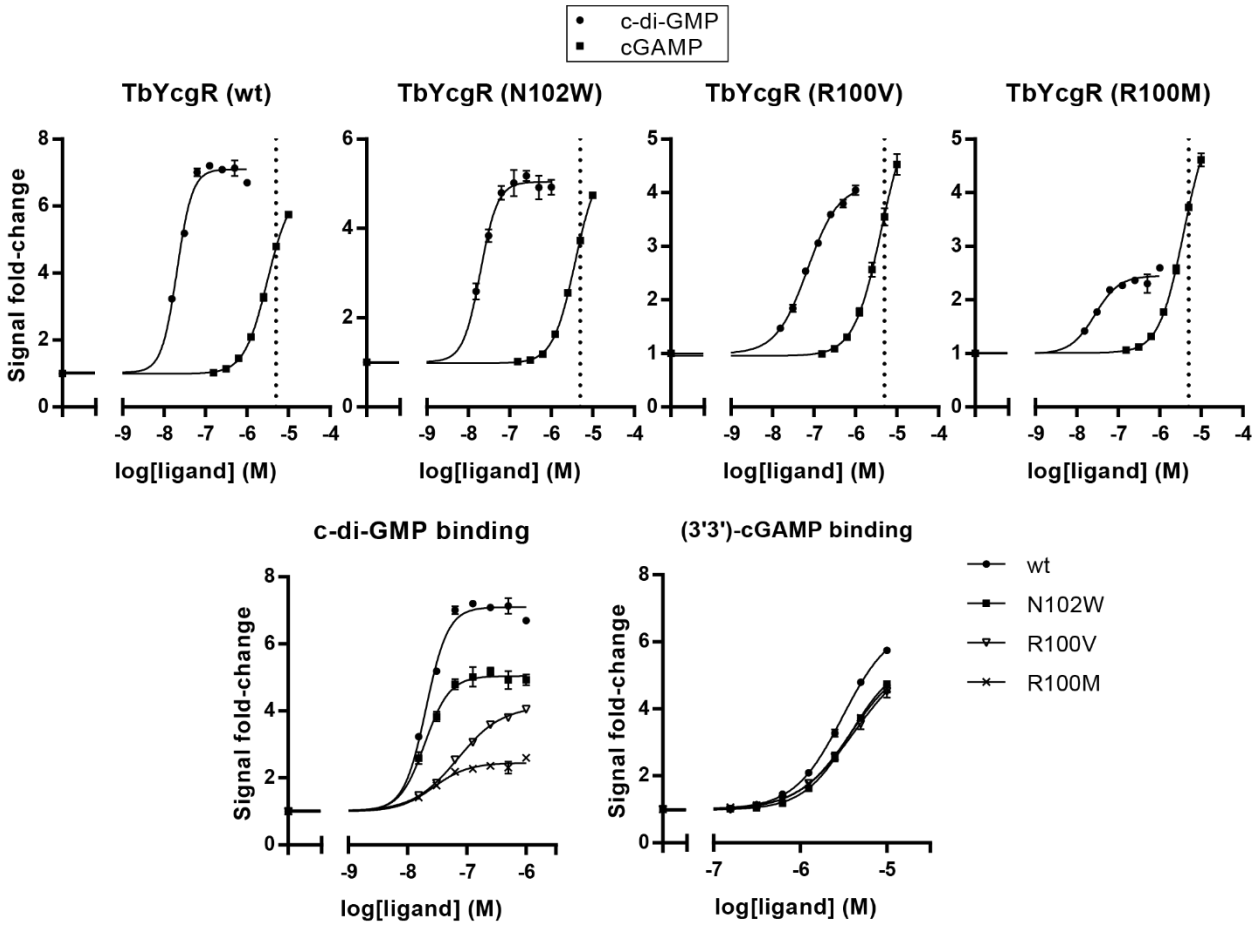

Figure 4.15 Binding affinity and selectivity of YNL-TbYcgR single mutants. Affinity measurements of purified single mutant YNL-TbYcgR biosensors. Data are from 3 replicates represented as mean ± SD.

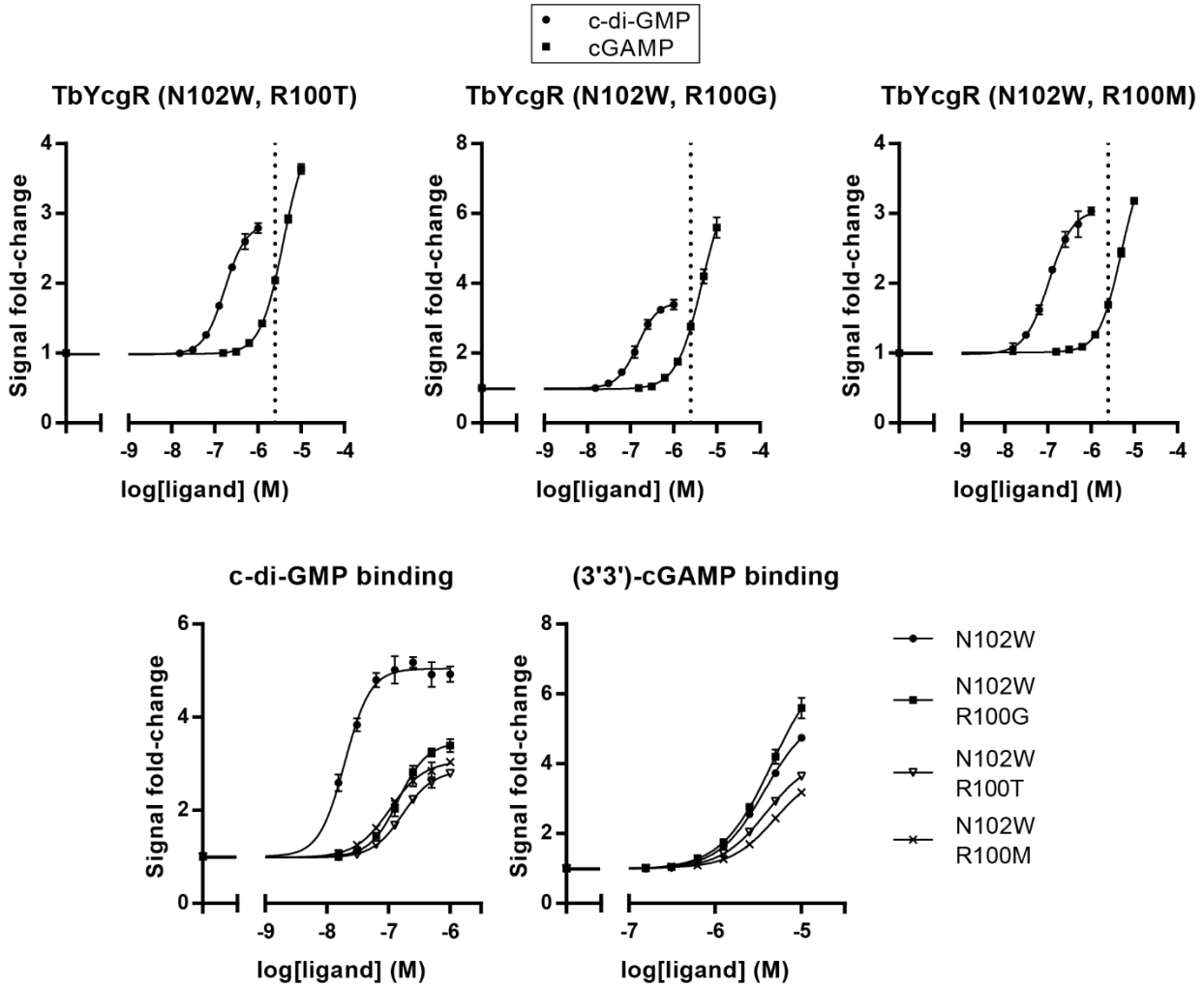

Figure 4.16 Binding affinity and selectivity of YNL-TbYcgR N102W double mutants. Affinity measurements of purified double mutant YNL-TbYcgR biosensors containing N102W parent mutation. Data are from 3 replicates represented as mean ± SD.

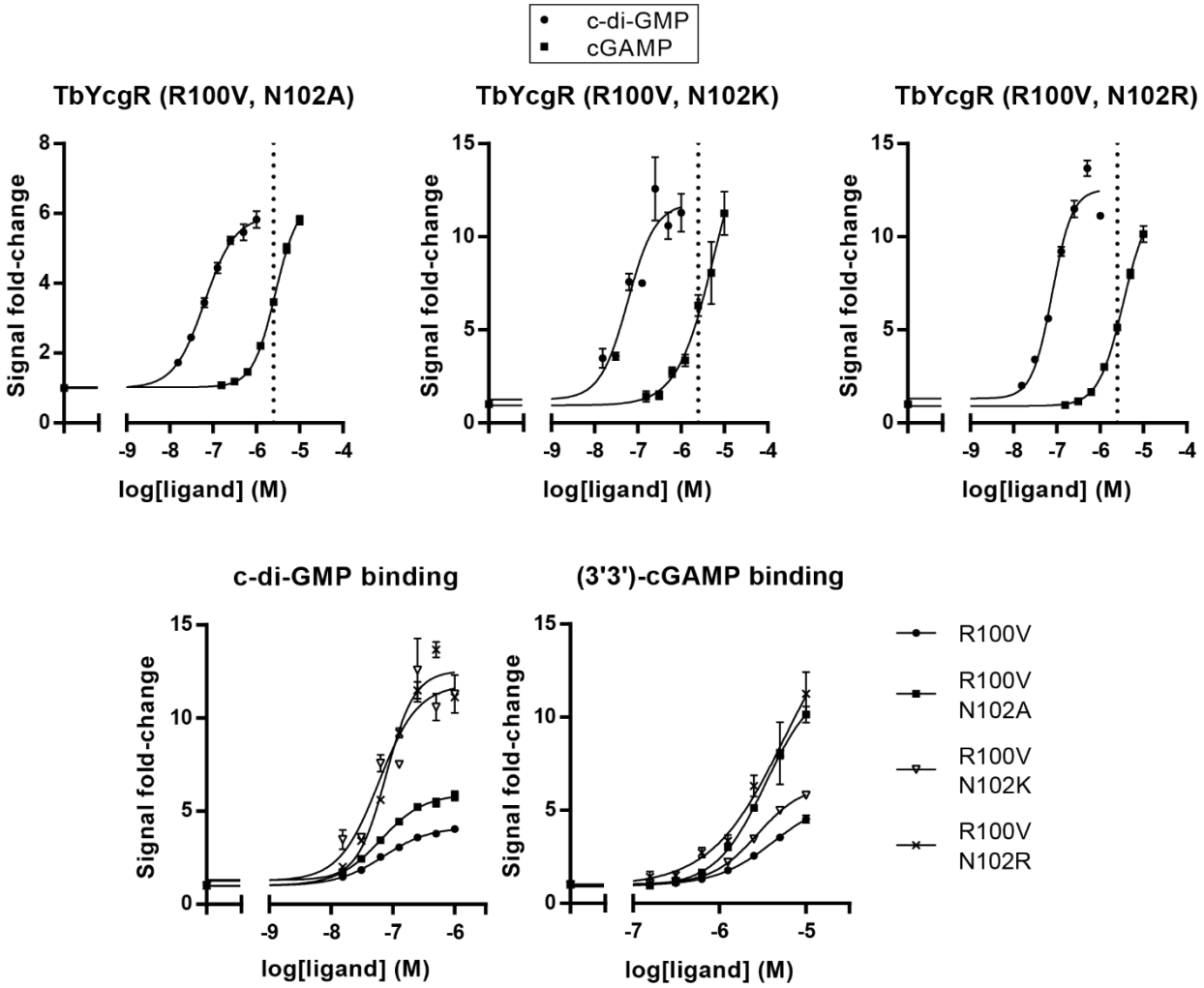

Figure 4.17 Binding affinity and selectivity of YNL-TbYcgR R100V double mutants. Affinity measurements of purified double mutant YNL-TbYcgR biosensors containing R100V parent mutation. Data are from 3 replicates represented as mean ± SD.

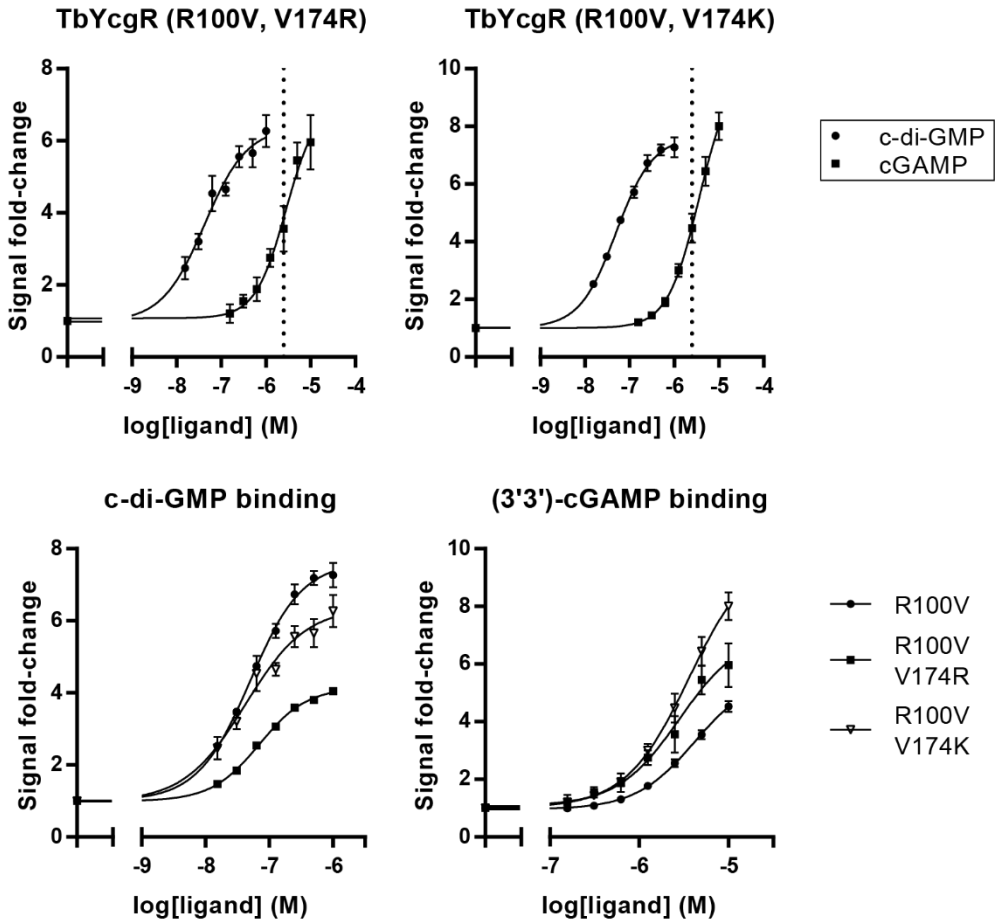

Figure 4.18 Binding affinity measurements of YNL-TbYcgR R100V double mutants. Affinity measurements of purified double mutant YNL-TbYcgR biosensors containing R100V parent mutation. Data are from 3 replicates represented as mean ± SD.

MATERIALS AND METHODS

General reagents and oligonucleotides. Commercial cyclic dinucleotide stocks were purchased from Axxora, LLC. Coelenterazine-h was purchased from NanoLight Technologies and stored as a ~6.15 mM stock in EtOH at –80 °C. Oligonucleotides used in molecular cloning were purchased from Elim Biopharmaceuticals or the University of Utah HSC Core Facility.

Molecular cloning. All initial site-saturation mutagenesis libraries were generated by around-the-horn style mutagenesis on the wild-type pET24-YNL-TbYcgR-mCherry template (see below for further details). For libraries containing 2 mutations, the corresponding single mutant pET24-YNL-TbYcgR-mCherry plasmid was used as the template. For protein purification, mutant TbYcgR sequences were amplified by PCR from the corresponding mutant pET24 template and cloned into the pRSET-YNL-TbYcgR scaffold between SacI and NcoI sites using Gibson cloning (Gibson, 2011).

Protein purification. Biosensor protein was purified as previously described (Dippel et al., 2018). *E. coli* BL21 (DE3) Star cells (Life Technologies) were co-transformed with the $pRSET_B$ vector encoding N-terminally His-tagged NL biosensor variants and the pCOLA-PdeH plasmid lacking a His-tag to enable purification of the biosensor without c-di-GMP bound. Transformants were cultured in 2xYT medium at 37 °C until OD reached ~0.8–1.0, followed by induction of protein expression with 0.1 mM IPTG for 20 h at 20 °C. Cells were collected and lysed by sonication in lysis buffer [50 mM Tris (pH 7.5), 150 mM NaCl, 20 mM imidazole, 5% (v/v) glycerol] with 300 µg/mL lysozyme and 1 mM PMSF added. Clarified lysate was bound to Ni-NTA agarose (Thermo Scientific), and resin was washed with lysis buffer supplemented with 500 mM NaCl prior to elution with lysis buffer supplemented with 300 mM imidazole. Using Amicon Ultra-15 Centrifugal Filter Units (molecular weight cutoff 10 kDa; Millipore), the elution fractions were concentrated and dialyzed to storage buffer [50 mM HEPES (pH 7.2), 100 mM KCl, 10% (v/v) glycerol]. Concentrated protein was flash frozen in liquid nitrogen then stored at -80 °C in small aliquots to prevent repetitive freeze-thaw cycles. Protein concentrations were determined using the absorption of Venus at 515 nm (extinction coefficient = 92200 M^{-1} cm^{-1}).

CDN synthase enzymes were purified as previously described with minor modifications (Kranzusch et al., 2014). His-tagged human cGAS (MBP-hcGAS), DncV (MBP-DncV), or mouse cGAS (SUMO-mcGAS) were transformed into *E. coli* BL21 (DE3) Star cells and transformants were cultured in ZYP-5052 auto-induction media [25 mM $(NH_4)_2SO_4$, 50 mM KH_2PO_4, 50 mM Na_2HPO_4, 1 mM $MgSO_4$, 0.5% (v/v) glycerol, 0.05% glucose, 0.2% α-lactose, 1% tryptone, and 0.5% yeast extract] (Studier, 2005) at 37 °C, 250 rpm for ~8 hours, followed by growth for an additional ~20 hours at 18 °C. Cells were collected and lysed by sonication in lysis buffer [20 mM HEPES (pH 7.5), 400 mM NaCl, 30 mM imidazole, 1 mM TCEP, 10% (v/v) glycerol] with 300 µg/mL lysozyme and 1 mM PMSF added. For cGAS purification, clarified lysate was supplemented with 50 µg/mL DNaseI and 10 mM $MgCl_2$ and incubated at 25 °C for 30 minutes to degrade any bound dsDNA. Clarified lysate was bound to Ni-NTA agarose (Thermo Scientific), and resin was washed with lysis buffer supplemented with 1 M NaCl prior to elution with lysis buffer supplemented with 300 mM imidazole. Using Amicon Ultra-15 Centrifugal Filter Units

(molecular weight cutoff 10 kDa; Millipore), the elution fractions were concentrated and dialyzed to storage buffer [20 mM HEPES (pH 7.5), 250 mM KCl, 1 mM TCEP, 10% (v/v) glycerol]. Concentrated protein was flash frozen in liquid nitrogen then stored at -80 °C in small aliquots to prevent repetitive freeze-thaw cycles. Protein concentrations were determined using A_{280} (MBP-hcGAS ε = 117230 M^{-1} cm^{-1}, MBP-DncV ε = 119750 M^{-1} cm^{-1}, SUMO-mcGAS ε = 45380 M^{-1} cm^{-1}).

Large scale enzymatic CDN synthesis and purification. MBP-DncV was used for large scale synthesis of (3'3')-cGAMP as previously described, with minor modifications (Launer-Felty and Strobel, 2018). A total of 2.5 µM enzyme was prepared in DncV reaction buffer [50 mM Tris (pH 7.5), 100 mM NaCl, 10 mM $MgCl_2$] with 1 mM ATP and 1 mM GTP (up to 10 mL scale reaction). The reaction was split into 1 mL aliquots and incubated at 37 °C for 3 hours, then at 70 °C for 10 min to quench. Precipitated components were removed by centrifugation (13200 rpm, 10 min), the supernatants were combined and filtered to remove residual particles, and then lyophilized. The lyophilized reaction was resuspended in ddH_2O (~10% of starting reaction volume) and the desired product was purified after separation on an Agilent 1260 Infinity HPLC using an Agilent Polaris 5 C18-A 250 x 10 mm column equipped with a Polaris 5 C18-A 50 x 10 mm guard. Reaction components were separated using a gradient of 100% solvent A to 95% solvent A over 15 minutes at 50 °C with a flow rate of 5 mL/min, solvent A being 100 mM NH_4OAc (pH 5) and solvent B being 100% acetonitrile. Purified fractions were combined and lyophilized at least 3 times to remove excess ammonia. Product purity was confirmed via LC-MS analysis.

SUMO-mcGAS was used for large scale synthesis of (2'3')-cGAMP and (2'3')-c-di-GMP. For (2'3')-cGAMP synthesis, a total of ~5-10 µM enzyme was prepared in cGAS reaction buffer [50 mM Tris (pH 7.5), 100 mM NaCl, 5 mM DTT, 10 mM $MgCl_2$, 0.1 mg/mL HT-DNA] with 1 mM ATP and 1 mM GTP. For (2'3')-c-di-GMP synthesis, a total of ~5-10 µM enzyme was prepared in modified cGAS reaction buffer [50 mM Tris (pH 8), 100 mM NaCl, 5 mM DTT, 10 mM $MnCl_2$, 0.1 mg/mL HT-DNA] with 2 mM GTP. Reactions were incubated at 37 °C for 16 hours, then quenched and purified as described above.

LC-MS analysis of CDNs. LC-MS analysis was performed on an Agilent 1260 Infinity HPLC equipped with a multi-wavelength detector and a 6120 Quadrupole MS. Samples were separated on an Agilent Poroshell 120 EC C-18 (2.7 µm particle, 4.6 x 50 mm) column equipped with a Poroshell 120 EC C-18 (2.7 µm particle, 4.6 x 5 mm) guard column. Separation was achieved using a previously published solvent system and gradient at a flow rate of 0.4 mL/min (Solvent A = 10 mM NH_4OAc with 0.1% acetic acid, Solvent B = 100% methanol) (Burhenne and Kaever, 2013).

Generation of site-saturation mutagenesis libraries. Site-saturation mutagenesis libraries were generated as previously described, with minor modifications (Kille et al., 2013). Oligonucleotides for each mutation site (3 mutant forward, 1 "silent" reverse) were phosphorylated using T4 PNK (NEB) following standard protocols. The three phosphorylated mutant primers were mixed in a 12:9:1 ratio (NDT:VHG:TGG) to generate the 22c forward primer mix (Table 4.5). An "around-the-horn" PCR was carried out using Phusion DNA polymerase (NEB) following standard protocols with ~5 ng template DNA and 1.5 µL each of the phosphorylated forward primer mix and

phosphorylated reverse primer per 50 µL PCR. After the PCR was complete, the template DNA was removed by adding 2 µL DpnI (NEB) per 50 µL reaction and incubating at 37 °C for >1.5 hours. The desired PCR product was separated by agarose gel electrophoresis, extracted, and purified. The gel-purified product was ligated overnight at 16 °C using T4 DNA ligase (NEB). The reaction was setup following standard protocols, except using 2 µL of T4 ligase and ~200 ng DNA per 20 µL reaction. Heat-inactivated T4 ligase reactions were transformed into chemically competent *E. coli* Mach1 cells (UC Berkeley QB3) (10 µL ligation + 100 µL competent cells). After heat shock and recovery in SOC media, a small aliquot of recovered cells was serially diluted (no dilution, 5x dilution, 25x dilution) and 10 µL of each dilution was spotted onto LB/Agar plates supplemented with 50 µg/mL kanamycin to determine transformation efficiency. For 22c libraries at least 100 CFUs are required to ensure sufficient library coverage, however >400 CFUs was deemed to be optimal. The remaining rescued cells were used to inoculate four 4 mL LB/Kan cultures that were grown overnight at 37 °C. Overnight cultures were miniprepped and combined to give the mixed library. Each library was sequenced and Q_{pool} values were calculated to ensure the quality ($Q_{pool} > 0.7$) (Sullivan et al., 2013).

Chemiluminescence measurements. All chemiluminescence measurements were performed in opaque white, 96-well LUMITRAC 600 plates (Grenier). Briefly, proteins and ligands were added to assay buffer [50 mM HEPES (pH 7.2), 100 mM KCl, 10 mM DTT, 0.1% BSA] to the given final concentrations in 100 µL reaction volume, then incubated at 28 °C for at least 10 min to reach binding equilibrium. All measurements using purified YNL biosensor proteins were made using 50 nM protein, except for the selectivity measurements in Figure 4.4, which were made using 100 nM protein. Chemiluminescent substrate was prepared by diluting coelenterazine-h to 60 µM in reagent buffer [50 mM HEPES (pH 7.2), 100 mM KCl, 300 mM ascorbate], and allowing the solution to equilibrate to RT for at least 30 min. Chemiluminescence at 28 °C was measured on a SpectraMax i3x platereader (Molecular Devices) by injecting 20 µL of chemiluminescent substrate, then integrating total chemiluminescent signal for 4 sec after a 3 sec delay.

Lysate-based screening of 22c libraries. The lysate-based assay for biosensor activity was carried out as previously described with minor modifications (Dippel et al., 2018). Single colonies of BL21(DE3) star *E. coli* cells transformed with pET24-biosensor-mCherry plasmids were resuspended in 500 µL of P-0.5G non-inducing media [0.5% glucose, 25 mM $(NH_4)_2SO_4$, 50 mM KH_2PO_4, 50 mM Na_2HPO_4, 1 mM $MgSO_4$] (Studier, 2005) supplemented with 100 µg/mL kanamycin in 2.2 mL 96-well deep well plates (VWR), then grown at 37 °C, 340 rpm, for 24 h to generate pre-cultures. A 5 µL aliquot of each pre-culture was used to inoculate 500 µL of ZYP-5052 auto-induction media [25 mM $(NH_4)_2SO_4$, 50 mM KH_2PO_4, 50 mM Na_2HPO_4, 1 mM $MgSO_4$, 0.5% (v/v) glycerol, 0.05% glucose, 0.2% α-lactose, 1% tryptone, and 0.5% yeast extract] (Studier, 2005) supplemented with 100 µg/mL kanamycin in deep well plates. Plates were grown at 37 °C, 340 rpm, for 20 h for biosensor expression. Cultures were harvested in the deep-well plate by centrifugation at 4700 rpm for 10 min at 4 °C. Supernatant media was removed and each cell pellet was resuspended in 350 µL screening buffer [50 mM Tris (pH 7.5), 100 mM KCl, 5% glycerol, 2 mM EDTA, 300 µg/mL lysozyme, 1 mM PMSF]. Cells were

gently lysed for 1 h at 4 °C and lysates were clarified by centrifugation at 6200 rpm for 40 min at 4 °C.

To obtain three samples, 90 µL aliquots of clarified lysates were pipetted into three wells of opaque white, 96-well LUMITRAC 600 plates (Grenier), being careful not to disturb the pelleted cell debris. For initial screening, each aliquot was mixed with 10 µL of either buffer, 10 µM c-di-GMP, or 50 µM (3'3')-cGAMP [in 50 mM HEPES (pH 7.2), 100 mM KCl] to produce final concentrations of 0, 1 µM c-di-GMP, and 5 µM (3'3')-cGAMP. For later screening rounds, different concentrations of 10x CDNs were used to achieve the desired final concentrations. Mixtures were incubated at 28 °C for at least 10 min to allow binding to occur, mCherry fluorescence signal (587 nm excitation, 615 nm emission) was measured for each well, then chemiluminescence was measured for each well as described above. Normalized lumin**e**scence (LUM/mCh) was determined for each well by dividing the total luminescent signal by the mCherry fluorescence for each well. Any clones that showed a LUM/mCh signal in buffer that was <1% of the WT (typically any LUM/mCh < 0.05) were classified as "dim" and disregarded from binding analysis. LUM/mCh values were used to calulate signal fold-changes for each clone (LUM/mCh signal with added ligand divided by LUM/mCh with no added ligand) and % signal with (3'3')-cGAMP over c-di-GMP (see equation below).

$$\%\ \boldsymbol{signal\ with\ (3'3')cGAMP\ over\ c-di-GMP} = \frac{(\boldsymbol{LUM/mCh})_{\boldsymbol{cGAMP}} - (\boldsymbol{LUM/mCh})_{\boldsymbol{buffer}}}{(\boldsymbol{LUM/mCh})_{\boldsymbol{c-di-GMP}} - (\boldsymbol{LUM/mCh})_{\boldsymbol{buffer}}} \times \mathbf{100}$$

Any clones that met the desired criteria were streaked from the NI media pre-culture onto LB/Agar plates supplemented with 50 µg/mL kanamycin to produce single colonies for re-screening. Pre-cultures were incubated at 37 °C, 340 rpm for ~1 hr prior to use. Single colonies from streak plates (typically 4 biological replicates each for re-screening) were resuspended in 500 µL of P-0.5G non-inducing media and re-screened as described above.

TABLES

Table 4.1 Relative selectivity of YNL-YcgR variants. Relative selectivity of YNL-YcgR variants against mixed-linkage and mixed-base CDNs, compared to c-di-GMP. Mixed-linkage corresponds to (2'3')-c-di-GMP; mixed-base corresponds to (3'3')-cGAMP; both corresponds to (2'3')-cGAMP. Data presented in figures 4.4 and 4.5.

	Selectivity *against*:		
	Mixed linkage	**Mixed base**	**Both**
*Tb*YcgR	100-fold	100-fold	>>2000-fold
*Cp*YcgR	200-fold	2000-fold	>>2000-fold
*Cb*YcgR	200-fold	2000-fold	>>2000-fold
*Tm*YcgR	2000-fold	>>2000-fold	>>2000-fold

Table 4.2 Screening results for sequenced TbYcgR mutants. Lysate screen results for sequenced mutants during "re-screen". Green color signifies increase compared to the parent sequence; red color signifies decrease compared to the parent sequence. Data presented in graphical form in figures 4.11 and 4.13. Data are from 4 biological replicates represented as the mean. [a]Percent signal value significantly greater than 100% due to differences in c-di-GMP and (3'3')-cGAMP binding.

	Parent	Mutation	% signal	Δ signal
Round 1 (5 µM cGAMP)	wt	--	65.5	5.7
	wt	R100V	100.3	3.0
	wt	R100L	109.5	2.8
	wt	R100K	89.7	3.5
	wt	R100M[a]	182.5	2.1
	wt	N102W	92.3	4.4
	wt	N102R	70.0	10.2
	wt	V136Q	48.7	16.6
	wt	S137Q	0.5	53.1
	wt	L142Y	7.4	11.3
Round 2 (2.5 µM cGAMP)	wt	N102W	52.8	3.7
	N102W	R100G	61.1	2.9
	N102W	R100T	69.9	2.4
	N102W	R100M	60.2	2.5
	N102W	V136Y	0.7	28.6
	N102W	V136Q	6.0	20.4
	N102W	S137Q	0.8	17.6
	wt	R100V	41.2	4.3
	R100V	N102R	50.5	9.8
	R100V	N102A	69.7	5.2
	R100V	N102K	67.9	7.7
	R100V	V174R	58.8	4.9
	R100V	V174K	56.4	5.6

Table 4.3 c-di-GMP-binding properties of purified YNL-TbYcgR mutants. Binding data quantified from graphs shown in Figures 4.15–4.18. Data are from 3 replicates represented as the mean. [a]Δsignal values are the "top" best-fit values calculated by the non-linear regression.

Sequence	K_D (nM)	Hill slope	Δ signal[a]
wt	<50	2.3	7.1
Single mutants			
N102W	<50	2.1	5.0
R100V	70	1.2	4.1
R100M	<50	1.5	2.4
N102W double mutants			
N102W, R100G	145	1.8	3.5
N102W, R100T	171	1.8	2.9
N102W, R100M	105	1.6	3.1
R100V double mutants			
R100V, N102R	77	1.9	12.6
R100V, N102A	64	1.2	5.9
R100V, N102K	59	1.4	11.8
R100V, V174R	<50	0.9	6.4
R100V, V174K	<50	1.1	7.6

Table 4.4 (3’3’)-cGAMP-binding properties of purified YNL-TbYcgR mutants. Binding data quantified from graphs shown in Figures 4.15–4.18. Data are from 3 replicates represented as the mean. [a]K_D values are calculated from “incomplete” curves and may not be accurate representations of the true affinity. [b]Δsignal values are the “top” best-fit values calculated by the non-linear regression.

Sequence	K_D (μM)[a]	Hill slope	Δ signal[b]
wt	3.1	1.6	6.5
Single mutants			
N102W	3.7	1.6	5.5
R100V	4.2	1.3	5.7
R100M	3.8	1.5	5.5
N102W double mutants			
N102W, R100G	4.6	1.5	7.1
N102W, R100T	3.9	1.6	4.2
N102W, R100M	4.9	1.7	3.8
R100V double mutants			
R100V, N102R	3.4	1.5	12
R100V, N102A	2.7	1.7	6.4
R100V, N102K	5.7	1	16.9
R100V, V174R	2.8	1.3	7.1
R100V, V174K	3.6	1.2	10

Table 4.5 Oligonucleotides used in this study. Oligos used for 22c library generation (all with 22c in the name) were ordered from the Utah HSC core as “40 nmol” synthesis to include cartridge purification and increase purity.

Name	Sequence (5' to 3')
FWD-TbYcgR-seq	TTAACCAGAAAGTGGAAGTGC
FWD-RLuc8-seq	GGTACCAAGGTGTACGACC
FWD-sensor domain-YNL 91-insert	GGCAACGGCAGCccat
REV-sensor domain-YNL 91-insert	TGGTCCAGCAGCCTGTAgagc
FWD-22c-S137-TbYcgR-1	ndtGGCGGCGGCCTGCTGA
FWD-22c-S137-TbYcgR-2	vhgGGCGGCGGCCTGCTGA
FWD-22c-S137-TbYcgR-3	tggGGCGGCGGCCTGCTGA
REV-22c-S137-TbYcgR	CACGTTCACGGTTTCGGTGCG
FWD-22c-N102-TbYcgR-1	ndtTTTGTGCGCGTGCCGGC
FWD-22c-N102-TbYcgR-2	vhgTTTGTGCGCGTGCCGGC
FWD-22c-N102-TbYcgR-3	tggTTTGTGCGCGTGCCGGC
REV-22c-N102-TbYcgR	ACGACGTTGGATACGACGAACCGTAC
FWD-22c-V136-TbYcgR-1	ndtAGCGGCGGCGGCCTG
FWD-22c-V136-TbYcgR-2	vhgAGCGGCGGCGGCCTG
FWD-22c-V136-TbYcgR-3	tggAGCGGCGGCGGCCTG
REV-22c-V136-TbYcgR	GTTCACGGTTTCGGTGCGATAAAT
FWD-22c-G139-TbYcgR-1	ndtGGCCTGCTGATTAAAAGCCCGTTTAAAC
FWD-22c-G139-TbYcgR-2	vhgGGCCTGCTGATTAAAAGCCCGTTTAAAC
FWD-22c-G139-TbYcgR-3	tggGGCCTGCTGATTAAAAGCCCGTTTAAAC
REV-22c-G139-TbYcgR	GCCGCTCACGTTCACGGTTTC
FWD-22c-R100-TbYcgR-1	ndtCGTAACTTTGTGCGCGTGCCG
FWD-22c-R100-TbYcgR-2	vhgCGTAACTTTGTGCGCGTGCCG
FWD-22c-R100-TbYcgR-3	tggCGTAACTTTGTGCGCGTGCCG
REV-22c-R100-TbYcgR	TTGGATACGACGAACCGTACTTGGC
FWD-22c-L142-TbYcgR-1	ndtATTAAAAGCCCGTTTAAACTGAGCGAAGG
FWD-22c-L142-TbYcgR-2	vhgATTAAAAGCCCGTTTAAACTGAGCGAAGG
FWD-22c-L142-TbYcgR-3	tggATTAAAAGCCCGTTTAAACTGAGCGAAGG
REV-22c-L142-TbYcgR	CAGGCCGCCGCCGCT
FWD-22c-V174-TbYcgR-1	ndtCGTGTGGAGGAAAAACGCGAACAG
FWD-22c-V174-TbYcgR-2	vhgCGTGTGGAGGAAAAACGCGAACAG
FWD-22c-V174-TbYcgR-3	tggCGTGTGGAGGAAAAACGCGAACAG
REV-22c-V174-TbYcgR	AACTTGACCACGGGCATTAACTGGACC
FWD-22c-R175-TbYcgR-1	ndtGTGGAGGAAAAACGCGAACAGAGCC
FWD-22c-R175-TbYcgR-2	vhgGTGGAGGAAAAACGCGAACAGAGCC
FWD-22c-R175-TbYcgR-3	tggGTGGAGGAAAAACGCGAACAGAGCC
REV-22c-R175-TbYcgR	AACAACTTGACCACGGGCATTAACTGG
FWD-22c-R100-TbYcgR N102W-1	ndtCGTTGGTTTGTGCGCGTGC

FWD-22c-R100-TbYcgR N102W-2	vhgCGTTGGTTTGTGCGCGTGC
FWD-22c-R100-TbYcgR N102W-3	tggCGTTGGTTTGTGCGCGTGC
REV-22c-N102-TbYcgR R100V	ACGCACTTGGATACGACGAACCGTAC
REV-22c-N102-TbYcgR R100V	ACGCACTTGGATACGACGAACCGTAC

REFERENCES

Ablasser, A., Goldeck, M., Cavlar, T., Deimling, T., Witte, G., Röhl, I., Hopfner, K.P., Ludwig, J., and Hornung, V. (2013). cGAS produces a 2′-5′-linked cyclic dinucleotide second messenger that activates STING. Nature *498*, 380–384.

Acevedo-Rocha, C.G., Reetz, M.T., and Nov, Y. (2015). Economical analysis of saturation mutagenesis experiments. Sci. Rep. *5*, 1–12.

Benach, J., Swaminathan, S.S., Tamayo, R., Handelman, S.K., Folta-Stogniew, E., Ramos, J.E., Forouhar, F., Neely, H., Seetharaman, J., Camilli, A., et al. (2007). The structural basis of cyclic diguanylate signal transduction by PilZ domains. EMBO J. *26*, 5153–5166.

Binkowski, B.F., Butler, B.L., Stecha, P.F., Eggers, C.T., Otto, P., Zimmerman, K., Vidugiris, G., Wood, M.G., Encell, L.P., Fan, F., et al. (2011). A luminescent biosensor with increased dynamic range for intracellular cAMP. ACS Chem. Biol. *6*, 1193–1197.

Bose, D., Su, Y., Marcus, A., Raulet, D.H., and Hammond, M.C. (2016). An RNA-Based Fluorescent Biosensor for High-Throughput Analysis of the cGAS-cGAMP-STING Pathway. Cell Chem. Biol. *23*, 1–11.

Burdette, D.L., Monroe, K.M., Sotelo-Troha, K., Iwig, J.S., Eckert, B., Hyodo, M., Hayakawa, Y., and Vance, R.E. (2011). STING is a direct innate immune sensor of cyclic di-GMP. Nature *478*, 515–518.

Burhenne, H., and Kaever, V. (2013). Quantification of Cyclic Dinucleotides by Reversed-Phase LC-MS/MS. In Methods in Molecular Biology, pp. 27–37.

Chen, Q., Sun, L., and Chen, Z.J. (2016). Regulation and function of the cGAS-STING pathway of cytosolic DNA sensing. Nat. Immunol. *17*, 1142–1149.

Chica, R.A., Doucet, N., and Pelletier, J.N. (2005). Semi-rational approaches to engineering enzyme activity: Combining the benefits of directed evolution and rational design. Curr. Opin. Biotechnol. *16*, 378–384.

Chou, S., and Galperin, M.Y. (2016). Diversity of Cyclic Di-GMP-Binding Proteins and Mechanisms. J. Bacteriol. *198*, 32–46.

Corrales, L., Glickman, L.H., McWhirter, S.M., Kanne, D.B., Sivick, K.E., Katibah, G.E., Woo, S.R., Lemmens, E., Banda, T., Leong, J.J., et al. (2015). Direct Activation of STING in the Tumor Microenvironment Leads to Potent and Systemic Tumor Regression and Immunity. Cell Rep. *11*, 1018–1030.

Diner, E.J., Burdette, D.L., Wilson, S.C., Monroe, K.M., Kellenberger, C.A., Hyodo, M., Hayakawa, Y., Hammond, M.C., and Vance, R.E. (2013). The Innate Immune DNA Sensor cGAS Produces a Noncanonical Cyclic Dinucleotide that Activates Human STING. Cell Rep. *3*, 1355–1361.

Dippel, A.B., Anderson, W.A., Evans, R.S., Deutsch, S., and Hammond, M.C. (2018). Chemiluminescent Biosensors for Detection of Second Messenger Cyclic di-GMP. ACS Chem. Biol. *13*, 1872–1879.

Eaglesham, J.B., Pan, Y., Kupper, T.S., and Kranzusch, P.J. (2019). Viral and metazoan poxins are cGAMP-specific nucleases that restrict cGAS–STING signalling. Nature *566*, 259–263.

Gaffney, B.L., Veliath, E., Zhao, J., and Jones, R.A. (2010). One-Flask Syntheses of c-di-GMP and the [Rp,Rp] and [Rp,Sp] Thiophosphate Analogues. Org. Lett. *12*, 3269–3271.

Gao, P., Ascano, M., Wu, Y., Barchet, W., Gaffney, B.L., Zillinger, T., Serganov, A.A., Liu, Y., Jones, R. a., Hartmann, G., et al. (2013). Cyclic [G(2′,5′)pA(3′,5′)p] is the metazoan second messenger produced by DNA-activated cyclic GMP-AMP synthase. Cell *153*, 1094–1107.

Gibson, D.G. (2011). Enzymatic assembly of overlapping DNA fragments. Methods Enzymol. *498*, 349–361.

Hepworth, D., Snyder, W., Tyminski, E., Horn, M., Pierce, B., Lin, D., Aulabaugh, A., Nistler, R., Wong, J., Weng, S., et al. (2017). Discovery of PF-06928215 as a high affinity inhibitor of cGAS enabled by a novel fluorescence polarization assay. PLoS One *12*, e0184843.

Kille, S., Acevedo-Rocha, C.G., Parra, L.P., Zhang, Z.G., Opperman, D.J., Reetz, M.T., and Acevedo, J.P. (2013). Reducing codon redundancy and screening effort of combinatorial protein libraries created by saturation mutagenesis. ACS Synth. Biol. *2*, 83–92.

Ko, J., Ryu, K.S., Kim, H., Shin, J.S., Lee, J.O., Cheong, C., and Choi, B.S. (2010). Structure of PP4397 reveals the molecular basis for different c-di-GMP binding modes by pilz domain proteins. J. Mol. Biol. *398*, 97–110.

Kranzusch, P., Lee, A.Y., Berger, J., and Doudna, J. (2013). Structure of Human cGAS Reveals a Conserved Family of Second-Messenger Enzymes in Innate Immunity. Cell Rep. *3*, 1362–1368.

Kranzusch, P., Lee, A.Y., Wilson, S., Solovykh, M., Vance, R., Berger, J., and Doudna, J. (2014). Structure-Guided Reprogramming of Human cGAS Dinucleotide Linkage Specificity. Cell *158*, 1011–1021.

Kranzusch, P.J., Wilson, S.C., Lee, A.S.Y., Berger, J.M., Doudna, J.A., and Vance, R.E. (2015). Ancient Origin of cGAS-STING Reveals Mechanism of Universal 2’,3’ cGAMP Signaling. Mol. Cell *59*, 891–903.

Lama, L., Adura, C., Xie, W., Tomita, D., Kamei, T., Kuryavyi, V., Gogakos, T., Steinberg, J., Miller, M., Ramos-Espiritu, L., et al. (2019). Development of human cGAS-specific small-molecule inhibitors for repression of dsDNA-triggered interferon expression. Nat. Commun. In Press.

Launer-Felty, K.D., and Strobel, S.A. (2018). Enzymatic synthesis of cyclic dinucleotide analogs by a promiscuous cyclic-AMP-GMP synthetase and analysis of cyclic dinucleotide responsive riboswitches. Nucleic Acids Res. 1–12.

Li, L., Yin, Q., Kuss, P., Maliga, Z., Millán, J.L., Wu, H., and Mitchison, T.J. (2014).

Hydrolysis of 2'3'-cGAMP by ENPP1 and design of nonhydrolyzable analogs. Nat. Chem. Biol. *10*, 1043–1048.

Patrick, W.M., Firth, A.E., and Blackburn, J.M. (2003). User-friendly algorithms for estimating completeness and diversity in randomized protein-encoding libraries. Protein Eng. *16*, 451–457.

Ramanjulu, J.M., Pesiridis, G.S., Yang, J., Concha, N., Singhaus, R., Zhang, S.-Y., Tran, J.-L., Moore, P., Lehmann, S., Eberl, H.C., et al. (2018). Design of amidobenzimidazole STING receptor agonists with systemic activity. Nature.

Rao, F., Pasunooti, S., Ng, Y., Zhuo, W., Lim, L., Liu, A.W., and Liang, Z.X. (2009). Enzymatic synthesis of c-di-GMP using a thermophilic diguanylate cyclase. Anal. Biochem. *389*, 138–142.

Reetz, M.T. (2011). Laboratory evolution of stereoselective enzymes: A prolific source of catalysts for asymmetric reactions. Angew. Chemie - Int. Ed. *50*, 138–174.

Reetz, M.T., and Carballeira, J.D. (2007). Iterative saturation mutagenesis (ISM) for rapid directed evolution of functional enzymes. Nat. Protoc. *2*, 891–903.

Ryjenkov, D.A., Simm, R., Römling, U., and Gomelsky, M. (2006). The PilZ domain is a receptor for the second messenger c-di-GMP: The PilZ domain protein YcgR controls motility in enterobacteria. J. Biol. Chem. *281*, 30310–30314.

Saito, K., Chang, Y.-F., Horikawa, K., Hatsugai, N., Higuchi, Y., Hashida, M., Yoshida, Y., Matsuda, T., Arai, Y., and Nagai, T. (2012). Luminescent proteins for high-speed single-cell and whole-body imaging. Nat. Commun. *3*, 1262.

Shang, G., Zhang, C., Chen, Z.J., Bai, X. chen, and Zhang, X. (2019). Cryo-EM structures of STING reveal its mechanism of activation by cyclic GMP–AMP. Nature *567*, 389–393.

Steiner, K., and Schwab, H. (2012). Recent Advances in Rational Approaches for Enzyme Engineering. Comput. Struct. Biotechnol. *2*, 1–12.

Studier, F.W. (2005). Protein production by auto-induction in high-density shaking cultures. Protein Expr. Purif. *41*, 207–234.

Sullivan, B., Walton, A.Z., and Stewart, J.D. (2013). Library construction and evaluation for site saturation mutagenesis. Enzyme Microb. Technol. *53*, 70–77.

Tang, L., Gao, H., Zhu, X., Wang, X., Zhou, M., and Jiang, R. (2012). Construction of "small-intelligent" focused mutagenesis libraries using well-designed combinatorial degenerate primers. Biotechniques *52*, 149–158.

Vincent, J., Adura, C., Gao, P., Luz, A., Lama, L., Asano, Y., Okamoto, R., Imaeda, T., Aida, J., Rothamel, K., et al. (2017). Small molecule inhibition of cGAS reduces interferon expression in primary macrophages from autoimmune mice. Nat. Commun. *8*, 1–12.

Yoh, S.M., Schneider, M., Seifried, J., Soonthornvacharin, S., Akleh, R.E., Olivieri, K.C.,

De Jesus, P.D., Ruan, C., De Castro, E., Ruiz, P.A., et al. (2015). PQBP1 is a proximal sensor of the cGAS-dependent innate response to HIV-1. Cell *161*, 1293–1305.